Réponse sismique à un forçage magmatique

Paola Traversa

Observatoire des Sciences de l'Univers de Grenoble
Laboratoire de Géophysique Interne et Tectonophysique

Thèse

présentée par

Paola TRAVERSA

Réponse sismique à un forçage magmatique.

Seismic response to magma forcing.

---

pour obtenir le titre de

Docteur de l'Université Joseph Fourier - Grenoble I

Spécialité : Terre Solide

Date de soutenance: le 22 octobre 2009

Composition du jury :

Ian MAIN	Grant Institute of Earth Science (Edinburgh, UK)	Rapporteur
Gilberto SACCOROTTI	Istituto Nazionale Geofisica Vulcanologia (Pisa, IT)	Rapporteur
Valérie CAYOL	Université Blaise Pascal (Clermont Ferrand)	Examinateur
Olivier COUTANT	Université Joseph Fourier (Grenoble)	Examinateur
Valérie FERRAZZINI	Institut de la Physique du Globe de Paris	Examinateur
Jean VANDEMEULEBROUCK	Université de Savoie (Chambery)	Examinateur
Jean-Robert GRASSO	Université Joseph Fourier (Grenoble)	Directeur de thèse

Abstract

This work focuses on the seismic response of a volcano to different magmatic processes with the aim of sheding light on their driving physics as tracked by seismicity. We study seismic time series recorded at basaltic volcanoes and identify generic seismicity patterns characteristic of (i) inter-eruptive, (ii) reservoir feeding, (iii) reservoir leak, and (iv) dyke injection phases of volcanic activity. Seismicity recorded during repose phases mimics the behavior of "ordinary" tectonic seismicity. During the last phase immediately before an eruption, the stationary seismicity rate accompanying the dyke injection we observe on different volcanoes, reveals that the fluid-driven crack propagation is a scale independent stationary process. This is reminiscent of the brittle creep damage recorded in strain driven settings and it prevents any prediction of the eruption time. It argues for the stationary seismicity rate accompanying the intrusion to be a proxy for a constant magma supply rate from the magma reservoir. Through a numerical model of dyke propagation we validate the hypothesis of constant magma flow rate feeding the dyke in the volcano dynamics setting. The impact of such a model allows us to bound a minimum size for the magma reservoir and a maximum value for the magma overpressure at Piton de la Fournaise volcano. The exploration of the seismic sequence driven by the 2000 Izu Islands (Japan) dyke intrusion allows us to quantify the stress perturbations induced over space and time by this giant intrusive episode. We show that the dyke intrusion can be assimilated to a "slow event" mainshock, which allows to follow the evolution of the brittle damage of the rock matrix during fracture propagation. On Ubinas andesitic volcano, we resolve an average acceleration of Long Period (LP) seismicity prior to both, explosions and LP events. It brings new evidence for LP events to be brittle damage events within a fluid-filled conduit.

Resumé

Dans ce travail nous étudions la réponse sismique d'un volcan à différents processus magmatiques, avec l'objectif de remonter à la physique qui les dirige. Les séries temporelles de sismicité enregistrées sur des volcans basaltiques nous ont permis d'identifier des motifs caractéristiques d'activité sismique pendant les phases (i) inter-éruptive, (ii) d'alimentation du réservoir, (iii) de fissuration du réservoir et fuite du magma, et (iv) d'injection de dyke. La sismicité enregistrée pendant les phases de repos reproduit le comportement de la sismicité tectonique ordinaire. Pendant la derniére phase immédiatement précedente l'éruption, nous observons un taux de sismicité stationnaire sur différents volcans, qui accompagne l'injection du dyke. Il nous révèle que la propagation de la fracture, guidée par le fluide, est un processus stationnaire, indépendant de léchelle. De telles caractéristiques évoquent l'endommagement enregistré lors d'essais de fluage à déformation contrôlée, et impliquent l'impossibilité de prédire le temps d'occurrence de l'éruption. Cela suggère que le taux de sismicité stationnaire qui accompagne une intrusion est proportionnel à un taux constant d'approvisionnement de magma du réservoir. Grace à un modèle numérique de propagation de dyke, nous avons validé l'hypothèse qu'un flux constant de magma qui alimente le dyke est en accord avec la dynamique du volcan. L'application de ce modè nous permet alors de contraindre une taille minimale pour le réservoir magmatique et une valeur maximale pour la surpression du magma dans le réservoir du Piton de la Fournaise (Réunion). L'exploration de la séquence sismique induite par l'intrusion d'un dyke en 2000 aux Îles Izu (Japon) nous permet de quantifier les perturbations de contrainte induites en temps et en espace par ce gigantesque dyke. Nous montrons que l'intrusion d'un dyke peut être assimilée à un "événement lent". Cela nous permet de suivre l'évolution de l'endommagement de la matrice rocheuse au cours de la propagation de la fracture. Pour le volcan andésitique Ubinas (Pérou), nous identifions une accéleration moyenne de sismicité Long Période (LP) précédant les explosions et autres LP. Cela apporte de nouvelles évidences que les LP correspondent à un endommagement fragile au sein d'un conduit rempli de fluide.

Contents

Remerciements

Ce travail de thèe a été pour moi, en plus qu'une possibilité d'apprendre qu'est que la recherche académique, d'étudier un sujet passionnant tel que la physique des séismes et des éruptions volcaniques, surtout il a été l'occasion de connaître, vivre et apprendre un pays qui est proche du mien, mais pas tout à fait pareil...

A l'issue de ce travail de thèse et de ces dernières trois années passées au sein du LGIT de Grenoble, j'aurai un nombre énorme de remerciement à faire, j'essaierai de me limiter à quelques mots. Premièrement je tiens à remercier Jean-Robert, mon directeur de thèse, qui un jour a décidé de me faire confiance, même si je manquais de toute experience sur le sujet. Il m'a guidée et soutenue tout le long de ces trois années, il m'a appris à faire confiance à mon intuition et à me servir toujours de ma fantasie. Partager ce travail et ce temps avec lui, toujours libre d'à-priori et de cadre rigide, toujours plein d'enthousiasme et prêt à écouter et à me remonter le moral lors des moments sombres, a été un vrai bonheur. Un grand merci aussi à tous ceux qui ont été impliqué plus ou moins diréctement dans mon travail de thèse. Merci à Virginie P., qui n'aurait pas pu arriver à un moment meilleur, en me proposant de travailler ensemble sur celui qui est devenu mon troisième chapitre de thèse, et qui m'a permis de ressortir toute ma motivation et ma passion pour le sujet à un moment où je commençais à douter de ma perseverance et à me demander si jamais j'aurai atteint le but (la thèse n'est pas rose tout le temps!!) Merci à Agnès H., pour toutes ses réponses à mes innombrables questions, doutes et problèmes techniques, réponses que pendant un bon moment m'étaient absolument obscures, mais qui, passé un certain cap, se sont toujours révélées précises et très précieuses. Merci à David A., pour les discussions à la cafét', ses conseils et ses contributions directes à mon travail, qui ont porté à l'explorartion de sujets de travail très stimulants, qui malheureusement n'ont pas pu être inclulses dans ce manuscrit. Fort vivement ils seront menés à terme dans un prochain futur. Merci à tous les memebres du projet Volume (et merci à l'Union Européenne de nous avoir financé!!), dont les rencontres semestrielles étaient une occasion trépidamment attendue

pour se revoir, en tant qu'amis, ainsi que collègues de travail passionnés et ouverts à l'échange et au partage des savoirs. Dans ce cadre je tiens à remercier en particulier l'équipe irlandaise (ou mieux Italo-Irlandaise) de l'UCD de Dublin pour les moments inoubliables passés ensemble à se balader par les volcans (et ailleurs) du monde, merci Chris, Aoife, Francesca, Rosi, Ivan, Gareth et Lorenzo. Merci également aux membres de l'INGV, Luciano, Mimmo, Giovanni, et surtout Gilberto, qui, premier, m'a introduite à la sismologie volcanique. Et merci encore à toute l'équipe Volcans du LGIT Chambery, qui m'a accueillie et adoptée dès le début de ma thèse. Merci Olivier, Aurélie, PF, Estelle, Florence, Fabien, Philippe, Jean, Jean-Luc, Bernard, David!

Un grand remerciement va aux membres de mon jury, pour leurs commentaires très intéressant, constructif et stimulant, pour avoir été présents le jour de ma soutenance, pour avoir alimenté la discussion fort intéressante qui a suivi la présentation et pour avoir terminé le journée ensemble devant une succulente pizza!!

Un gros remerciement est du aussi à tous ceux qui n'ont pas forcement participé directement à mon travail de thèse, mais qui ont rendu ce trois ans spéciales, riches, drôles, trop courts? Merci à Jacques P. pour son aide irremplaçable (et toujours donné avec un sourire) dans toutes mes démarches administratives, tout juste debarquée en France et après! Merci à tous les autres membres de l'équipe administrative, Zoubida, Sophie, France, Gaëlle, pour toute les fois que je vous ai cassé les pieds avec mes ordres de mission!!

Parce qu'ils m'ont supportée et encouragée au quotidian une grosse portion de mes remerciements va également à tous les amis: merci à Elisabeth et Lucille, qui ont partagé avec moi toutes les étapes de cette expérience et avec qui, chacune à son tour, on a écouté patiemment les plaintes et les frustration des autres, devant notre incontournable tasse de thé de 17h00. Merci à tous les copains qui ont partagé au moins un bout de ces trois ans et participé à rendre l'ambience chaleureuse et agréable, au boulot comme les soirées et weekends: Florence, Aloé, Seb H., Steph, Louis, Laurent, Pierre, Nathalie, Thomas, Antony, Renaud, Seb B., Ben T., Ben B., Lionel. Merci à tous les colocs (au moins ceux que j'ai connu!) de la maison du Bonheur de St. Egrève, où la fantasie des soirée était inepuisable et sympathie et chaleur n'ont jamais manqué, Pam, Mik, MatQ, Oliv, Ben, Gaëlle, Beb...!

Merci à mes parents, qui ont accepté plus ou moins de bon gré le fait de me voir partir (probablement définitivement) à l'étranger, et qui du coup ont réussi à prévoir toute une forme de 50kg de parmesan pour mon pot de thèse, probablement pour être sûrs de me rappeler d'où je viens...

Et enfin la personne qui plus de tous a été à mes cotés pour me soutenir, m'encourager, supporter mes quelque gros coups de stress, faire de mes weekends du relax, des fantastiaques moments ensemble, du divertissemnt, des balades, du soleil, de l'air libre... Merci Guillaume pour tout ce que tu me fais vivre!

General Introduction

Volcanoes are complex dynamical systems [e.g. *Sparks*, 2003; *Lahaie and Grasso*, 1998] within which several non-linear, stochastic processes coexist and interact, eventually resulting in an eruption [e.g. *Grasso and Bachelery*, 1995; *Lahaie and Grasso*, 1998; *Melnik and Sparks*, 1999; *Sparks*, 2003]. Such non-linear and unsteady interactions potentially lead to volcano behaviors which are inherently unpredictable [*Melnik and Sparks*, 1999]. Indeed, although possible systematic evolutionary trend and quite periodic behaviors may exist, deterministic eruption prediction still fails in forecasting if, how and when a reactivated volcano will erupt [e.g. *McGuire and Kilburn*, 1997; *Sparks*, 2003; *Grasso and Zaliapin*, 2004].

Physical properties of magmas are strongly dependent on temperature, melt composition, water content, degassing and crystallization processes [e.g. *Melnik and Sparks*, 1999; *Sparks*, 2003]. Besides, the edifice rock materials within which magma moves and interacts, are composite and heterogeneous, hosting fracture networks with hierarchical structure [e.g. *Grasso and Bachelery*, 1995]. During magma chamber evolution and magma transport via dyke propagation, several processes take place, such as pressure changes, heat transfers and chemical reactions. Hence, magma undergoes profound changes in physical properties during its ascent to the volcano surface. Such pressure, temperature changes and chemical reactions, which characterize active magmatic systems, interact with their surroundings, inducing ground deformation, rock failure, hydrothermal or groundwater system disturbance, degassing and other effects. These phenomena generate geophysical and geochemical observables (e.g. seismicity, ground deformation, gas emissions) on volcano surface, which thus allow observers to indirectly detect mass movements within volcanoes.

This has motivated the setting up and installation of several types of monitoring equipment networks on volcanoes, with the aim of improving the understanding on the physics of volcano processes and eventually to develop forecasting procedures on eruption

occurrence.

In this work, among the monitored observables, we consider volcano seismicity as the surface expression of magma processes occurring at depth within the edifice. Our goal is to understand the physics and dynamics governing volcano processes eventually leading to an eruption, as tracked by seismicity. The idea at the base of this work is to isolate simple volcano processes and to detect characteristic patterns of contemporary seismicity, as described by its spatio-temporal distributions. From this mechanical response of the volcanic system to a perturbation induced by a given volcano process, we derive implications on the physics driving such active process. Further, we aim at exploring and quantifying the peculiarities of volcano seismicity as described by its spatio-temporal characteristics and organization during different phases of volcanic activity.

Seismicity at volcanoes manifests itself into two distinct type of processes, those originating in the fluid (i.e. gases and geothermal fluids) and those originating in the solid matrix. The first provide information about the state of the fluid, while the earthquakes related to the processes originating into the solid are associated to brittle shear failures within the rock matrix [e.g. *Chouet*, 1996; *McNutt*, 2002; *Sparks*, 2003, and references therein]. The first category includes different types of events, such as Long Period (LP), Very Long Period (VLP) and tremor activity, while the brittle failures of the rock matrix are called Volcano Tectonic (VT) events, due to their similarity to tectonic earthquakes. [e.g. *Minakami*, 1960, 1974; *Chouet*, 1996; *McNutt*, 2002].

VT earthquakes are considered as prominent precursors and contemporaries of magma creating its pathway towards the surface [e.g. *Sparks*, 2003; *Collombet et al.*, 2003; *Chastin and Main*, 2003; *Grasso and Zaliapin*, 2004]. The origin of VT seismicity has to be sought in the deformation of heterogeneous volcanic rock mass induced by pressure and temperature variations, or mass movements within the edifice [e.g. *Rubin and Gillard*, 1998]. VT earthquakes are thus the brittle response of the solid matrix to the stress perturbations induced by magma processes within the volcanic edifice. Their importance as surface observables for underlying magma processes lies thus in the fact that they are thought to act as gauges that map stress concentrations distributed over a large volume surrounding magma conduits and reservoirs [*Grasso and Bachelery*, 1995; *Chouet*, 1996; *Rubin and Gillard*, 1998].

This manuscript focuses essentially on the study of Volcano Tectonic events, their relationships with their driving magma processes, and their spatio-temporal occurrence

peculiarities. Particular attention is addressed to the mechanisms that govern earthquake generation and its spatio-temporal organization as a result of (i) the forcing imposed by the active volcano process and (ii) the interactions between earthquakes. This leads us to derive some deductions and implications about the peculiarity of volcano seismicity when compared to "classic" tectonic seismicity.

The first introductory chapter is meant to provide a theoretical background on all the geophysical objects and tools that are used throughout the following pages. After this initial overview, we enter the heart of our work. Since a large amount of our effort has been devoted to the study of dyke intrusions at basaltic volcanoes, we decided to divide the manuscript into two major parts. The first focuses on such very last phase preceding a basaltic eruption, i.e. the magma ascent via dyke injection from a shallow reservoir towards the surface. In the second part, the relationship between induced seismicity and different driving volcano processes is explored. Further, the temporal patterns of seismic occurrence accompanying several processes are studied and compared.

In the second chapter we describe the brittle response of a basaltic volcano to dyke intrusions, with the aim of deriving entailments about the physics controlling this very last phase before the eruption onset. Dykes are the most efficient mean of moving magma from depth to the volcano surface. Such sheet-like fluid-filled fractures are created through fluid-induced fracturing, held open by the fluid pressure, and rose by fluid dynamics [*Lister*, 1990a,b; *Lister and Kerr*, 1991; *Rubin*, 1995; *Menand and Tait*, 2002; *Roper and Lister*, 2005]. Dykes propagate within the host rocks under the action of ambient stress and mostly act against the confining pressure rather than the strength of the materials [e.g. *Rubin et al.*, 1998]. We show that dyke-induced seismicity at basaltic volcanoes is characterized by a scale independent stationarity in terms of seismic and energy release rates, such that any prediction for eruption time is prevented. This stationarity, which evidences the dyke injection is a steady-state brittle creep process, suggests a constant volume change induced into the edifice by the magma intrusion in the unit time. It argues for the stationary seismicity rate accompanying the intrusion to be a proxy for the constant magma supply rate from the reservoir.

Although already employed in dyke propagation modeling [*Lister*, 1990a,b], such hypothesis of constant magma flux withdrawn from the reservoir to feed the dyke growth, has been considered "geologically non appropriate" [*Meriaux and Jaupart*, 1998; *Roper and Lister*, 2005] face to the other boundary condition of a constant overpressure in the reser-

voir [*Rubin*, 1993a,b; *Meriaux and Jaupart*, 1998; *Roper and Lister*, 2005]. On the other hand, *Ida* [1999] claims that only in the case of an extremely large and compressible magma reservoirs, the melt pressure is actually able to keep constant as the dyke propagates. This puzzle motivates our third chapter, where we employ a two-phase dyke propagation numerical model to test the validity of the constant magma flux hypothesis and to explore under which geophysical conditions this is realistic. We demonstrate that such two apparently mutually excluding boundary conditions have no reason to be. In the numerical model we test, we do not impose one rather than the other initial condition. This two-phase dyke propagation model allows us to follow the dynamics of dyke propagation from an overpressured magma source to the eruption site without a-priori on the reservoir behavior. In addition, the application of the model to a real and well-observed case of dyke propagation enables us to bound physical parameters characterizing the magma reservoir at the Piton de la Fournaise volcano (La Réunion).

Results illustrated in chapter three drive us to conclude that seismicity contemporary to dyke intrusion is controlled by the volume change induced to the system in the unit time by the intruding magma. This suggests that dyke-induced seismicity is controlled by the stressing rate change generated by the intruding dyke, as indeed *Toda et al.* [2002] show for the 2000 Izu Islands volcano-induced seismic swarm.

If the dyke-induced seismicity is generated by the stressing rate change, we can quantitatively follow the stress history to which the system is subject during the intrusion. This is achieved in the fourth chapter by assuming a simple Coulomb stress model for seismicity and a rate and state formulation for the friction [*Deterich*, 1994]. It allows us to estimate the amount of seismicity directly triggered by the intruding dyke during the 2000 Izu Islands swarm. The high quality data recorded during this volcano-induced seismic swarm, the most energetic swarm ever recorded [e.g. *Toda et al.*, 2002], allow us to study the spatio-temporal response of the system to a long-lasting stress perturbation and to compare it with the response we would expect for a sudden stress change (i.e. the occurrence of a large earthquake). Results suggest that a dyke intrusion is comparable to a "silent slip" event, where a forcing is applied for a finite time. This induces in the system a kind of "damped" behavior. The active stressing rate continuously feeds the system all along the seismic crisis. As a result, seismicity continues to be triggered and the system cannot truly relax until the external forcing has vanished. Once this happens, an Omori style seismic relaxation is observed. Keeping this in mind, the spatio-temporal character-

istics of dyke-induced seismicity are very similar to those of aftershocks following a given mainshock in tectonic environments.

In the second part of the manuscript we explore the seismic signature of other simple volcano processes and we speculate on the physics of the driving process and on the peculiarities of volcano seismicity with respect to tectonic seismicity.

In the fifth chapter we review different time scales and patterns of VT seismicity prior to eruptions at basaltic volcanoes. We isolate three major phases within the reservoir dynamics leading to an eruption, (i) the long term (years) reservoir replenishment, (ii) the medium term (weeks) leak of the reservoir, and (iii) the dyke injection from the reservoir to the surface. We compare the brittle damage during these three phases and derive implications for the competing processes and relative scalings between quantities at stake.

In the sixth chapter we consider VT seismicity recorded during inter-eruptive phases on different dynamic style volcanoes. The patterns of earthquake organization in time we observe are compared with those of both, VT seismicity during dyke injection phases and "classic tectonic" seismicity. Our aim is to test how earthquakes interact in response to volcano dynamics, and to explore why such behavior is different form that of "classic" tectonic seismicity. We identify the origin of such peculiarity in the rate of forcing acting in each case. It allows us to discuss implications about the process that triggers the observed seismicity, as represented by the volcano process, or the interactions between earthquakes. In particular we give an explanation to the puzzling question on why existing declustering techniques fail in quantifying the seismicity directly driven by the external forcing when applied to the case of an intruding dyke.

The seventh and last chapter is dedicated to the processes occurring within the fluid in a pressurized magmatic system. Average accelerations of LP seismicity rate prior to explosions seems promising for forecasting goals. In these last pages we thus enjoy ourselves by applying a forecast algorithm to predict explosion occurrence on Ubinas volcano (Perú). The aim of the play is to use Long Period (LP) seismicity to predict explosion occurrence and thus to activate an alarm on an impending explosion few hours in advance.

Introduction Générale

Les volcans sont des systèmes dynamiques complexes [e.g. *Sparks*, 2003; *Lahaie and Grasso*, 1998] au sein desquels plusieurs processus stochastiques non-linéaires coexistent et interagissent, conduisant éventuellement à une éruption [*Grasso and Bachelery*, 1995; *Lahaie and Grasso*, 1998; *Melnik and Sparks*, 1999; *Sparks*, 2003]. Ces interactions non-linéaires et instables mènent potentiellement à des comportements du volcan qui sont imprédictibles par nature [*Melnik and Sparks*, 1999]. En effet, bien que tendances d'évolution systématiques et comportements assez périodiques peuvent exister, une prédiction déterministe des éruptions échoue encore en prévoir si, comment et quand un volcan réactivé éructera [e.g. *McGuire and Kilburn*, 1997; *Sparks*, 2003; *Grasso and Zaliapin*, 2004]. Les propriétés physiques du magma dépendent fortement de la température, de la composition du fluide, du contenu en eau, du dégazage et des processus de cristallisation [e.g. *Melnik and Sparks*, 1999; *Sparks*, 2003]. D'ailleurs, les matériaux rocheux qui constituent l'édifice à l'intérieur desquels le magma se déplace et interagit, sont composites et hétérogènes. Ils hébergent des réseaux de fractures organisés hiérarchiquement [e.g. *Grasso and Bachelery*, 1995].

Pendant l'évolution de la chambre magmatique et le transport du magma à travers la propagation de dykes, plusieurs processus ont lieu, tels les changements de pression, les transferts de chaleur et les réactions chimiques. Le magma donc, subit de changements profonds dans ses propriété physiques pendant son ascension vers la surface du volcan. Ces changements de pression et température et ces réactions chimiques, qui caractérisent les systèmes magmatiques actifs, interagissent avec leur entourage, induisant déformations, fracturation des roches, perturbations des systèmes hydrothermales ou des nappes phréatiques, dégazage et autres effets. Ces phénomènes engendrent toute une série d'observables géophysiques et géochimiques (tels sismicité, déformation de surface, émission de gaz) à la surface du volcan. Cela permet aux observateurs de détecter de manière indirecte les mouvements de masse à l'intérieur de l'édifice. Cela a poussé à la création et l'installation de différents types de réseaux de monitorage pour les

volcans, avec l'objectif d'améliorer la compréhension de la physique des processus volcaniques et éventuellement de développer des procédures de prédiction sur l'occurrence des éruptions. Dans ce travail, entre les observables surveillés, nous considérons la sismicité volcanique comme l'expression superficielle des processus magmatiques qui ont lieu en profondeur dans l'édifice. Notre but est d'utiliser la sismicité enregistrée en surface pour comprendre la physique et la dynamique qui gouverne les processus volcaniques menant à une éruption. L'idée à la base de ce travail est d'isoler de simple processus volcaniques et de détecter des motifs caractéristiques dans la sismicité qui les accompagne, en considérant ses distributions spatio-temporelles. A partir de cette réponse mécanique du système volcanique à une perturbation induite par un processus volcanique donné, nous dérivons des implications sur la physique qui gouverne ce processus actif.

D'autre part, nous visons à explorer et quantifier la particularité de la sismicité volcanique en utilisant ses caractéristiques et organisation spatio-temporelles pendant plusieurs phases de l'activité volcanique. La sismicité des volcans se manifeste en deux types différents de processus, ceux qui ont origine dans le fluide (i.e. gaz et fluides géothermales), et ceux qui sont générés dans la matrice rocheuse. Les premiers nous fournissent informations sur l'état du fluide, tandis que les séismes liés aux processus qui ont lieux dans le solide sont associés à la fracturation fragile de la matrice rocheuse [e.g. *Chouet*, 1996; *McNutt*, 2002; *Sparks*, 2003, et références indiqées]. La première catégorie inclut plusieurs types d'événement tels les Longue Période (LP), les Très Longue Période (VLP) et le trémor, tandis que les séismes issus de la fracturation de la matrice rocheuse sont connus comme événements Volcano Tectonic (VT), à cause de leur similarité avec les séismes tectoniques [e.g. *Minakami*, 1960, 1974; *Chouet*, 1996; *McNutt*, 2002]. Les séismes VT sont considérés comme des précurseurs et contemporaines importants de la remontée du magma qui crée son chemin vers la surface du volcan [e.g. *Sparks*, 2003; *Collombet et al.*, 2003; *Chastin and Main*, 2003; *Grasso and Zaliapin*, 2004]. L'origine des événements VT doit être recherchée dans la déformation des masses rocheuses hétérogènes constituant l'édifice induite par les variations de pression et température, ou par les mouvements de masse à l'intérieur de l'édifice volcanique même. L'importance de ce type d'événements en tant qu'observables superficiels des processus magmatiques profonds réside dans le fait qu'ils sont considérés comme une mesure qui dessine la distribution des concentrations de contrainte dans un volume large autour des conduits et réservoirs magmatiques [*Grasso and Bachelery*, 1995; *Chouet*, 1996; *Rubin and Gillard*, 1998].

Ce manuscrit se concentre essentiellement sur l'étude des événements Volcano Tec-

toniques, de leurs relations avec les processus magmatiques qui les génèrent, et des particularités spatio-temporelles d'occurrence. Une attention particulière est adressée aux mécanismes qui gouvernent la génération des séismes et leur organisation spatio-temporelle, qui résulte (i) du forçage imposé par le processus volcanique actif et (ii) des interactions entre les séismes. Cela nous amène à dériver quelque déduction et implication sur la particularité de la sismicité volcanique vis à vis de la sismicité tectonique "classique". Le premier chapitre introduit le contexte théorique de tous les objets géophysiques et les outils qui vont être utilisés tout le-long de pages suivantes. Suite à cette vue d'ensemble initiale, nous entrons dans le vif du sujet. Puisque une partie importante de notre travail a été consacrée à l'étude des intrusions de dyke aux volcans basaltiques, nous avons décidé de séparer le manuscrit en deux parties majeures. La première est concentrée sur cette toute dernière phase précédente une éruption basaltique, i.e. l'ascension du magma vers la surface à travers d'un dyke. Dans la seconde partie nous explorons la relation entre la sismicité induite et les différents processus volcaniques qui la génèrent. En plus, les motifs temporels d'occurrence sismique qui accompagnent les différents processus sont étudiés et comparés.

Dans le deuxième chapitre nous décrivons la réponse fragile d'un volcan basaltique à une intrusion de dyke, avec l'objectif de dériver des implications sur la physique qui contrôle cette dernière phase avant le début de l'éruption. Les dykes sont le moyen le plus efficace de transporter du magma d'en profondeur à la surface. Ces fractures très fines et allongées, remplies de fluide sont crées par fracturation hydraulique, gardées ouvertes par la pression du fluide, et faites monter par la dynamique des fluides [*Lister*, 1990a,b; *Lister and Kerr*, 1991; *Rubin*, 1995; *Menand and Tait*, 2002; *Roper and Lister*, 2005]. Les dykes se propagent dans la matrice rocheuse sous l'action de la contrainte régionale et exercent leur pression principalement contre la pression de confinement, plutôt que contre la résistance des matériaux [e.g. *Rubin et al.*, 1998]. Nous montrons que la sismicité induite par un dyke dans des volcans basaltiques est caractérisée par une stationnarité indépendante de l'échelle en termes de taux de sismicité et de taux d'énergie sismique. Cette stationnarité, qui évidence que l'intrusion d'un dyke est un processus stable de fluage fragile, suggère que l'intrusion magmatique induit un changement de volume constant dans l'unité de temps dans l'édifice. Cela soutient l'idée que le taux de sismicité stationnaire qui accompagne l'intrusion est représentatif d'un taux d'approvisionnement de magma du réservoir constant. Bien que cette hypothèse de retrait à taux constant de magma du réservoir magmatique pour alimenter un dyke qui monte vers la surface aie été employée jadis dans la modélisation de la propagation des dykes [*Lister*, 1990a,b],

elle a ensuite été considéré "géologiquement non-appropriée" [*Meriaux and Jaupart*, 1998; *Roper and Lister*, 2005] face à une condition limite de surpression constante dans le réservoir [*Rubin*, 1993a,b; *Meriaux and Jaupart*, 1998; *Roper and Lister*, 2005]. D'autre part, *Ida* [1999] affirme que seulement dans le cas d'un réservoir magmatique extrêmement large et compressible, la pression du fluide peut effectivement rester constante pendant que le dyke se propage.

Cet énigme nous motive dans notre troisième chapitre où nous utilisons un modèle numérique de propagation de dyke en deux phases pour tester et valider l'hypothèse de flux constant de magma et pour explorer sous quelles conditions géophysiques cela est réaliste. Nous démontrons que ces deux conditions limites, apparemment mutuellement exclusives, n'ont pas raison de l'être. Dans le modèle numérique que nous testons, nous n'imposons pas une condition initiale plutôt que l'autre. Ce modèle en deux phases nous permet de suivre la dynamique de la propagation d'un dyke à partir d'une source magmatique sur-pressurisée vers le site d'éruption sans aucun à-priori sur le comportement du réservoir. En plus, l'application de ce modèle à un cas réel et bien contraint de propagation de dyke nous permet de donner une estimation sur les paramètres physiques qui caractérisent le réservoir magmatique au Piton de la Fournaise (La Réunion). Les résultats montrés dans le troisième chapitre nous amènent à la conclusion que la sismicité qui accompagne l'intrusion d'un dyke est contrôlée par le changement de volume induit dans le système dans l'unité de temps par le magma qui remonte vers la surface. Cela nous suggère que la sismicité induite par le dyke est contrôlée par le changement de taux de contrainte généré par le dyke en intrusion, comme montré par *Toda et al.* [2002] pour le cas de l'essaim sismique induit par l'intrusion de dyke qui a eu lieu en 2000 aux îes Izu (Japon).

D'autre part, si la sismicité induite par le dyke est générée par le changement de taux de contrainte, nous pouvons suivre la de manière quantitative l'histoire de contrainte à laquelle le système est sujet pendant l'intrusion. Ceci est atteint dans le quatrième chapitre en assumant un simple modèle de Coulomb pour la sismicité, et une formulation "Rate and State" pour la friction [*Deterich*, 1994]. Cela nous permet d'estimer la quantité de sismicité qui est directement déclenchée par l'intrusion du dyke qui accompagne l'essaim sismique du 2000 aux îles Izu. La qualité des données enregistrées pendant cet essaim sismique, qui s'est avéré être l'essaim sismique d'origine volcanique le plus énergétique jamais produit [e.g. *Toda et al.*, 2002], nous permet d'étudier la réponse sismique du système à une perturbation de contrainte de longue durée et de la comparer a celle que nous aurions attendu d'un changement de contrainte soudaine (par exemple l'occurrence d'un gros séisme). Les résultats suggèrent que l'intrusion d'un dyke est comparable à un événement silencieux, dont le forçage est appliqué pendant un

temps de durée finie. Cela induit une sorte de comportement amorti dans le système. Le taux de contrainte actif, alimente continûment le système tout le long de la crise sismique. Il en résulte que la sismicité continue à être déclenchée et que le système ne peut se relaxer qu'au moment où le forçage externe cesse. Une fois que cela arrive, nous observons une relaxation de la sismicité qui suit la loi d'Omori. A la lumière de cela, les caractéristiques spatio-temporelles de la sismicité induite par le dyke sont très proches de celles des répliques qui suivent un "mainshock" pour les environnements tectoniques.

Dans la deuxième partie du manuscrit nous explorons la signature sismique d'autres processus volcaniques simples et nous en dérivons des implications sur la physique et la dynamique des processus qui la gouvernent et sur la particularité de la sismicité volcanique par rapport à la sismicité tectonique. Dans le quatrième chapitre nous passons en revue les diverses échelles de temps et les motifs de sismicité VT avant les éruptions des volcans basaltiques. Nous distinguons trois phases majeures pour la dynamique du réservoir qui mène à une éruption, (i) le remplissage du réservoir à grande échelle (années), (ii) la fissuration du réservoir à moyenne échelle (semaines), et (iii) l'injection du magma du réservoir à la surface (heures). Nous comparons la réponse fragile pendant ces trois phases et nous en dérivons des implications sur les processus en compétition et les échelles respectives entre les quantités en jeu.

Dans le sixième chapitre nous considérons la sismicité VT enregistrée pendant les phases inter-éruptives sur plusieurs volcans à style dynamique différent. Les motifs observés d'organisation temporelle de la sismicité sont comparés avec ceux de la sismicité VT pendant les phases d'injection et de la sismicité tectonique "classique". Notre objectif est de tester comment les séismes interagissent entre eux en réponse à la dynamique du volcan et d'explorer en quoi et pourquoi tel comportement est différent de celui de la sismicité tectonique classique. Nous identifions l'origine de cette particularité dans le taux de forçage actif pour chaque cas. Cela nous permet de discuter les implications sur le processus qui déclenche la sismicité observée, représenté par le processus volcanique ou les interactions entre les séismes. En particulier nous donnons une explication à la déroutante question de pourquoi les techniques de declustering actuelles échouent à quantifier la sismicité générée directement par le forçage externe quand appliquées au cas d'une intrusion de dyke.

Le septième et dernier chapitre est dévoué aux processus qui ont lieu à l'intérieur du fluide dans un système magmatique pressurisé. Nous observons des accélérations moyennes de taux de sismicité Long Période avant les explosions. Cela est très prometteur pour des fins de prédiction. Dans ces dernières pages nous nous délectons en appliquant un algorithme de

prédiction à fin de prédire l'occurrence des explosions sur le volcan Ubinas (Pérou). Le but du jeu est d'utiliser la sismicité LP pour prédire l'occurrence d'une explosion, et donc pour activer une alerte sur une explosion imminente quelques heures en avance.

Chapter 1

Theoretical background

Résumé

Ce chapitre est un chapitre introductif orienté à créer des bases et à présenter tous les outils qui sont employés tout le long des pages de ce manuscrit. Nous commençons en donnant un cadre historique sur la sismologie volcanique et en décrivant la richesse et la variété de signaux sismiques observés dans les environnements volcaniques. Ensuite nous passons à détailler les processus de transport de masse au sein des édifices volcaniques, de la récolte du fluide en poches dans la croûte à l'arrivée du magma à la surface. Nous passons aux processus de génération des séismes, avec un aperçu de mécanique de la fracture et puis de mécanique des séismes. Nous introduisons la sismicité induite par un dyke en propagation, pour finir sur les aspects statistiques de l'occurrence des séismes.

1.1 Volcano seismology

Earthquakes were associated with volcanic eruptions from ancient times. Pliny the Younger gave the first scientific description of the 79 A.D. eruption at Mt. Vesuvius, which led to the destruction of the Roman cities of Herculaneum and Pompeii and the death of tens of thousand people. When Pliny the Elder observed the eruption from Misenum, at a distance of 30 km, he set out on the first expedition devoted to the study of a volcanic process. He died in the attempt. Pliny the Younger stayed at home, where he had a spectacular view of the eruption, and wrote the first eye-witness account of

the phenomenon [*Sigurdsson et al.*, 2000]. In his report, Pliny the Younger wrote about numerous earthquakes related to this eruption [*Zobin*, 2003].

Vesuvius volcano takes a leading role in the history of the study of seismic signals associated with volcanic activity. It was the first volcano whose earthquakes were mentioned in scientific literature, it was the first volcano to have a Volcanological Observatory in 1848, and it was the first to be monitored using seismological equipment. The Palmieri electromagnetic seismograph, built in 1862, was the first seismic instrument to record volcano seismicity [*http://www.ov.ingv.it/inglese/storia/storia.htm*].

"Volcano Seismology" was born as a science when the Japanese seismologist Fusakichi Omori begun to investigate seismic signals related to the 1910 eruptions of Usu-San and Asama [*Omori*, 1911, 1914, 1912], and the 1914 eruption of Sakurajima volcano [*Omori*, 1914, 1922]. Omori defined the volcanic earthquake as "seismic disturbance, which is due to the direct action of the volcanic force, or whose origin lies under, or in the immediate vicinity of a volcano, whether active, dormant, or extinct." [*Omori*, 1912]. Omori disposed of a three-component seismic station, installed near the craters of Usu-San. This station allowed him to record volcanic earthquakes and micro-tremors. The micro-tremors were observed only during volcanic activity. In particular, *Omori* [1911] pointed out a good correlation between the appearance of micro-tremors and the occurrence of volcanic explosions. He also observed that many eruptions at Japanese volcanoes were preceded by a large number of earthquakes. With regard to this, he wrote that "In such cases, seismograph observations close to the center of volcanic activity would give people a warning on the approaching outburst". Analysis of volcanic earthquakes became thus the main instrument for monitoring volcanic activity [*Zobin*, 2003]. Afterwards, Volcano Observatories were created for other Japan, Kamchatka and Hawaii volcanoes.

Observations from continuously operating seismographs allowed *Minakami* [1960, 1974] to propose a classification of volcanic earthquakes into four types, according to their hypocenter location, their relationship with eruptions, and the nature of the earthquake motion. Although some of the classification criteria proposed by *Minakami* [1974] have been relaxed, dropped or changed over the years, such classification has been the basis of volcano seismology up to present. The different types of events recorded on volcanoes are listed as follows (figure 1.1):

1. *High Frequency* or *Volcano Tectonic (VT)* events: they are associated with shear failure or slip on faults; their frequency content is typical of tectonic earthquakes,

with clearly defined P- and S-phase [e.g. *Minakami*, 1960, 1974; *Chouet*, 1996; *Rubin and Gillard*, 1998; *McNutt*, 2002]. They are considered as the sign of renewed volcanic activity since they usually accompany volcano processes typically occurring in form of swarms [*McNutt*, 2002].

2. *Low Frequency or Long Period (LP)* events: they have emergent onset, with unclear S-phase. Their triggering mechanism is still not well understood [e.g. *Neuberg et al.*, 2000], even if most studies devoted to investigate the source of this type of events have relied on fluid-filled resonator models [e.g. *Aki et al.*, 1977; *Chouet*, 1986, 1988; *Neuberg et al.*, 2000; *Kumagai et al.*, 2005]. They are therefore thought to be generated by fluid pressurization processes such as bubble formation and collapse [e.g. *Neuberg et al.*, 1998; *McNutt*, 2002]. The frequency content of LP events usually ranges from 0.2 to 5 Hz and is characterized by narrow spectral peaks [e.g. *OâĂŹBrien and Bean*, 2004].

3. *Explosion* earthquakes: they accompany explosive eruptions, and are characterized by the presence of an air shock phase on the seismograms, since the energy is released partly as seismic waves, and partly as acoustic or air waves [*Minakami*, 1974; *McNutt*, 2002; *Zobin*, 2003]. Typically, the wavefield generated by volcanic explosions includes a low-frequency signal (1-3 Hz) followed by a higher-frequency seismic wave field (5-10 Hz) [e.g. *Ripepe et al.*, 2001]

4. *Volcanic tremor*: it is a continuous harmonic or spasmodic signal with duration from minutes to days or longer. The wave form is similar to that of LP events, in which the main part consists of surface waves. Many authors have in fact concluded that tremor is a series of subsequent LP events [e.g. *Neuberg et al.*, 2000; *McNutt*, 2002]. It is commonly assumed to be related to fluid transfer, either magma or gas. Various spectral characteristics have been observed, depending on the volcano, or its period of activity. Volcanic tremor almost always accompanies eruptive lava flows at basaltic volcanoes like Piton de la Fournaise [*Aki and Ferrazzini*, 2000; *Battaglia et al.*, 2005a], Kilauea [*Fujita et al.*, 1995] or Etna [*Gresta et al.*, 1991; *Alparone and Privitera*, 2001]. *Battaglia et al.* [2005a] propose a model of volcanic tremor at Piton de la Fournaise volcano in which higher frequencies are directly generated at the eruption sites, while lower frequencies seems to be related to processes occurring deeper within the plumbing system. Tremor events are commonly found to contain

the same temporal and spectral components as LP events, indicating that the source mechanism might be the same, differing only in duration [e.g. *Chouet*, 1988].

5. *Hybrid* events: they share attributes from high and low frequency events. In particular they have an impulsive first arrival, a high frequency beginning preceding the low-frequency coda [e.g. *Miller et al.*, 1998]. They are thought to results from brittle faulting in zones of weakness intersecting a fluid-filled crack, and thus to involve both, double-couple and volumetric source components [e.g. *Lahr et al.*, 1994].

6. *Very Long Period (VLP)* earthquakes: their frequency content is of still lower range than the LP events, i.e. periods of 3-20 sec, and they have fairly small amplitudes. They have been associated to either, eruptions, or vigorous fumarolic activity [e.g. *Neuberg et al.*, 1994; *Aster et al.*, 2003].

7. *Superficial* events: they are local signals generated by shallow processes, which include non-volcanic processes such as glacial events, shore ice movement and landslides, as well as volcanic processes such as outburst floods and lahars (volcanic mudflows), pyroclastic flows, and rockfalls from crumbling lava domes.

The goals of volcano seismicity include the study of the physical processes acting at volcanoes, the understanding of the dynamics driving such processes, the determination of the physical properties of the active magmatic systems. The perspective leads to the understanding of the eruptive processes and behaviours and assessing of volcanic hazard. Key developments in volcano seismology have been the attempts to link the different types of earthquake listed above to particular volcanic phenomena [*Sparks*, 2003].

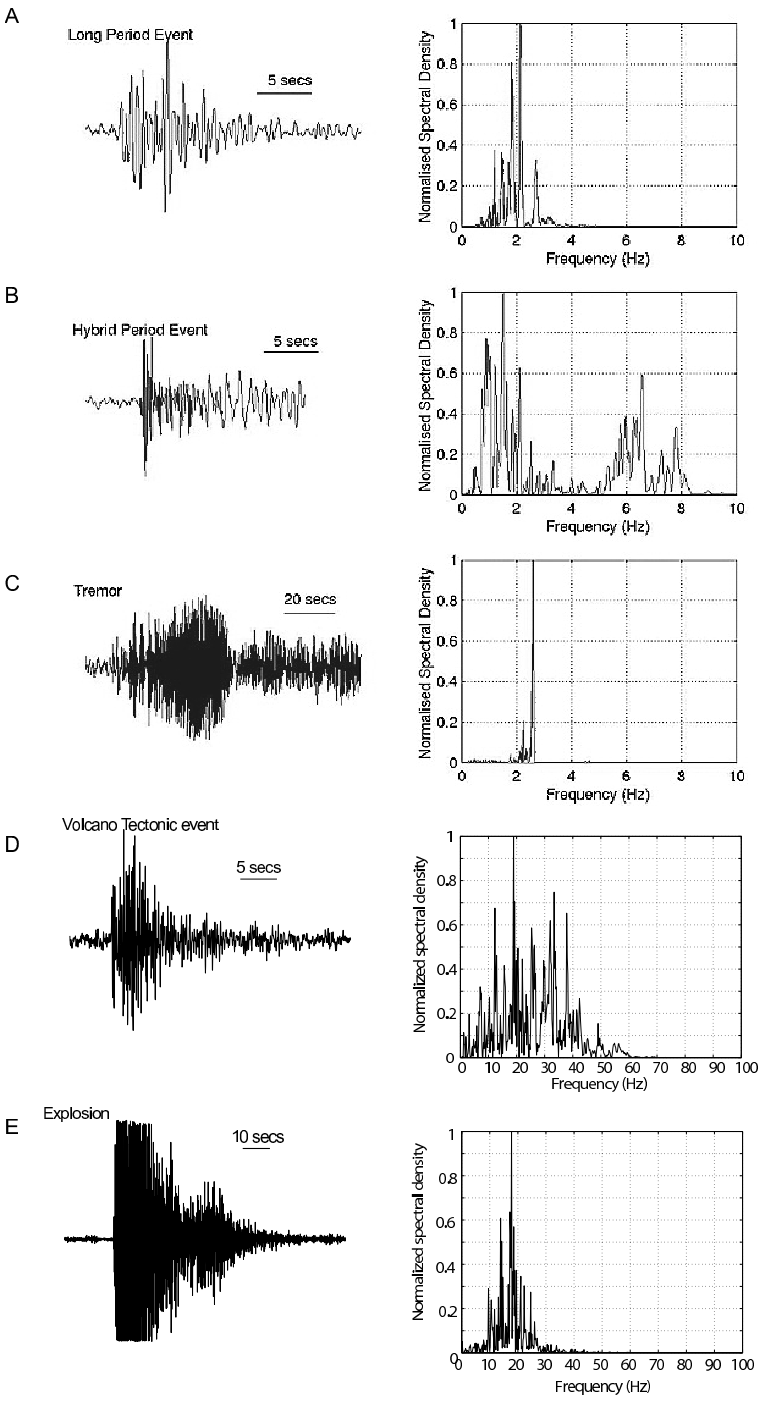

Figure 1.1: Examples of volcanic earthquakes waveforms. (A) Long Period event, Deception Island, Antarctica; (B) Hybrid event, Deception Island, Antarctica; (C) Tremor activity, Deception Island, Antarctica (from [*OâĂŹBrien and Bean*, 2004]); (D) Volcano Tectonic event, Piton de la Fournaise, Reunion Island; (E) Explosion, Ubinas, Perú.

1.2 Mass Transport Processes at Volcanoes

At volcanoes, processes of mass transport include porous flow in partially molten and deformable rocks, flow through fractures in elastic/brittle rocks, and diapiric ascent. Among these, transport in narrow fractures, or dykes, is the most efficient mean of moving magma through cold lithosphere [for a review on magma transport see *Rubin*, 1995].

Measurements of seismic velocities at volcanoes indicate that the melt initially collects in reservoirs within the crust, where density discontinuities create favorable conditions for magma accumulation, i.e. where the density of the melt equals that of the surrounding rocks (named the Level of Neutral Buoyancy) [e.g. *Ryan*, 1987; *Lister*, 1990a,b; *Hill et al.*, 2002]. Magma processes within the reservoir, such as buoyancy, refilling from depth, exolution of volatile components, crystallization, or bubble rising, induce pressure growth within the chamber. When the reservoir pressure exceeds a critical value, a fissure is created in the walls of the reservoir and propagates upwards [*Lister*, 1990a]. Such a fissure may reach the surface directly, leading to an eruption, or feed a shallower magma chamber, as it is frequently the case at basaltic volcanoes [e.g. *Tilling and Dvorak*, 1993; *Hill et al.*, 2002]. From this latter, only a portion of the magma is subsequently erupted through secondary dykes rising to the surface (figure 1.2).

Dykes are tabular sheets through which magma rises across the solid matrix, their growth involve parting the host rock along pre-existing or magma-created fractures [*Rubin*, 1993b]. The surrounding solid matrix, subject to the ambient stress and usually considered to be elastic, is pushed apart with relatively little internal deformation, resulting in typical dyke thickness/length ratios of about 1/1000 [*Rubin*, 1993b]. Individual dykes in homogeneous media grow thus as self-similar cracks normal to the direction of the least principal stress, acting mostly against the confining pressure rather than the intrinsic strength of the rock [*Rubin et al.*, 1998]. The direction of crack growth is modified, however, by local stress concentrations [*Pollard*, 1973; *Hill*, 1977]. The propagation velocity is mostly controlled by the magma viscosity and can vary in the range $0.01 - 10$ m/s at basaltic volcanoes [e.g. *Klein et al.*, 1987; *Rubin*, 1995; *Peltier et al.*, 2005, 2007], which allows dykes to propagate great distances before freezing [*Rubin*, 1993b, and references therein].

The difficulty of making direct observations of the plumbing system at volcanoes has limited our knowledge about the parameters and physical balances governing the magma movement at volcanoes [*Lister and Kerr*, 1991]. The principal forces at stake in controlling

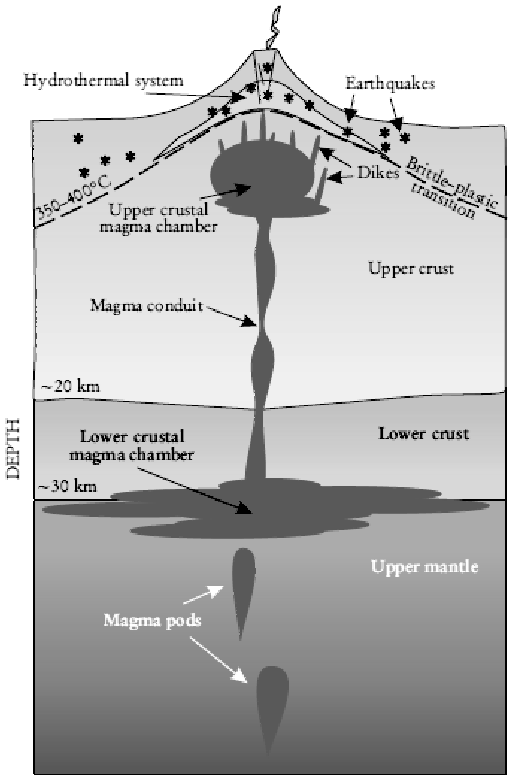

Figure 1.2: Sketch illustrating the anatomy of a continental volcano [from *Hill et al.*, 2002].

the crack propagation are the following [e.g. *Lister*, 1990b; *Lister and Kerr*, 1991; *Rubin*, 1995]:

- the pressure required to open the crack against elastic forces;
- the hydrostatic pressure due to the density difference between the magma and the host rock, i.e. the buoyancy force;
- the viscous pressure drop caused by flow in the crack;
- the magma driving overpressure;
- the tensile stress required for fracture extension against the strength of the host rock;
- the regional pre-existing stress field.

Several authors have applied analytical models of fluid-filled fracture to dyke emplacement and propagation to the eruption site. These models leans on different initial conditions, which have been tested over the years.

Pioneer works [e.g. *Weertman*, 1971a; *Rubin and Pollard*, 1987; *Pollard*, 1988] neglect dynamical effects such as the viscous pressure drop in the fluid, and focus on computing the stress field around a static fluid-filled crack and on evaluating the conditions under which the crack extends. Crack growth occurs when the stress intensity factor at the tip of the crack exceeds the critical value for the material. The vertical extent of the fluid-filled fracture cannot exceed a certain value without causing the upper tip of the crack to propagate or the lower tip to close [*Weertman*, 1971a]. For geological settings, this value is of order a hundred meters [*Lister*, 1990a]. This is not realistic for common tabular dykes, which are able to feed eruptions whose volume of lava emitted is often larger than the volume of the feeding dyke. The solutions proposed in these studies can be considered as equilibrium shapes of stationary fluid-filled cracks. They are therefore valid only once magma has come to rest, but is still molten [*Lister and Kerr*, 1991].

Initial attempts to include dynamic effects have been carried out neglecting buoyancy forces [*Spence and Sharp*, 1985; *Emerman et al.*, 1986; *Spence and Turcotte*, 1985]. The problem of density difference between melt and rock mass, therefore, is not considered. This makes them relevant only when considering propagation through sill (i.e. lateral dyke) [*Lister and Kerr*, 1991].

On the other hand, through an experimental approach in which various liquidus are injected into gelatin, *Takada* [1990] concludes that buoyancy is the quantity that governs dyke propagation. In his experiments, *Takada* [1990] tests two boundary conditions for crack growth: constant injection rate of fluid into the gelatin, and a constant volume for the fluid-filled crack.

Spence et al. [1987] and *Lister* [1990a] give then analytic solutions governing the steady upward propagation of a two-dimensional buoyancy-driven dyke from a prescribed constant flow rate source. *Lister* [1990a] shows that the width and rate of propagation of the crack are determined by the geometry of the source feeding the crack and the magma supply rate. *Lister* [1990a,b] show that the pressure associated with elastic deformation and the strength of the country rock only affect the vicinity of the dyke tip. This allows for simple solutions of dyke shape far from its tip [*Spence and Turcotte*, 1990]. *Lister* [1990b] derives then expressions for the lateral extent and the lateral cross-section of a dyke rising from a localized source, as well as for the rate of a fluid-filled crack laterally propagating in a stratified solid at the Level of Neutral Buoyancy (LNB).

Lister and Kerr [1991] study of the effect of fluid viscosity, elasticity and buoyancy on the fluid-filled crack propagation, concluding that none of these effects can be neglected. They demonstrate that magma ascent is mainly driven by buoyancy. Indeed, after the vertical extent of the dyke exceeds a value of order a hundred of meters, the buoyancy forces are much greater than fracture resistance of rocks. From then on, the dominant resistance to further crack growth is provided by the viscous pressure drop in the melt as it flows towards the dyke tip. Near the dyke tip, on the other hand, the balance between viscous and elastic pressures controls crack growth. However, the authors show that is fluid dynamics who governs dyke propagation, and the ascent ceases near the LNB of the magma. Here dykes can propagate laterally driven by the buoyancy forces arising from the density difference between the magma and the underlying and overlying rocks.

Judging the boundary conditions of constant magma supply from the reservoir into the dyke [*Lister*, 1990a,b; *Lister and Kerr*, 1991] geologically inappropriate, *Meriaux and Jaupart* [1998] propose a dyke propagation driven by buoyancy from a constant over-pressure reservoir through an elastic plate of finite thickness. In this configuration both, the dyke width and the magma injection rate (which depends on the conduit width) increases as dyke ascends to the surface. They identify two different fracturing mechanism during crack growth, (i) the fracture initiation (sub-critical crack growth) and (ii) the subsequent

propagation by tensile hydrocracking. Consequently, elastic stresses in the dyke conduit cannot be neglected as the dyke extends.

Ida [1999] point out however that a very large volume reservoir would be required for the magma overpressure in the reservoir to remain constant as the dyke propagates.

Mériaux et al. [1999] consider dyke propagation within host rock with distributed damage. They conclude that the rate of magma-driven propagation is indeed determined by fluid dynamics [as proposed by *Lister and Kerr*, 1991]. This is because the host-rock response is linear except in the damaged tip region. A part from this small zone, therefore, the rock resistance can be neglected, and the resistance to dyke propagation is given by the viscous head loss.

The same conclusion is attained by *Menand and Tait* [2002], who go back to the problem of dyke growth from a constant overpressure chamber, but from an experimental point of view. They conclude that, initially, the crack growth is controlled by a balance between the chamber over-pressure and the fracture toughness of the host rock. Once the buoyancy pressure overcomes the source pressure, a steady state is achieved, in which the fissure develops a bulbous head fed by a thinner tail. This steady state depends on the source overpressure.

Recently *Roper and Lister* [2005] considered analytically the case of crack propagation under the influence of buoyancy and overpressure in an infinite impermeable solid. They find solutions which depend on the length of the crack relative to the buoyancy length, which measures the relative importance of the elastic pressure gradient and buoyancy. In both cases, short and large cracks, the overpressure at the source acts to make the width of the crack grow in proportion to its length. This leads to an increase in the flux, whose driving force is dominated either, by the elastic pressure gradient for short cracks, or by buoyancy for large cracks. In agreement with the experimental results obtained by *Menand and Tait* [2002], *Roper and Lister* [2005] find that, for large cracks, the solution develops a head-and-tail structure: in the tail the elastic pressure gradient is negligible and the flow is buoyancy-driven. In the head the elastic pressure gradient becomes comparable to buoyancy.

In conclusion, the studies that have been carried out since the early 70's have led to fundamental understandings of the processes driving and accompanying dyke ascent from the reservoir to the surface. In particular they have established that the influence of of the toughness of rocks on dyke propagation only affects fracture growth at an initial stage.

Subsequently the resistance of the country rock can be neglected and the fluid dynamics determine the propagation rate of the dyke. It means that the dyke ascent is driven by buoyancy, which allows for pushing the host rock aparts against elastic stresses, while resistance to dyke growth is given by the viscous head loss. One point is still debated, i.e. whether the feeding of the dyke from the magma reservoir can occur at constant magma injection rate, or whether the best initial condition is given by a constant overpressure at the dyke inlet.

1.3 Origin, Mechanics and Characteristics of Earthquake Occurrence

The aim of this section is to describe the state of the art about theory of earthquake occurrence, in order to provide the reader with a background about all the tools we use throughout the following chapters. Most of the tools we describe here come from the "classic" tectonic seismicity, and have been adapted here to suit volcano seismology. We briefly describe useful notions of fracture mechanics, the processes related to earthquake generation and the statistical features of seismic occurrence.

1.3.1 Notions of Fracture Mechanics

Understanding about rock strength properties dates back to ancient times, but the pioneer work of *Griffith* [1921, 1924] poses this wonder at a more fundamental level, in the form of an energy balance for crack propagation [for a detailed description see *Scholz*, 2002; *Janssen et al.*, 2003]. According to the Griffith's theory, then modified by *Irwin* [1958] and *Rice* [1968], in order the crack growth to occur, the potential energy G released by the extension of the crack is sufficient to provide the energy necessary for fracture G_c (i.e. the instantaneous elastic stress field surrounding the crack tip defined on the basis of a global energy change [*Rice*, 1968]). Owing to practical difficulties of this energy approach, later in the 1950's, Irwin develops the stress intensity approach, according to which the crack extension occurs when the crack-tip stress intensity factor K reaches a critical value K_c. The factor K gives the magnitude of the elastic stress field, and depends on the crack size and loading configuration [e.g. *Janssen et al.*, 2003; *Rubin*, 1993a, 1995], while K_c is the rock fracture toughness. The macroscopic strength of a material is thus related to the intrinsic strength of the material through the relationship between the applied stresses and the crack-tip stresses [*Scholz*, 2002]. According to the displacement field generated by the crack extension, the fracture can be divided into three basic types, or modes (figure 1.3). Mode I is tensile, or opening, Mode II is in-plane shear, and Mode III is anti-plane shear.

Faults correspond to mode II fractures, in which the displacements are in the plane of the discontinuity. Dykes, on the other hand, correspond to mode I fractures, in which the displacements are normal to the discontinuity walls. Earthquakes recorded on Earth surface are thus the expression of natural shear and opening mode cracks.

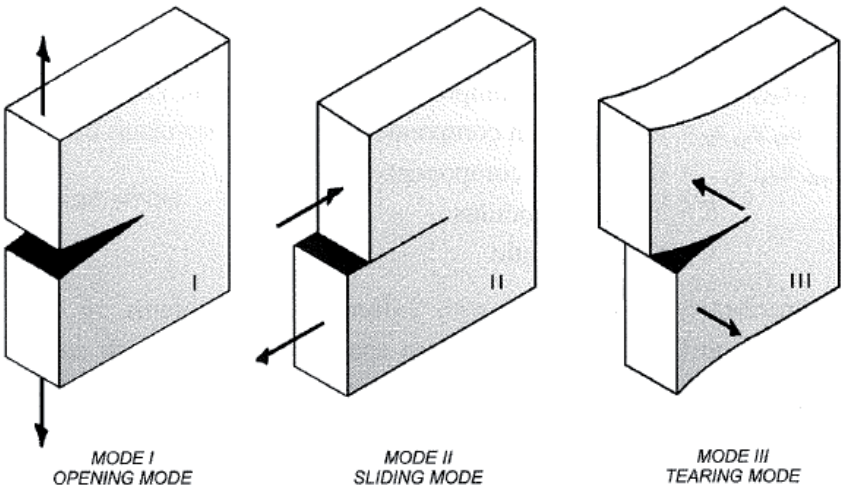

Figure 1.3: The three modes of crack surface displacements, from *Janssen et al.* [2003]

1.3.2 Mechanics of Earthquakes

According to the Elastic Rebound theory [*Reid*, 1911], the tectonic plate motion induces stress accumulations on faults, due to the fact that friction on the fault plane "locks" it and prevents the sides from slipping. Eventually the strain accumulated in the rock is more than the rocks on the fault can withstand, and the fault slips, resulting in an earthquake that relaxes all the available energy. However, strain released by earthquakes can occur in a variety of forms resulting from e.g. the nature of crust materials and the local stress field [e.g. *Kanamori*, 1973].

According to more recent views, earthquakes are indeed triggered as a consequence of stress perturbations. Such stress perturbations are, however, due to both, external forcing (i.e. either tectonic plate motion, or volcano processes in tectonic and volcanic environments, respectively) and earthquake interactions. From the simple view point of an isolated homogeneous fault loaded at constant stress rate, characteristic earthquakes occur periodically by rupturing the whole fault, with a period equal to ratio of the stress drop divided by the rate of stress loading [e.g. *Scholz*, 2002, and references therein]. These earthquakes are the signatures of the tectonic loading [e.g. *Helmstetter*, 2002]. However, statistical and geological studies show that faults are complex structures organized into complex and interacting networks [for a review see *Bonnet et al.*, 2001]. There are indeed abundant evidences of fault (and thus earthquake) interacting through their static

stress field, which results in earthquakes triggered by the static stress change induced by a previous event. However, the physics driving these interactions is not fully understood and various different mechanisms have been proposed [e.g. *Helmstetter et al.*, 2005, and references therein].

The manner in which fracture system properties at different scales relate to each other, has thus recently received increased attention motivated by the promise of statistical prediction that scaling laws offer [e.g. *Bonnet et al.*, 2001]. Recent studies on tectonic earthquake occurrence through a stochastic model of seismicity (see section 1.3.4), demonstrate that earthquakes have a key role in the triggering of other earthquakes [e.g. *Helmstetter and Sornette*, 2002a; *Helmstetter*, 2003; *Helmstetter and Sornette*, 2003].

Assuming the validity of the stress triggering mechanism for earthquakes, the Coulomb stress change $\Delta\sigma_f$ defined below, will enhance or retard the potential for rupture to nucleate on a given fault.

$$\Delta\sigma_f = S = \Delta\tau - \mu(\Delta\sigma_n - \Delta P). \tag{1.1}$$

where $\Delta\tau$ is the shear stress change on a fault (positive in the direction of fault slip), $\Delta\sigma_n$ and ΔP are the changes in normal stress and pore pressure on the fault (positive for compression), and μ is the friction coefficient. Failure is encouraged if $\Delta\sigma_f$ is positive, and inhibited if $\Delta\sigma_f$ is negative. Both, increased shear and unclamping of faults promote failure [*Stein*, 1999]. Coulomb stress changes refer to static stress changes that occur instantaneously and permanently [*Steacy et al.*, 2005].

Computations of Coulomb stress change indeed show that enhancement of seismicity rather occurs in areas of stress increase, while seismic quiescence is observed in stress drop shadow areas [e.g. *King et al.*, 1994; *Harris*, 1998; *Stein*, 1999; *King and Cocco*, 2000]. *Steacy et al.* [2005], commenting on *Toda et al.* [2005] results, affirm that triggering primarily represent clock-advanced failure, rather than creation of new fractures.

Observations of aftershocks occurring in stress shadow areas seem to contradict the stress triggering mechanism [*Hardebeck et al.*, 1998; *Catalli et al.*, 2008]. However, *Helmstetter and Shaw* [2006]; *Marsan* [2006] demonstrate that small-scale slip variability, which might not be directly measured, may explain the absence of quiescent regions in the first period of aftershock activity.

Based on this model and on the observation that stress and earthquake rate changes are not linearly correlated, *Deterich* [1994] proposes a constitutive law for the rate of earthquake production, leaning on experimentally derived rate- and state-dependence of

fault friction. He models the seismicity as a sequence of nucleation events whose occurrence depends on the distribution of initial slip conditions on the fault and on the stress history to which the fault is subjected. An evolving variable representative of the state of the fault over time allows to quantify the rate of earthquake production resulting from an applied stress history.

According to this formulation, the earthquake rate R in a specified magnitude range is given by

$$R = \frac{r}{\gamma \dot{S}_r}, \tag{1.2}$$

where

$$d\gamma = \frac{1}{A\sigma}[dt - \gamma dS], \tag{1.3}$$

γ is a state variable, t is time, the constant r is the steady-state earthquake rate at the reference stressing rate $\dot{S}_r$, A is a dimensionless fault constitutive parameter, and S is the Coulomb stress function of equation (1.1). See appendix B for details on equations about the effect of stressing history on Earthquake rate).

On the bases of this formulation, *Dieterich et al.* [2000] uses seismicity rate changes to compute stress changes prior and contemporary to the 1983 flank eruption at Kilauea volcano. The results they obtain well agree with the deformation model obtained for the same episode by *Cayol et al.* [2000]. It evidences that accompany this eruption are promoted by Coulomb stress changes induced by the expansion of a dyke-like magma system within the Kilauea rift zones, coupled with aseismic creep. *Toda et al.* [2002] show a linear relationship between the stressing rate change induced by the 2000 dyke opening at Izu Islands (Japan), and the increase in seismicity rate. *Feuillet et al.* [2004] show that earthquakes recorded at Alban Hills volcano (Italy) are promoted by elastic stress changes induced by a magmatic intrusion.

All these argue for the fact that just as earthquake occurrence perturb the stress state in surrounding areas, so does mass transport and volcano processes at volcanic environments. Here, stress perturbations induced by magmatic processes may thus promote faulting and earthquake activity. Indeed, major volcanic events are generally associated with dramatic increases of seismic activity. Conversely, a volcanic system may be perturbed by stress changes induced by neighboring earthquakes [e.g. *Dieterich et al.*, 2003; *Hill et al.*, 2002; *Lemarchand and Grasso*, 2007].

1.3.3 Dyke-Induced Seismicity

The Volcano Tectonic (VT) seismicity associated to mass movements within a volcano is driven by the superposition of two contemporary acting processes: the ambient stress accumulation and the stress perturbation induced by the propagating dyke [*Rubin and Gillard*, 1998]. By calculating plane-strain solutions in the context of a shallow propagating dyke, *Rubin and Gillard* [1998] investigate the likelihood of earthquake occurrence for the following cases (see figure 1.4):

1. Fault slip away from the tip cavity.
2. Fault slip near the tip cavity
3. Shear failure of intact rock

Rubin and Gillard [1998] show that the most dyke-induced VT seismicity should be interpreted as resulting from slip along suitably aligned existing fractures for any of the first two cases. On the other hand, shear fracture of previously intact rock seems unlikely. They conclude that the distribution of (recorded) dyke-induced seismicity reflects the distribution of ambient stresses that are near to failure, and does not necessarily reflect the extent of the dyke.

This conclusion confirms the results found by *Grasso and Bachelery* [1995] on statistical arguments about scaling attributes of volcanic-induced earthquakes, dykes, fissures lengths and erupted lava volumes. Such scaling organization of the dynamic magma induced observables on the volcano makes the authors argue about dealing with a system near to the critical point.

All these argue for rejecting fracturing recorded on surface as the trajectory of dyke movement.

On the other hand, *Hill* [1977] propose a model of magma-filled dyke clusters embedded in brittle volume of the crust. As the dyke grows and the volume reaches a critical state, the shear failures accompanying dyke propagation would occur on a system of conjugate faults joining en echelon offset dyke tips at oblique angles (see figure 1.5). Such a model would imply to observe a migration of earthquakes accompanying dyke propagation from depth. However, no case of documented upward and monotonic migration of the seismicity illustrating the ascent of magma could be found, with exception of the early phase of the 1998 Piton de la Fournaise (PdlF) eruption case, discussed by *Battaglia*

et al. [2005b]. According to the *Hill* [1977] model, *Battaglia et al.* [2005b] suggest that the observed seismicity may indicate the position of the uppermost extremity of the dyke, propagating from a possible deep magma storage zone towards the surface. Generally, however, the PdlF eruptions are fed from the shallow magma reservoir system [e.g. *Lénat and Bachèlery*, 1990; *Peltier et al.*, 2005, 2007], and no earthquake migration contemporary to magma rising is observed. Eruptions are heralded by a few hours of precursory diffuse VT seismicity occurring in form of swarms [e.g. *Toutain et al.*, 1992; *Grasso and Zaliapin*, 2004; *Peltier et al.*, 2007].

Gambino et al. [2004], through a precise relocation of the seismic activity preceding the 2002-2003 eruption at Mt. Etna, observe that earthquakes accompanying magma ascent are peripheral with respect to the dyke rise under the central cone. They conclude that magma-induced strains are dissipated away from the summit region, such that the observed seismicity may reflect stress redistributions along pre-existent regional structures due to magma-induced edifice deformation.

The seismicity we record at the volcano surface represents therefore a global response of the solid matrix to the deformation induced within the edifice by the acting volcano process.

1.3.4 Statistical Features of Seismicity and ETAS model

Evidence of earthquake interaction comes from the fact that earthquakes are generally part of a sequence. From the classical seismology view point, a seismic sequence is constituted by "foreshock" and "aftershock" sequences closely associated with a larger event called "mainshock". The existence of aftershocks (i.e. triggered seismicity) is particularly evident following large earthquakes in tectonic areas. The seismicity rate considerably increases following the mainshock, and decays $\sim$ as the inverse of time [*Omori*, 1894; *Utsu*, 1961]. Aftershock activity eventually dies off and the background seismicity return to be predominant. Prior to the next major earthquake, foreshocks are expected to appear [e.g. *Mogi*, 1968], even if less numerous than aftershocks [*Ogata*, 1988].

Earthquake sequences where no clear mainshock-aftershock pattern is recognizable are called "swarms" [e.g. *Scholz*, 2002].

At volcanoes, subsurface mass movements are are generally accompanied by earthquake swarms of either, VT and LP events [e.g. *Chouet*, 1996; *Saccorotti et al.*, 2002; *Toda*

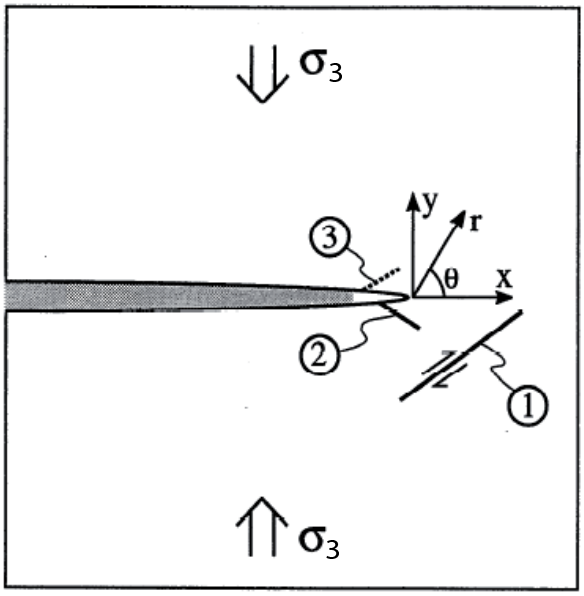

Figure 1.4: Schematic diagram of blade-like dyke and the three types of deformation that could be induced by the propagating dyke, see the text for details. x indicates the dyke propagation direction; σ_3 is the confining pressure. The three type of inelastic deformation *Rubin and Gillard* [1998] consider are: (1) slip on existing faults away from the tip cavity; (2) slip on existing faults adjacent to the tip cavity; (3) shear failure of intact rock adjacent to the tip cavity [from *Rubin and Gillard*, 1998].

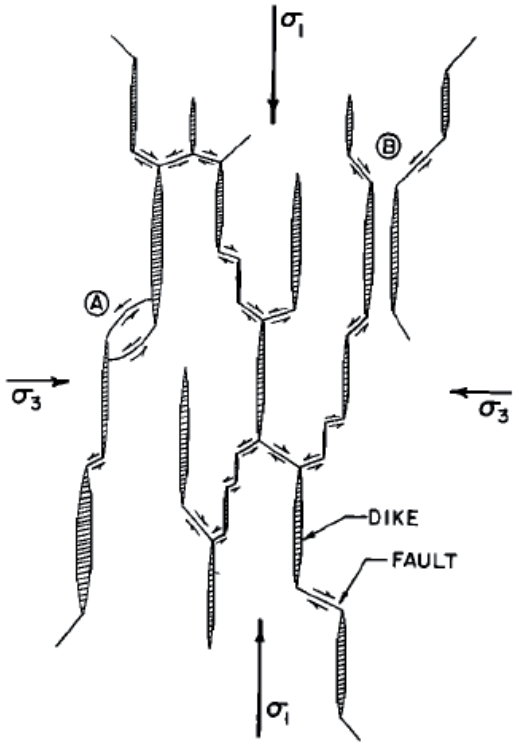

Figure 1.5: Schematic representation of dykes and conjugate fault planes with respect to greatest and least principal stresses σ_1 and σ_3. A and B illustrate typical patterns of crack interactions near adjacent dyke tips in homogeneous media. From *Pollard* [1973].

et al., 2002; *Feuillet et al.*, 2004; *Wright et al.*, 2006; *Pedersen et al.*, 2007]. A clear and straightforward relationship between the volcanic process and associated seismic swarm is however lacking. This is due to the fact that temporal characteristics of earthquake swarms are complex and locally variable [e.g. *Toda et al.*, 2002; *Matsuúra and Karakama*, 2005].

Due to the difficulty in classifying an earthquake as a foreshock, an aftershock, or a mainshock even in tectonic environments, the classic formulation has been revolutionized in recent studies, where the distinction of foreshock-mainshock-aftershock events is removed. Such a discrimination in fact, has no reason to be, since all earthquakes, no matter their magnitude, trigger their own aftershocks, which in turn trigger other aftershocks and so on. Contrary to aftershocks then, which exist at all scales [*Mogi*, 1967; *Scholz*, 1968], individual foreshock sequences are rare and mostly irregular [e.g. *Helmstetter et al.*, 2003a]. Nonetheless, foreshock sequences following an inverse Omori's law emerge from stacking over many mainshocks when conditioning on the time of the mainshock [*Helmstetter et al.*, 2003a]. In this framework, mainshocks are "aftershocks of conditional foreshocks" [*Helmstetter et al.*, 2003a].

In this spirit, the Epidemic Type Aftershock Sequence (ETAS) model introduced by *Kagan and Knopoff* [1981, 1987] and *Ogata* [1988] allows to explore the temporal clustering of the seismic activity without any a-priori on event classification. ETAS model is a stochastic point process describing the seismic activity within a seismically active region. It is a generalization of the modified Omori law and takes into account the secondary aftershock sequences triggered by all events. In this model, therefore, all events can simultaneously play the role of mainshock, aftershock, and possibly foreshock [e.g. *Helmstetter and Sornette*, 2002a; *Helmstetter et al.*, 2003a].

According to the ETAS model, the seismicity can be described, in time, simply as the superposition of two types of earthquakes: a background uncorrelated activity λ_0, and the events triggered by a prior earthquake. An observed aftershock sequence, therefore, is the the result of the activity of all events triggering events, which in turn trigger other events, and so on taken together [*Helmstetter and Sornette*, 2002a]. The works of *Felzer et al.* [2002]; *Helmstetter and Sornette* [2002a]; *Helmstetter* [2003]; *Helmstetter and Sornette* [2003]; *Helmstetter et al.* [2003a] have brought major advances about this subject, by demonstrating that all earthquakes are able to trigger other events, in an amount which is related to their magnitude.

ETAS model is built on the basis of three well-known statistical laws for earthquakes:

1. the Gutenberg-Richter distribution of earthquake sizes, or magnitudes M [*Gutenberg and Richter*, 1949]:

$$P(M) = b\ln(10)10^{-b(M-M_0)}, \tag{1.4}$$

where b is an empirical coefficient and M_0 is a lower bound magnitude corresponding to the completeness of the catalog. At tectonic environments the b-value is generally observed to be close to 1 (the observed range is $0.6 - 1.1$). In volcanic areas, however, higher b-values have been observed, apparently in zones adjacent to magma bodies identified by other techniques, or in zones of high either, thermal gradients, or heterogeneity [for a review see *McNutt*, 2002]. It questions about the use of the b-value as a diagnostic tool for inferring changing processes or mapping magma bodies [e.g. *Wyss et al.*, 1997]. In the ETAS model event magnitudes are drawn from the Gutenberg-Richter law. It implies that the magnitude of a triggered event is statistically independent of the magnitude of the event that have triggered it.

2. the modified Omori law for the aftershock rate R decay following a mainshock [*Omori*, 1894; *Utsu*, 1961]:

$$R(t) = \frac{K}{(t+c)^p}, \tag{1.5}$$

where K, c and p are empirical constants and t is time since the mainshock occurrence. p-values largely vary for different aftershock sequences (the observed range is $0.3 - 2$ [e.g. *Utsu et al.*, 1995]). In tectonic environments, however, they are usually found in the range $0.8 - 1.2$ [e.g. *Utsu et al.*, 1995; *Helmstetter and Sornette*, 2002a].

3. the productivity law, relating the number of aftershocks n_M triggered by a mainshock of magnitude M:

$$n_M \sim 10^{\alpha M}. \tag{1.6}$$

where the exponent α has been estimated within the range $0.8 - 1$ for Southern California seismicity [*Helmstetter*, 2003]. This parameter controls the relative role of small compared to large earthquakes in triggering the seismicity, i.e. how fast the average number of daughter earthquakes per mother event increases with the magnitude of the mother [*Helmstetter and Sornette*, 2002a; *Helmstetter*, 2003; *Helmstetter et al.*, 2005]. Precisely, the number of triggered events born from a mother event of magnitude M has the form:

$$n_M = K10^{\alpha(M-M_0)}, \tag{1.7}$$

4. the fractal structure of faults along which earthquakes are clustered in space [*Kagan*, 1991]:

$$P(r) \sim r^{D-1} \tag{1.8}$$

where $P(r)$ is the time-independent density of distances r between hypocenters, and D is the fractal dimension of the fault network. The area affected by the stress variation induced by an earthquake increases with the rupture length, while the stress drop induced by the same earthquake is independent of its magnitude [*Utsu*, 1961; *Kagan*, 2002; *Kanamori and Anderson*, 1975; *Helmstetter*, 2003]. Assuming that the aftershocks are triggered by the stress change induced by the mainshock, the density of triggered earthquakes is independent of the mainshock magnitude for distances r proportional to the rupture length L from the mainshock. Analogously, the distance between the mother and the daughter events is assumed to be independent of the magnitude of the first and of the delay between the first and the seconds [*Helmstetter and Sornette*, 2002a; *Helmstetter*, 2003]. However, larger earthquakes influence seismicity in a wider area, proportional to the mainshock rupture area [*Kagan*, 2002; *Helmstetter et al.*, 2005]. Consequently, the increase in the number of triggered events with the mainshock magnitude simply arises from the increase in the aftershock zone size with the rupture length [*Helmstetter*, 2003]. This latter is usually related to the magnitude as follows [*Kanamori and Anderson*, 1975]:

$$L \sim 10^{0.5M} \tag{1.9}$$

On the other hand, since aftershocks are distributed on a fractal structure, the number of aftershocks triggered by a mainshock of magnitude M is [*Helmstetter*, 2003]:

$$n_M \sim r^D \tag{1.10}$$

where r is the characteristic length of the aftershock zone [*Helmstetter*, 2003]. Combining the last two equations we get

$$n_M \sim 10^{0.5DM}. \tag{1.11}$$

D is the fractal dimension of the spatial distribution of aftershocks. D values have been observed in the range $1.5 - 2.8$ [*Guo and Ogata*, 1997; *Helmstetter*, 2003]. For California seismicity, *Helmstetter* [2003] finds $D = 1.6$, i.e. $D = 2\alpha$, where α has been described in point 3. It implies that the aftershock productivity α can be related to the fractal structure of the spatial distribution of seismicity [*Helmstetter*, 2003].

In conclusion, according to the ETAS model, an earthquake can trigger other earthquakes of any magnitude (drawn from the Gutenberg-Richter law). That is, the triggered events can be larger, equal, or smaller than the earthquake that triggered them. *Felzer et al.* [2002]; *Helmstetter and Sornette* [2002a]; *Helmstetter* [2003]; *Helmstetter and Sornette* [2003]; *Helmstetter et al.* [2003a] show that secondary aftershocks (i.e. events triggered by previous earthquakes which are already aftershocks) dominate an aftershock sequence, so that subsequent large aftershocks are more likely to be triggered indirectly by a previous aftershock of the mainshock.

The ETAS model is currently considered as a null hypothesis for earthquake statistics and earthquake predictability, and it should therefore be rejected first before evidence for new effects is demonstrated [*Saichev and Sornette*, 2007].

According to the ETAS model, the seismicity rate can be written in time as follows:

$$\lambda(t) = \lambda_0 + \sum_{t<t_i} \frac{K\ e^{\alpha(M_i - M_0)}}{(t - t_i + c)^p}. \tag{1.12}$$

where λ_0 is the background event rate, and the second term contains the cascading process that gives birth to the triggered seismicity [e.g. *Ogata*, 1988; *Utsu et al.*, 1995; *Helmstetter and Sornette*, 2002a]. The background seismicity is modeled as a stationary Poisson process whose events are statistically independent from each other [e.g. *Ogata*, 1988; *Helmstetter and Sornette*, 2002a].

The λ_0 term represents the direct response of the solid matrix to the external forcing process, i.e. the tectonic loading or, at volcanic environments, the acting volcano process, such as mass movements or pressure and temperature variations within the volcano. Likewise, *Collombet et al.* [2003] suggest that, on volcanoes, aftershock events are noise that prevent a direct mapping of the seismicity rate onto the volcanic processes.

With the aim of quantifying the underlying physical processes that drive seismicity, various attempts of quantifying these two types of seismicity have been made, giving birth to a series of declustering techniques. Pioneer techniques are based on space-time distance between the events [e.g. *Reasenberg*, 1985; *Frohlich and Davis*, 1990; *Davis and Frohlich*, 1991] and are heavily parameter dependent since based on arbitrary rules [*Marsan and Lengliné*, 2008].

Recently more sophisticated methods of stochastic declustering have been proposed. They work on determining the probability that a given earthquake triggered another given earthquake [*Zhuang et al.*, 2002]. In this case, however, the result is model-dependent, as

the influence of a given earthquakes is constrained to follow a specific law, whose parameters have to be inverted [*Marsan and Lengliné*, 2008].

Marsan and Lengliné [2008] propose a new model in which probability of directly and indirectly triggered aftershocks can be estimated with no a-priori model. Taking advantage of the characteristic shape of the interevent time distribution of earthquakes [*Corral*, 2003, 2004a,b; *Molchan*, 2005], *Hainzl et al.* [2006], propose a different style of declustering technique, based simply on the memory between successive earthquakes, which influences the distribution of interevent times.

One must note, however that a limit of all these techniques arise from the assumption that background seismicity is stationary over time, which represent a very strong and often unacceptable assumption when considering seismic sequences driven by highly non-stationary processes such as many volcano processes.

Part I

Seismic Signature of Dyke Propagation

Chapter 2

Brittle creep damage as the seismic signature of dyke propagations within basaltic volcanoes

Paola Traversa and Jean-Robert Grasso

Laboratoire de Géophysique Interne et Tectonophysique,
CNRS - OSUG - Univeristé Joseph Fourier, BP 53 38041 Grenoble Cedex 9, France

Paper published under the reference: *Bull. Seismol. Soc. America* (2009) *99*(3), 2035-2043.

Abstract

Contemporary to 9 dyke intrusions on Piton de la Fournaise, Etna and Miyakejima volcanoes, we recover stationary seismicity rate and energy release over time, whatever the dyke reaches the surface or not. This generic seismicity pattern for the dyke propagation of low viscosity magma argues for the fluid driven crack propagation to be a scale independent stationary process. This prevents any prediction of the time to eruption during the dyke propagation phase using seismicity rate alone. The seismic signature of the volcano deformation triggered by dyke injections corresponds to brittle creep damage in a strain

driven setting. Whether mechanical properties of host rock structure or geometrical effects influence this generic stationary response is not resolved by the seismic data. Since a few if any aftershocks are resolved contemporary to dyke intrusions, the seismicity is purely driven by the dyke dynamics, i.e. a proxy for the dyke volumetric growth.

Résumé

Pendant neuf intrusions de dyke aux volcans du Piton de la Fournaise (La Réunion), Etna (Sicile) et Miyakejima (Japon), nous retrouvons des taux de sismicité et d'énergie libérée stationnaires au cours du temps, peu importe si le dyke atteint la surface ou non. Ce motif générique de sismicité, qui caractérise la propagation des dykes de magma peu visqueux, suggère que la propagation d'une fracture conduite par le fluide est un processus indépendant de l'échelle et stationnaire. Cela rend impossible toute prédiction du temps de début de l'éruption pendant la phase de propagation du dyke en utilisant le seul taux de sismicité. La signature sismique de la déformation d'un volcan sous l'effet d'une injection de dyke correspond à de l'endommagement en forme de fluage fragile dans un cadre à déformation contrôlée. Si les propriétés mécaniques de l'encaissant ou des effets géométriques influencent cette réponse stationnaire générique ne peut pas être résolu avec les données de sismicité. Puisque peu ou pas de répliques ont été observées contemporainement à l'intrusion du dyke, la sismicité est directement gouvernée par la dynamique du dyke, cet à dire elle est une mesure de la croissance volumétrique du dyke.

2.1 Introduction

Abrupt changes in seismic activity have often proved to be a clear observable attesting ongoing magmatic processes in volcanic areas around the world [e.g. *Rubin and Gillard*, 1998; *Aki and Ferrazzini*, 2000; *Toda et al.*, 2002; *Smith et al.*, 2004; *Aloisi et al.*, 2006; *Pedersen et al.*, 2007]. The seismicity associated with intrusive events has been related to the distribution of ambient stresses near to failure [e.g. *Rubin and Gillard*, 1998; *Pedersen et al.*, 2007], or to the variations in the stressing rate induced by the intruding magma [e.g. *Toda et al.*, 2002].

A few analogical [e.g. *Menand and Tait*, 2002; *Rivalta et al.*, 2005; *Rivalta and Dahm*, 2006, among many others] and analytic models [for a review see *Rubin*, 1995] of dyke propagation have also been proposed, allowing to improve the understanding of this process.

However, a clear and unambiguous relationship between dyke propagation and induced seismicity is still missing.

In this study we use the seismic response of volcanoes to low viscosity magma transfers in order to constrain the mechanical processes that drive fluid transfers during the last stage before an eruption, i.e. the dyke propagation. We analyze seven dyke intrusions on the (PdlF) Piton de la Fournaise volcano, Reunion Island, Indian Ocean, during the period 1988-1992, which preceded a 6 years repose period. We compare these patterns to the intrusion feeding the 2002 Etna eruption, Sicily, Italy, and the 2000 Miyakejima intrusion, Izu Island, Japan.

During the considered period, seismicity accompanying dyke propagations at PdlF volcano is dominated by Volcano-Tectonic (VT) events [*Aki and Ferrazzini*, 2000, e.g.]. The same holds for the Etna 2002 and Miyakejima 2000 intrusions [Patané and Saccorotti, personal communication, 2007 and JMA catalogue]. On these 3 volcanoes and during their dyke propagations, the VT events map the brittle damage induced in the host rock structure by the magma movement on his way toward the volcano surface [e.g. *Grasso and Bachelery*, 1995; *Rubin and Gillard*, 1998]. The brittle damage we record during dyke propagations as seismic events is the sum of diffuse events corresponding to the deformation of the heterogeneous volcano rock mass to dyke intrusion, plus the localized cracking at the dyke tip during its opening. From theoretical argument, the latter is expected to be, in most cases, too high frequency and too small in size to be recorded at the volcano surface [e.g. *Cornet*, 1992; *Rubin*, 1995].

We first characterize the seismicity and energy rate patterns during seven dyke intrusions at PdlF. Second, we validate on Etna and Miyakejima volcanoes how generic, for low viscosity dyke intrusions, the PdlF dyke propagation patterns are. Third, we derive, from the observed seismicity patterns, mechanical implications for the dynamics of the dyke intrusions.

2.2 Data

Although the PdlF eruptions still remain difficult to predict in time, space and size domains [e.g. *Grasso and Zaliapin*, 2004], the distinguishing mark of the pre-eruptive history at PdlF is the existence of a so-called seismic crisis preceding each eruption. These crises are swarms of shallow VT events which are the hallmark of the few hours ultimate

stage before the magma reaches the volcano surface [*Aki and Ferrazzini*, 2000, and references therein]. They are characterized by seismicity rates more than ten times larger than the ones normally recorded during the last week before each of the eruption onsets [*Grasso and Zaliapin*, 2004, e.g.].

We analyse the 7 crises that occurred on the period 1988-1992 at PdlF volcano, six of them leading to surface lava flow (see table 2.1). During this period, the seismic crises are only recorded by three summit stations of the PdlF seismic network. Time series of earthquake occurrences were extracted from analogical signal recordings (see Data and Resources Section), each event being characterized by an arrival time and a signal duration. This latter is converted into a local magnitude using, $Md = -0.9 + 2\log 10(\tau)$, τ being the seismic signal duration [OVPF (Observatoire Volcanologique du Piton de la Fournaise), personal communication]. Accurate earthquake locations were not available for most of these events, but previous studies on the seismicity at PdlF volcano during the study period show that, when available, the few located events are shallow, primarily above sea level, and below the summit crater, i.e. within one or two km below the summit caldera [e.g. *Lénat and Bachèlery*, 1990; *Aki and Ferrazzini*, 2000]. During the period 1988-1992, the absence of deep seismicity and the short duration, i.e. 0.5-4.5 hrs, of the pre-eruptive seismic swarms, suggest a shallow origin of the magma storage area [e.g. *Lénat and Bachèlery*, 1990].

The intrusion onset is defined by the arrival time of the first event of the accompanying seismic crisis. These onsets are easily identified since the seismicity rate jumps from a maximum of 10 events/day to 2-5 events/minute for each crisis onset. The end of the crisis is defined by the emergence of the volcanic tremor on the recorded signals, which is contemporary to surface fluid flow within 10-20 minute time lags [*Aki and Ferrazzini*, 2000, and OVPF, personal communication]. The durations of the seismic crisis range from 0.5 to 4.5 hrs, with a 1.6-2.6 maximum magnitude range (table 2.1).

On Mt. Etna volcano we analyse seismic events in the 20:12, 10/26/2002 - 04:00, 10/27/2002 (LT) period. This period includes an initial vertically ascending dyke on the S-SW flank followed by a migration of the injection path toward the NE flank [e.g. *Aloisi et al.*, 2006]. On Miyakejima, following previous studies, we considered the period characterized by the lateral migration of the magma towards the northwest of the island up to the first summit eruption, i.e. 9:00, 06/27/2000 - 18:40, 07/08/2000 (LT) [e.g. *Ueda et al.*, 2005].

There is no recorded Long Period (LP) event during the 2002-2003 Etna eruption

Table 2.1: Seismicity during dyke injections

Intrusion* (mm/yy)	Duration (hr)	$M_c^{\dagger}$	$M_{max}^{\ddagger}$	$N_{M \geq M_c}^{\S}$	$\langle R^{\|} \rangle$ (N/day)	$b - value^{\sharp}$	V_{erupt}^{**} (x 10^6 m^3)
PdlF (05/88)	0.5	0.5	2.6	58	2735	1.0 ± 0.1	30
PdlF (08/88)	2.3	0.7	2	153	1518	1.4 ± 0.1	< 4
PdlF (12/88)	4.5	0.7	2.2	199	1079	1.0 ± 0.1	8?
PdlF (01/90)	0.3	0.2	1.6	34	2661	0.9 ± 0.2	< 1
PdlF (07/91)	0.75	0.5	2.3	50	1529	1.0 ± 0.1	8?
PdlF (12/91)	0.5	0.5	2.1	44	2209	0.9 ± 0.2	< 1
PdlF (08/92)	0.7	0.2	2.1	97	3656	1.0 ± 0.1	5
ET (10/02)	6.3	2.4	4.2	70	267	1.2 ± 0.1	Intrusion
MI (07/00)	278.6	3.0	6.5	1923	166	0.97 ± 0.01	Mostly phreatic

* Piton de la Fournaise, PdlF; Etna, ET; Miyakejima, MI.
$^{\dagger}M_c$ is the completeness magnitude.
$^{\ddagger}M_{max}$ is the maximum magnitude.
$^{\S}N_{M \geq M_c}$ is the number of events with $M \geq M_c$. $^{\|}\langle R \rangle$ is the average seismicity rate.
$^{\sharp}b$-value of the Gutenberg-Richter law (values and errors calculated by maximum likelihood [*Aki*, 1965]).
$^{**}V_{erupt}$ is the volume of lava erupted. See the Data and Resources section for the source of the values for the PdlF intrusions. The values for Etna intrusions are from *Aloisi et al.* [2006].

[Patané and Saccorotti, personal communication, 2007]. LP events are 0.7% of the seismicity during Miyakejima intrusions as listed from the Japan Meteorological Agency (JMA) catalogue.

At PdlF, on the period 1988-1992, the magnitude frequency distribution of each of the seismic crises induced by dyke injections follows the Gutenberg Richter law over three orders of magnitude. The b-values are in the 0.9 - 1.4 range, with a 1.0 average value (table 2.1). This value reminds the $b \sim 1$ value estimated for the PdlF volcano seismicity, apart from intrusion phases, on the same 1988-1992 period [*Grasso and Bachelery*, 1995]. Gutenberg Richter distributions are also recovered for the seismicity during Etna and Miyakejima dyke intrusions (table 2.1).

2.3 Seismicity patterns during dyke intrusions

2.3.1 Direct and indirect magma driven seismicity during dyke intrusions

In terms of conditional intensity, the seismic activity can be described, in time, as the superposition of two types of earthquakes: a background uncorrelated seismicity λ_0 and the events triggered by another earthquake. The former is modelled as a stationary

Poisson process whose events are statistically independent from each other, and the latter by a power law decay of event rate following the occurrence of a given event [e.g. *Utsu et al.*, 1995; *Helmstetter and Sornette*, 2003]. The seismicity rate R can thus be expresses as following:

$$R = \lambda_0 + \sum_{t<t_i} \lambda_i(t). \tag{2.1}$$

This triggered seismicity (the so-called aftershocks) emerges from a cascading process of earthquake interactions. Rough estimates of these two types of earthquakes for tectonic seismicity lead to 30-90% of the tectonic earthquakes to be aftershock events. The result accuracy remains strongly dependent on the declustering techniques used, [e.g. *Helmstetter and Sornette*, 2003].

In volcanic contexts, the background seismicity is driven by mass movements, pressure and temperature variations within the volcano. Likewise, *Collombet et al.* [2003] suggested that, on volcanoes, aftershocks events are noise that prevents a direct mapping of the seismicity rate onto the magma transfer. During dyke intrusions, we cannot recover the Omori power law pattern of seismicity following single events (fig. 2.1), arguing for either, a negligible amount of aftershocks, or the correlated seismicity to be hidden under a considerably high background event rate. In both cases, the VT events we work with on the PdlF, Etna and Miyakejima volcanoes, are almost purely driven by the dyke propagations rather than by earthquake interactions. Unfortunately we cannot not obtain a robust estimate of the two portions of seismicity during dyke intrusion with any of the available declustering techniques. This may be due to non-stationarities in the temporal evolution of the two reciprocal quantities during the intrusion. Such non-stationarities have been reported by *Lombardi et al.* [2006] for the Izu Island 2000 seismic swarm when considering the whole seismic sequence. All this argues for the dyke-induced seismicity to be peculiar with respect to tectonic seismicity.

Note that we tested that this lack of aftershock pattern is not recovered when analyzing PdlF, Etna and Miyakejima volcano seismicity apart from their dyke injections periods.

2.3.2 Seismicity rate patterns of dyke propagations

On PdlF, the normalized time evolutions of the cumulative number of earthquakes for each dyke intrusion do not show any specific change in pattern toward eruption time (fig.

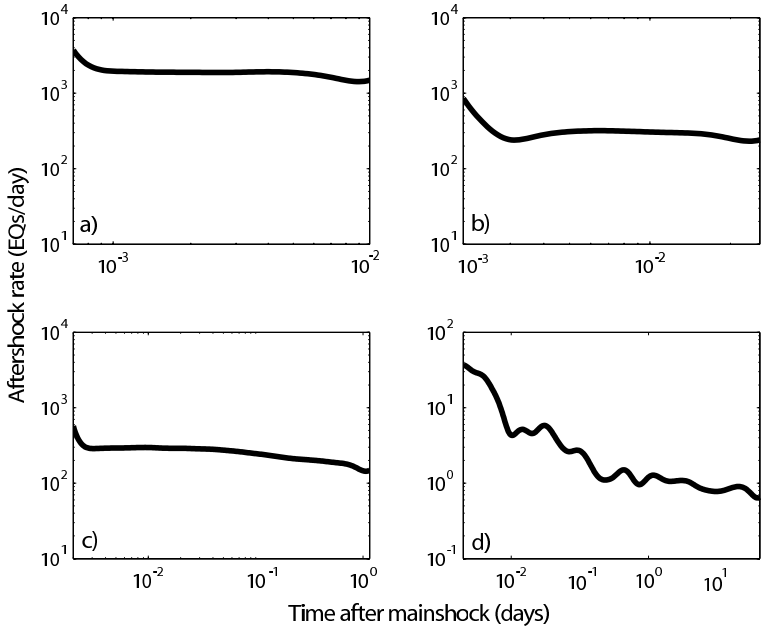

Figure 2.1: Aftershock rates vs time since mainshock. a) PdlF Aug. 31 1988 eruption; b) Etna 2002 eruption; c) MI 2000 dyke intrusion; d) Etna seismicity apart from any intrusion (10/29/2002 âĂŞ 12/31/2003). $t = 0$, mainshock occurrence, $t > 0$, averaged seismicity rates following mainshocks. Mainshocks are events (i) of any magnitude not preceded by another event for a time equal to the median of the inter-occurrence times and (ii) occurring within 10% - 90% of the intrusion duration window to avoid border effects [Helmstetter 2007, personal communication]. Curves are averaged over: (i) all mainshocks from a given magnitude class, and (ii) all magnitude classes. The power law decay of seismicity rate quantifies the percentage of aftershock, which is negligible for a), b) and c) and close to 20-25% for d), with a $1/t^{0.7}$ decay within 0.2 days after the mainshock.

2.2). The upward and downward bending patterns appear as not significant when tested against a Poisson process. As shown in figure 2.3 and 2.4, most of them are within the fluctuations we reproduce when sub-sampling Poisson time series two orders of magnitude larger in size than single datasets. From each generated Poisson time series, we draw one hundred subsets having the same small size as datasets ($34 \leq N \leq 199$). The envelopes of the one-hundreds-subsets mostly contain data fluctuations, preventing from discriminating observed from Poisson distributions. When tested for single PdlF seismic datasets (fig. 2.3) five distribution fluctuations over seven are not significant when tested against a random Poisson process. It indicates a more than 70% probability that data distributions are described by a Poisson process. There is no correlation between the shape of the seismicity rate curves and either the erupted volumes or the durations of the seismic swarms (fig. 2.2, 2.3, table 2.1).

When stacking seismic time series before PdlF eruptions in the period 1988-1992, *Collombet et al.* [2003], resolve an average power law increase in the average daily VT seismicity rate 10-15 days prior to the eruption. Excluding the very eruption day data, the authors focus their attention to the reservoir fracturing phase. On the same period of study, and by using the same stacking techniques on the following dyke injection phase, average VT rate does not show any power law accelerating pattern towards eruption time. Red dashed curve in fig. 2.2 indicates a power law pattern with an a exponent of 0.7 [*Collombet et al.*, 2003]. The same result holds for Etna 2002 and Miyakejima 2000 dyke intrusions (fig. 2.4), while time durations, induced seismicity rates and maximum earthquake sizes span on 3 orders of magnitude (table 2.1). Note that from now on, we treat the average of the 7 dyke injection at PdlF as a single intrusion in order to ease comparisons among the three volcanoes.

To compare the earthquake productivity per surface and volume unit during dyke injections on the three volcanoes, we normalize each seismicity rate by its completeness magnitude, magnitude span, dyke surface and volume (tables 2.1 and 2.2). We find that no matter whether the system is open (i.e. Etna and PdlF volcanoes) or closed (i.e. Miyakejima), the seismic productivities are close together during dyke injection, $\sim$ 103 eqs/day/km^2. It suggests that a dyke propagation produces similar fracture densities during its propagation no matter the volcano system is defined as open or not. Any possible viscosity effect on seismicity rate cannot be quantified for these 3 volcanoes.

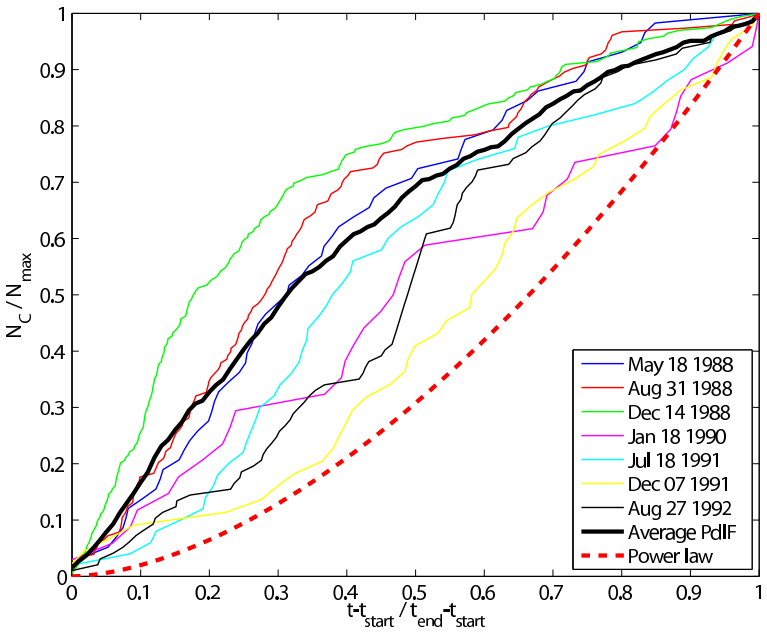

Figure 2.2: Normalized cumulative seismicity rate versus normalized time: 7 intrusions at PdlF: May 18 1988, thin dark blue line; Aug 31 1988, thin purple line; Dec 14 1988, thin green line; Jan 18 1990, thin pink line; July 18 1991, thin light blue; Dec 07 1991, thin yellow line; Aug 27 1992, thin black line; Average pattern for the 7 intrusions at PdlF, thick black line. For reference: dashed red: power law pattern with exponent 0.7. t_{start} and t_{end} are the beginning and the end of the seismic crisis, respectively; N_c and N_{max} are the cumulative and the total number of earthquakes for the considered crisis.

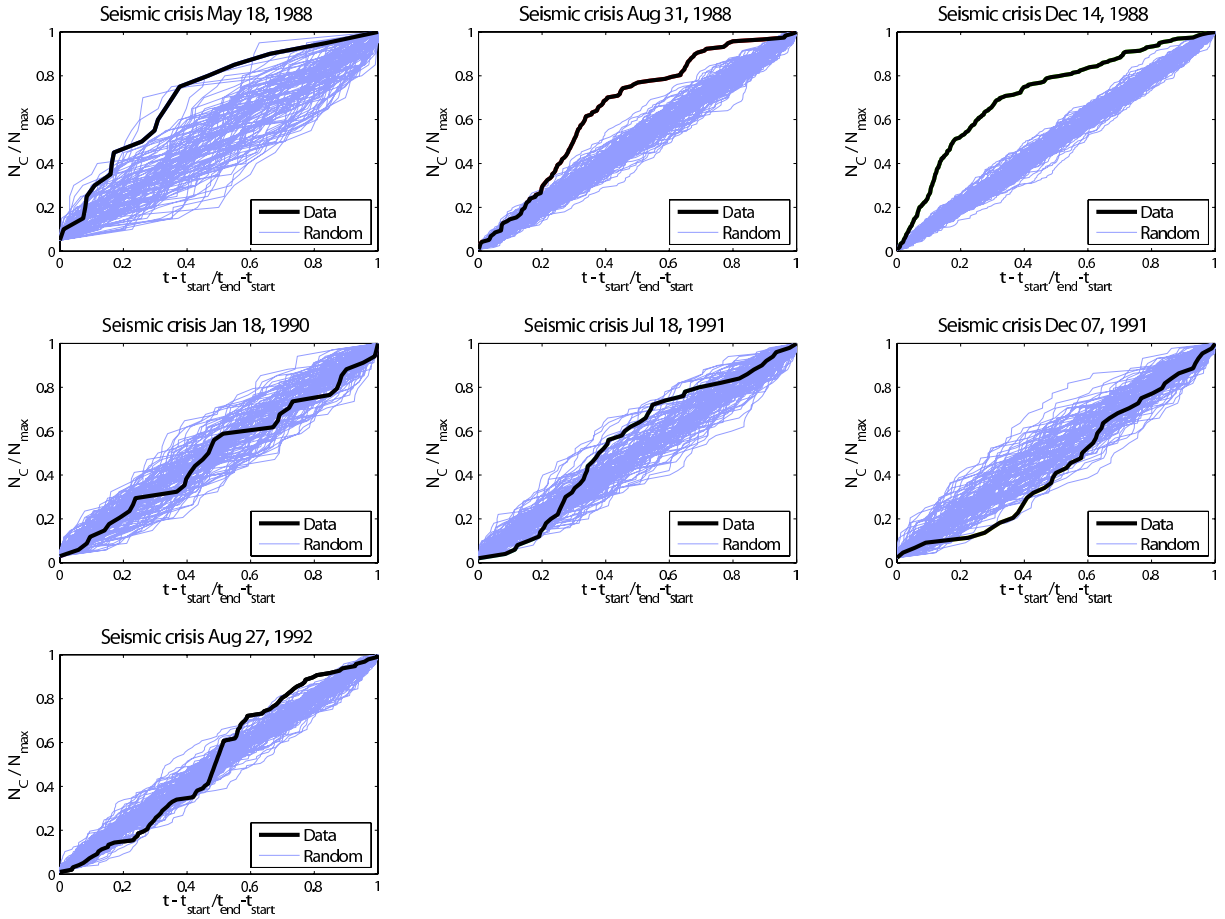

Figure 2.3: Normalized cumulative seismicity rate versus normalized time for each dyke intrusion at Piton de la Fournaise during the period 1988-1992. Thick black lines: cumulative seismicity; thin gray lines: Poisson subsets. t_{start}: beginning of the seismic crisis; t_{end}: end of the seismic crisis/eruption onset. N_c and N_{max}: cumulative and the total number of earthquakes for the considered crisis. Each subset has the same size as datasets. The Poisson process is two magnitude orders bigger in size than single datasets.

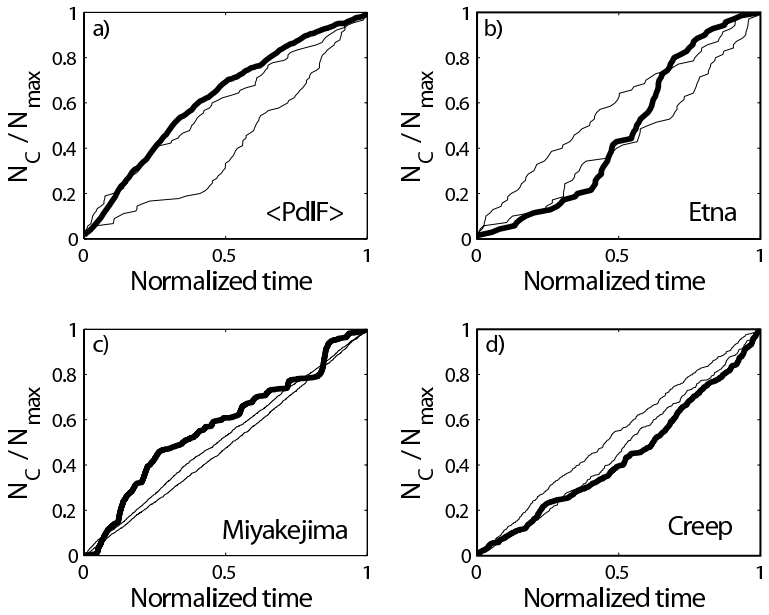

Figure 2.4: Normalized cumulative seismicity rate versus normalized time. Average pattern for 7 intrusions at PdlF: thick black line; Etna 2002: thick red line; Miyakejima 2000: thick blue line; Secondary creep simulation of rock damage with incremental exponential time-to-failure *Amitrano and Helmstetter* [2006]: thick violet line. Light lines in each graph: envelopes of sub-sampling sets drew from a homogeneous Poisson process. Each sub-set has the same size as datasets. The Poisson process is two magnitude orders bigger in size than single datasets. Normalized time is the time since the start of the crisis divided by the crisis duration; N_c and N_{max} are the cumulated and the total number of earthquakes, respectively.

2.3.3 Seismic energy release rate patterns during dyke intrusions

Analogously to the seismicity rate, the rate of seismic energy release during the dyke propagations at PdlF, Etna and Miyakejima intrusions, turned out to be constant in average (fig. 2.5). The fluctuations we observe apart from the mean value are reproduced by randomly picking the same number of events as our time series in the corresponding Gutenberg Richter law for each volcano. It confirms the lack of any temporal trend. The steady state of energy release pattern over time is confirmed by the constant b-value recovered during the Miyakejima dyke propagation, after a very short duration initial transient (fig. 2.5, inset). This initial transient may be due to the lack of some smaller events in the seismic catalogue at the very beginning of the seismic crisis.

The average energy release rate during PdlF dyke propagations is one order of magnitude smaller than during the Etna and Miyakejima intrusion (fig. 2.5). This mimics the relative scaling between the dyke sizes for the three volcanoes we work with. *Pedersen et al.* [2007] demonstrate that background stress state is a dominant factor governing seismic energy release during magmatic-induced seismic crisis. The above statement could therefore entail similar reference stress states for the three considered cases. To further check for any possible scaling effect, we normalize the observed seismicity rates on the three volcanoes by the same virtual completeness magnitude (mc=0.2) and magnitude spread ($\Delta M = 1.4$). Scaling of these normalized rates (R^*) on the three cases, mimics the one we observe when comparing the size of the largest brittle fracture during each intrusion, $M_{max} = 2.6 - 4.2 - 6.5$, to the dyke lateral extension $B =< 1 - 6.6 - 20$ km, for PdlF, Etna and Miyakejima respectively, see table 2.2. It argues for the seismicity rate during dyke injection to be mostly dependent on the dyke size. Lack of precise magma viscosity estimates prevents for evaluating the role of this parameter in determining the fracturing density induced by the magma intrusion. In this framework the larger magnitudes we observe at Miyakejima than, at Etna and PdlF, respectively, emerge from a higher number of events drew from a Gutenberg-Richter distribution on Miyakejima than on the other two volcanoes.

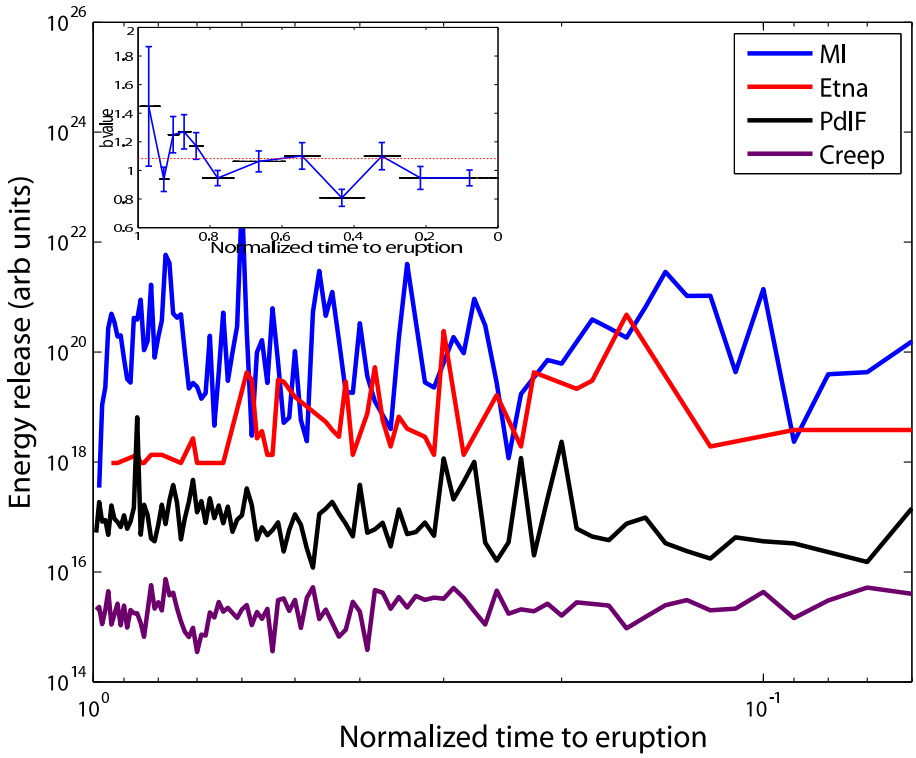

Figure 2.5: Seismic energy release rate during dyke intrusion vs normalized time to eruption. $t = 0$ is end of the intrusion or eruption time. Average pattern for 7 intrusions at PdlF, thick black line; Etna 2002, thick red line; Miyakejima 2000, thick blue line; Secondary creep simulation of rock damage with incremental exponential time-to-failure [*Amitrano and Helmstetter*, 2006], thick violet line. Inset: time evolution of Gutenberg-Richter b-value Miyakejima intrusion. Normalized time to eruption is the time to eruption divided by the crisis duration.

2.4 A generic model for dyke propagation in basaltic volcanoes as mapped from VT seismicity patterns

When analyzing the seismicity contemporary to nine dyke intrusions, i.e. PdlF: 6 eruptions and 1 intrusion, 1988-1992; Etna: 2002 eruption and Miyakejima: 2000 intrusion, we recover stationary seismicity and energy rates (fig. 2.2, 2.3, 2.4 and 2.5). Note that this seismicity rate is 2-3 orders of magnitude larger than the background seismicity rate. We tested that most of the fluctuations around the average constant event and energy rates can be reproduced when sub-sampling a Poisson time series and the Gutenberg-Richter magnitude distribution, respectively.

Using Acoustic Emissions (AE) at laboratory scales, similar stationary patterns are reproduced during strain controlled experiments, e.g. paper peeling, [*Salminen et al.*, 2006], or during secondary creep deformation of rocks, [e.g. *Amitrano and Helmstetter*, 2006]. Numerical simulations of static fatigue of rock during creep processes [*Amitrano and Helmstetter*, 2006] reproduce both the stationary pattern for energy and seismicity rates and the lack of aftershock patterns within local brittle failures, similarly to the seismicity patterns we resolve contemporary to the dyke intrusions (fig. 2.4, 2.5). This holds during the simulated secondary creep phase, when *Amitrano and Helmstetter* [2006] assume an exponential relationship between time-to-failure and applied stress. Accordingly, the seismicity patterns we observe during dyke propagations, further argue for the dyke propagation to be a scale independent strain driven process that induces diffuse brittle damage within the volcano host rock. As discussed by *Rubin and Gillard* [1998]; *Grasso and Bachelery* [1995], the seismic response of a volcano to dyke injection is a diffuse brittle damage within the shallow volcanic edifice. It evidences the best candidate for driving the seismicity induced by the dyke propagation is the (ΔV) volume change induced by the ongoing dyke intrusion within the shallow volcano structure.

For incompressible magmas, the magma flux in the dyke equals the volume of magma injected through the cross section into the dyke in the unit time. It corresponds to the volume change generated by the dyke within the volcano system in the unit time. The observed stationary seismicity rate accompanying dyke injection highlights therefore a stationary volumetric flow rate $q(z,t)$ of magma into the dyke, in agreement with the hypothesis made by *Lister* [1990a], who numerically solved the equations governing crack width and fluid pressure for a buoyancy driven crack.

Table 2.2: Dyke geometry and Induced Seismicity

Intrusion*	EQ.		Dyke					$\langle R^* \rangle^\sharp$	$\langle R^* \rangle / S_D^\sharp$	$\langle R^* \rangle / V_D^\sharp$
	$M_{max}^\dagger$	$S_{M_{max}}^\ddagger$	$B^\S$	$H^\S$	$S_D^{\ddagger\ddagger}$	$w^\|$	$U^\sharp$			
(mm/yy)		(km^2)	(km)	(km)	(km^2)	(m)	(m/s)	(eqs/d)	(eqs/d/km^2)	(eqs/d/km^3)
$\langle PdlF \rangle$	2.6	0.08	$< 1^{**}$	1-2**	< 1	$\lesssim 1^{**}$	0.2-2**	4 x 10^3	4 x 10^3	4 x 10^6
ET (10/02)	4.2	2.29	6.6††	4.6††	30.4	$\sim 1^{\dagger\dagger}$	0.3††	1.3 x 10^5	4.3 x 10^3	4.3 x 10^6
MI (07/00)	6.5	269.1	$18 - 20^{\ddagger\ddagger}$	8-15‡‡	144-300	$\sim 1^{\ddagger\ddagger}$	0.03‡‡	1.2 x 10^6	4-8.3 x 10^3	2-4.3 x 10^6

*$\langle PdlF \rangle$ is the PdlF average. ET is the Etna 2002 intrusion. MI is the Miyakejima 2000 intrusion.
†M_{max} is the maximum magnitude.
‡$S_{M_{max}}$ is the rupture surface generated by an earthquake of M_{max} [*Wells and Coppersmith*, 1994].
§B and H are the lateral and vertical extension, respectively, of the dyke wall intended as a rectangular surface.
‖w is the dyke opening.
♯$BH = S_D$ is the dyke surface. $S_D w = V_D$. U is the dyke propagation velocity. $\langle R^* \rangle$ is the average seismicity rate normalized to $M_c = 0.2$ and $\Delta M = 1.4$. b-value of each volcano (see the text for details).
**OVPF (personal communication, 2007, and *Lénat and Bachèlery* [1990]).
‡‡*Aloisi et al.* [2006].
‡‡*Toda et al.* [2002].

2.4.1 Seismicity rate and dyke velocity in homogeneous medium

In the previous section we related the seismicity rate induced by the dyke intrusion to the flux injected at the dyke inlet. Because most of the physical and numerical experiments simulate dyke propagations in a homogeneous medium, we discuss here the possible relationship between the seismicity rate and the dyke injection velocity in the homogeneous medium context.

Rivalta et al. [2005]; *Rivalta and Dahm* [2006] suggest a direct relationship between the dyke propagation velocity and the number of dyke-induced earthquakes on the base of laboratory experiments on homogeneous gelatin. On this hypothesis, the stationary seismicity rate we observe on the three volcanoes during dyke propagation would imply a constant propagation velocity of the fluid-filled fracture within a homogeneous medium.

On the other hand, during the initial phase of the vertical dyke propagation, when the excess pressure dominates the propagation, a dimensional estimate of the dyke propagation velocity, U, argues the dyke velocity to scale with the dyke length during dyke growth [*Rubin*, 1995]:

$$U \sim \mu^a m^e P_o^c l^d, \tag{2.2}$$

where μ is the magma viscosity, m is related to the rock matrix mechanical properties, P_o is the overpressure at the dyke inlet, and l is the dyke length. Values for the exponents are given by *Rubin* [1995]: a = -1, e = -2, c = 3, d = 1. This scaling does not depend on the a-priori assumption on the dyke propagation to be driven either, by a specific source flux

or by a specific source pressure.

Dyke length increase leads to a progression from excess-pressure dominated flow to buoyancy-dominated flow [e.g. *Rubin*, 1995]. When equation 2.2 describes the dyke propagation velocity, we are bounded to recover an l^d accelerating dyke velocity through time. This is in contrast with the stationary inelastic host rock deformation we observe on the three volcanoes (fig. 2.2, 2.3, 2.4). It argues for a complex scaling, if any, between dyke velocity and seismicity rate, which may arise during dyke growth or acceleration/deceleration phases [e.g. *Smith et al.*, 2004; *Battaglia et al.*, 2005b].

First, the constant seismicity recorded at volcanoes during dyke propagation may be deaf both, to the dyke fracturing tip, and to the excess-pressure driven dyke propagation [*Cornet*, 1992; *Rubin*, 1995; *Menand and Tait*, 2002; *Roper and Lister*, 2005, e.g.]. Second, our observations fit the average pattern of the second regime observed in Menand and Tait, [2002] lab experiments, where buoyancy overcomes the source pressure as the driving force, and vertical steady-state propagation emerges, with constant velocity, flux and strain energy release. Consequently, for eq. 2.2 to fit the observed stationary seismic rate we need the dyke length, l, to keep constant during the dyke propagation. This length, the buoyancy length, is a characteristic length for dyke propagation [*Weertman*, 1971a,b, e.g.]. Numerically, *Chen et al.* [2007] investigated the propagation of a dyke driven by a constant over-pressured source into a semi-infinite elastic solid with graded mass density. Seeking a constant stress intensity factor at the dyke tip, they demonstrated that only continuously decreasing overpressure in the magma chamber could result in steady-state dyke propagation. It argues for a finite size of the storage system relatively to the intruded volume for the volcanoes we are working with.

2.5 Concluding remarks

Stationary seismic event rates recorded during dyke propagations on three basaltic volcanoes evidence the opening of the dyke walls to be a steady-state brittle creep process. This prevents any prediction of time to eruption using seismicity rate alone. We observe the seismic response is scale independent in the 102 - 104 m ranges of intrusion lateral dimensions. Fracture densities of the same order of magnitude are needed for the dyke to reach its final size on the three volcanoes. This argues for the brittle damage induced during dyke intrusions to be a generic process whatever the volcanoes are defined as open

or close systems, such as PdlF and Etna, and Miyakejima volcanoes, respectively (table 2.2).

For each intrusion there is no evidence for changes in seismicity rate with either, rock property changes within the volcanoes, distance to the free surfaces, or vertical to lateral dyke propagation styles. Any possible intermittency is not significant when tested against random distribution. This means that VT seismicity alone is deaf to both, geometric and mechanic heterogeneities characterizing dyke propagation towards the surface. The stationary inelastic host rock deformation observed during dyke intrusion, suggests, instead, a constant volume change within the volcanic shallow edifice. It highlights a constant flow rate at the dyke inlet over time. Within such a strain driven system we do not resolve any cascading seismicity. It is to say that most of the seismicity is directly driven by the magma flux. To invert the seismicity rates and energy release rates for the flux value, it remains to quantify how host rock properties on each volcanoes influence the seismic response of the volcano rock matrices to a volume perturbation.

2.6 Data and Resources

On Piton de la Fournaise, time series of earthquake occurrences are extracted from analogical signal recordings, [OVPF (Observatoire Volcanologique du Piton de la Fournaise)]; Izu Island 2000 seismic swarm is extracted from the JMA (Japan Meteorological Agency) catalogue; Etna data are from the EMULP-VOLUME database (*http://www.volume-project.net/*). Plots of this paper are made using Matlab R2006a.

Acknowledgements

We thank A. Helmstetter, V. Pinel, D. Amitrano, G. Daniel, V. Ferrazzini, D. Patané, J. Rosti, M. Alava and J. Koivisto for stimulating discussions, S. Toda for providing Miyakejima seismic data and M. Collombet for help during PdlF data reading. We are very grateful to an anonymous reviewer for his constructive and interesting comments. PT and JRG are supported by Volume EC-FP6 and TRIGS projects.

Chapter 3

A Constant Influx Model for Dyke Propagation. Implications for Magma Reservoir Dynamics

Paola Traversa[1], Virginie Pinel[2] and Jean-Robert Grasso[1]

[1] Laboratoire de Géophysique Interne et Tectonophysique,
CNRS - OSUG - Univeristé Joseph Fourier, BP 53 38041 Grenoble Cedex 9, France

[2] Laboratoire de Géophysique Interne et Tectonophysique,
CNRS - IRD - Université de Savoie, 73376 Le Bourget du Lac Cedex

Paper in press under the reference: *J. Geophys. Res.* (2010) *115*(B01201), doi:10.1029/2009JB006559

Abstract

Most observations of seismicity rate during dyke propagation on basaltic volcanoes show: (i) rate stationarity despite possible variations of the dyke tip velocity, (ii) frequent lack of clear and monotonic hypocenter migration following dyke propagation, (iii) event occurrences located backwards with respect to the dyke tip position. On these bases, the origin of the seismicity contemporary to dyke intrusion within basaltic volcanoes cannot be solely

related to the crack-tip propagation. Seismicity rather appears to be the response of the edifice itself to the volumetric deformation induced by the magma intruding the solid matrix. This in the unit time being the flux of magma entering the fracture, it argues for the stationary seismicity rate accompanying the intrusion to be a proxy for a constant magma supply rate from the magma reservoir. We consider a two-phase dyke propagation model, including a first vertical propagation followed by a lateral migration along a lithological discontinuity. We explore (i) under which geophysical conditions the vertical dyke is fed at constant flow rate of magma and (ii) dyke propagation patterns. Implications entailed by constant volumetric flux on the Piton de la Fournaise volcano case study suggest a minimum size for the magma reservoir of about 1 km^3, and a maximum value for the initial magma reservoir overpressure of about 2.2 MPa. Considering similar magma inflow rates during vertical and lateral dyke propagation phases, we reproduce independent estimates of propagation velocities, rising times and injected volumes when applying the model to the August 2003 Piton de la Fournaise eruption.

Résumé

La plupart des observations concernant le taux de sismicité pendant la propagation des dykes aux volcans basaltiques montrent : (i) un taux stationnaire malgré des possibles variations de la vitesse de propagation de la pointe du dyke, (ii) une manque fréquente de migration des hypocentres claire et monotone suivant la propagation du dyke, (iii) l'occurrence d'événement localisés à l'arrière de la pointe du dyke. Sur ces bases, l'origine de la sismicité contemporaine à une intrusion de dyke sur des volcans basaltiques ne peut pas être simplement liée à la propagation de la pointe de la fracture. La sismicité apparaît comme ma réponse de l'édifice même à la déformation volumétrique induite par le magma en intrusion dans la matrice rocheuse. Ceci par unité de temps étant le flux de magma qui rentre dans la fracture, cela suggère que le taux de sismicité stationnaire qui accompagne l'intrusion est proportionnel à un taux d'approvisionnement de magma constant du réservoir. Nous utilisons un modèle numérique de propagation de dyke en deux phases, incluant une première phase de propagation verticale, suivie d'une migration latérale le long d'une discontinuité lithologique. Nous explorons (i) dans quelles conditions géophysiques le dyke vertical est alimenté par un taux d'approvisionnement constant de magma et (ii) les motifs de propagation du dyke. Les implications d'un flux volumétrique constant pour un cas étude au volcan du Piton de la Fournaise suggèrent que le réservoir

magmatique a une taille minimale d'environ 1 km^3 et que la surpression du réservoir magmatique a une valeur maximale d'environ 2.2 MPa. A travers l'application de ce modèle au cas de l'éruption d'août 2003 au Piton de la Fournaise et en considèrant des taux d'approvisionnement similaires pendant les phases verticale et horizontale de propagation, nous reproduisons des estimations indépendantes de vitesses de propagation, temps de montée et volumes injectés.

3.1 Introduction

Magma-driven fracture is a commonly observed mechanism that allows to rapidly transport melt through cold and brittle country rock without extensive solidification [*Lister and Kerr*, 1991]. It therefore differs from porous flow through a deformable and partially molten matrix, which is characteristic of melt generation in the mantle [e.g. *McKenzie*, 1984] and from slow diapiric rise of granite through viscous country rock [*Pitcher*, 1979; *Rubin*, 1993b].

The difficulty of making direct observations of the plumbing system and of the dynamics of conduit formation within volcanoes makes only approximate the knowledge of the parameters and physical balances that govern the propagation of the fissure system.

Previous authors have proposed analytical models of fluid-driven fracture [e.g. *Lister*, 1990a,b; *Lister and Kerr*, 1991; *Roper and Lister*, 2005]. These studies suppose that dykes are fed from a reservoir of magma at depth; the crack is initiated within the chamber walls, where favorable conditions promote dyke propagation, leading to magmatic injections.

The competing pressures, whose balance drives the dyke propagation, are: (i) the elastic stresses generated by deformation of the host rock; (ii) the stresses required to extend the tip against the rock resistance; (iii) the buoyancy forces related to the difference between magma and country rock densities; (iv) the viscous pressure drop due to magma flow; (v) the magma driving overpressure; and (vi) the regional pre-existing stress field [e.g. *Lister*, 1990b; *Lister and Kerr*, 1991]. In this framework *Lister* [1990a] concludes that the fracture mechanics only characterise the crack tip zone, while the crack width and the rate of crack propagation are determined by the fluid dynamics. Static or quasi-static solutions for equilibrium crack are therefore inappropriate. It follows that the most important role in the pressure balances is played by (i), (iii), (iv) and (v). Note that (ii) is negligible "soon" away from the crack tip, and (vi) mainly acts on the dyke orientation [*Lister*, 1990b; *Lister and Kerr*, 1991].

In the literature, dyke propagation has been modeled according to two basic independent boundary conditions. On one hand some authors consider the fluid fracture as driven by a constant overpressure magma chamber at its base [*Rubin*, 1993a,b; *Meriaux and Jaupart*, 1998; *Roper and Lister*, 2005]. On the other hand *Lister* [1990a,b] assume a constant influx condition. The first hypothesis has been claimed geologically more appropriate than the second one [e.g. *Meriaux and Jaupart*, 1998]. The dyke growth model from a finite size magma chamber proposed by *Ida* [1999], however, leads the author to conclude that only in the case of extremely large and compressible magma reservoirs the melt pressure is actually able to remain constant as the dyke propagates.

From the observation point of view, we only have indirect access to dyke propagation, the only parameter we can estimate being the propagation velocity, i.e. few meters per second on basaltic volcanoes. These velocities can be deduced either from observations of the seismic signals associated with the advancing crack tip [*Aki et al.*, 1977; *Shaw*, 1980; *Battaglia et al.*, 2005b], or inferred from the size and composition of xenolithes carried by the flow [*Carmichael et al.*, 1977; *Spera*, 1980; *Pasteris*, 1984], or inferred from surface deformation measurements [e.g. *Toutain et al.*, 1992; *Battaglia and Aki*, 2003; *Peltier et al.*, 2005; *Aloisi et al.*, 2006; *Peltier et al.*, 2007]. As pointed by *Battaglia et al.* [2005b] and *Klein et al.* [1987], however, well-documented cases of earthquake hypocenters migrating simultaneously to the injected magma toward the surface are rare. A question mark remains on the fact that this lack of well-documented upward an monotonic earthquake migration contemporary to magma ascent prior to an eruption could simply be an artifact due to a poor station coverage on many of the world's active volcanoes [Battaglia et al., 2005]. Available observations suggest however that, while vertical hypocenter migrations are uncommon, horizontal migrations appear to be more frequent (e.g. the 1978 Krafla intrusion [*Einarsson and Brandsdottir*, 1980], the 2000 Izu Islands magma migration [e.g. *Toda et al.*, 2002]).

From scale-invariance explorations [*Grasso and Bachelery*, 1995] and theoretical considerations [*Rubin and Gillard*, 1998], the distribution of recorded dyke-induced earthquakes is suggested to map the distribution of rock mass sites that are near to failure, and does not necessarily reflect the extent of the dyke. To note that only in the case of an homogeneous medium the maximum deformation occurs at the dyke head, where we therefore expect most of the seismicity to occur [*Lister*, 1990a; *Pinel and Jaupart*, 2004]. Besides, earthquakes generated from the tensile propagation of the dyke tip are likely to be

too small in magnitude [*Rubin*, 1995; *Rubin et al.*, 1998] and too high in frequency [*Cornet*, 1992] to be detected by standard seismic network that operate at volcano surface. The shear-type of the generally recorded seismicity accompanying magma movement, moreover, is not compatible with the signal associated to a dynamic propagation of the dyke tip (i.e. a tensile fracture) [*Cornet*, 1992].

Observations of Volcano-Tectonic (VT) seismicity during dyke propagation on basaltic volcanoes show a constant seismicity rate over time [*Traversa and Grasso*, 2009-Chapter2]. This characteristic pattern for the seismic signature of dyke propagation demonstrates to be reproducible on different volcanoes: Piton de la Fournaise (PdlF): 7 dyke intrusions in the period 1988-1992; Etna: 2002 dyke intrusion; and Miyakejima (MI): 2000 dyke intrusion.

For the Piton de la Fournaise dyke intrusions, *Traversa and Grasso* [2009-Chapter2] report diffuse VT seismicity within the shallow edifice. On these bases, *Traversa and Grasso* [2009-Chapter2] argue for the seismicity generated during dyke injection to be a generic response of the volcanic edifice to the intrusion instead of an accurate mapping of the dyke tip propagation.

Toda et al. [2002] show that the change in seismicity rate generated by the 2000 dyke intrusion at Izu Islands (Japan) scales with the change in stressing rate induced by the propagation and opening of the dyke. This result demonstrates that the stressing rate governs the seismicity. It moreover supports the hypothesis of magma flow rate scaling with the seismicity rate [*Pedersen et al.*, 2007].

All these argue for the stationary seismicity rate accompanying the dyke propagation to be the response of the brittle lithosphere to a constant volumetric deformation rate (i.e. a constant influx of magma over time) induced by the intrusion [e.g. *Traversa and Grasso*, 2009-Chapter2].

Following *Traversa and Grasso* [2009-Chapter2] observations, the aim of this paper is therefore primarily (i) to analyze how a constant flow rate of magma injected into the dyke from the reservoir is consistent with the dynamics of a fluid-driven fracture propagating under realistic conditions for the magma chamber overpressure, and (ii) to evaluate the implications for the volcano dynamics. This is achieved by considering a two-phase dyke propagation model involving an initial vertical propagation phase followed by a horizontal migration phase.

Such two-phase propagation style for dyke propagating from a magma source at

shallow depth to the surface, is commonly observed on basaltic volcanoes worldwide, e.g. Mt. Etna (southern Italy) [e.g. *Aloisi et al.*, 2006]; Miyakejima (southern Japan) [e.g. *Nishimura et al.*, 2001]; and in particular on Piton de la Fournaise [e.g. *Toutain et al.*, 1992; *Bachélery*, 1999; *Peltier et al.*, 2005, 2007].

For the vertical rise of a buoyant fluid-filled crack from a shallow storage system towards the surface, we consider two boundary conditions at the dyke inlet, constant and variable reservoir overpressure. In the latter case the overpressure variation is controlled by the withdrawal of magma from the chamber induced by the dyke growth. Subsequently, the effect of a lithological discontinuity at depth is introduced by reducing the buoyancy of the fluid in the upper layer. This density step induces a slow down of the rising magma and favours melt accumulation and subsequent lateral dyke propagation.

We apply the two-phase dyke propagation model to the magmatic intrusion that fed the August 2003 Piton de la Fournaise (PdlF) eruption. The stationary rate of VT earthquakes accompanying the August 2003 PdlF dyke intrusion supports the result found by *Traversa and Grasso* [2009-Chapter2] in the 1992-1996 period. Accordingly we expect stationary flux of magma to feed the propagating dyke. Besides, the number of works devoted to its study make it one of the best studied intrusive episodes observed on PdlF volcano in the last years.

This application allows us to derive possible generic implications on the mechanisms driving magma movements on basaltic volcanoes. This so-called "proximal" eruption (according to *Peltier et al.* [2008] classification) is a good example to validate our model, first as being accompanied by a stationary seismicity rate over time, and second as being constituted of a vertical- and lateral-phase dyke propagation, which is the generally accepted feature describing flank eruptions at PdlF volcano [e.g. *Toutain et al.*, 1992; *Bachélery et al.*, 1998; *Bachélery*, 1999; *Peltier et al.*, 2005, 2007].

3.2 Models of dyke propagation

3.2.1 Vertical dyke propagation

In this section we focus on the vertical propagation of a buoyant fluid-filled crack, from a shallow storage system towards the surface (see figure 3.1). The crack is fed from a magma reservoir whose overpressure ΔP_c is either constant over time, or evolves as a

consequence of the withdrawal of magma from the reservoir. In particular, the aim of this section, is to individuate whether and under which conditions, a magma reservoir is able to feed a propagating dyke with constant flux of magma input from the reservoir.

Model description

For simplicity we consider a two-layer elastic half-space, characterized by Poisson ratio ν and shear modulus G and subject to a lithostatic stress field. The magma-filled fracture originates from the roof of a magma reservoir located at depth H, which is taken as the reference level. The z-axis is oriented positively upwards, with $z = 0$ at the reference level, where magma (of density ρ_m) has developed the overpressure ΔP_c with respect to the surroundings. A lithological discontinuity is located at depth H_b, such that the rock density as a function of depth is given by (see figure 3.1)

$$\begin{aligned} \rho_r(z) &= \rho_{rl} \text{ for } z < H - H_b \text{ (lower layer)}, \\ \rho_r(z) &= \rho_{ru} \text{ for } z > H - H_b \text{ (upper layer)}. \end{aligned} \tag{3.1}$$

As demonstrated by previous authors [e.g. *Lister*, 1990a,b; *Lister and Kerr*, 1991], once the dyke length is large enough, the influence of the toughness of rocks on dyke propagation can be neglected. The fluid-filled crack propagation is in fact dominated by fluid dynamics, except during the early nucleation of the crack, [*Lister*, 1990a]. On these bases, we neglect the strength of the surrounding rocks in the force balance, and hence do not treat stress singularity at the tip. We focus instead on the interplay between buoyancy, viscous head loss and elastic stresses. By considering also flow-induced stresses, the stress induced by the dyke opening is given by [*Pinel and Jaupart*, 2000]:

$$\sigma_o(z) = \Delta P_c + \sigma_b(z) + p_v, \tag{3.2}$$

where p_v is the viscous head loss and $\sigma_b(z)$ is the magma overpressure due to buoyancy. $\sigma_b(z)$ is given by:

$$\sigma_b(z) = \int_0^z (\rho_r(z') - \rho_m) g dz', \tag{3.3}$$

Following *Pinel and Jaupart* [2000] and *Maaløe* [1998], we fix the dyke breadth a and we assume that the dyke adopts an elliptical cross section with semi-axes a and b characterized by $b(z,t) \ll a$, see figure 3.1.

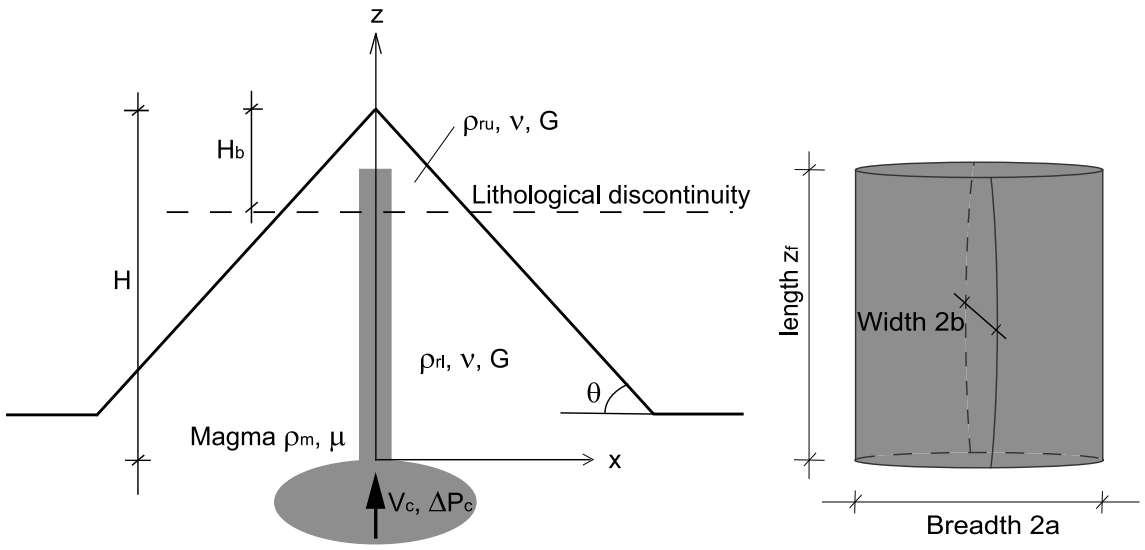

Figure 3.1: Sketch illustrating the geometry of a vertical dyke (left) and the shape of the fissure (rigth). $2\,b \ll 2\,a \leq z_f$. Half breadth a is assumed a priori.

In this case, the dyke-induced stress is given by [*Muskhelishvili*, 1963]

$$\sigma_o(z,t) \approx \frac{G}{1-\nu}\frac{b(z,t)}{a}, \tag{3.4}$$

Magma is considered as Newtonian, viscous and incompressible. Flow proceeds in a laminar regime. According to *Pinel and Jaupart* [2000], we obtain the following equation for the case of null lateral stress variation:

$$\frac{\partial b(z,t)}{\partial t} = -\frac{1}{4\mu}\frac{\partial}{\partial z}\left(\frac{\partial \sigma_b}{\partial z}b^3\right) + \frac{G}{16\mu a(1-\nu)}\frac{\partial^2 b^4}{\partial z^2} \tag{3.5}$$

where μ is magma viscosity.

We scale the pressures by the initial overpressure within the magma reservoir, $\Delta P_c(t = 0) = \Delta P_0$, and the front height z_f by the reservoir depth H. Scales for time, flux and fracture width for the vertical propagation are the following

$$[t] = \frac{16\mu H^2 G^2}{\Delta P_0^3 a^2 (1-\nu)^2}, \tag{3.6}$$

$$[Q] = \frac{(1-\nu)^3 \Delta P_0^4 a^4}{16 G^3 \mu H}, \tag{3.7}$$

$$[b] = \frac{\Delta P_0 a (1-\nu)}{G}. \tag{3.8}$$

These are the reference quantities in the computation, i.e. $[t]$ is the time-scale for opening the crack over a length H with a uniform overpressure ΔP_0. Length-scale $[b]$ is the fracture width originated by an overpressure ΔP_0. The scale for the dyke propagation velocity is then given by: $[v] = H/[t]$. The initiation of the fracture on the reservoir walls is imposed a priori with an elliptical profile. This affects the fracture growth only for a duration needed for an initial adjustment stage [*Ida*, 1999]. We can define three dimensionless numbers. The dimensionless number R_{1l} characterizes the magnitude of the buoyancy force scaled to the initial overpressure, as follows

$$R_{1l} = \frac{(\rho_m - \rho_{rl}) g\, H}{\Delta P_0} \tag{3.9}$$

Dimensionless numbers R_{1u} and R_2 characterize the lithological discontinuity, as follows:

$$R_{1u} = \frac{(\rho_m - \rho_{ru}) g\, H}{\Delta P_0} \tag{3.10}$$

$$R_2 = \frac{H_b}{H} \tag{3.11}$$

We have therefore the following dimensionless problem to solve

$$\frac{\partial b\,(z,t)}{\partial t} = -4\frac{\partial}{\partial z}\left(\frac{\partial \sigma_b}{\partial z} b^3\right) + \frac{\partial^2 b^4}{\partial z^2}, \tag{3.12}$$

$$b_{(z=0,\,t)} = \Delta P_c(t); \tag{3.13}$$

When there is no lithological discontinuity, $R_{1l} = R_{1u} = R_1$, and equation 3.12 reduces to:

$$\frac{\partial b\,(z,t)}{\partial t} = 4R_1\frac{\partial b^3}{\partial z} + \frac{\partial^2 b^4}{\partial z^2}, \tag{3.14}$$

This is solved numerically using a semi-implicit finite difference scheme with Dirichlet boundary conditions.

In this framework, equation 3.12 allows to follow the dynamics of dyke propagation on its way towards the surface. We checked that mass conservation was satisfied on the scale of the whole dyke, which requires the instantaneous volume change to be equal to the basal flux, both values being issued from the numerical computation. The dimensions of the fracture at its base (i.e. the imposed a value and the calculated $b(0,t)$, which depends on the overpressure at the dyke inlet) determine the volume of magma intruding into the fissure per time unit. The velocity of the dyke propagating towards the surface is given by dz_f/dt, where z_f is the fracture front height (see figure 3.1).

When magma is injected from the reservoir into the dyke, it induces a decrease of the magma reservoir volume ΔV_c, which might in turn induce a decrease of the reservoir overpressure ΔP_c as well. Considering the elastic deformation induced by a point source (i.e. the magma reservoir) embedded in an infinite medium, the evolution of the reservoir overpressure follows the equation [V. Pinel and C. Jaupart, 2009, personal communication]:

$$d\,\Delta P_c(t) = \frac{dV_c(t)}{V_c(t)} \frac{4KG}{4G + 3K} \tag{3.15}$$

where K is the magma bulk modulus. The volume variation in the magma reservoir can be related to the volume of magma injected into the dyke by

$$dV_c(t) = -Q(t)dt, \tag{3.16}$$

with Q the flux of magma entering the dyke. When magma is fully compressible, $K = 0$ and the magma reservoir overpressure remains constant trough time. For incompressible magma, $K \to \infty$ and equation 3.15 becomes

$$d\Delta P_c(t) = \frac{dV_c(t)}{V_c(t)} \frac{4G}{3} \tag{3.17}$$

To fully describe the evolution of the reservoir pressure, we introduce two new dimensionless numbers:

$$R_3 = \frac{\Delta P_0\, a^2\, (1 - \nu)\, H}{G\, V_c}, \tag{3.18}$$

which is the inverse dimensionless reservoir volume, and

$$R_4 = \frac{4KG}{\Delta P_0\, (4G + 3K)}. \tag{3.19}$$

which relates the overpressure variation in the reservoir to the initial overpressure value.

Results

We study the propagation of a vertical dyke from a shallow reservoir, according to the geometry illustrated in figure 3.1. We investigate under which conditions the magma flux injected into the dyke remains constant during dyke growth. Using the dimensionless numbers above described, we discuss the role played by each parameter in determining the regime of magma flux carried by the rising dyke. We solve the problem for three different configurations, described here below.

(i) Dyke rising from a constant overpressure magma reservoir in a homogeneous medium,
(ii) Dyke rising from a variable overpressure magma reservoir in a homogeneous medium,
(iii) Dyke rising from a variable overpressure magma reservoir in a layered medium.

First we consider the case of a dyke rising from a constant overpressure magma reservoir ($\Delta P_c = \Delta P_0 = \text{const.}$) in a homogeneous medium (i.e. $\rho_{rl} = \rho_{ru}$, $R_{1l} = R_{1u} = R_1$). As shown in figure 3.2, after some numeric adjustment iterations (whose number decreases with R_1 value), the flux of magma in the growing dyke evolves similarly to the propagation velocity (figure 3.2, A and B). This is related to the fact that, in this case, the dyke growth depends on tip propagation. Since fracture half-breadth a is assumed constant a priori and the medium is homogeneous, the dyke only grows along the propagation direction (figure 3.2, C). In this first case, the only dimensionless number affecting the regime of magma flux over time is R_1. We consider as negligible a flux variation less than 5% between dimensionless dyke heights $z_f = 0.3$ and $z_f = 0.9$. The choice of the first limit is imposed by discarding initial numerical adjustment iterations. As shown in figure 3.3 (black open squares), the magma flux withdrawn from the reservoir remains constant during dyke rising for $R_1 \leq -3.55$. In this constant overpressure case, and for a given reservoir depth, the only parameter determining the regime of the magma flux carried by the growing dyke is the ratio between the buoyancy force and the magma overpressure at the dyke inlet.

Second we consider the same case as above, but with the reservoir overpressure varying as magma is withdrawn. Through the dimensionless numbers R_3 and R_4, we explore the role of the magma chamber volume V_c and of the magma bulk modulus K, which relates changes in reservoir volume with changes in pressure, on the regime of magma flux withdrawn from the reservoir. As illustrated in figure 3.3 (plain symbols), the smaller the dimensionless number R_3, the more the flux tends to remain constant during dyke propagation and viceversa. It means that the larger the chamber volume with respect to the dyke scale volume, the more negligible a withdrawal of magma is in terms of variations in magma flow rate and reservoir overpressure during dyke rising. In the same way, the smaller the dimensionless number R_4, the smaller the magma flux variation obtained during dyke rising and viceversa. This implies that the more the magma tends to be incompressible, i.e. $K \to \infty$, the more the flow of magma injected into the dyke varies over time as the dyke propagates. As shown in figure 3.3 legend, this scenario corresponds to larger variations in the reservoir overpressure ($\Delta P_c\, variation$) face to the withdrawal of magma from the

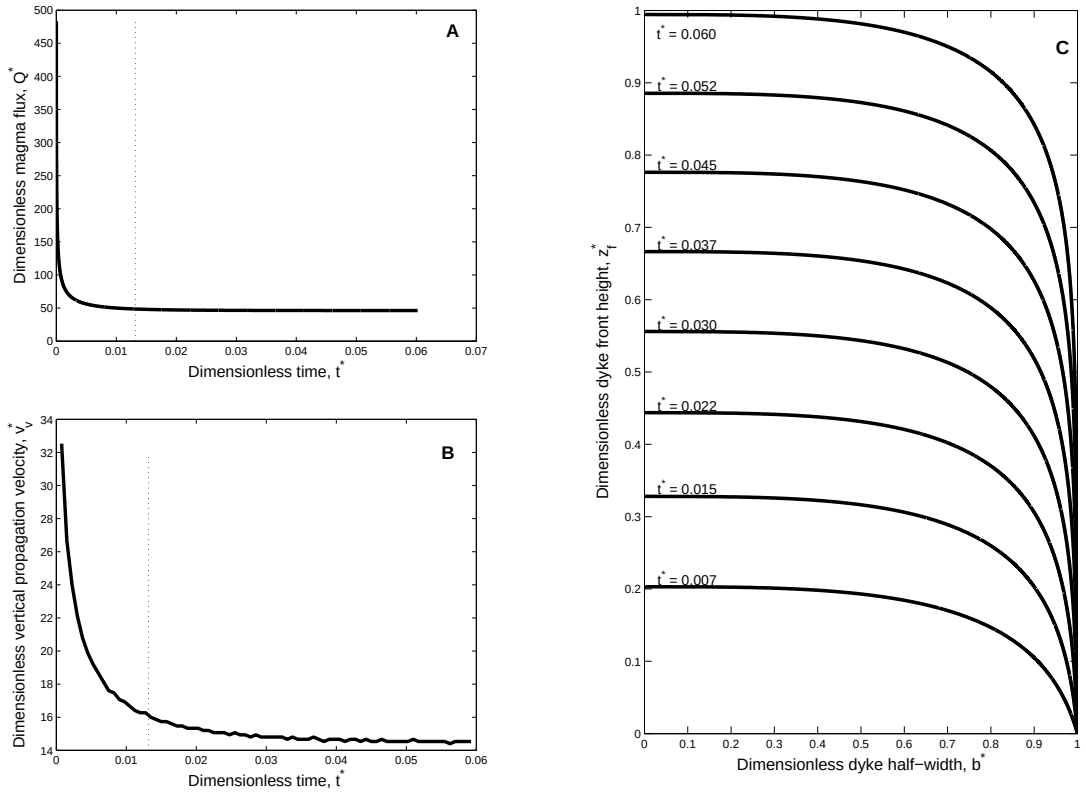

Figure 3.2: Magma-filled dyke rising in a homogeneous medium from a constant overpressure magma chamber at depth. A: dimensionless magma flux injected into the dyke over time; B: dimensionless propagation velocity versus time; C: Evolution of the crack shape for progressive growth stages. R_1 ($R_1 = (\rho_m - \rho_r)gH/\Delta P_0$) value used in the calculation is -3.55. Stipple-lines in plots A and B indicate $z_f^* = 0.3$. Reminder: $t = t^*[t]$, $Q = Q^*[Q]$, $v_v = v_v^*[v]$, $b = b^*[b]$, $z_f = z_f^*[H]$, where scales for time $[t]$, flux $[Q]$ and fracture width $[b]$ are given in equations (3.6) to (3.8), lengths are scaled by the reservoir depth H, and scale for propagation velocity is $[v] = [H]/[t]$.

reservoir. Conversely, more compressible magmas, i.e. $K \to 0$, allow for smaller variations in the magma flow rate over time, which correspond to smaller overpressure variations accompanying magma withdrawn from the reservoir. However, only small overpressure variations ($\Delta P_c\, variation$ less than $\sim 2\%$) in the magma reservoir allow for the magma flow rate to remain constant during dyke propagation.

As a third case we consider a lithological discontinuity within the volcanic edifice. This discontinuity is intended in terms of rock densities, which are chosen such that magma has intermediate density between the lower and upper rock layers ($\rho_{rl} > \rho_m > \rho_{ru}$). This allows for considering a twofold effect: on one hand the higher fracturing of the solid medium close to the surface, which implies a lower density of the shallow layer and, on the other hand, the fact that magma degasses while rising, becoming more and more dense as approaching the surface. The effect of this density step is to slow down the rise of magma, creating favorable conditions for magma accumulation at the discontinuity depth H_b.

Figure 3.4 illustrates the variation of the dimensionless magma flux, propagation velocity, and dyke shape during dyke propagation from an over-pressured magma chamber, in a two-layer medium. After an initial numeric adjustment transient, the magma flux remains constant over time, being blind to the lithological discontinuity (figure 3.4A). The dyke volume continues therefore to regularly grow as dyke rises. On the other hand, the dyke propagation velocity, computed as dz_f/dt, significantly decreases when the dyke reaches the depth of the density step (figure 3.4B), as also shown by *Taisne and Jaupart* [2009].

Reminding that the seismic response of a volcanic edifice to dyke propagation is reported to be stationary over time [*Traversa and Grasso*, 2009-Chapter2], this result supports the hypothesis of scaling between seismicity rate accompanying the dyke intrusion and the volumetric flux of magma entering the dyke. On the other hand, it excludes the possibility of a direct scaling between the seismicity rate and the dyke propagation velocity. The density step does not affect the shape of the fracture at the dyke inlet (figure 3.4C). In our model, for a given magma viscosity, the magma flux supply only depends on the shape of the crack at the junction with the reservoir roof. It can therefore remain constant over time as dyke grows.

While dyke half-breadth a is assumed to be constant over time, the dimensionless numbers R_{1rl}, R_{1ru} and R_2 play a role in determining the width of the dyke at the inlet, and therefore the regime of magma flux carried by the propagating dyke. The parameter

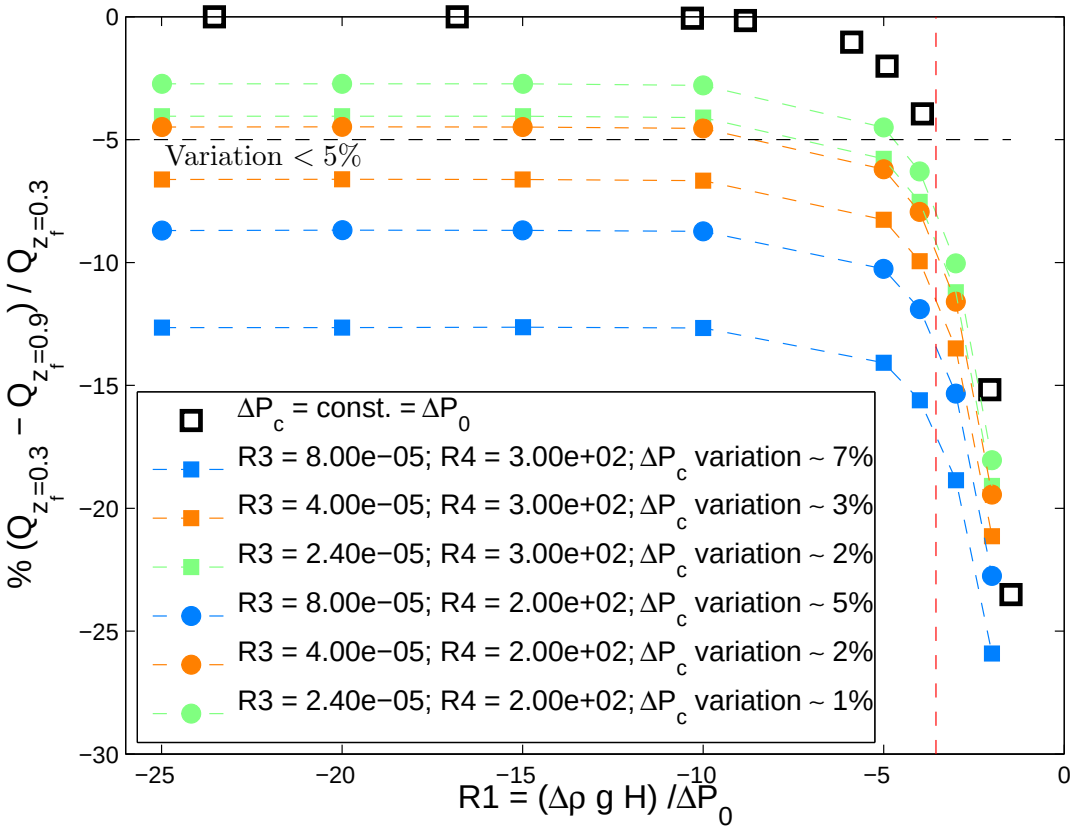

Figure 3.3: Percentage of magma influx variation during dyke growth within a homogeneous medium as function of the dimensionless number R_1 ($R_1 = (\rho_m - \rho_r)gH/\Delta P_0$). Black squares: constant overpressure at the dyke inlet; colored symbols: variable overpressure in the chamber. Color of solid symbols is related to the V_c value; circles or square symbols depend on the K value. Reservoir overpressure variations $\Delta P_c\, variation$ indicated in the legend are issued from the computation.

R_{1rl} has been discussed above, while figure 3.5 shows the effect of R_{1ru} and R_2 dimensionless numbers on the regime of magma flow over time. In analogy with the previous discussion, we consider as negligible a variation in the magma flux less than 5% between dimensionless front heights $z_f = 0.3$ and 0.9. Variation in magma flux during dyke rise are eligible for $R_{1Ru} < 1.5$ and for $R_2 < 0.5$. These imply that, in order for the flux of magma to remain constant over time, the densities of the magma and the upper layer should be quite close in value, and that the discontinuity should not be deeper than half the reservoir depth.

As shown in figure 3.13C, when magma buoyancy faints, due to a decrease in the surrounding rock density, an inflation starts to grow at the dyke head. Here elastic stresses may exceed the rock toughness and new fractures may initiate.

3.2.2 Lateral propagation at the Level of Neutral Buoyancy

Exhaustive description of the solution for dyke propagation at a lithological boundary fed by either, constant flux or constant volume of magma is given by *Lister* [1990b] and *Lister and Kerr* [1991]. They assume that buoyancy forces do not depend on horizontal distance. The effects of lateral variations of the stress field induced by a volcanic edifice load on the lateral propagation are studied by *Pinel and Jaupart* [2004]. In this paper we consider an horizontal lithological boundary located within the volcanic edifice. We therefore adapt the solutions given by *Pinel and Jaupart* [2004] in order to take into account the variation of the external lithostatic pressure induced by the volcano slope along the propagation direction.

Model description

Figure 3.6 illustrates the geometry and main parameters used in this section. ρ_{ru} and ρ_{rl} are, respectively, the rock densities in the upper and lower layer. For this case, we define the origin of the vertical coordinate z at the discontinuity level, oriented positive upwards. The vertical extension of the dyke is called $2a(x)$. $z_u(x)$ and $z_l(x)$ stands for the positions of the upper and lower dyke tips respectively, such that we have:

$$2a(x) = z_u(x) - z_l(x) \tag{3.20}$$

We also define

$$m = \frac{z_u + z_l}{z_u - z_l} \tag{3.21}$$

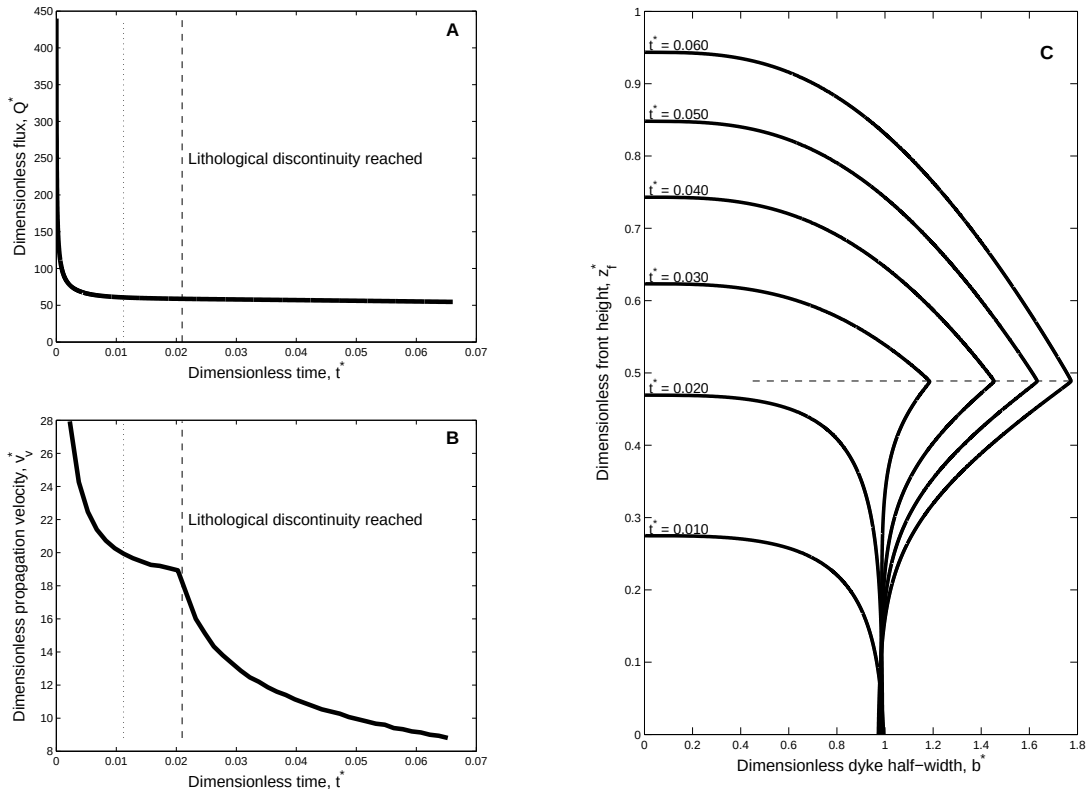

Figure 3.4: Magma-filled dyke rising in a homogeneous medium from a constant overpressure magma chamber at depth. A: dimensionless magma flux injected into the dyke over time; B: dimensionless propagation velocity versus time; C: Evolution of the crack shape for progressive growth stages. Parameter values used in the computation are: $R_{1l} = -4.82$, $R_{1u} = 1.37$, $R_2 = 0.51$, $R_3 = 6.9\text{x}10^{-9}$, $R_4 = 1.125$. Stipple-lines in plots A and B indicate $z_f^* = 0.3$. Reminder: $t = t^*[t]$, $Q = Q^*[Q]$, $v_v = v_v^*[v]$, $b = b^*[b]$, $z_f = z_f^*[H]$, where scales for time $[t]$, flux $[Q]$ and fracture width $[b]$ are given in equations (3.6) to (3.8), lengths are scaled by the reservoir depth H, and scale for propagation velocity is $[v] = [H]/[t]$; $R_{1u} = (\rho_m - \rho_{ru})gH/\Delta P_0$, $R_{1l} = (\rho_m - \rho_{rl})gH/\Delta P_0$, $R_2 = H_b/H$, $R_3 = (\Delta P_0\, a^2\,(1-\nu)\,H)\ (G\,V_c)$, $R_4 = 4KG/(\Delta P_0\,(4G+3K))$.

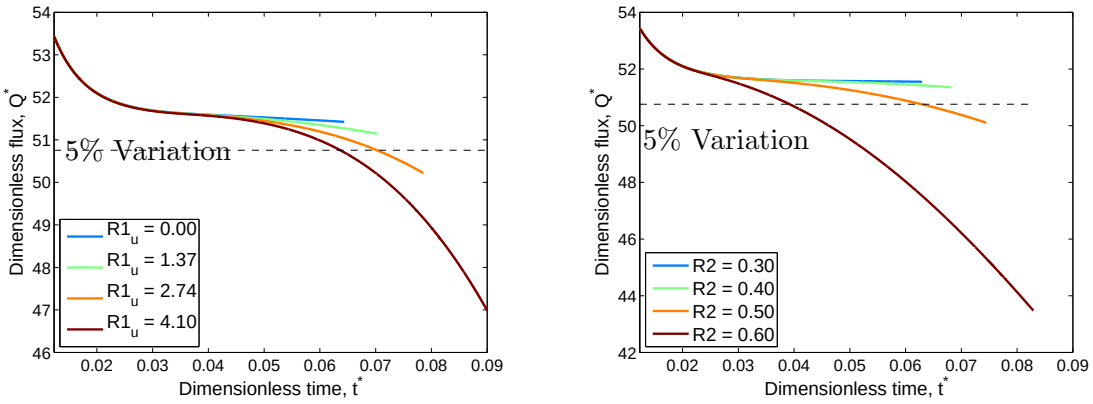

Figure 3.5: Left: effect of the dimensionless number R_{1ru} on the magma flux evolution over time during dyke propagation, $R_2 = 0.43$. Right: effect of the dimensionless number R_2 on the magma flux evolution over time during dyke propagation, $R_{1ru} = 1.37$. For both cases $R_{1rl} = -4.1$, $V_c = 5\,\mathrm{km}^3$ and $K = 1\mathrm{x}10^9$ Pa. Final time corresponds to surface attainment. Reminder: $R_{1u} = (\rho_m - \rho_{ru})gH/\Delta P_0$, $R_{1l} = (\rho_m - \rho_{rl})gH/\Delta P_0$, $R_2 = H_b/H$, $R_3 = (\Delta P_0\, a^2\,(1-\nu)\,H)\ (G\,V_c)$, $R_4 = 4KG/(\Delta P_0\,(4G+3K))$.

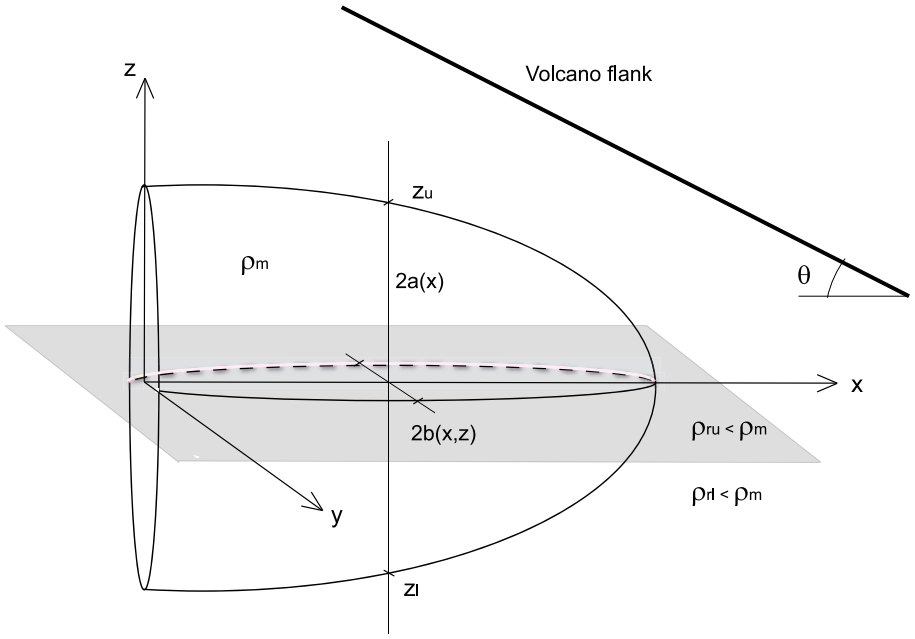

Figure 3.6: Sketch illustrating the geometry and the main parameters of a dyke horizontally propagating at the Level of Neutral Buoyancy

We neglect the effects of the free surface [*Pinel and Jaupart*, 2004], so that the stress generated by the pressure difference between the interior and the exterior of the dyke, σ_o, is given by

$$\sigma_o(x,z) = (\rho_{ru} - \rho_m) g\, z - \sigma_l(x) + p, \quad \text{if } z > 0 \tag{3.22}$$

$$\sigma_o(x,z) = (\rho_{rl} - \rho_m) g\, z - \sigma_l(x) + p, \quad \text{if } z < 0, \tag{3.23}$$

where p is the internal magma pressure, which varies due to viscous friction, and σ_l is the lithostatic pressure at the lithological boundary, defined by:

$$\sigma_o(x) = \rho_{ru} g (H_b - \theta x), \tag{3.24}$$

with θ the volcano slope.

We consider that the lateral dyke length is larger than its height and we neglect vertical pressure gradients due to upward flow within the dyke [*Lister and Kerr*, 1991; *Pinel and Jaupart*, 2004]. In this case, the internal magma pressure p depends only on the lateral position x. As before, the condition for the crack to remain open is $\sigma_o > 0$.

We consider that the dyke propagates in damaged rocks, and therefore we set to zero the stress intensity factor at both dyke tips [*Mériaux et al.*, 1999]. Following *Pinel and*

Jaupart [2004], this leads to

$$\arcsin m + m\sqrt{1-m^2} = \frac{\pi}{2}\frac{\rho_{rl}+\rho_{ru}-2\rho_m}{\rho_{rl}-\rho_{ru}} \tag{3.25}$$

$$\sigma_o(x, z=0) = \frac{g}{\pi}(\rho_{rl}-\rho_{ru})a(x)(1-m^2)^{3/2} \tag{3.26}$$

It means that for given values of densities ρ_{ru}, ρ_{rl} and ρ_m, once the overpressure at the lithological discontinuity is known at a given lateral distance x, there is a unique solution for the half-height $a(x)$ and the tip locations $z_u(x)$ and $z_l(x)$. This solution can be subsequently used to calculate the dyke width $b(x,z)$ using the solution derived from *Pinel and Jaupart* [2004]. For $-1 < s < 1$, the half-width $b(s)$ is given by:

$$\begin{aligned} b(s,x) = \; & \tfrac{(1-\nu)\sigma_o(x,z=0)}{G}\sqrt{1-s^2} \\ + \; & \tfrac{a(x)(1-\nu)g(\rho_{rl}-\rho_{ru})}{G\pi} \quad [\sqrt{1-s^2}(-\frac{1}{2}\sqrt{1-m^2} - \frac{1}{2}s\arcsin m - m\arcsin m) \\ & -\frac{1}{2}(s+m)^2\ln|\frac{1+sm+\sqrt{(1-s^2)(1-m^2)}}{s+m}| \\ & +\frac{\rho_{ru}+\rho_{rl}-2\rho_m}{\rho_{rl}-\rho_{ru}}\sqrt{1-s^2}(\frac{1}{4}s\pi + \frac{1}{2}m\pi)] \end{aligned} \tag{3.27}$$

where s is defined by:

$$s = \frac{z}{a(x)} - m. \tag{3.28}$$

From equation 3.25, we can see that dyke extension in the upper medium is equal the extension in the lower medium ($m = 0$) just in case $\rho_{rl} - \rho_m = \rho_m - \rho_{ru}$. As there is no lateral variations of the stress field vertical gradient, m is a constant.

The dyke internal pressure σ_o, which keeps the dyke open, varies laterally because of both, the volcano flank slope and the viscous head losses due to horizontal magma flow. Magma is considered as Newtonian, viscous and incompressible. Flow proceeds in laminar regime.

Following *Pinel and Jaupart* [2004] analytical procedure, the dyke half-height $a(x,t)$, is the solution of the following equation

$$\begin{gathered} c_1\, g(\rho_{ru}-\rho_m)\tfrac{\partial a(x,t)^3}{\partial t} = \\ \tfrac{c_3(1-\nu)^2}{3\mu\, G^2}\tfrac{\partial}{\partial x}\Big[a(x,t)^7 g^3(\rho_{ru}-\rho_m)^3\Big(\tfrac{g(\rho_{rl}-\rho_{ru})}{\pi}(1-m)^{3/2}\tfrac{\partial a(x,t)}{\partial x} - \rho_{ru}g\theta\Big)\Big]. \end{gathered} \tag{3.29}$$

where

$$c_n = \int_{-1}^{1} f(s)^n ds, \tag{3.30}$$

$$f(s) = \frac{Gb(s)}{g(1-\nu)(\rho_{ru}-\rho_m)a(x)}. \tag{3.31}$$

We scale the pressures by the lithostatic load of the rock mass above the density step,

$$[P] = \rho_{ru}\, g\, H_b. \tag{3.32}$$

the flux by the input flux of magma Q_{in} and all length dimensions by the depth of the lithostatic discontinuity H_b. The scale for the time refers to the opening of a fissure over a length H_b with a magma flux equal to Q_{in}, and is given by the following equation:

$$[t] = \Big(\frac{\mu\ (1-\nu)\, H_b^9}{G\, Q_{in}^3}\Big)^{1/4}, \tag{3.33}$$

As shown by *Pinel and Jaupart* [2004], two dimensionless numbers can be defined:

$$N_1 = \frac{3Q_{in}^{3/4}\mu^{3/4}G^{9/4}}{H_b^{9/4}(1-\nu)^{9/4}[P]^3} \tag{3.34}$$

$$N_2 = -\frac{2H_b^3(1-\nu)^3[P]^4}{3\mu Q_{in}G^3} \tag{3.35}$$

Equation 3.29 can be rewritten in the dimensionless form:

$$\frac{c_1}{c_3}N_1\frac{\rho_{ru}-\rho_m}{\rho_{ru}}\frac{\partial a^3}{\partial t} = -\theta\frac{(\rho_{ru}-\rho_m)^3}{\rho_{ru}^3}\frac{\partial a^7}{\partial x} + \frac{(1-m)^{3/2}(\rho_{ru}-\rho_m)^3(\rho_{rl}-\rho_{ru})}{8\pi\rho_{ru}^4}\frac{\partial^2 a^8}{\partial x^2} \tag{3.36}$$

The dimensionless flux is given by:

$$\frac{q}{Q_{in}} = N_2 c_3 a(x,t)^7 \frac{(1-m)^{3/2}(\rho_{ru}-\rho_m)^3(\rho_{rl}-\rho_{ru})}{8\pi\rho_{ru}^4}[\frac{\partial a(x,t)}{\partial x} - \theta] \tag{3.37}$$

We solve numerically this equation with a semi-implicit finite difference scheme with a Neumann boundary conditions at the source ($x = 0$).

Results

In this section we discuss the effect of the model parameters on the propagation of a dyke at a lithological boundary, fed by a constant flux of magma. As discussed in the previous section, the dyke propagation is affected by the variation in the external lithostatic

pressure induced by the volcanic slope along the propagation direction, while vertical stress gradients do not vary laterally.

Lister [1990b], discusses the case of a dyke fed by constant flux or constant volume of magma, laterally propagating in a medium with no lateral stress variations. In this case the breadth of the dyke ($2a(x)$ in figure 3.6) varies in time all along its length, being however always largest at the origin ($2a(x = 0)$). *Pinel and Jaupart* [2004] consider the effect of the volcanic edifice load on the propagation of a lateral dyke at depth. In this case, the breadth of the dyke varies at the head during lateral propagation, due to lateral variations of vertical stress gradients. For the present case, the lateral stress variations are only due to the flank slope of the edifice. Figure 3.7 shows that, with small flank slopes ($\theta \to 0$), the breadth of the dyke grows at the origin as the dyke propagates, reminding the case discussed by *Lister* [1990b]. With higher flank slopes, the half-breadth a tends to a constant value as the dyke laterally propagates. Such constant value does not depend on the propagation distance from the origin. In this sense, the effect of the volcano flank slope θ is such that it carries back to the previously discussed vertical propagation case, where the breadth $2a$ of the dyke was assumed to be constant during propagation.

3.3 Case study: The August 22 2003, Piton de la Fournaise eruption

3.3.1 Overview on PdlF storage and eruptive system

The Piton de la Fournaise (PdlF), Reunion Island, Indian Ocean, is a well-studied basaltic intraplate strato-volcano, with a supply of magma from hotspots in the mantle [see e.g. *Lénat and Bachèlery*, 1990; *Aki and Ferrazzini*, 2000; *Battaglia et al.*, 2005b; *Peltier et al.*, 2005, among others]. There are five conceptual models describing the shallow storage system at PdlF volcano. First, *Lénat and Bachèlery* [1990] propose a model of summit reservoir composed by many small independent shallow magma pockets, located above sea level at a depth of about 0.5-1.5 km beneath Dolomieu crater. This model is supported by the cellular automaton model of *Lahaie and Grasso* [1998] during the 1920-1992 period, which considers basaltic volcanoes as complex network of interacting entities at a critical state. A 1-10 x 10^6 m^3 volume has been estimated for such magma batches through spatial extent of seismicity [*Sapin et al.*, 1996]. This range spans the volumes of lava emitted by

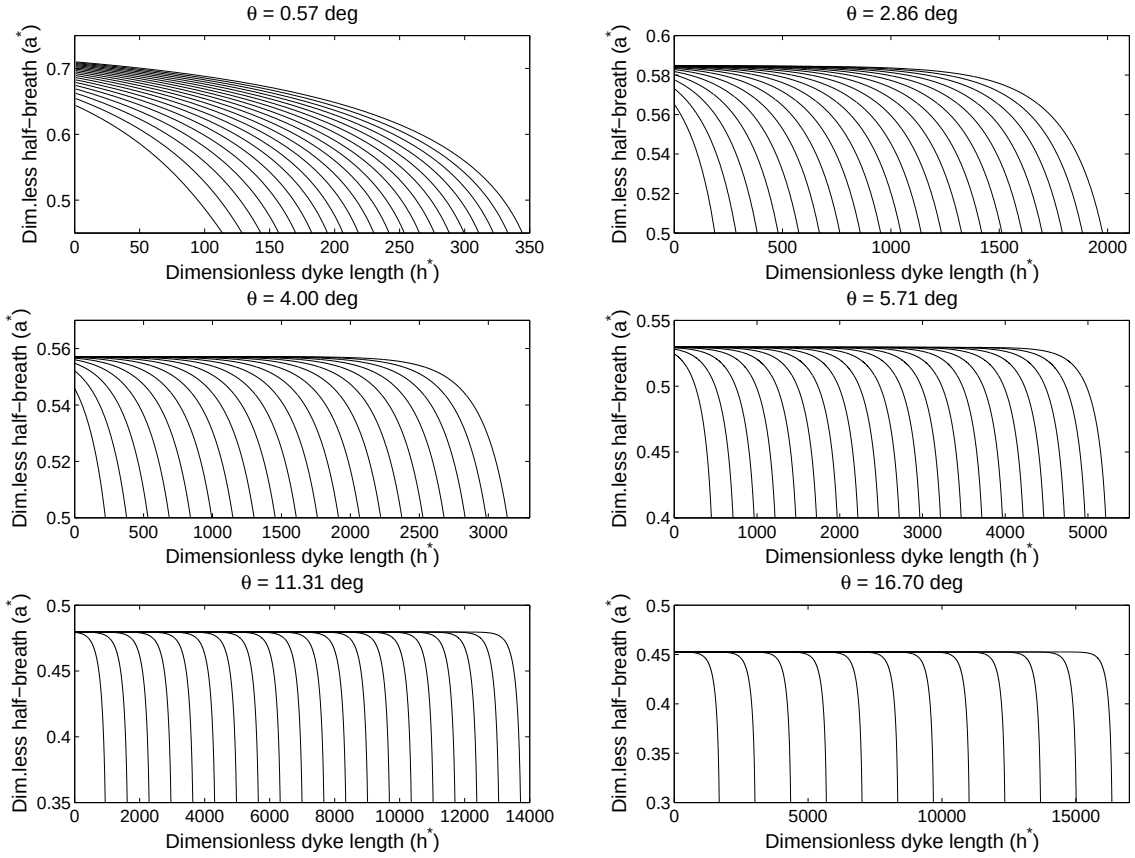

Figure 3.7: Lateral dyke propagation: effect of the edifice flank slope on the fracture shape evolution over time. Parameters used in the calculations are: $\rho_{rl} = 2700\,\mathrm{kg\,m^{-3}}$, $\rho_{ru} = 2300\,\mathrm{kg\,m^{-3}}$, $\rho_m = 2400\,\mathrm{kg\,m^{-3}}$. Dimensionless time step between following curves is 10^{-6}. Dimensionless numbers values are: $N_1 = 1.65\,\mathrm{x}\,10^{-4}$ and $N_2 = -1.48\,\mathrm{x}\,10^{8}$. Reminder: $N_1 = (3Q_{in}^{3/4}\mu^{3/4}G^{9/4})/(H_b^{9/4}(1-\nu)^{9/4}[P]^3)$, $N_2 = -(2H_b^3(1-\nu)^3[P]^4)/(3\mu Q_{in}G^3)$.

the eruptions occurred at PdlF in the period 1972-1992 [*Sapin et al.*, 1996; *Peltier et al.*, 2009], while about 32% of eruptions occurred since 1998 emitted lava volumes larger than 10 x 10^6 m^3 [*Peltier et al.*, 2009].

Second *Sapin et al.* [1996], on crystallization arguments point out, however, that in order to produce eruptions with lava volumes of order 1-10 x 10^6 m^3, the volume of magma in the chamber needs to be larger than the emitted volume. They therefore suggest, as a better candidate for the Piton de la Fournaise magma reservoir, the low seismic-velocity zone identified by *Nercessian et al.* [1996] at about sea level. This aseismic zone is located just below the depth at which pre-eruptive seismic swarms are generally located, and extends at depths of 1.5-2 km below sea level. It implies a second magma chamber model volume of 1.7-4.1 km^3.

Third, *Albarède* [1993], by applying Fourier analysis of the Ce/Yb fluctuations in the Piton de la Fournaise lavas over the 1931-1986 period, estimates a magma residence time in the reservoir between 10 and 30 years. This result, combined with magma production rates, lead the author to conclude that the maximum size of the PdlF magma chamber may hardly exceed 1 km^3.

Fourth *Sigmarsson et al.* [2005] uses ^{238}U-series desequilibria of basalts erupted at PdlF during the period 1960-1998 to estimate magma residence time and to infer a volume of 0.35 km^3 for the Piton de la Fournaise shallow magma reservoir.

Five, *Peltier et al.* [2007, 2008], on tilt, extensometer and GPS data basis, describe the PdlF eruptions since 2003, as fed from a common magma chamber located at a depth of 2250-2350 m beneath the summit and with a radius of $\sim$ 500 m. This corresponds to a reservoir volume of about 0.5 km^3. The eventuality of deeper storage systems has been discussed by *Aki and Ferrazzini* [2000], *Battaglia et al.* [2005b], *Prôno et al.* [2009] and *Peltier et al.* [2009]. Hence, the presence, location and size of reservoirs below Piton de la Fournaise still remain an open question.

As discussed in previous studies [e.g. *Toutain et al.*, 1992; *Bachélery et al.*, 1998; *Peltier et al.*, 2005], flank eruptions at Piton de la Fournaise generally consist of two phases: an initial vertical rise of magma followed by a near-surface lateral migration towards the eruption site.

For the 2000-2003 period, *Peltier et al.* [2005] observe a correlation between the duration of the lateral propagation stage and the distance of the eruptive vents from the summit. Since the seismic crisis onset coincides with the beginning of the first propagation

phase [e.g. *Peltier et al.*, 2005, 2007; *Aki and Ferrazzini*, 2000], *Peltier et al.* [2005] calculate a mean vertical speed of about 2 m s^{-1}, while lateral migration velocities range between 0.2 and 0.8 m s^{-1}. This results are similar to those reported by *Toutain et al.* [1992] for the April 1990 PdlF eruption (i.e. 2.3 m s^{-1} for the vertical propagation and 0.21 m s^{-1} for the lateral migration) and *Bachélery et al.* [1998] for the eruptions taking place during the first sixteen years of the PdlF Observatory (1980-1996).

In this paper we focus on the August 2003 dyke intrusion, which has been extensively studied through extensometer, tiltmeter, GPS and INSAR data by *Peltier et al.* [2005, 2007], *Froger et al.* [2004] and *Tinard* [2007]. The dyke intrusion is accompanied by a seismic crisis of around 400 volcano-Tectonic (VT) events within 152 min (figure 3.8).

Seismic data illustrated in figure 3.8 confirm for the August 2003 case the seismic rate stationarity observed by *Traversa and Grasso* [2009-Chapter2] for the PdlF intrusions in the 1988-1992 period.

3.3.2 Relationships between magma flux regime and initial conditions for magma reservoir

Following the results obtained in section 3.2.1 for the vertical propagation stage, and referring to the parameters listed in table 3.1, we can calculate an upper bound for the reservoir initial overpressure and a lower bound for the magma reservoir volume values, such that the reservoir is able to sustain a constant influx magmatic intrusion.

The upper bound for the reservoir overpressure able to sustain a constant magma flux injection, can be computed by referring to the vertical propagation stage within a homogeneous medium (i.e. we neglect the effect of the upper layer, dimensionless number $R_2 = 0$). We choose a large magma reservoir volume with fully compressible magma (i.e. $R_3 \to 0$, $R_4 \to 0$). The upper limit for the initial reservoir overpressure is given by the dimensionless number R_1 corresponding to less than 5% variation in the magma flux during dyke growth (see figure 3.3, black empty squares). This is: $R_1 < -3.55$.

For parameters listed in table 3.1, this implies an initial reservoir overpressure $\Delta P_0 <$ 2.2 MPa. Such upper limit is compatible with the average overpressure a the dyke inlet estimated for the August 2003 PdlF dyke intrusion, i.e. 1.7 MPa using InSAR data [*Tinard*, 2007] and at 1.1 MPa using GPS and tiltmeter data [*Peltier et al.*, 2007]. Dyke inlet overpressure values computed using GPS data for PdlF eruptions between 2004 and 2006

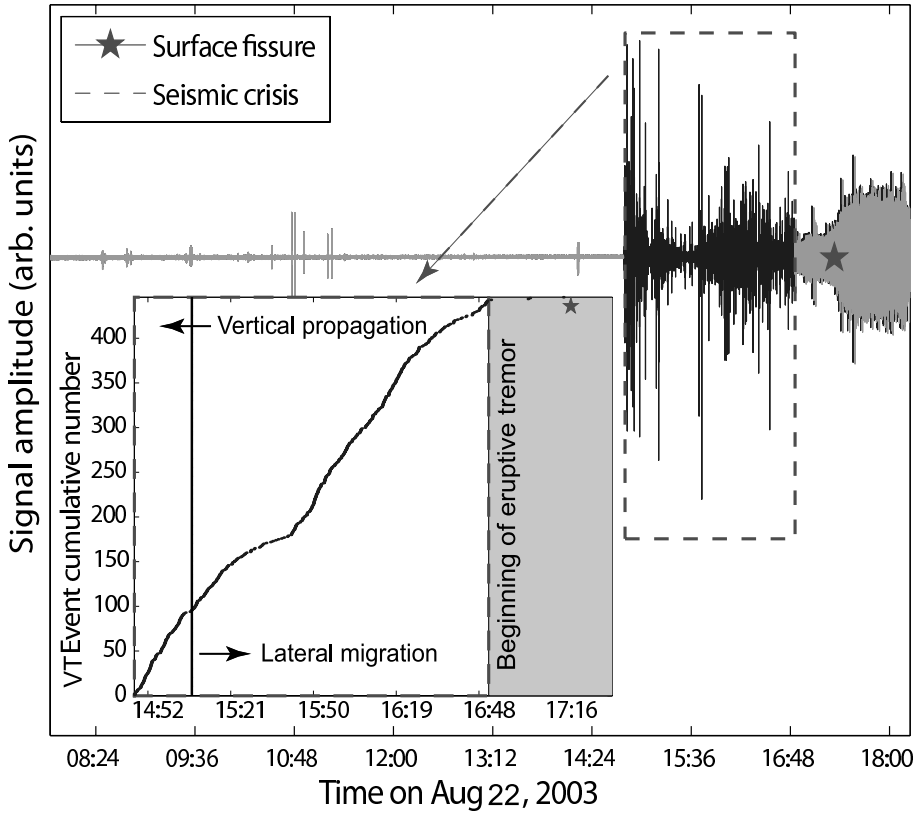

Figure 3.8: Seismic signal and cumulated seismicity (inset) hand-picked from continuous recordings recorded at the BOR summit station during the August 22 2003 dyke intrusion at Piton de la Fournaise volcano. Times related to the different stages of activity are from *Peltier et al.* [2007].

also are in the range 1.1 - 2.2 MPa [*Peltier et al.*, 2008].

Note that this value is one order smaller than commonly observed rock resistances. It may be characteristic of PdlF volcano, which endured 25 eruptions in the period 1998-2007 [*Peltier et al.*, 2009].

As regarding to the generic lower bound for the magma reservoir volume able to sustain a constant magma influx intrusion, we already discussed in section 3.2.1 the influence of the dimensionless numbers R_3 and R_4 on the flux regime of the propagating dyke. As shown in figure 3.9 for the vertical dyke propagation within a homogeneous medium case, a magma compressibility K of about 1 GPa implies that the minimum reservoir volume required for the flux of magma to remain constant over time is $> 1\,\mathrm{km}^3$. The volume of magma mobilized by the lateral injection has the effect of increasing the minimum size of the magma reservoir required in order to keep the flux constant over the two-phase dyke propagation. In addition, the smaller the magma chamber volume, the smaller the R_1 value necessary to keep the magma flux constant over time. For given reservoir depth, magma and rock densities, this implies smaller initial overpressures sustaining a constant influx of magma over time will be.

3.3.3 Relationship between magma volumes and reservoir overpressure conditions

Traversa and Grasso [2009-Chapter2] assimilate the intrusion process on basaltic volcanoes to a strain-driven, variable-loading process, reminiscent of secondary brittle creep. In such a strain-driven process, the loading is free to vary over time. It means that the overpressure at the dyke inlet is free to vary over time.

Most of PdlF eruptions occurring in the last decades, however, are flank eruptions, with eruptive vents located close or within the central cone, [*Peltier et al.*, 2005, 2007, 2008]. According to the model proposed by *Peltier et al.* [2008] for the magma accumulations and transfers at PdlF since 2000, there is a hierarchy between the so-called 'distal' eruptions (occurring far from the summit cone), which release the reservoir overpressure, and 'proximal' or 'summit' eruptions (occurring close to or within the summit cone), which have negligible effect on the reservoir overpressure state. In this sense, we therefore expect most of PdlF recent eruptions to be accompanied by small variations of the magma reservoir overpressure.

For the August 2003 PdlF eruption, the total amount of magma withdrawn from the reservoir i.e. the volume of lava emitted plus the volume of the dyke that keeps stuck at depth) has been estimated by *Peltier et al.* [2007] and *Tinard* [2007] at 7.2 and 7.8 x 10^6 m^3, respectively.

The model of small independent magma pockets proposed by *Lénat and Bachèlery* [1990] implies a substantial emptying of the lens feeding each individual eruption. This is consistent with large overpressure variations accompanying the dyke intrusion. On the other hand, for the other four conceptual models proposed for the PdlF reservoir system, i.e. reservoir volumes of 1.7-4.1 km^3 [*Nercessian et al.*, 1996; *Sapin et al.*, 1996], 0.1-0.3 km^3 [*Albarède*, 1993], 0.35 km^3 [*Sigmarsson et al.*, 2005] and 0.5 km^3 [*Peltier et al.*, 2007, 2008], the magma volume withdrawn from the chamber during the August 2003 eruption represents between $\sim$ 0.2% and $\sim$ 2.5% of the reservoir volume. These values argue for very small overpressure variations accompanying the dyke intrusion.

In order to test which of these configurations (i.e. large or small overpressure variations) applies to the PdlF case, we calculate the minimum reservoir size that would be required for the overpressure to vary of a defined small percentage during dyke injection. By integrating equation 3.15 we obtain:

$$V_c = \frac{\Delta V_c}{exp\left(\Delta P_{c\,var}\left(\frac{4G+3K}{4GK}\right)\right) - 1}. \tag{3.38}$$

where ΔV_c is the variation in reservoir volume, $\Delta P_{c\,var}$ is the variation in reservoir overpressure induced by the dyke intrusion, G is the rock shear modulus, and K is the magma bulk modulus.

We assume that the volume variation induced in the magma reservoir from the August 2003 dyke growth corresponds to the estimations of the dyke volume, i.e. $\Delta V_c = 1 - 1.6$ x $10^6 m^3$ [*Peltier et al.*, 2007; *Tinard*, 2007]. This is related to the fact that observations of seismicity rate during dyke injection [*Traversa and Grasso*, 2009-Chapter2] do not give any information about the flux evolution after the eruptive activity begins. We thus limit the validity of the constant influx model only to the dyke injection, allowing that possible larger pressure and flux variations could occur during lava flow at surface. The estimated volume of lava erupted during the August 2003 eruption is 6.2 x $10^6 m^3$ [*Peltier et al.*, 2007]. The total volume of magma withdrawn from the chamber is therefore as large as 7.2-7.8 x 10^6 m^3.

We take as the initial reservoir overpressure the upper bound we calculated previ-

Table 3.1: Parameters used in the calculations for the case of a dyke rising in a homogeneous medium from a large and fully compressible magma reservoir. †: from *Peltier et al.* [2007]; ‡: assumed parameters, as generic basalt values.

Parameter	Symbol	Value
Depth of the reservoir (m)†	H	2250
Poisson's ratio‡	ν	0.25
Shear modulus (Pa)‡	G	$1.125\text{x}10^9$
Rock density (kg m^{-3})‡	ρ_r	2750
Magma density (kg m^{-3})‡	ρ_m	2400

ously, i.e. $\Delta P_0 = 2.2$ MPa and we compute the reservoir volume required for the magma overpressure variation $\Delta P_c\, variation$ to be the 5% of the initial reservoir overpressure, i.e. ~ 0.085 MPa. Equation 3.38 gives $V_c = 5 - 8$ km^3 as the corresponding reservoir size.

When applying our model for vertical dyke propagation, computations of overpressure variations induced in a realistic reservoir ($V_c = 0.5 - 5$ km^3 [*Nercessian et al.*, 1996; *Sapin et al.*, 1996; *Peltier et al.*, 2007, 2008]) by a vertical dyke fed at constant flux, are showed in figure 3.3 legend. These variations are $< 6\%$, for reservoir volumes between 0.5 and 5 km^3 and magma compressibility between 1 and 10 GPa.

3.3.4 Relationships between constant magma influx and dyke injection dynamics

In this section we derive the implications of the two-phase model on dyke injection dynamics and we test the model for the dyke intrusion that fed the August 2003, Piton de la Fournaise eruption.

The August 2003 PdlF eruption involves three eruptive fissures, the first within the summit zone (at 17h20 UTM), the second on the northern flank, at 2475 m asl (at 18h10 UTM), and the third lower on the northern flank, at about 2150 m asl (at 19h30 UTM) [Staudacher, OVPF report]. The eruptive activity of the first two fissures was negligible compared to the last one (the former stopped at the end of the first day of the eruption, while only the third fissure remained active throughout the eruption) [*Peltier et al.*, 2007,

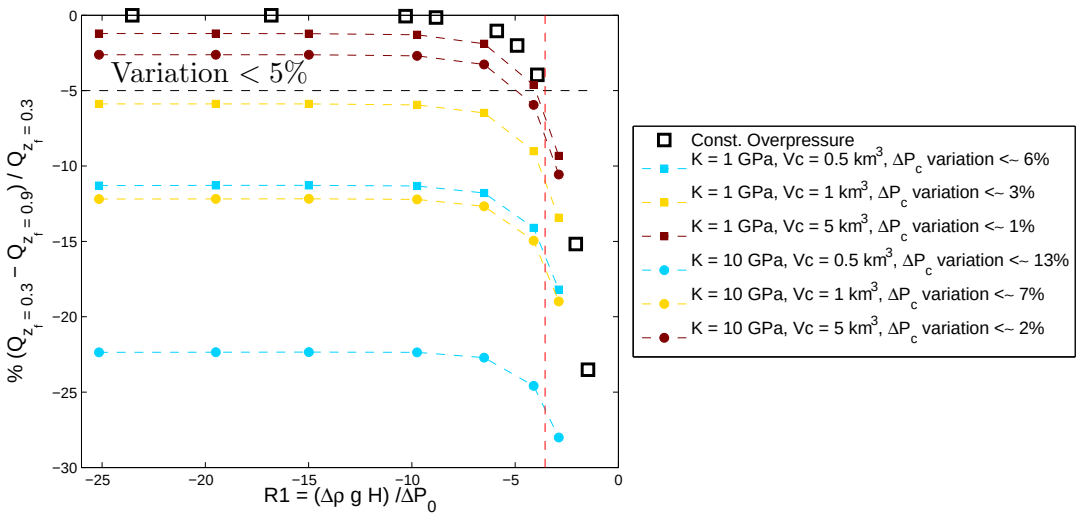

Figure 3.9: Interrelationship between magma influx and reservoir characteristics. Percentage of magma influx variation during dyke growth within a homogeneous medium as function of the dimensionless number R_1 ($R_1 = (\rho_m - \rho_r)gH/\Delta P_0$). Black squares: constant overpressure at the dyke inlet; colored symbols: variable overpressure in the chamber. Colors of plain symbols are related to the V_c value; circles or square symbols depend on the K value. Reservoir overpressure variations ΔP_c *variation* indicated in the legend are issued from the computation. Parameter values used are: $G = 1.125\text{x}10^9$ Pa, $\nu = 0.25$, $a = 100$m, $g = 9.81\,\text{m}\,\text{s}^{-2}$. V_c values derive from conceptual models of PdlF storage system [*Nercessian et al.*, 1996; *Sapin et al.*, 1996; *Peltier et al.*, 2007, 2008].

and Staudacher OVPF report]. As modeled by deformation data, the intrusion preceding this PdlF eruption includes a ∼20 minutes duration (from 14h55 to 15h15 UTM) vertical dyke propagation followed by a ∼125 minutes (from 15h15 to 17h20 UTM) lateral injection toward the north [*Peltier et al.*, 2007]. Although the 17h20 UTM time corresponds to the opening of the first summit fracture [Staudacher OVPF report], tilt data clearly indicate that the lateral dyke has already fully propagated to the flank eruption site by this time. Indeed, no further evolution of the deformation is observed after 17h20 UTM [*Peltier et al.*, 2007].

By inverting deformation data, *Peltier et al.* [2007] estimate the origin of the August 2003 dyke at 400 ±100 meters asl, and the origin point of the lateral dyke at 1500 ±350 m asl. The lateral dyke travels 2.4 ±0.1 km before breaching the surface [*Peltier et al.*, 2007]. On deformation data basis, *Peltier et al.* [2007] estimate an average velocity of 1.3 $\mathrm{m\,s^{-1}}$ for the vertical rising stage, and of 0.2 - 0.6 $\mathrm{m\,s^{-1}}$ for the lateral injection phase. The uncertainties related to vertical and horizontal propagation velocities, obtained from deformation data inversion, are 0.26 $\mathrm{m\,s^{-1}}$ and 0.13 $\mathrm{m\,s^{-1}}$, respectively [uncertainties from A. Peltier 2009, personal communication].

In the following we calibrate the input parameters for the two-stage dyke propagation model. First we derive the relationships among the parameters at stake for the two steps. Second we obtain calibrations of the same parameters by using independent estimates of dyke propagation velocities in the two phases.

We consider a dyke rising vertically within a homogeneous medium (i.e. $R_2 = 0$), from a large magma reservoir with fully compressible magma (i.e. $R_3 \to 0$, $R_4 \to 0$). Reservoir depth H, magma and rock densities ρ_m, ρ_r are listed in table 3.1. In this case, the flux of magma injected into the dyke only depends on the initial overpressure at the dyke inlet and is inversely proportional to the magma viscosity,as shown in figure 3.10:

$$Q \propto \frac{1}{\mu}, \tag{3.39}$$

When we fix the vertical velocity and we let the dyke half-breadth a free to vary, however, we can write:

$$Q = A\,\mu, \tag{3.40}$$

where

$$A = \frac{v_v^2\, Q^*\, 16 H\, G}{v_v^{*2}\, \Delta P_0^2\, (1-\nu)} \tag{3.41}$$

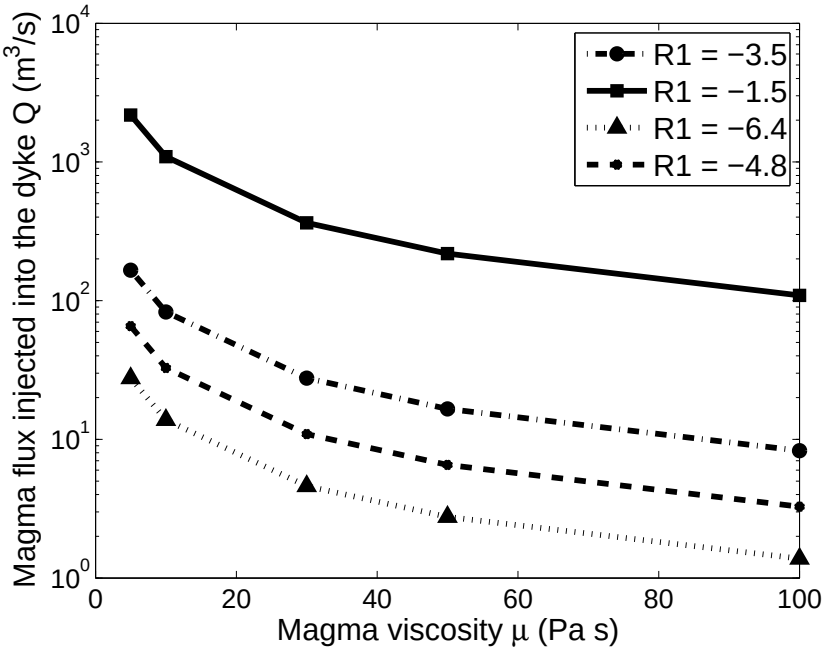

Figure 3.10: Dyke rising vertically within a homogeneous medium from a constant overpressure magma reservoir. Magma flux injected into the dyke as function of the magma viscosity and of the dimensionless number R_1 ($R_1 = (\rho_m - \rho_r)gH/\Delta P_0$). Parameters used are: $H = 2250$ m, $\rho_m = 2400$ kg m^{-3}, $\rho_r = 2750$ kg m^{-3}, $a = 100$ m, $\nu = 0.25$, $G = 1.125$ x 10^9 Pa.

v_v is the vertical propagation velocity, Q^* is the dimensionless flux of magma entering into the dyke (i.e. $Q/[Q]$) and v_v^* is the dimensionless vertical propagation velocity (i.e. $v_v/[v]$). The vertical propagation velocity, in turn, is given by

$$v_v = C\frac{a^2}{\mu}. \tag{3.42}$$

where

$$C = \frac{v_v^*(1-\nu)^2\,\Delta P_0^3}{16\,H\,G^2}. \tag{3.43}$$

For a given dimensionless number R_1, the dimensionless flux and velocity (i.e. Q^* and v_v^*) are fixed. Then, for given values of vertical propagation velocity, depth of the reservoir, and initial magma overpressure, we obtain the A value.

We take $R_1 = -3.55$ (i.e. the upper limit for a 5% flux variation in the constant reservoir overpressure, homogeneous medium case as shown in figure 3.3) and the parameters listed in table 3.1.

The lateral propagation velocity depends on the magma viscosity and on the amount of magma injected into the dyke in the unit time. We then inject different magma flux and viscosity pairs into the lateral dyke. Figure 3.11 shows how the magma flux injected in the dyke is related to the lateral propagation velocity.

In particular, a dyke lateral propagation velocity between 0.2 and 0.6 m s^{-1} (shadow box in figure 3.11), requires the magma flow rate injected into the laterally migrating dyke to be less than about 60 $m^3\,s^{-1}$. Through equation 3.40 this implies a magma viscosity $\mu = 14\,\mathrm{Pa\,s}$. This allows to constrain the value of the vertical dyke half-breadth $a = 100$ m (equation 3.42).

The value we estimate for viscosity is in good agreement with the values found by *Villeneuve et al.* [2008] for re-molten basalts from the 1998 lava flow of the Piton Kapor, on the northern part of Dolomieu crater. Viscosity measurement experiments conducted at constant stress indicate (i) liquidus temperature of the 1998 sample at about 1200°C and (ii) viscosities between 49 and 5 Pa s measured at temperatures between 1195°C (glass transition) and 1386°C (superliquidus), respectively.

For the case of a dyke propagating within a stratified medium from a finite size, compressible magma chamber, more parameters play a role in characterizing the dyke propagation, i.e. magma bulk modulus K, magma chamber volume V_c, rock densities in the upper ρ_u and lower ρ_l layers and the depth of the lithological discontinuity H_b. We refer to the geometry illustrated in figure 3.12, and we use the parameters listed in table 3.2 in

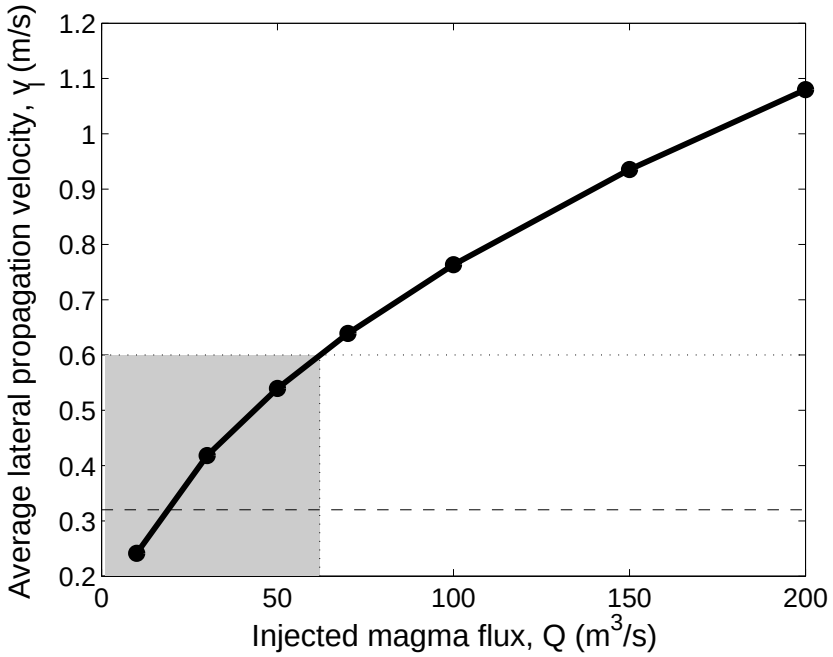

Figure 3.11: Lateral dyke propagation: average propagation velocity versus influx of magma injected into the dyke. Shaded area bounds the lateral propagation velocities estimated by *Peltier et al.* [2007] at Piton de la Fournaise. Parameters used are the following: $\theta = 11.8$ deg, $\rho_{rl} = 2750$ kg m^{-3}, $\rho_{ru} = 2300$ kg m^{-3}, $\rho_m = 2400$ kg m^{-3}, $H_b = 1150$ m, $G = 1.125$ x 10^9 Pa. Each magma flux value corresponds to a viscosity value, according to equation 3.40, where $A = 4.3936$ (from the vertical homogeneous case $R_1 = -3.55$). Reminder: $R_1 = (\rho_m - \rho_r)gH/\Delta P_0$.

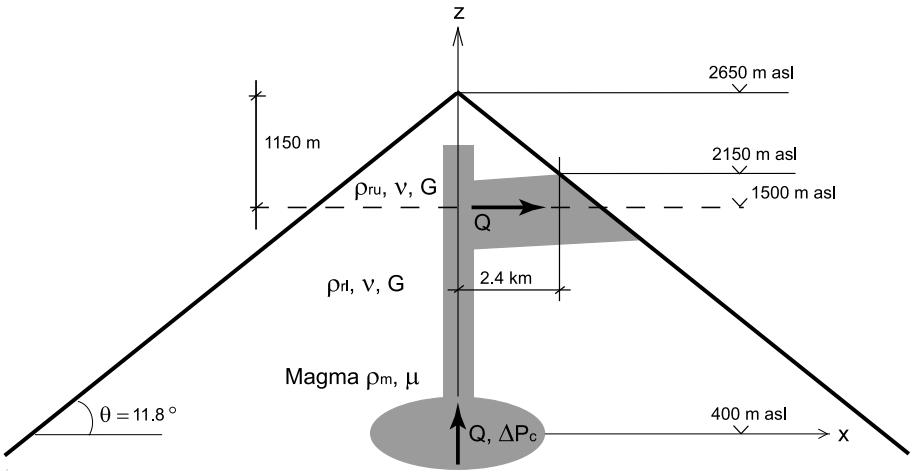

Figure 3.12: August 2003 PdlF case study. Sketch illustrating the geometry used in the model. Dotted line: input lithological discontinuity, position from *Peltier et al.* [2007]. Gray zones indicate magma path. All elevation data come from *Peltier et al.* [2007].

the calculations. Table 3.3 compares results issued from the computation with independent parameter estimates.

From the computation we obtain a dyke which rises vertically at an average velocity of $\sim$1.2 m s^{-1} up to the lithological discontinuity. Figure 3.13 shows the effect of the density barrier on the propagation of the vertical dyke. It quantifies injected magma flux and volume and dyke vertical propagation velocity over time (figure 3.13A, B, C). The shape of the vertical dyke for different propagation steps is illustrated in figure 3.13, D. The flow of magma injected into the vertical dyke over time is $\sim$35 m^3 s^{-1}, through a fracture of width $b \sim 30$ cm, which matches with the value found by *Peltier et al.* [2007], *Froger et al.* [2004] and field observations [*Peltier et al.*, 2007].

The dyke extends above the discontinuity, but its upward propagation is set back by the negative buoyancy [*Pinel and Jaupart*, 2004]. At the density step depth, magma overpressure grows as the dyke head inflates. It may eventually exceed rock toughness and a new fracture may propagate laterally away. Here we set up a lateral dyke, which propagates towards the northern flank. We assume all the magma flux rising through the vertical dyke is injected into the lateral one. The slope of the edifice and the lack of lateral variation in stress gradients, allow for the dyke half-breath a to be constant during the lateral propagation (see figure 3.7).

The computed lateral dyke breadth $2a$ is $\sim$950 m. The upper bound of the fracture

Table 3.2: Parameters used in the calculations applied to the August 2003 eruption at Piton de la Fournaise. †: parameter values estimated by *Peltier et al.* [2007]; ‡: assumed parameters as generic basalt values; § derived parameters; ⊛ parameter values from literature [e.g. *Lénat and Bachèlery*, 1990; *Nercessian et al.*, 1996; *Sapin et al.*, 1996; *Pinel and Jaupart*, 2000, 2004; *Peltier et al.*, 2008].

Parameter	Symbol	Value
Depth of the reservoir(m)†	H	2250
Half-length of the fracture(m)§	a	100
Poisson's ratio‡	ν	0.25
Shear modulus (Pa)‡	G	1.125x10^9
Rock density in the upper layer (kg m^{-3})‡	ρ_{ru}	2300
Rock density in the lower layer (kg m^{-3})‡	ρ_{rl}	2750
Depth of the lithological discontinuity (m)†	H_b	1150
Density of magma (kg m^{-3})‡	ρ_m	2400
Magma viscosity (Pa s)§	μ	11
Initial magma chamber overpressure (MPa)§:	ΔP_0	1.7
Edifice slope (deg)§	θ	11.8
Magma chamber volume (km^3)⊛	V_c	1.7
Magma bulk modulus (Pa)‡	K	1x10^9
Dimensionless numbers		
$R_{1l} = (\rho_m - \rho_{rl})gH/\Delta P_0$	R_{1l}	-4.54
$R_{1u} = (\rho_m - \rho_{ru})gH/\Delta P_0$	R_{1u}	1.30
$R_2 = H_b/H$	R_2	0.51
$R_3 = (\Delta P_0\, a^2\, (1-\nu)\, H)\ (G\, V_c)$	R_3	1.5 x10^{-5}
$R_4 = 4KG/(\Delta P_0\, (4G + 3K))$	R_4	352.90

Table 3.3: Model validation on the August 2003 Piton de la Fournaise eruption. Comparison between independent parameter estimations based on deformation data (from *Peltier et al.* [2007]) and computation results. *: [Peltier 2009, personal communication].

Parameter	Observation estimate	Model output
Vertical average dyke propagation velocity ($\mathrm{m\,s^{-1}}$)	$1.3 \pm 0.26^\star$	1.23
Lateral average dyke propagation velocity ($\mathrm{m\,s^{-1}}$)	$0.2 - 0.6 \pm 0.13^\star$	0.48
Lateral phase duration (min)	125	81
Lateral covered distance (m)	$2400 \pm 100^\star$	2300
Dyke total volume ($\mathrm{m^3}$)	$1 \pm 0.23^\star$ x 10^6	0.82 x 10^6

breaches the surface at a height of about 2000 m asl after 2.3 km lateral propagation, in agreement with field observations of eruptive fracture location [*Peltier et al.*, 2007; *Tinard*, 2007]. The average propagation velocity we compute for the lateral dyke is ~ 0.48 m $\mathrm{s^{-1}}$, in agreement with the upper limit value estimated by *Peltier et al.* [2007] by deformation data inversion (0.2 to 0.6 m $\mathrm{s^{-1}}$).

We remind that the flux of magma injected in the vertical and lateral dykes is related to the respective initial dyke breadth. From the computation we get lateral dyke breath ($a = 476$ m) about five times the vertical dyke one ($a = 100$ m). This is related to the fact that horizontal velocity is much lower than the vertical, which has the effect of making the dyke growing less along the propagation direction and to develop crosswise. The propagation velocity ratio, therefore, somehow inversely mimics the dyke breath ratio between the vertical and the lateral phases.

3.4 Conclusions

Seismic observations contemporary to dyke propagation on basaltic volcanoes show stationary seismicity rate during dyke propagation in the last phase before an eruption, despite possible variations of the dyke-tip velocity [*Traversa and Grasso*, 2009-Chapter2]. Also, a clear and monotonic hypocenter migration of the seismicity contemporary to dyke propagation has been rarely observed. These suggest that the observed dyke-induced seis-

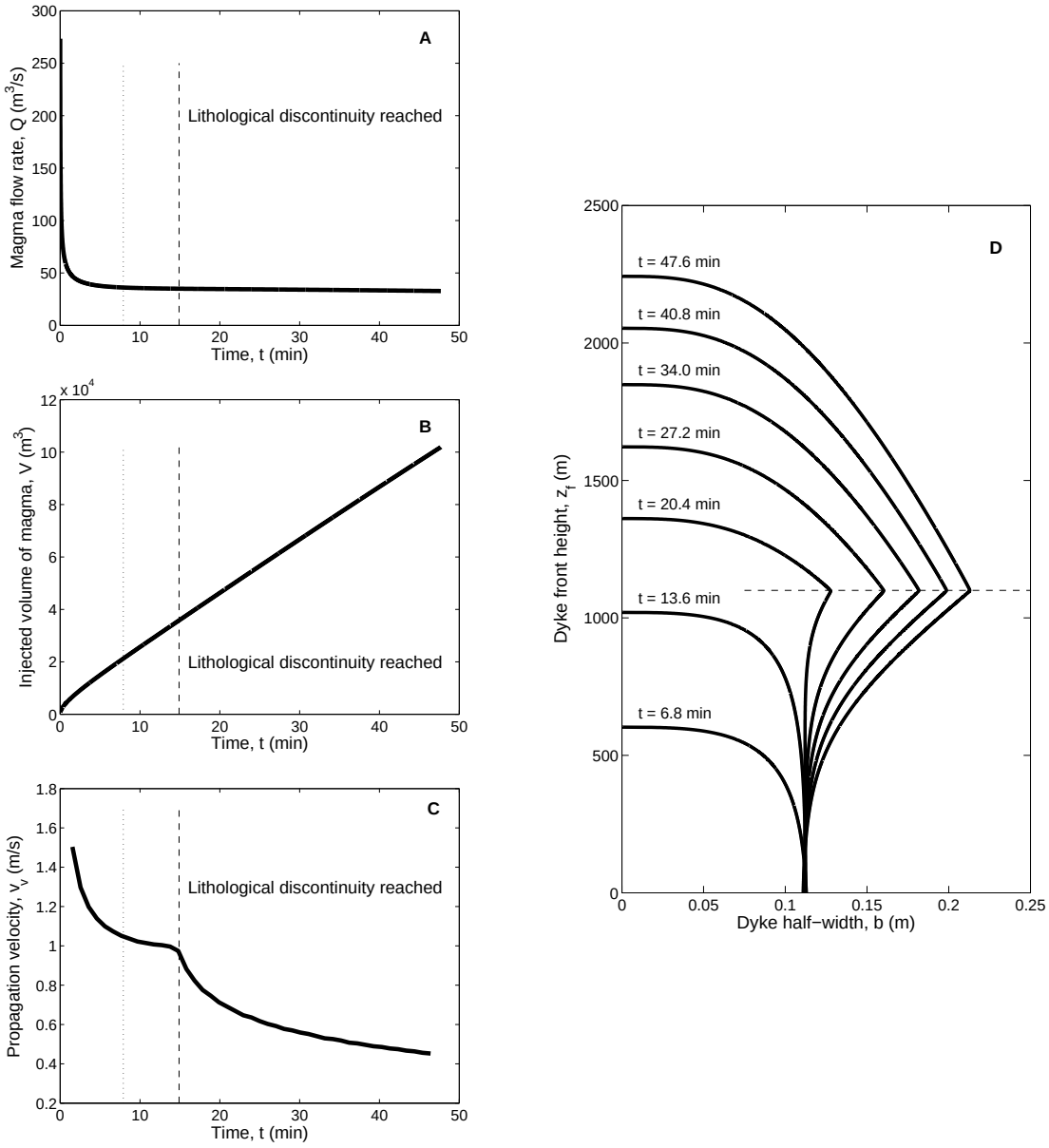

Figure 3.13: The effect of a lithological discontinuity on the vertical propagation of a magma-filled dyke. A: magma flux injected into the dyke over time; B: dyke volume (i.e. cumulative volume of magma injected into the dyke over time); C: propagation velocity versus time; D: Evolution of the crack shape for progressive growth stages. Parameter values used in the calculation are listed in table 3.2. Stipple-lines in plots A, B and C correspond to $z_f/H = z_f^* = 0.3$.

micity is the response of the edifice to the volumetric deformation induced by the magma intruding the solid matrix [*Traversa and Grasso*, 2009-Chapter2]. Accordingly, *Traversa and Grasso* [2009-Chapter2] argue for the stationary seismicity rate contemporary to the intrusion to be a proxy for a constant flux of magma entering the dyke in the unit time.

In order to test the implications of this assertion with respect to the volcano fluid dynamics, we implement a two-phase dyke propagation model, including a first vertical propagation followed by a lateral migration.

We demonstrate that, although propagation velocity varies of one order of magnitude among the different propagation phases (i.e. 1.3 $\mathrm{m\,s^{-1}}$ and 0.2 to 0.6 $\mathrm{m\,s^{-1}}$ for the vertical and lateral propagation, respectively), the flow rate of magma injected into the dyke can remain constant over time under given conditions. This is related both, to the fact that velocity depend on dyke size for the two propagation phases, and to the evolution of dyke growth, which is not limited only to elongation. It supports the idea of direct scaling between the magma flux intruding the solid and the observed seismicity rate through volumetric deformation. On the other hand it rejects a direct scaling between the seismicity rate and the dyke propagation velocity. In this sense the seismicity rate recorded at low-viscosity volcanoes during dyke intrusion represents the response of the solid matrix to a stationary volumetric deformation induced by the intrusion itself.

Obeying the laws governing fluid dynamics, the constant magma flux can be sustained by either, a constant or a slightly variable overpressure at the base of the dyke. The model we propose, however, does not allow for asserting one hypothesis with respect to the other. Indeed it allows to investigate the implications of such a stationary flux hypothesis. For the vertical propagation, once the geometry and the physical parameters are fixed, the constant influx assumption bounds the range of possible initial magma overpressures and volumes of the magma reservoir.

Specifically, only a magma reservoir with sufficiently small initial overpressure and sufficiently large volume is able to sustain a dyke injection fed at constant flux.

The flux value computed in the vertical phase is injected in the lateral propagation phase and it determines, together with static conditions of pressure equilibrium, dyke size and lateral propagation rate. In this way, the model we discuss in this paper allows to constrain the ratio between vertical and horizontal dyke thickness.

We validate the model in an application to the August 2003, Piton de la Fournaise eruption. It consists of two main phases: a vertical propagation, followed by a horizontal

migration towards the eruption site [*Lénat and Bachèlery*, 1990; *Toutain et al.*, 1992; *Bachélery et al.*, 1998; *Bachélery*, 1999; *Peltier et al.*, 2005, 2007, 2008]. According to the classification proposed by *Peltier et al.* [2008], the August 2003 PdlF eruption is a so-called 'proximal' eruption, with eruptive activity concentrated on the volcano flank, close to the central cone.

In this framework, the small values of initial reservoir overpressure (i.e. ≤ 2.2 MPa), and the small variations of this overpressure accompanying dyke propagation (i.e. $\leq 6\%$) we obtain from the computation, argue for this eruption to belong to an early stage of a PdlF refilling cycle [see *Peltier et al.*, 2008]. The small overpressure variations argue for either, the volume of magma withdrawn from the reservoir during the injection to be small compared to the reservoir volume, or the magma flow rate injected into the dyke in the unit time to be small compared to a possible continuous magma flow refilling the shallow reservoir from depth (as proposed by *Peltier et al.* [2007]).

The average intrusion velocities we compute for the dykes feeding the August 2003 PdlF eruption well reproduce the values estimated by *Peltier et al.* [2007] on deformation data basis. It further support the validity of our model.

In conclusion, the dyke propagation model we propose, allows for validating the constant magma influx initial condition as geophysically realist for volcano processes.

Acknowledgments

We thank B. Taisne and A. Peltier, for suggestions and interesting discussions. We acknowledge two anonymous reviewers for the care devoted to the review and the interesting and constructive remarks made. The data used in this study have been acquired by the Piton de la Fournaise Volcanological Observatory (OVPF/IPGP). Special thanks to V. Ferrazzini, in charge of the OVPF seismological network. P.T. and J.R.G. are supported by VOLUME-FP6 and TRIGS projects, contracts n. 08471 and 043386, respectively.

Chapter 4

Space and Time Seismic Response to a 60-Day-Long Magma Forcing. The 2000 Izu dyke Intrusion Case

Résumé

Dans ce chapitre nous explorons l'évolution spatio-temporelle de la séquence sismique qui a accompagné l'intrusion de dyke des îles Izu de 2000. Le but est d'éclaircir les processus physiques qui relient l'intrusion magmatique à l'occurrence des séismes. Nous assumons un modèle de contrainte de Coulomb pour la production des séismes et une loi de friction de type "Rate and state". Avec cela nous utilisons la sismicité observée pour remonter à l'évolution spatio-temporelle du forçage externe qui dirige le système, c'est à dire le processus intrusif en cours. Nous reproduisons la sismicité observée en modélisant l'intrusion du dyke comme un événement de glissement "silencieux", où le dyke en intrusion induit un taux de contrainte qui évolue dans le temps dans la matrice solide. Nous estimons qu'environs 30% de la sismicité est dirigée directement par le processus intrusif. Nous montrons que les motifs de la sismicité associée à l'intrusion sont évocateurs de ceux qui caractérisent la sismicité tectonique "classique", bien que la dureé de la perturbation de contrainte et la manière à travers laquelle telle perturbation est induite sont bien différents dans les deux cas. Cependant, puisque le processus déclencheur est actif de manière continue pendant 60 jours dans le cas de l'intrusion aux Izu, la cascade de répliques qui décroît avec le temps attendue selon la loi d'Omori, est inhibée par une sismicité de fond continuellement alimentée. Cela résulte en un système "amorti" au sein duquel le taux

de contrainte qui déclenche la sismicité décroît progressivement, mais continue à alimenter le système tout le long de la crise intrusive. Au moment où le forçage disparaît, nous observons une décroissance en loi de puissance du taux de sismicité. Une intrusion de dyke induit donc une perturbation de l'état de contrainte qui, même si différente en durée et mode de fracturation, a les mêmes effets de celle induite par un choc principale en sismicité tectonique. Le dyke des îles Izu de 2000 agit comme une source sismique ralentie (0.5 km/jour contre 2-3-5 km/s de propagation de la fracture pour le dyke et pour un sésme, respectivement), ce qui permet de suivre l'évolution de réponse mécanique tout le long du processus de fracturation même.

4.1 Introduction

Miyakejima (Northern Izu islands, Japan) is a basaltic volcanic island located at the boundary between the Pacific and the Philippine Sea plates. The Miyakejima stratovolcano is a rather active volcano, with repeated flank eruptions at intervals of about 20 years in the twentieth century [e.g. *Furuya et al.*, 2003a]. A total of 14 historical eruptions are documented in the past millennium [*Nishimura et al.*, 2001]. The typical eruptive style of Miyakejima volcano is fissure basaltic eruption from the flank of the volcano [*Nishimura et al.*, 2001; *Ozawa et al.*, 2004; *Yamaoka et al.*, 2005]. However, the 2000 eruption is much different from the previous ones.

After a 17 years long repose period, on June 26, 2000, small shallow Volcano Tectonic (VT) earthquakes begin to be recorded at seismic stations west to the summit of the Miyakejima volcano [*Nishimura et al.*, 2001; *Uhira et al.*, 2005]. These mark the beginning of one of the most energetic swarms ever recorded [*Toda et al.*, 2002].

From the evening of June 26, earthquake hypocenters start migrating westwards during about 12 hours, and then continue moving northwestward, for a total of about 30 km by July 1st, 2000 (figure 4.1) [e.g. *Nishimura et al.*, 2001; *Toda et al.*, 2002; *Furuya et al.*, 2003b,a].

After July 2 the seismicity continues moving back and forth, without any further migration and develops northern and southern lobes (figure 4.2) [*Toda et al.*, 2002]. The intense seismic activity, associated with large deformation rates, lasts until late August and then fades away. During this $\sim$60 day-lasting-period, several eruptions occur (8 July (small), 14-15 July (phreatomagmatics), 18 August (the largest), 29 August).

The 2000 Izu Island dyke intrusion has been intensely monitored and number of works

have been published in the attempt of understanding the dynamics of this extraordinary event. Indeed, several different datasets have been used to model the 2000 Miyake intrusion. These include geodetic [*Nishimura et al.*, 2001; *Ito and Yoshioka*, 2002; *Ozawa et al.*, 2004; *Irwan et al.*, 2003; *Yamaoka et al.*, 2005], gravity [*Furuya et al.*, 2003b], and combinations of either, GPS and tilt [*Ueda et al.*, 2005], or GPS, elevation and gravity data [*Furuya et al.*, 2003a].

Though all these studies give slightly different results, they seem to converge on several common features characterizing the evolution of the magmatic intrusion. The contemporary migration of seismicity and deformation data during the first phase of the intrusion (i.e. June 26 to July 1st, 2000) suggests that the earthquake hypocentral locations are reliable indicators of the dyke tip position over time [e.g. *Ito and Yoshioka*, 2002; *Furuya et al.*, 2003a]. During this period, and up to the first summit eruption (on July 8, 2000) the laterally intruding dyke is fed from a reservoir beneath Miyakejima volcano. The total amount of tensile deformation observed over the whole sequence, however, is much larger than the deflation induced by the magma withdrawal from this source [*Ito and Yoshioka*, 2002; *Furuya et al.*, 2003a; *Yamaoka et al.*, 2005]. This leads *Ito and Yoshioka* [2002], *Furuya et al.* [2003a] and *Yamaoka et al.* [2005] to propose the existence of another magma source identified in sub-crustal magma pockets nearby Kozushima volcano island that would feed the dyke from July 8 on. This hypothesis is also endorsed by *Uhira et al.* [2005] on seismic location arguments.

The seismic sequence accompanying the dyke intrusion has been studied by *Toda et al.* [2002], who conclude that the seismicity rate accompanying the active volcano processes linearly scales with the stressing rate change induced by the processes itself. They also show that the rate and state friction formulation can explain the aftershock decay duration following largest earthquakes of the sequence.

Later, *Lombardi et al.* [2006] studied the Izu 2000 seismic sequence from a stochastic point of view. Following the work of *Hainzl and Ogata* [2005], they interpret earthquake occurrence as a point process and use non-stationary ETAS model to simulate the temporal occurrence of seismicity during the 2000 swarm. Their best fitting of the data is obtained using both, background seismicity rate, and Omori p-exponent variable with time. The interest of this approach is that, according to the ETAS model [e.g. *Ogata*, 1988; *Utsu et al.*, 1995; *Helmstetter and Sornette*, 2002a], seismic intensity can be described in time as the superposition of two types of events: a background uncorrelated seismicity, and the

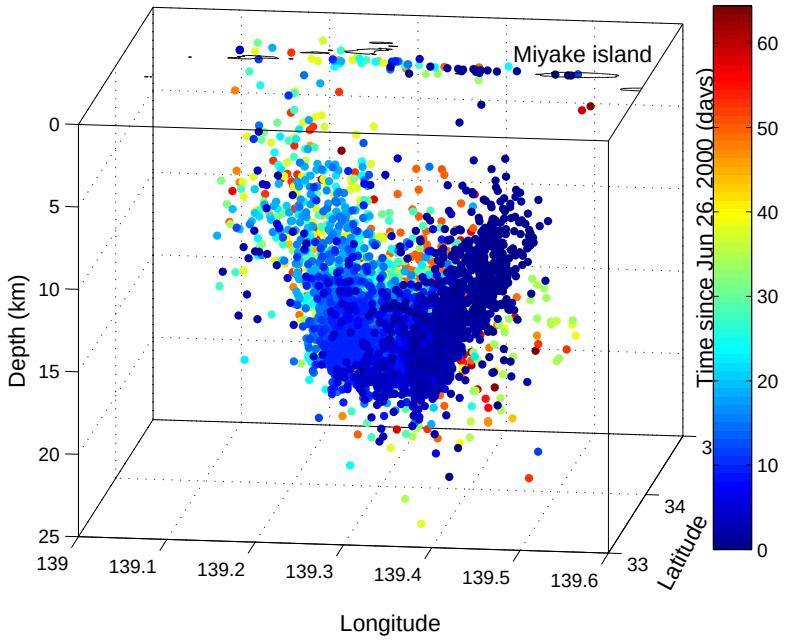

Figure 4.1: 3D view of seismic event locations during the seismic swarm associated to the 2000 Izu islands dyke intrusion. Color of the dots represents time since the intrusion onset on June 26 2000.

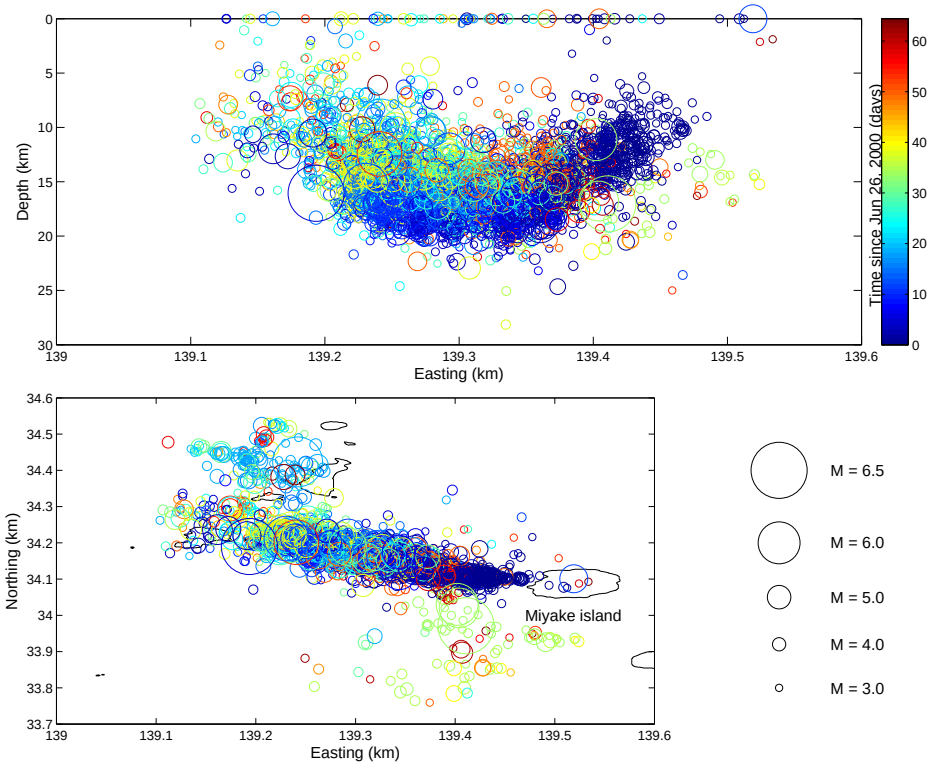

Figure 4.2: Izu 2000 volcano-induced seismic swarm (2000/06/26-2000/08/31 period). Top and bottom illustrate cross section and map view of earthquake location, respectively. Color is function of time, as indicated in the colorbar on the top right. Circle radius is function of event magnitude, as shown in the legend on the bottom right.

earthquakes triggered by previous events. The former represents the part of the seismic activity directly driven by the source process, i.e. the magmatic processes, or the plate tectonics in volcanic or tectonic environments, respectively [e.g. *Ogata*, 1988; *Utsu et al.*, 1995; *Helmstetter and Sornette*, 2002a]. The latter are the cascading process resulting from earthquake interactions. For the 2000 Izu swarm, therefore, the background seismicity rate is the response of the crust to the magmatic intrusion. Such a direct link between the background rate and the magma-induced forcing, makes very attractive the quantification of the former quantity in the study of the physical process driving seismic occurrence. The effectiveness of current ETAS model inversions of observed seismicity, however, is a debated subject within the seismologic community due to the non-uniqueness and frequent instability of the solution [e.g. Helmstetter A., 2007 and Werner M., 2008, personal communications]. The Omori p-exponent is instead thought to be positively correlated with crustal temperature [*Mogi*, 1967; *Klein et al.*, 2006; *Lombardi et al.*, 2006].

In this work we explore the spatio-temporal evolution of the seismic sequence accompanying the 2000 Izu intrusion in order to shed light on the physical processes that rely magma intrusions with earthquake occurrence. By assuming a Coulomb stress model for seismicity and a rate and state dependent friction law, we use the observed seismicity to recover the spatio-temporal evolution of the external forcing that directly drives it, that is the ongoing intrusive process. The estimation of such a forcing rate, allows us to explore the effects of a finite long-duration external forcing on the spatio-temporal occurrence characteristics and interaction patterns of the induced seismicity. We show that these patterns are reminiscent of those observed when considering "ordinary" tectonic seismicity, although both, the duration of the stress perturbation, and the way this perturbation is transferred to the solid matrix, are different in the two cases.

4.2 Data

The magma intrusion-induced seismic swarm that stroke the Izu islands (south Japan) begins at around 18:00 (LT) on June 26, 2000 and lasts until the end of August. Recorded seismic events are reported in the Japan Meteorological Agency (JMA) seismic catalog.

Events are initially detected by the eight seismic stations deployed on Miyakejima by JMA and the Tokyo Metropolitan Government headquarters [*Uhira et al.*, 2005]. All the stations are equipped with three-components short-period seismometers (L4C, 1s sensors,

Markproduct Inc.). Signals are transmitted to the head office of JMA, where they are sampled at 100 Hz and continuously recorded. All the events recorded on the early evening of June 26, 2000, are located by the local seismic network and have magnitude M less than 1.5 [*Uhira et al.*, 2005].

Westward hypocenter migration starts at around 22:00 LT on June 26 and continues the following day. From June 27 on, solutions for migrating hypocenters need then to include stations on Kozushima and Mikurajima islands, some of which are part of a Nationwide seismic network. From this wide seismic network, JMA determines hypocenter locations for earthquakes $M \geq 3$ even at the peak of the swarm. Most of earthquakes recorded on June 26 have not been included in the JMA catalog, except for four events [*Uhira et al.*, 2005]. The resulting seismic catalog is composed by $\sim$ 20000 events with magnitude between 0 and 6.5 characterized by their velocity magnitude M_V and location.

For events shallower than 60 km, as in the present case, M_V is determined by using velocity-amplitude data according to the formula [*Tsuboi*, 1954]:

$$M_V = \log_{10} A + 1.73 \log_{10} \Delta - 0.83, \tag{4.1}$$

where Δ is the epicentral distance (km), and A is the maximum recorded amplitude, given by $\sqrt{A_{NS}^2 + A_{EW}^2}$. A_{NS} and A_{EW} are half the maximum peak-to-peak amplitudes for the horizontal components. This formula was designed to give almost the same value as the Gutenberg-Richter magnitude [1949], which is a weighted mean between body-wave M_B and surface-wave M_S magnitudes [*Katsumata*, 1996].

In the following, only earthquakes with magnitude M_V larger than the completeness of the catalog $M_c = 3$ are considered, i.e. about 5000 events. M_c is estimated from the magnitude frequency distribution, and corresponds to the value reported by *Toda et al.* [2002]. In the period 2000/06/26-2000/08/31, the average seismicity rate is 75.4 eqs/day. Figure 4.3 illustrates the cumulated seismicity and the seismicity rate recorded in the zone $33°.6 - 34°.6$ N latitude, $139°.1 - 139°.6$ E longitude over time during 2000, while figure 4.4 focuses on the volcano-induced seismic swarm, in the period 2000/06/26 to 2000/08/31.

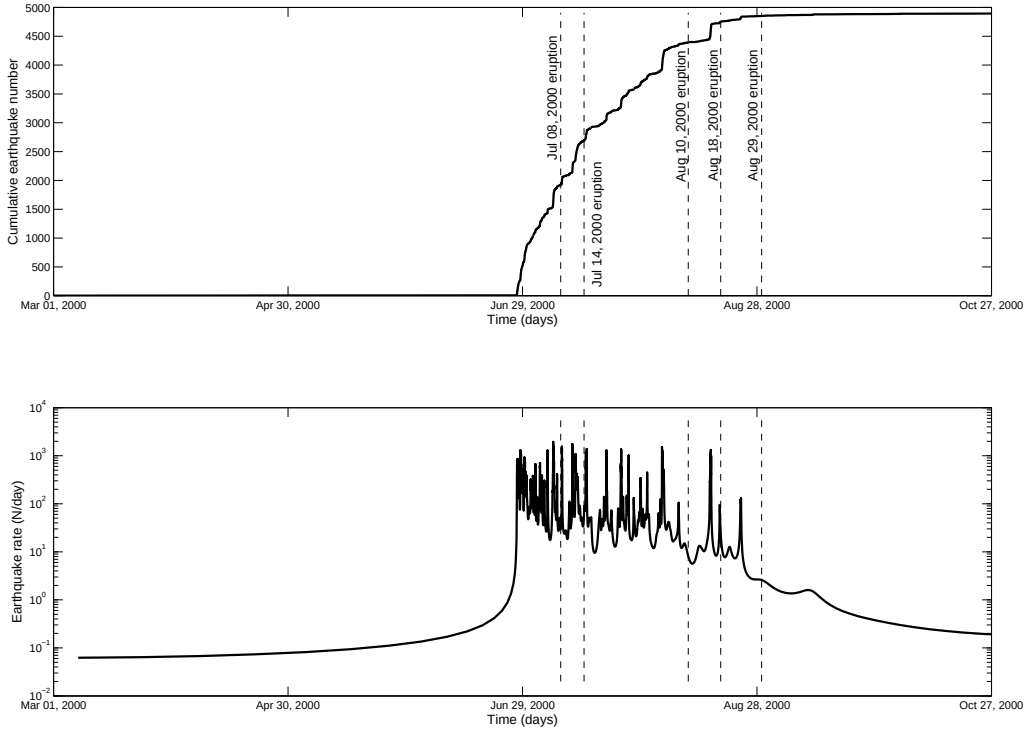

Figure 4.3: Seismicity recorded at the Izu islands zone during 2000. Top: Cumulative earthquake number versus time; Bottom: Seismicity rate over time. On top and bottom graphs, dashed lines indicate the eruption onset times. Only $M_V \geq M_c = 3$ events are considered.

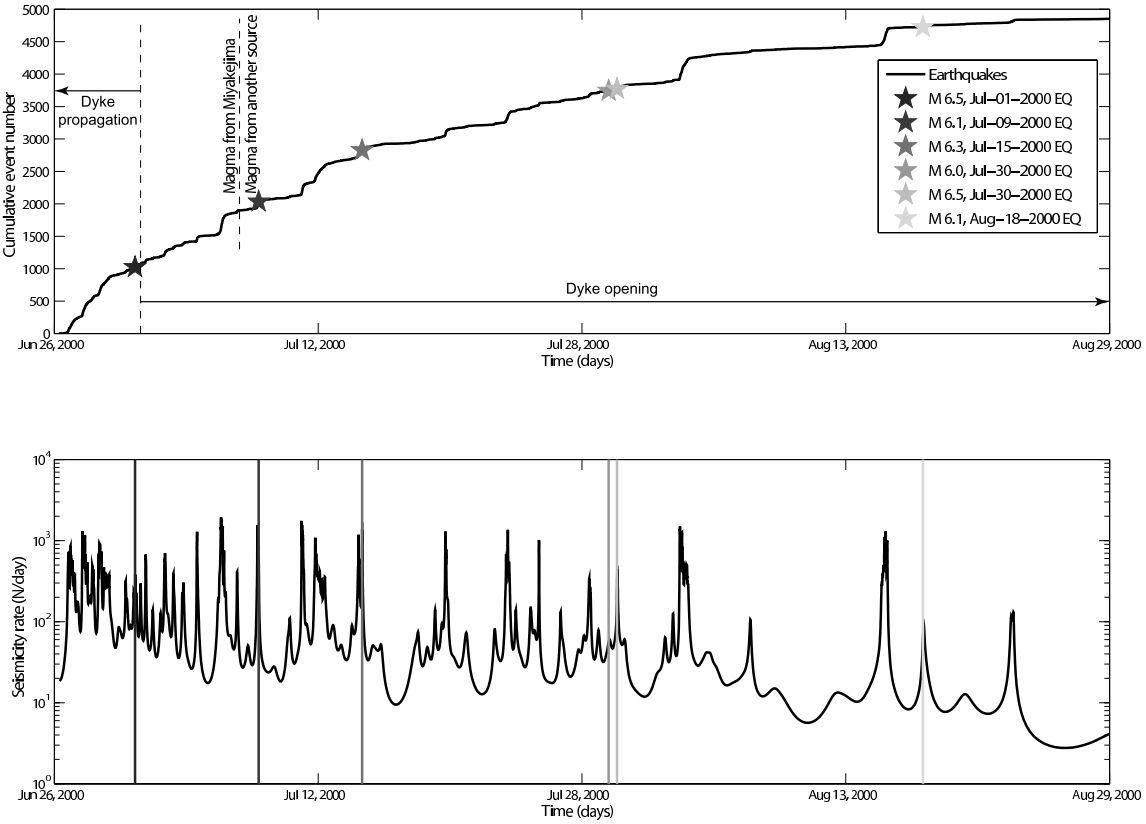

Figure 4.4: Seismicity recorded at the Izu island during the 2000/06/26-2000/08/31 seismic swarm. Top: Cumulative number of earthquakes versus time; dashed lines indicate (i) the time at which the dyke reaches its full length (July 1^{st}, 2000), and (ii) the time at which another magma source different from the Miyakejima reservoir starts collaborating to feed the intrusion (July 8, 2000); stars indicate the occurrence of $M \geq 6$ earthquakes. Bottom: seismicity rate over time; vertical plain lines indicate the occurrence of $M \geq 6$ earthquakes.

4.3 From the earthquake rate to the stress history

4.3.1 Overview

Earthquake triggering results from stress perturbations and redistributions induced into the rock matrix by both, external forcings (i.e. either, tectonic plate motion or volcano processes in tectonic and volcanic environments, respectively), and earthquake interactions. The close association we generally observe, between seismic and volcanic activity, indicates that fault systems and volcanic sources are mechanically coupled [*Hill et al.*, 2002]. That is, stress perturbations related to the deformations induced in the solid matrix by volcano processes can promote faulting and earthquake activity [e.g. *Dieterich et al.*, 2000; *Toda et al.*, 2002; *Pedersen et al.*, 2007].

Assuming a simple Coulomb friction model for earthquakes, the potential for failure is given by the following criterion:

$$\Delta S = \Delta\tau + \mu(\Delta\sigma + \Delta P), \tag{4.2}$$

where $\Delta\tau$ is the shear stress change on a fault (positive in the direction of fault slip), $\Delta\sigma$ is the normal stress change (positive if the fault is unclamped), ΔP is the pore pressure change in the fault zone (positive in compression), and ν is the friction coefficient (in the range 0-1). Slip is encouraged if ΔS is positive, and inhibited if ΔS is negative. Such Coulomb stress changes refer to stress perturbations that occur instantaneously and permanently on a site [e.g *Steacy et al.*, 2005]. Number of observations of seismic occurrence variations induced by sudden [e.g. *Das and Scholz*, 1981; *Stein and Lisowski*, 1983; *King et al.*, 1994; *Harris*, 1998; *Stein*, 1999; *King and Cocco*, 2000] or longer duration stress changes [e.g. *Dieterich et al.*, 2000; *Toda et al.*, 2002; *Segall et al.*, 2006] have supported the validity of this criterion as a good candidate to explain the physics of earthquake triggering.

However, seismicity rate changes and Coulomb stress changes are not linearly correlated. From an experimental approach, *Deterich* [1994] proposes a constitutive law for earthquake production. In his formulation, the seismicity is modeled as a sequence of slip events in which the distribution of initial conditions over the fault population and the stressing history to which the sources are subject, drive the earthquake occurrence. Earthquake sources are fault patches with rate- and state-dependent constitutive properties derived from laboratory fault-slip experiments. In the absence of stress perturbation, seismicity rate is constant. The non-linearity between the change in stress and the change in earth-

quake occurrence rate comes from the large number of earthquake sources on the fault plane, which implies a non-linear dependence of time-to-instability on the stress change [*Deterich*, 1994]. Appendix B illustrates Dieterich's model constitute equations.

According to the rate and state formulation, the earthquake rate can be written as follows:

$$R = \frac{r}{\gamma \dot{S}_r}, \tag{4.3}$$

where

$$d\gamma = \frac{1}{A\sigma}[dt - \gamma dS], \tag{4.4}$$

where γ is a state variable, t is time, S is a Coulomb stress function in which the friction term in equation (4.2) is defined as $\mu = \tau/\sigma - \alpha$; the constant r is the steady-state earthquake rate at the reference stressing rate $\dot{S}_r$, A is a dimensionless fault constitutive parameter.

4.3.2 Stress history driving earthquake occurrence

According to the rate and state formulation, a stress change, i.e. the occurrence of an earthquake, has a transient effect on the rate of triggered earthquakes. The duration t_a of this transient is inversely proportional to the stressing rate $\dot{S}$ to which the fault is subject at the moment of the stress change, as follows [*Deterich*, 1994]:

$$t_a = \frac{A\sigma}{\dot{S}}. \tag{4.5}$$

This provides a physical model for aftershocks, including the time-dependent Omori law decay of aftershocks following a mainshock.

For the 2000 Izu island seismic swarm, *Toda et al.* [2002] demonstrate that, in agreement with the rate and state formulation, and equation (4.5) in particular, properties of aftershock decay following large mainshocks (i.e. $M \geq 6$) depend on the stress imparted by the magmatic intrusion. In particular they show that the aftershock sequence durations following $M \geq 6$ earthquakes, are inversely proportional to the seismicity rate, which in turn is proportional to the active stressing rate [*Toda et al.*, 2002]. Figure 4.5 shows the observed aftershock rates following each of the five $M \geq 6$ events of the sequence.

$M \geq 6$ events occurring when seismicity rate is larger (figure 4.4 and table 4.1 for seismicity rate values) are followed by a faster aftershock decay, which merges into a

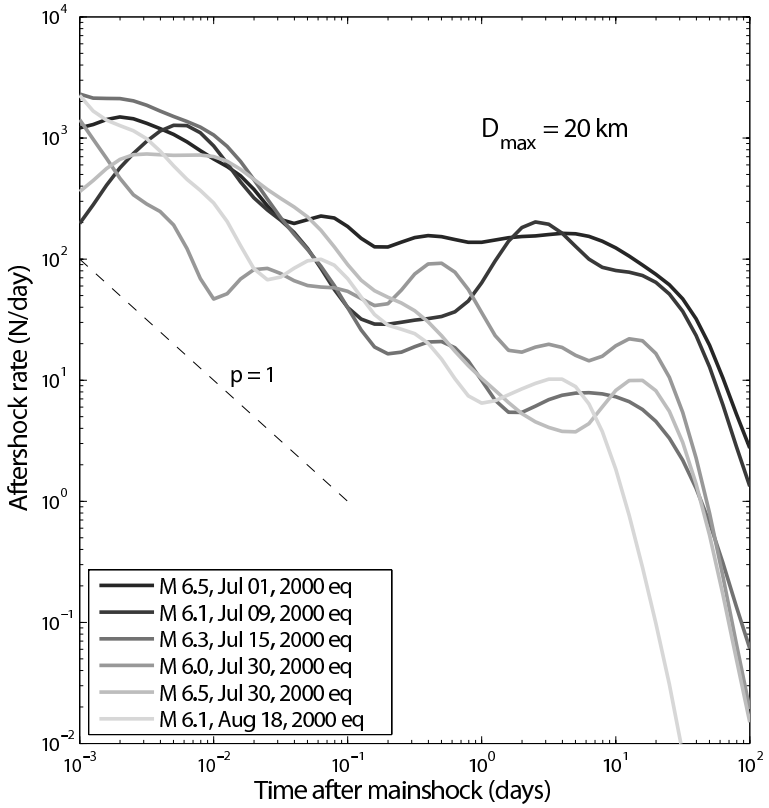

Figure 4.5: Aftershock rates following earthquakes with $M \geq 6$. Aftershocks are defined in a space circular window of 20 km radius around the respective main event. Gray scale refers to the occurrence time of the main event along the seismic swarm, as indicated in the legend.

higher level background rate, while main events occurring later in the sequence, when the seismicity rate has already started to decrease, are followed by longer duration aftershock sequences (figure 4.5). Since changes in stressing rate are linearly related to changes in stressing rate [*Toda et al.*, 2002], this non-stationarity in the background seismic rate argues for a non-stationary forcing rate acting on the system.

In the following we use the observed seismicity rate to recover the stress history to which the system is subject by assuming a rate- and state-dependence of friction [*Deterich*, 1994]. We can assimilate the dyke intrusion to a "silent" slip, or "slow" event, i.e. a long duration event which is silent as itself, but which directly drives the background seismicity. This triggers its aftershocks, which in turn trigger their own aftershocks and so on. Altogether, the background and the earthquake interaction driven seismicity, constitute the 2000 Izu islands seismic swarm.

We quantitatively relate the 2000 Izu dyke intrusion to the induced seismicity by modeling the intrusion as a series of stressing rate changes. This allows to reproduce the observed non-stationarity in the seismicity rate. A similar approach has been followed by *Segall et al.* [2006], who approximate the slip history of the 2000 slow-slip event observed on the south flank of Kilauea volcano (Hawaii) by a ramp function. It allows the authors to reproduce the recorded seismicity accompanying this event.

First, a change point analysis is carried out on the seismic sequence. It allows us to get a preliminary idea about the number of most significant regimes characterizing the time history, i.e. the possible variations in the source process. At this purpose, we can use the non-parametric method proposed by *Mulargia and Tinti* [1985]; *Mulargia et al.* [1987] (described in appendix C), as discussed by *Lombardi et al.* [2006]. This procedure is based on the Kolmogorov-Smirnov two sample test, and can be satisfactorily applied when the number of regimes is unknown, the regimes follow different statistical distributions, and the regimes possibly involve a relatively small sample size. Our results agree with those of *Lombardi et al.* [2006], who identify four major change points. The beginning (June 26, 2000) and the end (August 23, 2000) of the sequence are the most significant ones. Intermediate change points are identified on July 29 and August 6 [*Lombardi et al.*, 2006]. We identified additional significant change points on July 7 and August 24.

Second we invert the recorded seismicity rate to obtain the stress history through a rate- and state-friction dependent model based on either, three, four or five different regimes (i.e. different stressing rates) characterizing the intrusion. Within each regime,

individual $M \geq 3$ earthquakes induce stress steps and transiently alter the local seismicity rate. Before intrusion onset, we use reference stressing rate $\dot{S}_r$= 0.1 bar yr^{-1} (estimated from strain rate by [*Sagiya et al.*, 2000]), and constitutive parameter $A\sigma = 0.1$ bar [*Toda et al.*, 2002]. Steady state $M \geq 3$ seismicity rate r in the region is estimated at 0.05 eq d^{-1} in the period 1980-1999 [*Toda et al.*, 2002]. The amplitude of the stress step induced by single events is let free to vary for each magnitude class and optimally estimated from the inversion. The inversion procedure computes optimal times for changes in stressing rate. The change points between different regimes computed above by the Mulargia technique are independent estimates we test the inversion results against.

From equations (4.3) and (4.4), the seismicity rate in each regime is computed considering that each stressing rate $\dot{S}_i$, is constant over the duration of regime i. For $t_{i-1} \leq t < t_i$, equation (4.4) has the solution:

$$\gamma = \left(\gamma(t_{i-1}) - \frac{1}{\dot{S}_i}\right) \exp\left(-\frac{\dot{S}_i\,(t - t_{i-1})}{A\sigma}\right) + \frac{1}{\dot{S}_i}. \tag{4.6}$$

The initial condition is given by $\gamma(t_0) = 1/\ \dot{S}_r$. Once γ as function of time is computed, the seismicity rate can be obtained substituting the solution of γ in equation (4.3), which gives:

$$R_i(t) = \frac{r/\ \dot{S}_r}{\left(\gamma(t_{i-1}) - \frac{1}{\dot{S}_i}\right) \exp\left(-\frac{\dot{S}_i(t-t_{i-1})}{A\sigma}\right) + \frac{1}{\dot{S}_i}}. \tag{4.7}$$

According to *Deterich* [1994], the seismicity rate as function of time following a mainshock of magnitude M occurring at time t_M, and inducing a stress step ΔS, is instead given by (see also Appendix B):

$$R_M(t) = \frac{r\ \dot{S}_i\ /\ \dot{S}_r}{\left[\frac{\dot{S}_i}{\dot{S}_r} \exp\left(\frac{-\Delta S}{A\sigma}\right) - 1\right] \exp\left[\frac{-(t-t_M)\dot{S}_i}{A\sigma}\right] + 1}, \tag{4.8}$$

where $\dot{S}_i$ is the stressing rate of regime i.

The best model among the proposed three, four or five regimes is chosen using the Akaike Information Criterion (AIC) [*Akaike*, 1974], which measures the goodness of fit of the estimated model. AIC is defined as follows:

$$AIC = 2P + n[\ln(2\pi\, RSS/n) + 1], \tag{4.9}$$

where P is the number of parameters of the model, RSS is the residual sum of squares and n is the number of observations. AIC values for the models based on three, four, or five regimes, are 6101, 6948 and 11760, respectively. The best model to fit the 2000 Izu island seismic dataset is therefore composed of three main forcing rate regimes.

Figure 4.6 shows a comparison between the seismicity computed through the rate and state inversion based on a three stressing rate regimes model and the observed data. Table 4.1 illustrates the best parameters issued from the inversion. As resumed in table 4.1, the seismic swarm contemporary to the 2000 Izu Islands dyke intrusion is therefore driven by an external forcing rate which is initially about 1600-fold the background stressing rate, and progressively fades away as time passes. Eventually, the external perturbation vanishes and the stressing rate goes back to the background value $\dot{S}_r$ (table 4.1). The stress as function of time can be simply calculated by integrating the stressing rate over time and by adding the stress steps induced by single events. Seismicity directly triggered by the external forcing triggers in turn cascades of aftershocks following individual events, altogether composing the 2000 Izu seismic sequence. Optimal times for stressing rate changes obtained by the inversion are within two days those obtained by changing point analysis [*Mulargia and Tinti*, 1985; *Mulargia et al.*, 1987].

4.3.3 Vanishing of the forcing: the relaxation of the system

In the previous section, the rate and state friction law has allowed to quantify the stressing rates and stresses responsible for the observed seismicity as function of the time. When the external forcing represented by the dyke intrusion starts weakening, the seismicity rate also progressively decreases. The arrest of the forcing and the return to the steady state stressing rate (t_3: August 23, 2000), is followed by a power law relaxation of the system (figure 4.7). This reminds of the power law decrease of aftershocks following mainshocks at tectonic environments [e.g. *Omori*, 1894; *Utsu*, 1961]. It argues for such a seismic relaxation to be simply driven by the vanishing of the perturbation which has driven the seismicity, no matter whether following an instantaneous stress step, or a longer duration high stressing rate.

Appendix B illustrates rate and state analytical and numerical computations of the seismicity rate that follows a stress relaxation as a decrease in the stressing rate to which the system is subject. Either after an instantaneous stress step induced by the occurrence

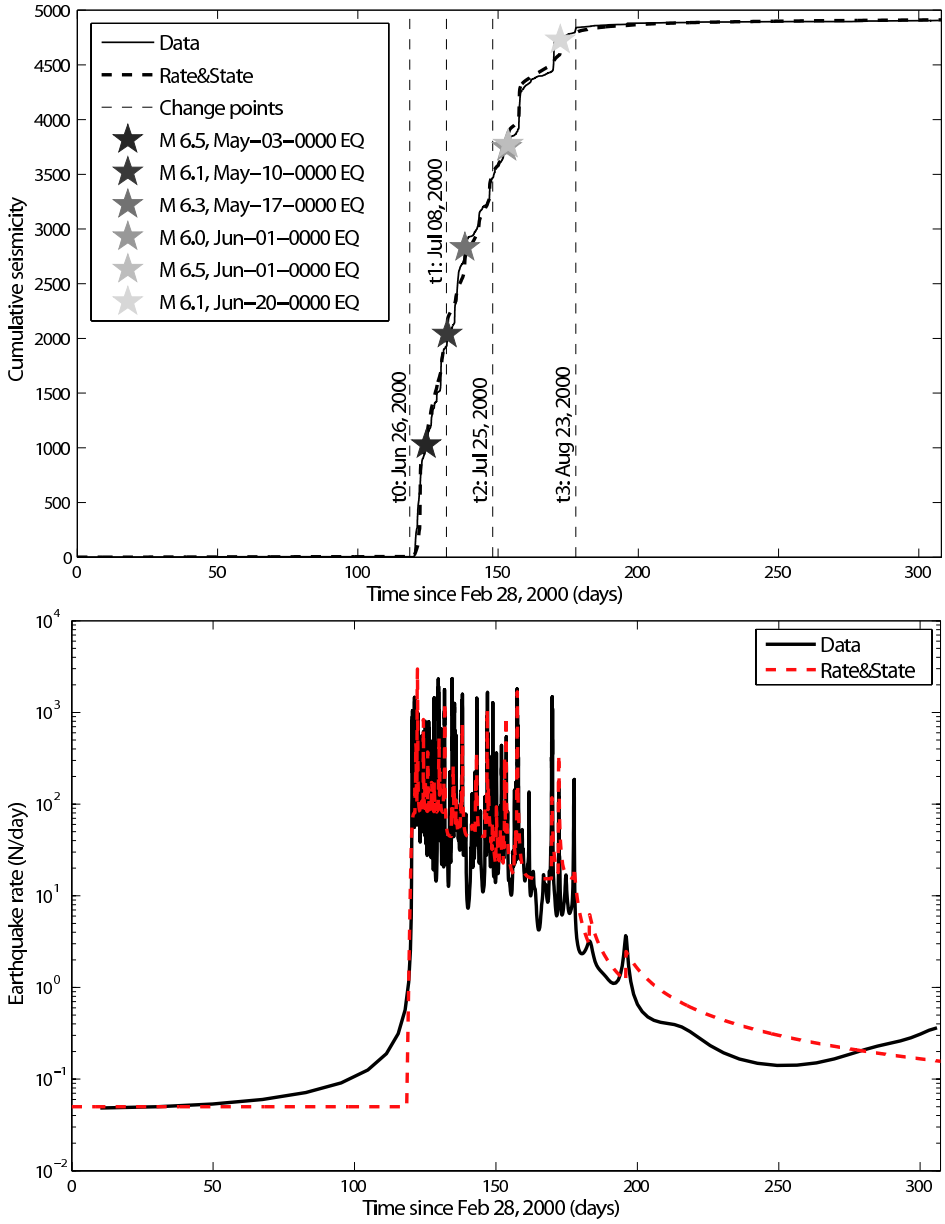

Figure 4.6: Comparison between seismic data recorded during the 2000 Izu Islands seismic swarm and the seismicity reproduced by the rate and state inversion over time. Top: cumulative seismicity: thin black solid line is observed seismicity, thick black dashed line is computed seismicity. Thin dashed black lines indicate times at which the stressing rate changes, i.e. change points issued from the inversion. Bottom: Seismicity rate, thin black solid line is observed seismicity, thick red dashed line is computed seismicity rate. The slight slope of the observed seismicity rate curve at the beginning of the swarm is induced by the smoothing with which the rate is computed. Thin dashed black lines indicate times at which the stressing rate changes, i.e. change points issued from the inversion.

Table 4.1: Rate and state model parameters. †: from *Toda et al.* [2002], ‡: from *Sagiya et al.* [2000], §: issued from the computation, ♯: observed.

Parameter	Symbol	Value
Reference stressing rate‡ ($t \leq t_0$)	$\dot{S}_r$	0.1 bar yr^{-1}
Steady state seismicity rate †	r	0.05 ev d^{-1}
Fault constitutive parameter‡	$A\sigma$	0.1 bar
Beginning of the seismic swarm♯	t_0	June 26, 2000
First regime: $t_0 \leq t < t_1$		
Stressing rate§	$\dot{S}_1$	161.8 bar yr^{-1}
Seismicity rate♯	R_1	164.0 ev d^{-1}
Change point§	t_1	July 8, 2000
Second regime: $t_1 \leq t < t_2$		
Stressing rate§	$\dot{S}_2$	88.5 bar yr^{-1}
Seismicity rate♯	R_2	94.5 ev d^{-1}
Change point§	t_2	July 25, 2000
Third regime: $t_2 \leq t < t_3$		
Stressing rate§	$\dot{S}_3$	30.6 bar yr^{-1}
Seismicity rate♯	R_3	46.2 ev d^{-1}
Change point§	t_3	August 23, 2000
End of the seimic swarm $t > t_3$		
Stressing rate§	$\dot{S}_f$	0.1 bar yr^{-1}
Seismicity rate♯	R_f	0.6 ev d^{-1}
Stress step $3 \leq M < 4$ earthquakes§	ΔS_3	9x10^{-3} bar
Stress step $4 \leq M < 5$ earthquakes§	ΔS_4	3x10^{-2} bar
Stress step $5 \leq M < 6$ earthquakes§	ΔS_5	8x10^{-2} bar
Stress step $M \geq 6$ earthquakes§	ΔS_6	0.23 bar

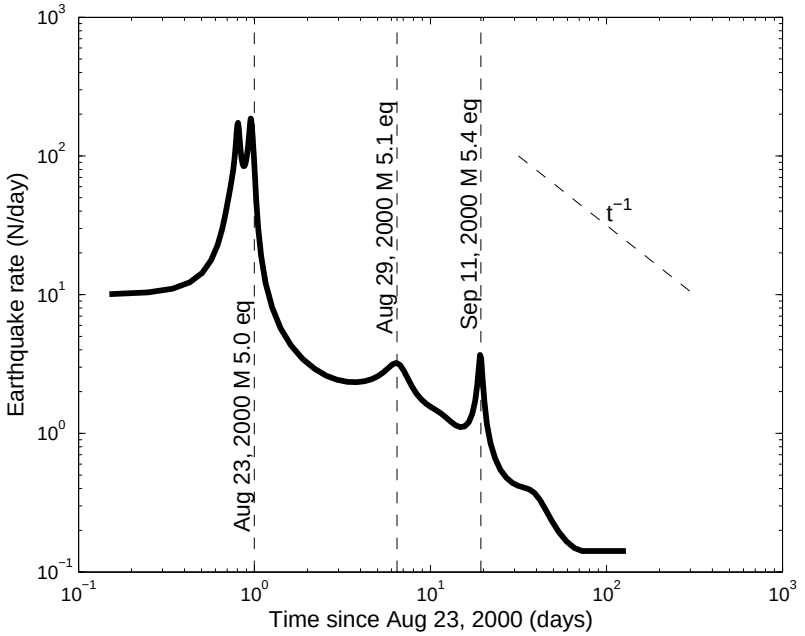

Figure 4.7: Relaxation of the 2000 Izu swarm: seismicity rate versus time following the last change point, i.e. t_3 = August 23, 2000. Vertical dashed lines are the three largest magnitude events, the reference for slope indicate an exponent 1 of temporal decay.

of a single earthquake, or after a decrease in the stressing rate acting on the system (i.e. the end of a silent slip event, or of a finite duration dyke intrusion), the resulting seismicity rate follows an Omori-like decay over time.

4.4 The forcing rate as a tool to estimate the background seismicity in a point process

4.4.1 Overview

Statistical studies of earthquake occurrence in time usually represent earthquake sources as point events. According to the characteristics of temporal clustering in an earthquake catalog, clusters are classified as (foreshock-)mainshock-aftershock sequences and earthquake swarms [e.g. *Mogi*, 1963; *Utsu*, 1970, 2002]. The temporal characteristics of these latter, however, are less understood and locally variable when described by daily or hourly earthquake frequencies [e.g. *Matsuúra and Karakama*, 2005]. Generally an earthquake swarm is defined as a cluster of earthquakes in which there is no predominantly large single earthquake, or as a sequence of earthquakes characterized by a lack of clear mainshock-aftershock signatures in space and time. *Vidale and Shearer* [2006] assert that swarm-like sequences mark the site of an underlying geophysical disturbance that changes the local risk for earthquakes. Most swarms occurring in volcanic areas accompany dyke intrusions [e.g. *Toda et al.*, 2002; *Aloisi et al.*, 2006; *Peltier et al.*, 2007; *Traversa and Grasso*, 2009-Chapter2], or are related to hydrothermal fluid movements [e.g. *Saccorotti et al.*, 2002; *Matsuúra and Karakama*, 2005]. In these cases, the patterns described above reflect the contribution of fluid activity at depth in addition to that of earthquake interaction [e.g. *Utsu*, 2002; *Lombardi et al.*, 2006; *Hainzl and Ogata*, 2005; *Traversa and Grasso*, 2010-Chapter6].

With the aim of shedding light on the earthquake triggering process, the statistics of seismic occurrence have been investigated through point-process analysis techniques. Among the proposed models are the trigger model [*Vere-Jones and Davies*, 1966; *Vere-Jones*, 1970; *Utsu*, 1972a,b; *Hawkes and Adamopoulos*, 1973], a generalized Poisson process [*Shlien and Nafi Toksoz*, 1970; *Bottari and Neri*, 1983; *De Natale and Zollo*, 1986], a form of branching process [*Kagan and Knopoff*, 1981, 1987], and the ETAS (Epidemic Type Aftershock Sequence) model [*Ogata*, 1988, 1992, 1999].

The ETAS model has universally been accepted as the null hypothesis in describing the statistics of seismic occurrence. It is a self-exciting model in which the seismicity rate is described, on time by the superposition of a background uncorrelated activity of constant occurrence rate λ_0 (modeled as a stationary Poisson process), and the cascade of aftershocks induced by earthquake interactions. The total occurrence rate is given by the sum of the background rate λ_0 plus the aftershocks induced by all preceding earthquakes, as follows:

$$\lambda(t) = \lambda_0 + \sum_{i:\, t_i<t} \lambda_i(t). \tag{4.10}$$

The cascade of correlated events, resulting from earthquake interactions, is governed by the modified Omori's law [*Utsu*, 1961], combined with the Gutenberg-Richter relation [see e.g. *Ogata*, 1988, 1999; *Helmstetter and Sornette*, 2002a; *Saichev and Sornette*, 2007]. In this model, the rate of aftershocks induced by an earthquake of magnitude M_i that occurred at time t_i is given by

$$\lambda_i(t) = \frac{K}{(c + t - t_i)^p}\ 10^{\alpha(M_i - M_c)}, \tag{4.11}$$

where K is the aftershock productivity, α defines the relation between the triggering capability and the magnitude of the triggering event, c takes into account the incompleteness of the catalog at early times following the triggering event [*Utsu*, 2002; *Helmstetter et al.*, 2003b; *Kagan*, 2004], p is the "local" Omori law exponent, controlling the temporal decay of events triggered by a previous earthquake, M_c is the completeness magnitude of the catalog. In the ETAS model, the parameters K_0, α, c, and p are constant.

The background rate λ_0, is usually assumed to result from stress accumulation due to tectonic plate motion at tectonic environments or, more generally, from stress perturbations induced by an external active forcing. In this sense, in volcanic contexts, the background uncorrelated events are driven by volcano processes, while the triggered events are noise that prevents a direct mapping of seismicity rate onto the mass transfer within the volcano.

Due to the direct relationship between the external process driving the seismicity and the rate of background events, many researchers have found attractive the possibility to separate and quantify the amount of background uncorrelated activity from the one that depends on earthquake interactions. These attempts have given birth to a series of declustering techniques, initially based on space-time window criteria [e.g. *Reasenberg*, 1985; *Frohlich and Davis*, 1990; *Davis and Frohlich*, 1991], then on determining the probability that a given earthquake triggered another given earthquake [*Zhuang et al.*, 2002],

on interevent time distributions [*Molchan*, 2005; *Hainzl et al.*, 2006], on variability coefficient [*Bottiglieri et al.*, 2009] and on the estimations of the a-priori-model-independent probability of directly and indirectly triggered aftershocks [*Marsan and Lengliné*, 2008].

When applied to the 2000 Izu Islands seismic swarm, however, none of these techniques demonstrate to be appropriate for quantifying the amount of background seismicity. This may be related to two main reasons. On one hand, the seismicity rate triggered by the dyke intrusion is about three orders of magnitude (between about 900- and 3000-fold in the third and first regime, respectively) larger than the steady state seismicity rate (table 4.1). It has been demonstrated that this fact, combined with an unvaried detection resolution of the recording system, alter the distribution of interevent times and prevent for quantifying the two different contributions of seismicity [*Traversa and Grasso*, 2010-Chapter6]. Such an increase of the seismicity rate makes the time separating two background events to reduce to the order of the time separating events within a correlated sequence. This leads to the overlapping of different aftershock sequences, such that the overall time series is apparently constituted by uncorrelated seismicity. The gamma distribution that describes the interevent time distribution for ordinary seismic sequences tends in this case to an exponential law. Besides, since the resolution of the recording system has remained unvaried, such distribution is truncated for short interevent times, which leads to a hybrid shape that prevents any quantification of the two types of seismicity through the technique proposed by *Molchan* [2005] and *Hainzl et al.* [2006]. On the other hand, all mentioned techniques rely on the hypothesis of a stationary background earthquake occurrence in time, which is not verified for the 2000 Izu Islands seismic swarm case, as demonstrated by the three different forcing regimes found in the previous section through the rate and state formulation, and by *Lombardi et al.* [2006]. Inverting an ETAS model with both, background seismicity rate and Omori's law exponent p varying over 5-day-time windows, *Lombardi et al.* [2006] quantifies the background fraction of about 10% of the observed seismicity rate. As mentioned in the introduction, however, the reliability of ETAS model inversions is a debated matter within the scientific community due to non-uniqueness of solution and instability of the inversion itself.

Combination of these two issues prevents from calculating the background uncorrelated amount of seismicity even when applying declustering techniques on running time-windows over the time series (see section Perspectives at the end of the chapter).

4.4.2 From stressing rate to the dyke-induced seismicity

As we mentioned before, for the 2000 Izu Island swarm case, we cannot quantify the uncorrelated and the correlated parts of seismicity. In the following we therefore leave this distinction between uncorrelated background seismicity and correlated events aside, and we estimate the amount of seismicity that is directly induced by the dyke forcing.

We assume that the stressing rate changes we estimated in the previous section through the rate and state formulation directly trigger the dyke-induced seismicity. These dyke-induced earthquakes are "purified" from earthquake interaction events, which are in contrast triggered by the stress steps generated by the stress steps generated by occurrence of single events. This allows us to compute a rough value for the dyke-induced seismicity rate in each regime, where the stressing rate (and therefore the background seismicity rate) is assumed to be stationary over the time interval. Figure 4.8 illustrates the observed seismicity versus the events directly related to the dyke intrusion. We estimate the global average dyke-induced seismicity fraction at about 30% of the observed seismicity.

As shown in figure 4.9, the power law relaxation of the system is indeed mainly driven by the vanishing of the dyke-induced stressing rate. All these suggest it exists a sort of analogy between the dyke intrusion, interpreted as a "slow earthquake", or "silent slip" and a "classic" tectonic earthquake. In the latter case the earthquake induces an instantaneous stress step on the system, which has a transient effect on the generation of seismicity, i.e. it generates aftershocks following the first event. For the long lasting event, as the Izu case, the system is continuously fed by a persistent external forcing, and therefore continuously generates seismicity. This continues even if the forcing is gradually decreasing, which creates a sort of damped system in which the seismicity rate progressively decreases, linearly with the forcing rate. As soon as the forcing completely vanishes, the system relaxes itself according to a "classic" Omori-style decay.

4.5 The effect of a long duration forcing on a system

4.5.1 Dyke model and seismic productivity

Among the dyke models proposed for the 2000 Izu Islands magma intrusion available in literature we use the one that best fit the locations of the seismic events, i.e. the model proposed by *Ozawa et al.* [2004], composed by two tensile segments, as illustrated in figure

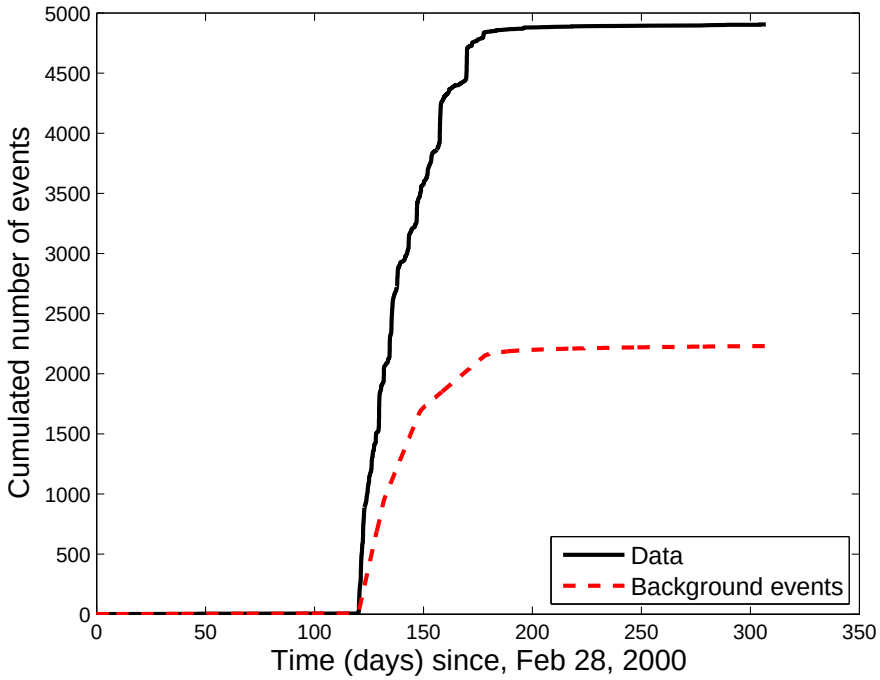

Figure 4.8: 2000 Izu Islands volcano-induced seismic swarm. Black solid line: cumulative number of observed earthquakes; red dashed line: cumulative number of dyke-induced events computed as the events directly triggered by the stressing rate induced by the intruding dyke on the system in a rate and state friction model [*Deterich*, 1994].

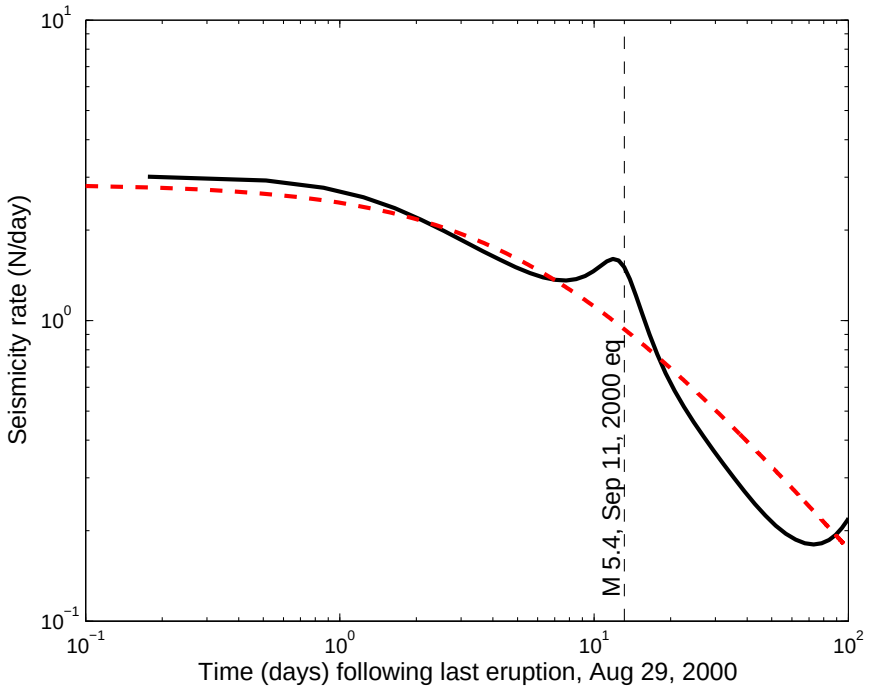

Figure 4.9: 2000 Izu Islands volcano-induced seismic swarm. Black solid line: seismicity rate following the vanish of dyke intrusion versus time; red dashed line: dyke forcing-induced seismicity rate, computed as the rate of events directly triggered by the stressing rate induced by the intruding dyke on the system in a rate and state friction model [*Deterich*, 1994]. Origin of time coincide with the last eruption (August 29, 2000).

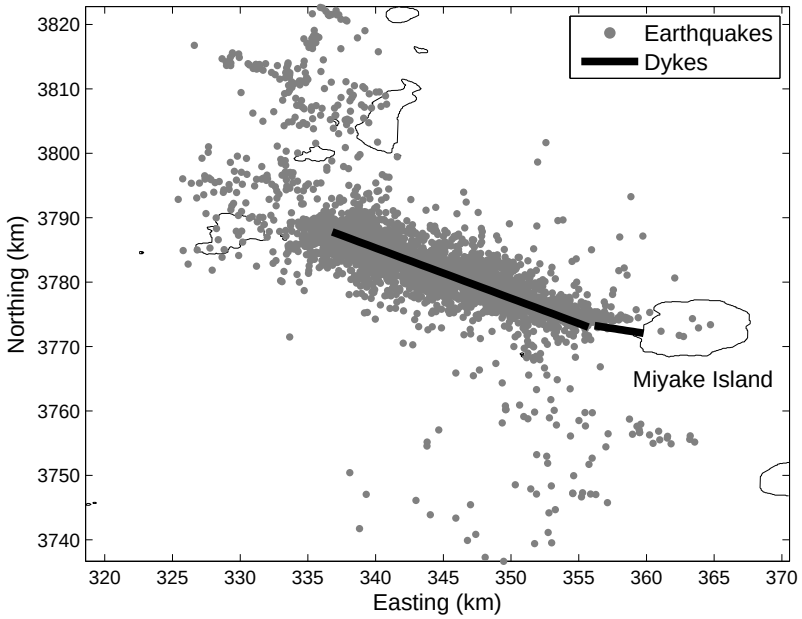

Figure 4.10: Map illustrating the dyke model used in this paper [proposed by *Ozawa et al.*, 2004] and the location of the recorded seismicity.

4.10. Dyke geometry parameters are listed in table 4.2.

As already mentioned in section 4.1, the magmatic intrusion include two different phases: a first propagation phase lasting about a week, followed by an extension phase which lasts ~ 50 days.

Assuming 1 m extension for the two tensile faults constituting the dyke at the end of the propagation period (i.e. June 26 to July 1^{st}, 2000), the amount of deformation induced by the intruding magma is about 0.24 km^3, accompanied by a seismicity rate of 216.94 eqs d^{-1}. It implies a seismic rate of about 904 eqs d^{-1} km^{-3} for unit volume of crustal

Table 4.2: Dyke model geometry [*Ozawa et al.*, 2004]

	Latitude (deg)	Longitude (deg)	Depth (km)	Strike (deg)	Dip (deg)	Width (km)	Length (km)	Opening (m)
Tens. fault 1	34.090	139.441	1.1	108.0	89.0	4.5	3.8	12.4
Tens. fault 2	34.088	139.436	8.7	309.0	88.0	10.0	21.9	28.8

deformation. The final extension of the two tensile faults is 12.4 and 28.8 m, respectively (table 4.2). It implies a total deformation volume of about 6.51 km^3, accompanied by an earthquake rate of 64.3 eqs d^{-1}. The unitary seismicity rate accompanying the extension phase is about 10.9 eqs d^{-1} km^{-3} for unit volume of crustal deformation.

It implies a seismic productivity in the first phase nearly 2 orders of magnitude larger than in the second phase. It argues for the dyke to initially dispose of a higher energy that allows it to propagate through the crust. As time passes energy is consumed, until the dyke is not able any more to propagate, but still to extend normally to the dyke walls. Eventually all the energy is consumed and the intrusion stops. It further support the hypothesis of a progressive decrease of the magma flux over time, which accompanies the waning seismicity rate, as proposed by *Traversa et al.* [2010-Chapter3].

4.5.2 Spatio-temporal organization of the 2000 Izu Islands seismic swarm

In order to investigate the coupled temporal and spatial component for the 2000, Izu Islands seismic swarm, we first apply the algorithm proposed by *Dieterich et al.* [2000] based on the rate and state formulation in a spatio-temporal mesh. It allows us to compute the active forcing at nodes located at different distances from the dyke, and then to evaluate the characteristics of the seismicity on these bases.

Space and time dyke-related Coulomb stress changes driving the system

Maps of Coulomb stress changes over given time intervals are obtained by repeatedly solving equation (4.3) and (4.4) at nodes of a grid superimposed to the Izu Islands zone, following the algorithm proposed by *Dieterich et al.* [2000] for the Kilauea (Hawaii) case. The grid has regular node spacing of 0.5 km in both, easting and northern directions. Seismicity rates are obtained within cylindrical volumes between hypocentral depths of 2 and 24 km, centered on each node. Within each volume, characterized by a starting radius of 0.3 km, we require a minimum average seismicity rate of 0.7 $M \geq 3$ events per month in a given time interval. If the seismicity within the initial volume does not meet this criterion, the search radius around the node is increased by increments of 0.3 km until the condition on the minimum seismicity rate is reached or the maximum search radius of 3 km is exceeded. At 3 km radius, if the corresponding volume did not produce at least 0.7

earthquakes per month, Coulomb stress change is not computed.

Figure 4.11 shows a map of total Coulomb stress changes between the beginning and the end of the intrusion, with seismicity rates computed averaging over the two phases: dyke propagation (i.e. June 26 to July 1^{st} 2000), and dyke extension (i.e. July 2 to August 23, 2000). Figure 4.12 shows the time history of both, earthquake rate and stress at different nodes, moving progressively away from the dyke.

Seismicity distribution as function of the distance from the dyke

In this section we investigate how seismicity patterns vary with distance from the dyke. Figure 4.13 illustrates variations of seismicity rate normal to the near-vertical tensile faults composing the dyke (reference model from *Ozawa et al.* [2004], illustrated in figure 4.10). Due to the verticality of the dyke walls (table 4.2), we only use the dyke normal distance $|x|$ as independent variable, ignoring bilateral asymmetry in seismicity [e.g. *Powers and Jordan*, 2009].

Distribution patterns for seismicity rates normal to near-vertical strike slip faults in California have been related to stress heterogeneity, damage zones, and degree of seismic coupling [*Powers and Jordan*, 2009]. In particular, clustered events in Southern California decay more rapidly (exponent ~ 1.50) than independent events (exponent $sim1$) [*Powers and Jordan*, 2009]. At a global level, using the Harvard centroid catalog (CMT), *Huc and Main* [2003] find a power law distribution of triggered events as function of the distance from the mainshock in the near field, with an exponential tail in the far field (i.e. $r/L \gg 1$, where L is the rupture length). Since such correlation distributions are also found in critical point phenomena [*Hergarten and Neugebauer*, 2002], *Huc and Main* [2003] suggest that a reason for earthquake triggering is that, at global scale, the crust is already in a near critical state. Similar thesis has been proposed for the generation of VT seismicity on Piton de la Fournaise volcano by *Grasso and Bachelery* [1995] on scale-invariance arguments.

As shown in figure 4.13, the dyke-normal distribution of seismicity has a flat peak within few hundred meters from the dyke, and then decays according to a power law with exponent of about 2 up to normal dyke distances of about $x_{max} \sim 10$ km (figure 4.13). [*Powers and Jordan*, 2009] suggest the width of the seismic scaling region $x_{max} \sim 10$ km is related to fault interaction distances [*Powers and Jordan*, 2009], while the scaling region $|x| < x_{max}$ decay is related to self-affine fault heterogeneity. *Huc and Main* [2003] find a correlation length x_{max} of order 10-20 km for moderate and large events of the CMT

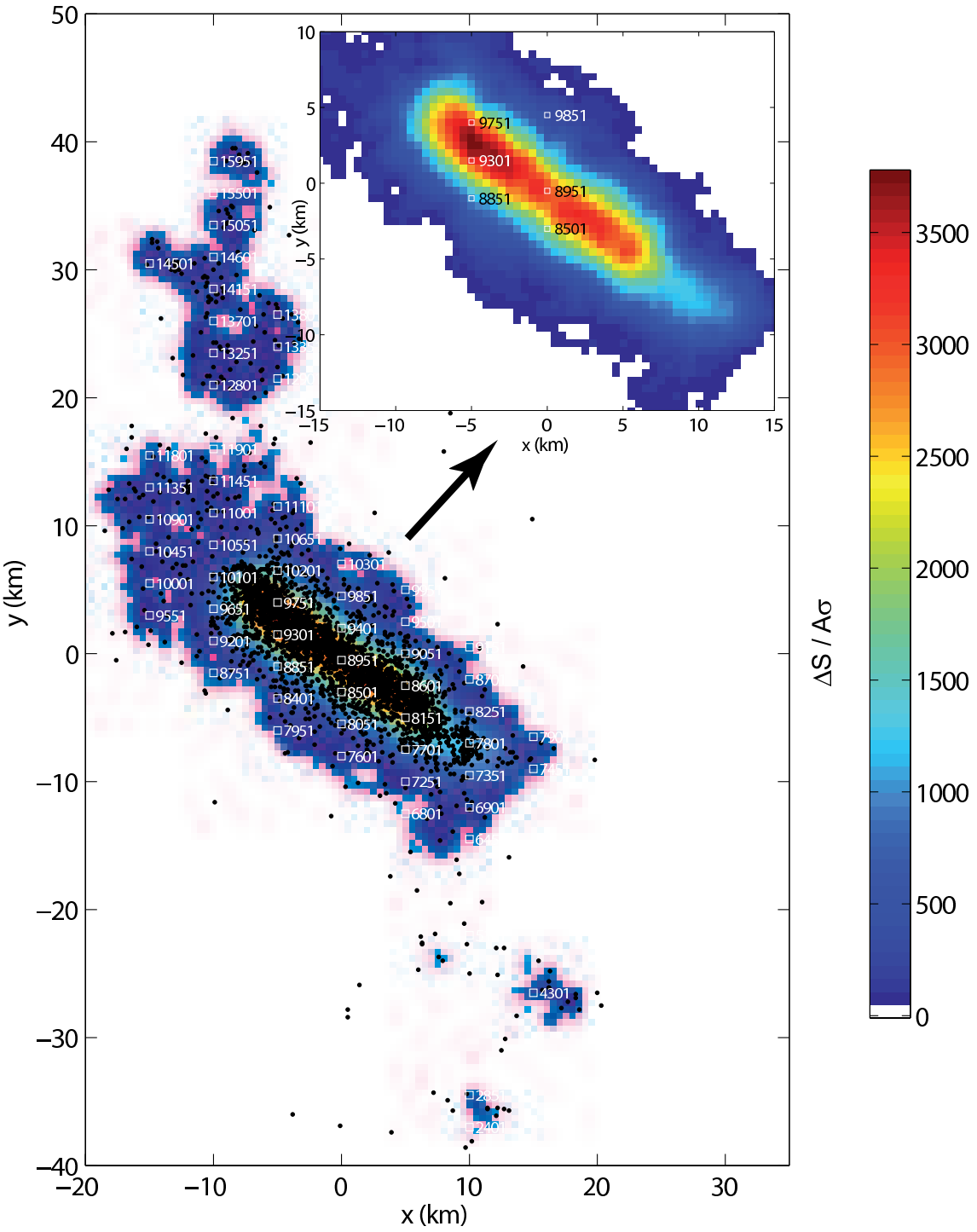

Figure 4.11: Map of Coulomb stress changes induced by the 2000 Izu Islands dyke intrusion. Color is related to the stress change value computed in each node normalized by $A\sigma$ parameter; Black dots indicate the earthquake locations.

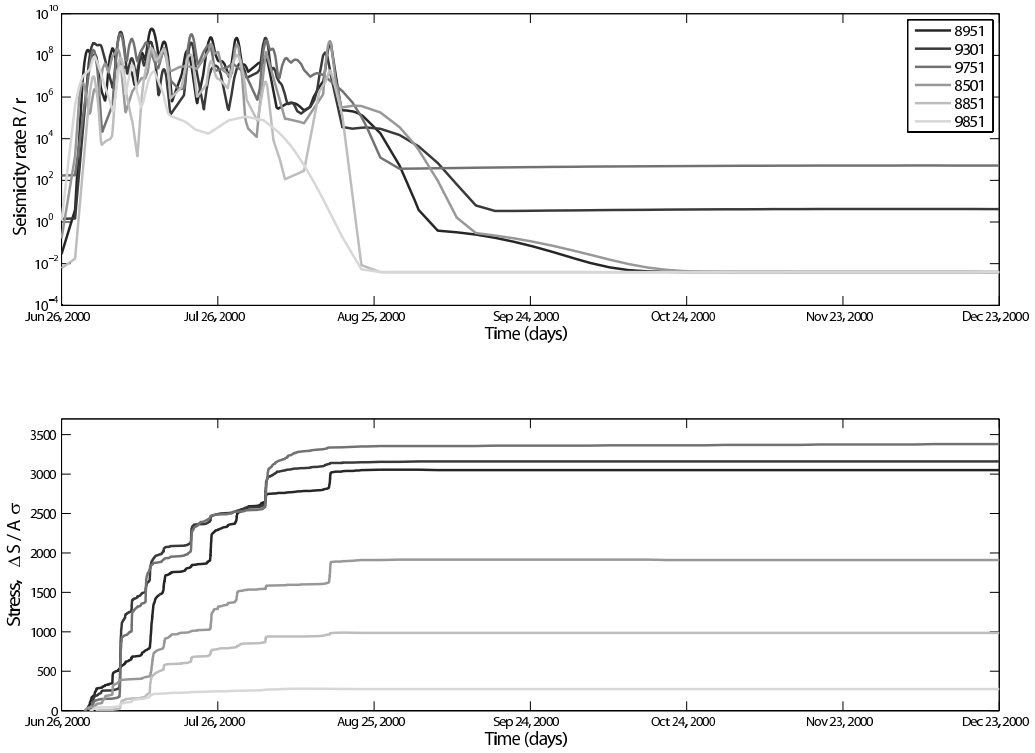

Figure 4.12: Time history of seismicity rate (top) and stress (bottom) computed at different nodes. Node number in the legend refers to figure 4.11. Different gray level is used for each computation node, where the gray scale is related to the distance of the node from the dyke.

catalog. The lack of dependence of such correlation length on the magnitude of the trigger event makes the authors suggest that the range within which triggered events may occur has a priori structural constraints.

The power law exponent of the seismic intensity decay with fault-normal distance and the extent of the "damage zone" are found to correlate with the vertical structure of the fault zone and particularly with the geothermal gradient [*Powers and Jordan*, 2009]. Following the results of *Powers and Jordan* [2009], the rapid decay of earthquakes with distance from the dyke may be indicative of an aftershock dominated seismic sequence for the 2000 Izu swarm. This recalls the value of about 70% of earthquake interaction induced activity we computed in section 4.3 for the Izu case.

The flat intensity distribution of seismicity up to few hundred meters near the fault is thought to correspond to a volumetric damage-zone where small-scale stress heterogeneity is attenuated by low rock strength [e.g. *Powers and Jordan*, 2009]. In our case this sort of characteristic length (if any) could be related to a higher ductility of crust materials in the proximity of the hot melt. The existence of such characteristic length should be tested on a relocated catalog of seismicity since its value is within the location error for 2000 Izu earthquakes (1 km in average [JMA catalog]).

Contrary to California near-vertical strike slip faults, the power law decay of seismic intensity with distance from the dyke for the 2000 Izu swarm case does not merge into the background. This is due to the extraordinary high seismicity rate characterizing the swarm against the very weak steady-state seismicity of the zone (between 46 and 164 ev d^{-1} [table 4.1] and 0.05 ev d^{-1} [*Toda et al.*, 2002], respectively).

By using two-dimensional rate and state simulations of seismicity, *Dieterich and Smith* [2006] compute fault-normal stress intensity from a given stress loading. This generates near fault stress heterogeneities with power law size distribution, and a power law decay in seismicity that satisfies the following equation:

$$\nu \sim |x|^{-D} \tag{4.12}$$

where ν is the seismic intensity, x is distance from the fault, and $D = 2 - H$ is the fractal dimension of the along-strike profile. The power law decay with distance from the dyke axis we observe for Izu seismicity satisfies equation (4.12). If the 2D approximation applies to our case, therefore, the power law exponent of the seismic decay with distance from the dyke implies $D \sim 2$ and $H \sim 0$. H has been related to the fault surface roughness [*Sagy*

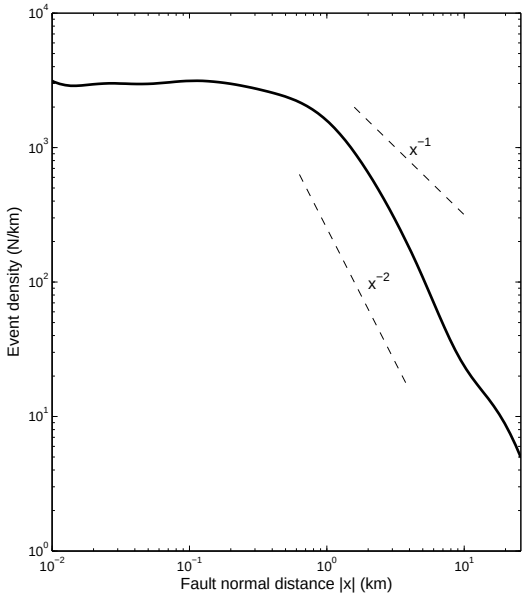

Figure 4.13: Earthquake density distribution as function of the the normal distance to the dyke during the 2000 Izu islands intrusion-induced seismic swarm.

et al., 2007], whose power spectrum would be, in the Izu case, pink noise-like.

Earthquake diffusion

A diffusely accepted model of aftershock triggering is related to static stress transfer and consequent increase of the Coulomb stress [*King et al.*, 1994; *Stein et al.*, 1994; *Stein*, 1999; *King and Cocco*, 2000; *Toda et al.*, 2002]. However, aftershocks also occur in regions of reduced static stress [e.g. *Parsons*, 2002], or at large distance from the mainshock [e.g. *Brodsky et al.*, 2000; *Gomberg et al.*, 2001]. Recent works have therefore suggested that also dynamic stresses related to seismic waves play a role in aftershock triggering [e.g. *Brodsky et al.*, 2000; *Gomberg et al.*, 2003; *Johnson and Jia*, 2005].

Using the 1984-2002 Southern California catalog, *Felzer and Brodsky* [2006] show that for short times after the mainshock, the aftershock decay is well fitted by a single inverse power law (with exponent about 1.4) over distances r in the range 0.5-50 km. They deduce that the same triggering mechanism is working over the entire range of distances. They show that static stress changes at the more distant aftershock locations are negligible, and that the aftershock decay has no discontinuity between closer and further locations from

the mainshock, so that dynamic triggering is considered the best candidate for triggering all the aftershocks. Since maximum amplitude of seismic waves decays somewhat faster than $1/r$ [*Campbell*, 2003], *Felzer and Brodsky* [2006] argue that the probability for triggering an aftershock is directly proportional to the amplitude of seismic shaking. If this is true, the ~ 2 exponent of the inverse power law decay of earthquake dyke-normal distances we found above (figure 4.13), would indicate that the most probable triggering mechanism for the observed seismicity is static stress transfer, which is thought to decay as $\sim 1/r^3$ in the far field.

On the other hand, no linear relationship has been found between seismicity rate and either, stresses or seismic wave amplitude. A relationship has been found instead between the stress change dS and the time to failure t_c of an induced earthquake, as follows [e.g. *Das and Scholz*, 1981; *Deterich*, 1994; *Lee and Sornette*, 2000]:

$$t_c \sim dS^{-n}, \tag{4.13}$$

where n is the stress corrosion index. The relation between aftershock and stress decay over space may therefore be more complex.

Equation (4.13), coupled with the fact that static stress decreases with distance according to $r^{-1/2}$ in the near field, suggests that the distance R of aftershocks occurring at time t after the mainshock increases as [*Huc and Main*, 2003]:

$$R(t) = t^{2/n} \tag{4.14}$$

Migration of aftershocks with time has been indeed observed, i.e. the so-called "aftershock diffusion" [e.g. *Mogi*, 1968; *Tajima and Kanamori*, 1985a,b; *Noir et al.*, 1997; *Jacques et al.*, 1999; *Marsan et al.*, 2000]. Aftershock zone is thus sometimes observed to move away from around mainshock rupture plane immediately after mainshock occurrence, at velocities in the range 1 km h^{-1} to 1 km yr^{-1} [*Jacques et al.*, 1999].

Diffusion of aftershocks is usually interpreted as a diffusion of the stress induced by the mainshock [see *Helmstetter et al.*, 2003b, and references therein]. However, *Helmstetter et al.* [2003b] point out that no stress diffusion process is necessary to explain aftershock diffusion. Aftershock diffusion is predicted by any model that assumes that (i) the time to failure increases as the applied stress decreases, and (ii) the stress change induced by the mainshock decreases with the distance from the mainshock [*Helmstetter et al.*, 2003b]. Consequently, aftershocks further away form the mainshock occur later than those closer to the mainshock [*Helmstetter et al.*, 2003b].

Multiple triggering process is therefore sufficient to explain aftershock diffusion, as demonstrated by *Helmstetter et al.* [2003b]. Accordingly, the distribution of distances between triggering and triggered earthquakes is assumed independent of time, and the increase of the characteristic size R of the aftershock cloud as function of time can be explained through the cascading process reproduced by ETAS model under the right conditions [*Helmstetter et al.*, 2003b]. The result obeys the diffusion equation:

$$R(t) \sim t^H. \tag{4.15}$$

where H is the diffusion exponent (equal to 0.5 for a normal diffusion process, i.e. similar to heat diffusion), and is function of both, the Omori law exponent p, and the exponents μ describing the spatial interaction between events.

We test for earthquake diffusion with respect to the dyke axis as function of the time. Diffusion can only be observed during the dyke opening phase, arguing for the hypocenter diffusion to be either, a product of the dyke injection from Miyakejima magma reservoir (June 26 to July 8, 2000), or the evolution of earthquake location as the dyke opens. The exponent of earthquake diffusion is slightly larger for earthquakes located on the west than for those located on the east of the dyke (figure 4.14). The $H \sim 0.3$ value found for the diffusion exponent is indicative of a slower, sub-diffusive process which cannot be explained by visco-elastic relaxation of the crust [*Marsan et al.*, 2000].

Temporal decay of seismic density with distance from the dyke

In "classic" tectonic seismicity, aftershocks are defined by their clustering properties both, in space and time. As discussed in section 4.4.4, the temporal clustering obeys the well established (modified) Omori law [*Omori*, 1894; *Utsu et al.*, 1995], according to which, the rate of aftershocks following a mainshock a time t_0 decays as:

$$\lambda(t) = \frac{A}{(t - t_0 + c)^p} \tag{4.16}$$

where the Omori exponent p is found in the range 0.5-2 and the offset time c accounts for the catalog incompleteness close to the mainshock [e.g. *Utsu*, 2002; *Helmstetter et al.*, 2003b; *Kagan*, 2004].

Spatial organization of aftershocks is more complex and less understood. Aftershocks occurring close to the mainshock rupture are thought to reflect local stress concentrations

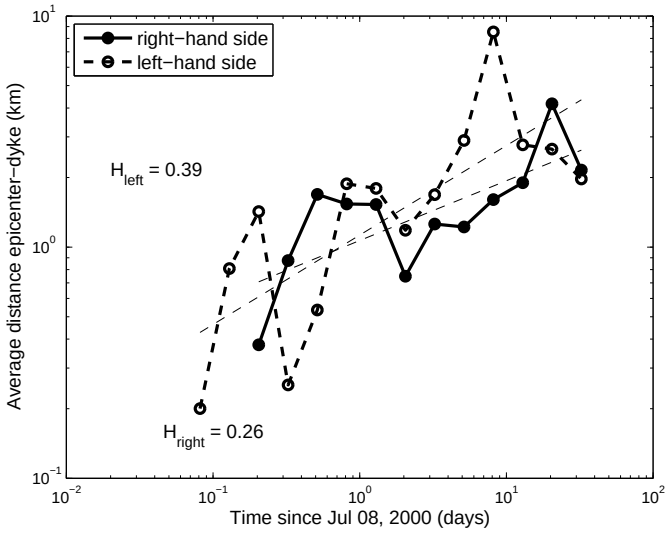

Figure 4.14: Average distance between earthquakes and dyke axis as function of the time since July 8, 2000. Distance increases as $R \sim t^H$, with $H = 0.26$ towards the east, and $H = 0.39$ towards the west.

at asperities that impede the rupture propagation [*Helmstetter et al.*, 2003b]. On the other hand, aftershocks also occurs further away from the fault rupture, due to various proposed triggering mechanisms [e.g. *Harris*, 1998; *Hill et al.*, 2002; *Freed*, 2005; *Helmstetter et al.*, 2005; *Steacy et al.*, 2005].

In order to investigate the evolution of the seismic swarm in space and time, we look at temporal patterns of the dyke-induced seismicity as function of the distance from the dyke (for classes of distance defined in figure 4.15). As shown in figure 4.16, the interevent time distribution of seismic events accompanying the dyke tends to a "classical" gamma distribution when moving away from the dyke axis. It allows to compute the background uncorrelated fraction of seismicity through the technique proposed by *Molchan* [2005] and *Hainzl et al.* [2006]. Departures from this "classic" distribution for tectonic seismicity are significant for small distances from the dyke. Moreover, the exponent of the small-to-medium scale interevent time distribution tends to decrease as getting away from the forcing (figure 4.17).

If we consider the dyke injection as a virtual mainshock, this would imply a larger Omori law p-exponent close to the dyke axis and smaller as moving away from it. A decrease in the Omori's law p-value with distance from the mainshock is also predicted

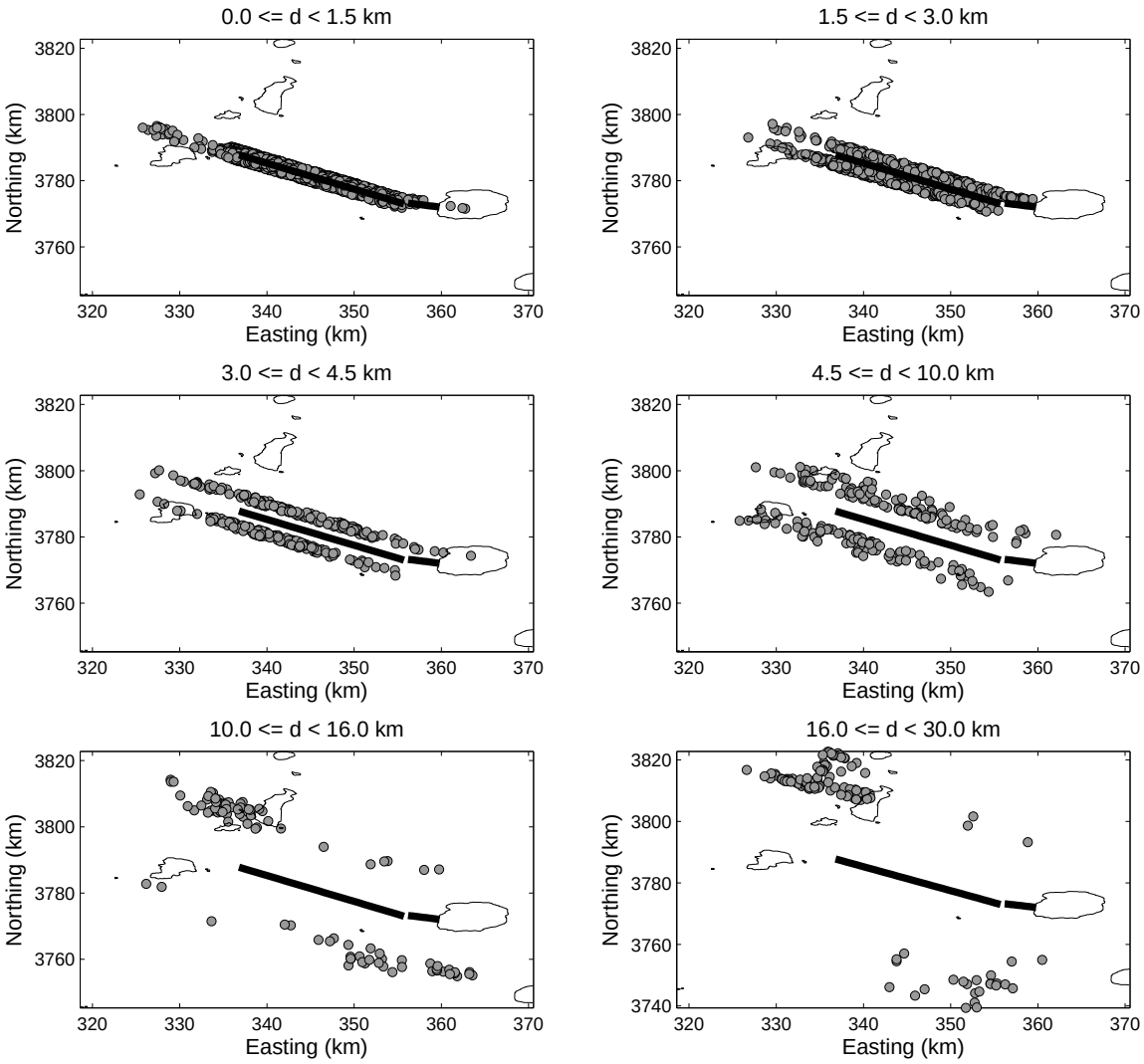

Figure 4.15: Spatio-temporal characteristics of the 2000 Izu islands dyke-induced seismic swarm. Maps of seismic event locations grouped in classes of distance from the dyke.

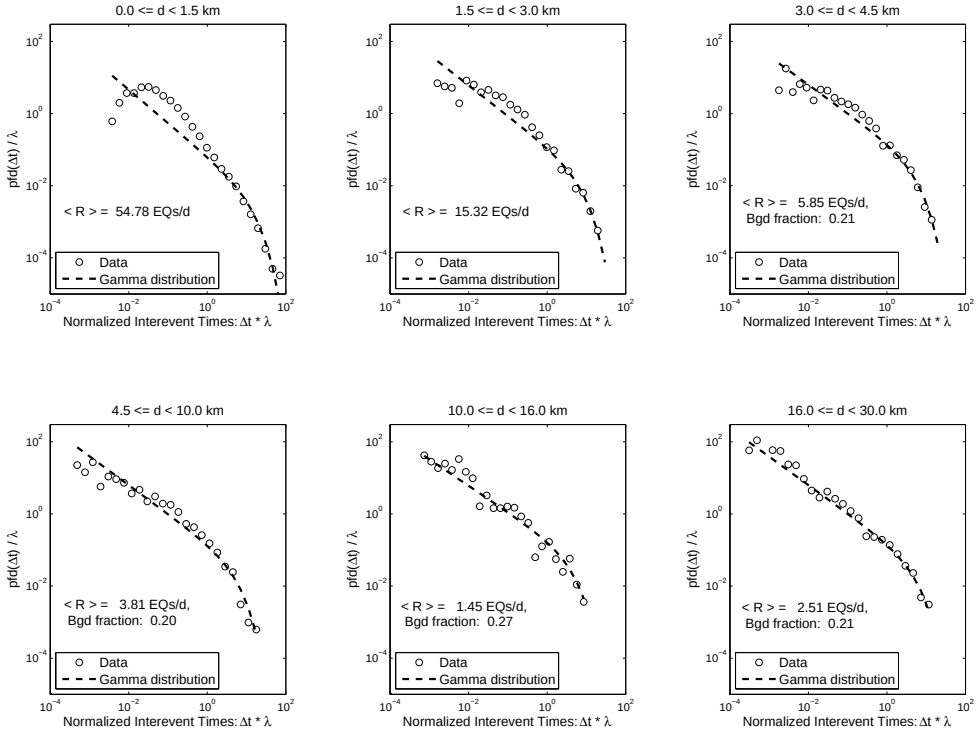

Figure 4.16: Interevent time distributions of dyke-induced earthquakes (black empty circles) and corresponding gamma distribution best fits (black dashed line). Each sub-graph refers to the distance-to-dyke classes defined in figure 4.15. When possible (i.e. the gamma distribution acceptably fits the data), the fraction of background uncorrelated events is computed using the technique proposed by *Molchan* [2005] and *Hainzl et al.* [2006].

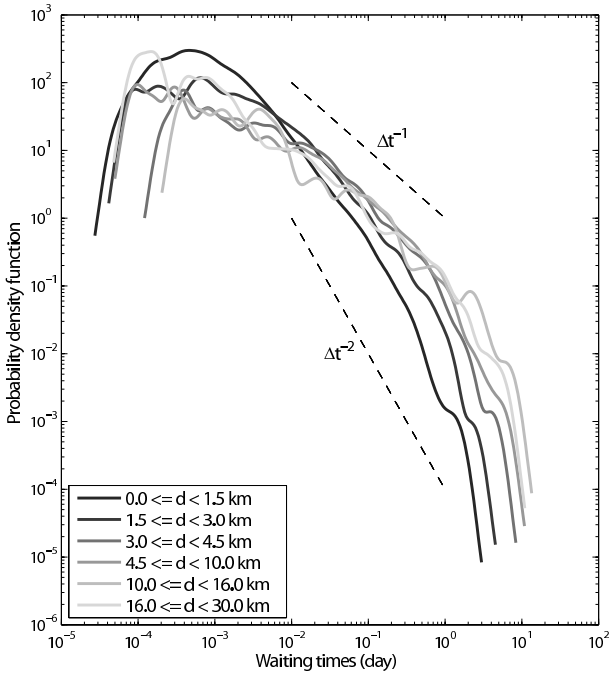

Figure 4.17: Interevent time distributions of dyke-induced earthquakes. Gray scale refers to the considered class of distance.

by the ETAS model when simulating the spatial organization of aftershocks following a tectonic mainshock [*Helmstetter and Sornette*, 2002a; *Helmstetter et al.*, 2003b]. Further, it suggests the validity of the proposed dependence of parameter p on the crust temperature [*Mogi*, 1968; *Klein et al.*, 2006; *Ojala et al.*, 2004].

4.6 Discussion and conclusions

We analyze the seismic sequence that accompanied the 2000 dyke intrusion from Miyakejima volcano (Izu islands, Japan). The sequence is composed by about 5000 $M_V \geq M_c = 3$ earthquakes occurring between June 26 and the end of August, 2000.

The dyke intrusion driving the observed seismicity first rises vertically under Miyakejima volcano (few hours on June 26), then moves laterally, first westwards, then northwestwards during about 1 week, covering a total distance of about 30 km (June 26 to July 1^{st}). Finally the two segments constituting the dyke extend during about 50 days (July 2 to end of August).

During the propagation phase the recorded seismicity migrates to the west and to

the northwest tracking the dyke tip position over time, while during the extension phase, hypocenters move back and forth along the existing fracture and develops southern and northern lobes. Strike slip earthquake focal mechanisms suggest that the response of the rock matrix to the magma intrusion organizes initially along near-tip, and later along further, pre-existing or not, shear faults [*Rubin and Gillard*, 1998].

During the propagation and initial extension of the dyke walls (i.e. the June 26 - July 8 2000 period), the dyke is fed from the magma reservoir beneath Miyakejima volcano. The contemporary seismicity rate is stationary over time. It suggests a constant flow rate of magma withdrawn from the magma chamber over time [*Traversa et al.*, 2010-Chapter3]. Subsequently (July 8 - August 23, 2000), the seismicity rate progressively decreases, suggesting the magma flux injected into the extending dyke from both, the Miyake reservoir and the additional sub-crustal magma pockets nearby Kosushima is waning.

Seismic productivity during the first propagating phase is larger than during the following extending phase. It suggests the system needs less energy to extend the existing fracture against the country rocks than to propagate a mode I crack.

This extraordinary seismic sequence contemporary to the dyke intrusion shows typical swarm-like patterns according to the *Vidale and Shearer* [2006] classification, such as e.g. the presence of intervals of steady seismicity rate, or the tendency of the largest events to occur later in the sequence. The authors propose the pore fluid pressure fluctuation as the most likely mechanism driving this kind of no-clear-mainshock-aftershock-pattern-seismic-sequences.

By assuming a simple Coulomb stress transfer model for earthquakes with a rate- and state-dependent friction, however, we demonstrate that these characteristics may just be the result of the 60-day-long forcing, which continues feeding the system and prevents it from relaxing until the forcing itself fades away. We reproduce the observed seismicity modeling the dyke intrusion as a non-stationary "silent slip" event, in which the intruding dyke induces an evolving stressing rate change that drives the seismicity. This suggests that the 2000 Izu islands dyke-induced swarm is primarily driven by the magma breaking and pushing apart the host rock. This first generation seismicity is however able to trigger second and further generations earthquakes. This allows us to roughly separate seismicity related to earthquake interactions from the part that is directly triggered by the magmatic process (i.e. the background activity), quantified at about 70 and 30%, respectively. Rough estimates of these two types of seismic events for tectonic seismicity indicate a $30\% - 90\%$

of tectonic earthquakes to be aftershocks [e.g. *Helmstetter and Sornette*, 2003].

Since the driver is however continuously active, the cascade of aftershocks decaying with time according to the Omori's law is inhibited by a continuously fed background activity. The end of the intrusion, i.e. the vanishing of the forcing, is followed by a clear earthquake rate decay similar to the Omori's aftershock decay following a given mainshock for "ordinary" tectonic seismicity. By assimilating the intruding dyke to a "silent 60-days lasting mainshock", we study the spatio-temporal characteristics of the induced seismicity. Computations of static stress changes on a spatial grid confirm that the seismicity is primarily generated by static stress transfer. Distributions of seismic intensity as function of the dyke normal distance show a flat peak within few hundred meters from the dyke axis and then a scaling region with exponent about 2 extending to distances up to about ten kilometers from the dyke (figure 4.13). It argues for a fractal organization of faults on which slips occur, and for fault roughness power spectral density of pink noise-like surfaces (Husdorff exponent $H = 0$) [e.g. *Hergarten and Neugebauer*, 2002; *Sagy et al.*, 2007; *Powers and Jordan*, 2009]. Such $D \sim 2$ value for the fractal correlation dimension of earthquake hypocenters for earthquakes with respect to the dyke (for distances in the range few hundred meters to 10 km, figure 4.13) is similar to that found by *Helmstetter et al.* [2005] for Southern California seismicity. This value is also close to the $D = 2\alpha$ (with α defined in equation (4.11) and relating the number of aftershocks triggered by a mainshock of a given magnitude [*Helmstetter*, 2003]) predicted by assuming that earthquake triggering is due to static stress [*Helmstetter et al.*, 2005]. It further argues for the triggering mechanism of the 2000 Izu islands seismic swarm contemporary to dyke intrusion to be the static stress change induced by the very dyke fracturing and pushing apart the host rock.

We observe diffusion of earthquake hypocenters moving away from the dyke axis with time during the dyke opening phase (July 2 to August 23, 2000), with diffusion exponent of about 0.3 (figure 4.14). It suggests a sub-diffusive process.

Statistics of interevent times are analyzed as function of the distance from the dyke axis. To this purpose, different distance classes have been defined and, within each class, the interevent time distribution has been computed. From distances larger than about 5 km from the dyke, waiting time distributions are well fitted by a gamma law (figure 4.17), which is accepted to describe "classic" tectonic seismicity time patterns [e.g. *Molchan*, 2005; *Hainzl et al.*, 2006]. It allows to quantify the background fraction of seismicity at

between 20 and 30%, which are normal values for seismicity occurring at tectonic areas or during inter-eruptive phases of volcanic activity [*Traversa and Grasso*, 2010-Chapter6]. Interevent time distributions of earthquakes located at distances less than about 5 km show significant departures from the gamma law, preventing from quantifying the amount of uncorrelated versus correlated seismicity. This may simply be the consequence of the higher seismicity rate observed close to the dyke axis, coupled with a constant detection resolution of the recording network [*Traversa and Grasso*, 2010-Chapter6]. Interevent time distributions have larger exponents for short distances from the dyke axis, which implies larger Omori's law p-values for earthquakes located closer to the dyke [e.g. *Utsu et al.*, 1995; *Corral*, 2004a; *Lindman et al.*, 2005]. Such decreasing p-value with distance from the dyke can be interpreted in two distinct ways. On one hand the ETAS model predicts a faster aftershock decay closer in space to the mainshock due to the diffusion of aftershocks, which is a product of the cascading process that is triggering earthquakes [*Helmstetter and Sornette*, 2002b]. The dyke intrusion would therefore simply behave as a tectonic mainshock (though with finite duration) triggering its aftershocks. On the other hand, the p-exponent is found to positively correlate with crust temperature and faster stress relaxation [*Mogi*, 1962, 1967; *Kisslinger and Jones*, 1991; *Creamer and Kisslinger*, 1993; *Ojala et al.*, 2004; *Klein et al.*, 2006]. The larger p-value may therefore be just the effect of the warmer crust close to the intruding magma.

All these argues for the 2000 Izu islands dyke intrusion to induce a stress perturbation that, even if basically different in terms of both, duration of the stress perturbation and fracturing mode, has similar effects on induced seismicity as a tectonic mainshock. The intrusion acts in fact as a sort of "silent slip" event that induces a stressing rate change of about 60 day duration, while a mainshock is interpreted as an instantaneous stress step. The fact that the external forcing is applied during a finite time duration for the dyke case, results in a sort of "damped" system: the stressing rate which is triggering the seismicity progressively decreases, but continuously "feeds" the system all along the crisis. As a result, the seismicity rate progressively diminish, but the system cannot truly relax until the external forcing has vanished. Once the forcing acting on the system ceases, an Omori's style relaxation of seismicity is observed, analogous to the one we would observe following an instantaneous stress perturbation induced by a tectonic earthquake.

In conclusion, the 2000, 60-days lasting Izu intrusion may be seen as a slow down seismic source: the 0.5 km d^{-1} fracture propagation velocity is several orders of magnitude

smaller than rupture velocities measured for earthquakes (of the order of 2-3 km s^{-1} [e.g. *Hartzell et al.*] up to 5 km s^{-1} for supershear cases [e.g. *Bouchon and Karabulut*, 2008]). We thus have a close-sight of the fracture process features, which allows to resolve the mechanical evolution throughout the fracture propagation. In this framework, the seismicity accompanying the intrusion may just be the sum of all the brittle damage representing the rupture process itself. The power law relaxation following the arrest of the rupture propagation is then just the well known Omori's law following a rupture event.

Part II

Seismic Signature of Simple Volcano Processes

Chapter 5

Seismic Signature of Magma Reservoir Dynamics at Basaltic Volcanoes, lesson from the Piton de la Fournaise Volcano

Paola Traversa[1], Jean-Robert Grasso[1], Olivier Lengliné[2] and Valérie Ferrazzini[3]

[1] Laboratoire de Géophysique Interne et Tectonophysique,
CNRS - OSUG - Univeristé Joseph Fourier, BP 53 38041 Grenoble Cedex 9, France

[2] Laboratoire de Géophysique Interne et Tectonophysique,
CNRS - IRD - Université de Savoie, 73376 Le Bourget du Lac Cedex

[3] Institut de la Physique du Globe de Paris,
Observatoire Volcanologique du Piton de la Fournaise, La Pleine des Cafres, La Réunion, france

Paper published in *The VOLUME Project - VOLcanoes, Understanding Mass MovEments* (2009), edited by C. Bean, B. A.K., I. Lokmer, F. Martini, and G. OâĂŹBrien, pp. 271âĂŞ287, VOLUME Project EU PF6 (N. 018471) Consortium, Dublin.

Abstract

Herein we review varying time scales and patterns of Volcano Tectonic (VT) seismicity recorded at Piton de la Fournaise, Etna and Hawaiian volcanoes prior to eruptions. It is possible to isolate three phases describing the reservoir dynamics: (i) An exponentially accelerating VT seismicity rate is interpreted as the long-term (years) replenishment of the storage area. (ii) An average power law increase of the VT seismicity rate, 1-2 weeks before the eruption day, is identified as damage of the reservoir walls prior to the magma leak. (iii) During the ultimate phase (hours) before the eruption onset, the stationary rate of shallow VT events is associated with the dyke propagation. We compare the brittle damage during these three phases before eruptions and derive implications for the competing processes and relative scalings between quantities. These patterns are tested on different periods on the 1988-2006 Piton de la Fournaise (PdlF), Reunion, Indian Ocean, eruptive history. The results are used to constrain a generic model for basaltic volcano seismicity before eruptions. The components for such a model must include at least 3 phases, whose time-scales and seismicity rate span 5 and 2 orders of magnitude, respectively.

Résumé

Dans ce travail nous passons en revue les différentes échelles de temps et les motifs de sismicité Volcano Tectonique (VT) enregistrée aux volcans du Piton de la Fournaise, Etna et Hawaiiens avant une éruption. Il est possible d'isoler trois phases décrivant la dynamique du réservoir : (i) l'accélération exponentielle de sismicité VT est interprétée comme le remplissage à longue échelle (années) de l'aire de stockage. (ii) Une croissance moyenne en loi de puissance du taux de sismicité VT 1-2 semaines avant l'éruption est identifiée comme l'endommagement des parois du réservoir précédente la fuite de magma. (iii) Pendant la dernière phase (heures) avant le début de l'éruption, le taux stationnaire d'événements VT peu profonds est associé avec la propagation du dyke. Nous comparons l'endommagement pendant ces trois phases avant une éruption et nous en dérivons des implications concernant les échelles relatives entre les quantités et les processus en jeu. Ces motifs sont testés sur plusieurs périodes de l'histoire éruptive du Piton de la fournaise (PdlF, La Réunion) entre 1988 et 2006. Les réultats sont utilisés pour contraindre un modèle numérique de sismicité précédant les éruptions aux volcans basaltiques. Les composantes de ce modèle incluent au moins trois phases dont les échelles de temps et les

taux de sismicité couvrent 5 et 2 ordres de grandeur, respectivement.

5.1 Introduction

Processes within a volcano, eventually resulting in an eruption, are complex as attested by the failure of deterministic eruption predictions [e.g. *Sparks*, 2003; *Grasso and Zaliapin*, 2004]. Magmas undergo profound changes in physical properties during their ascent to the volcano surface. The pressures and temperatures vary during magma chamber evolution and ascent via dyke propagation.

Such pressure and temperature changes, which characterize active magmatic systems, interact with their surroundings, causing ground deformation, rock failure and other effects such as groundwater system disturbances and degassing. These processes and interactions are geophysically observable, and accompany mass movement within volcanoes. The coupling of highly non-linear dynamic processes leads to a wide range of observed behaviours. It is difficult to isolate each of the volcanic processes involved in eruption dynamics and to investigate each independent physical step leading to an eruption. In this paper we focus on tracking the seismicity and use this as a tool to help understand the "damage process" of the reservoir zone and magma flow in this region. Piton de la Fournaise (PdlF) volcano was used for this study; the PdlF database includes good quality seismic data since the 1980s.

The PdlF volcano is a basaltic intra-plate strato-volcano with a supply of magma from mantle hotspots. The frequency of the PdlF eruptions makes it one of the most active volcanoes in the world, with a period of particularly intense activity in recent decades [*Peltier et al.*, 2008], i.e. 7, 8 and 10 eruptions in the 1988-1992, 1998-2001, 2003-2005 periods, respectively (figure 5.1).

In this paper we compare different time-scales of seismic observations on PdlF volcano in order to identify the components and constraints that are necessary to build a generic model of seismicity triggered by reservoir dynamics for this volcano. According to some previous reports, these patterns may also apply to Hawaiian volcanoes and Mt Etna, Italy [e.g. *Chastin and Main*, 2003; *Klein*, 1984; *Lengliné et al.*, 2008; *Traversa and Grasso*, 2009-Chapter2], and therefore may help to constrain a generic model for seismicity before an eruption at basaltic volcanoes.

5.2 Brittle damage models for PdlF reservoirs dynamics, the State of the Art

Using seismicity rate, recent works on PdlF, isolate three possible phases describing the reservoir dynamics. First, an exponentially accelerating Volcano-Tectonic (VT) seismicity rate is interpreted as the long-term (years) replenishment of the storage area [*Lengliné et al.*, 2008]. Second, an average power law increase of the VT seismicity rate, 1-2 weeks before the eruption day, is identified as the damage of the reservoir walls prior to the magma leak that will drive the magma ascent towards the surface [*Collombet et al.*, 2003]. Third, during the ultimate phase (hours) before the eruption onset, the stationary rate of shallow VT events is associated with the dyke intrusion [*Traversa and Grasso*, 2009-Chapter2]. Note that this last seismicity rate is 2-3 orders of magnitude larger than during the two previous phases. During all phases, the magnitudes of the recorded events remain below $M_L = 4$.

5.2.1 Reservoir replenishment

The evolution of the VT seismicity rate prior to the 1998 eruption at PdlF volcano is described by an exponential growth by *Lengliné et al.* [2008]. The authors interpreted this phase as a magma accumulation stage within a storage area, and used the inflation of a spherical magma reservoir at depth, fed by magma rising through a cylindrical conduit, to reproduce the observed pattern. They assumed no magma leaves the reservoir during the accumulation period.

Under given assumptions for the reservoir, the conduit geometries and assuming the relationship between the volume of injected magma and the variation of overpressure [*Delaney and McTigue*, 1994], the overpressure $\Delta P(t)$ through time is given by the following expression:

$$\Delta P(t) = P\left[1 - \exp\left(\frac{-t}{\tau}\right)\right]. \tag{5.1}$$

where τ is a characteristic time and P is a constant pressure term depending on the interplay between source pressure, reservoir pressure and buoyancy [*Lengliné et al.*, 2008]. *Delaney and McTigue* [1994] interpreted the summit and near summit seismicity at basaltic volcanoes as the result of brittle failure in a disordered medium. Studies of failures in heterogeneous media reveal that the evolution of the cumulative damage D, prior to the global

failure, with the controlling stress, exhibits a relation of the form

$$D = A + B(\sigma_c - \sigma)^{-\gamma} \tag{5.2}$$

where σ_c is the critical stress and γ the critical exponent [*Garcimartín et al.*, 1997; *Zapperi et al.*, 1997; *Johansen and Sornette*, 2000]. *Lengliné et al.* [2008] interpret the cumulative damage, D, as the cumulative number of earthquakes. Given the stress evolution found in equation (5.1), and assuming that the asymptotic final stress of the system is assimilated to the critical stress, the time evolution of the earthquake rate, is given by;

$$D(t) = A + B' \exp\left(\frac{\gamma t}{\tau}\right) \tag{5.3}$$

i.e. they obtain an exponential acceleration of the seismicity.

This model is tested for seismicity at three basaltic volcanoes during the magma accumulation phase (i.e. Kilauea and Mauna Loa, Hawaii, and PdlF). While the exponential law gives slightly better fits than the power law for cumulated seismicity at PdlF and Hawaii volcanoes, only the exponential model reproduces also the decelerating deformation data recorded at Kilauea and Mauna Loa volcano surface similar to equation (5.1).

5.2.2 Reservoir Leak

Collombet et al. [2003] stacked VT seismicity time series preceding 15 eruptions in the 1988-2001 period, excluding the last day of the crisis corresponding to the dyke injection. They find a power law increase in the average seismicity rate two weeks before the eruption day, which evolves with time according to the following relation:

$$< \dot{N} > \sim (t_e - t)^{-a} \tag{5.4}$$

where t_e is the eruption time and the exponent a is determined by linear regression and is equal to 0.7 ± 0.2. The authors considered the 15 VT time series in the period 1988-2001, each of them preceding a flank eruption. Note than none of the single time series fits the average pattern. According to the classification by *Peltier et al.* [2008], no distal eruption occurred in this period.

The reservoir leak, leading eventually to the dyke injection, is characterized by a mean field accelerating behaviour of the seismicity, which has not been recorded prior to each of the individual eruptions for the Kilauea and for PdlF [*Chastin and Main*, 2003; *Collombet*

et al., 2003]. This average power-law acceleration of seismicity at mid-time scales (weeks) prior to an eruption is reminiscent of the power law time clustering of earthquake-eruption pairs when looking at the worldwide correlation between earthquake an volcano activity [*Lemarchand and Grasso*, 2007].

5.2.3 Brittle damage and Dyke Injections

At basaltic volcanoes, ongoing dyke intrusion is generally associated to the so-called seismic crisis preceding each eruption [e.g. *Bachélery et al.*, 1998; *Bachélery*, 1999; *Peltier et al.*, 2005, 2007; *Patané et al.*, 2005; *Aloisi et al.*, 2006]. At PdlF, in particular, these crises are swarms of shallow VT earthquakes occurring beneath the central cone [e.g. *Nercessian et al.*, 1996; *Sapin et al.*, 1996; *Aki and Ferrazzini*, 2000]. They are characterized by seismicity rates 2-3 orders of magnitude larger than the background seismicity rate recorded during the final weeks before the onset of each eruption [*Grasso and Zaliapin*, 2004; *Traversa and Grasso*, 2009-Chapter2].

Traversa and Grasso [2009-Chapter2] use the seismic response of volcanic edifices to low-viscosity magma injections in order to constrain the mechanical processes that drive fluid transfers during the last stage before an eruption, i.e. the dyke propagation. They analysed seven dyke intrusions at PdlF volcano during the 1988-1992 period, which preceded a 6-year repose period. The authors show that the normalized time evolutions of the cumulative number of VT earthquakes for each of the dyke intrusion do not indicate any specific change in pattern preceding the eruption. This argues for the seismicity rate during magma injection in the last phase before an eruption to be stationary in time, independent of whether the magma breaches the surface or not.

Most of the fluctuations around the average constant event rate can be reproduced when sub-sampling a Poisson time series distribution [*Traversa and Grasso*, 2009-Chapter2]. These patterns are recovered during the intrusion feeding the 2002 Mt Etna eruption (Italy) and the 2000 Miyakejima intrusion (Japan) [*Traversa and Grasso*, 2009-Chapter2]. This constant seismicity rate, as the signature of the dyke propagation, argues for the intrusion to be a scale independent stationary strain driven process that induces diffuse brittle damage within the volcano host rocks. It is reminiscent of the brittle damage recorded during secondary creep process [e.g. *Amitrano and Helmstetter*, 2006]. The stationary nature of the inelastic host rock deformation suggests a constant volume change induced by the dyke

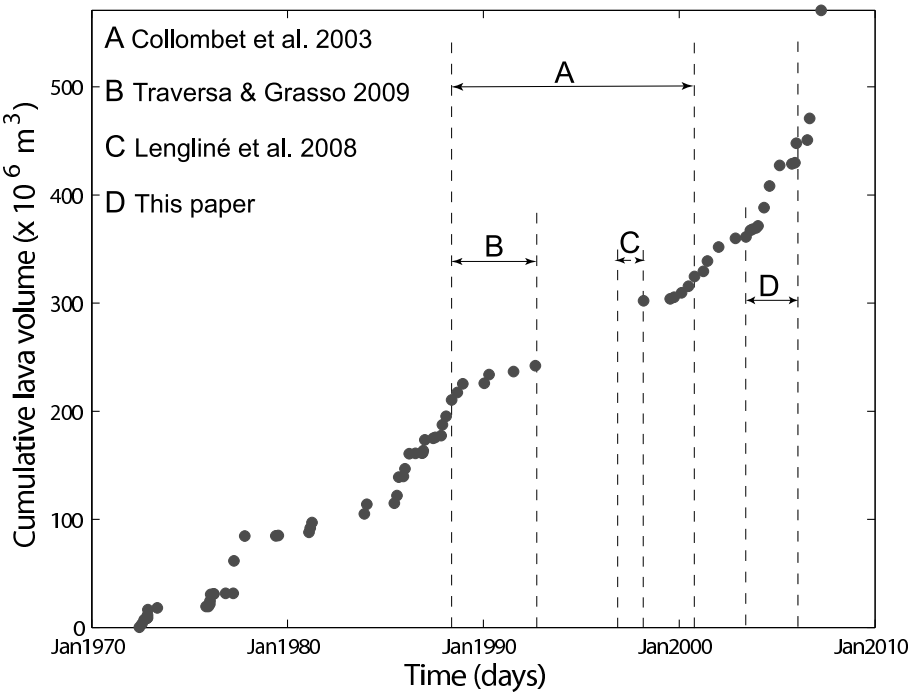

Figure 5.1: Cumulative volume of lava emitted by PdlF eruptions in the period 1970-2007 and indication of the study periods considered in this paper (and references herein) A & D: Reservoir leak [*Collombet et al.*, 2003, and this study]; B: Dyke propagation [*Traversa and Grasso*, 2009-Chapter2]; C & D: Reservoir replenishment [*Lengliné et al.*, 2008, and this study]. Data from *Peltier et al.* [2009].

within the shallow volcanic edifice. This implies a constant flow rate of magma entering the dyke over time.

5.3 Testing models for PdlF reservoirs dynamics

In the previous section we described the seismicity patterns of PdlF volcano prior to an eruption. These brittle responses of the volcano to magma reservoir processes provide insight into the physics governing reservoir dynamics at PdlF. We discuss these dynamics as constrained by the seismicity, and compare it to existing knowledge of the PdlF storage system.

The geometry and location of the PdlF volcano storage system is still controversial. *Lénat and Bachèlery* [1990] propose a shallow, i.e. above sea level, reservoir model de-

scribed as a lens network. The frequent small eruptions characteristic of PdlF volcano are sustained by the emptying of one or more of the magma pockets, which are refilled by deeper magma transfers [*Bachélery*, 1999, e.g. the 1977 eruption case]. As emphasised by *Peltier et al.* [2008] however, the mechanism and timing of âĂŸfeedingâĂŹ these different storage zones since 1998 remains unknown. It is also unclear if the deep and the shallow storage systems are continuously or transiently connected, or completely independent of each other.

Nercessian et al. [1996]; *Sapin et al.* [1996] proposed a model of a single magma chamber located at a depth of $\sim$ 2.5 km beneath the summit on the basis of a low-velocity aseismic zone inferred by seismic wave inversion. This is consistent with the magma body constrained by displacement data proposed by *Peltier et al.* [2008]. Finally, a deeper ($\sim$5 km depth) storage systems has been discussed by *Aki and Ferrazzini* [2000] based primarily on long-period (LP) events and coda localization. Following the seismicity patterns, a three-phase process is proposed to describe the shallow magma reservoir dynamics leading to an eruption:

5.3.1 The long-term (years) reservoir replenishment from a magma source region at depth (but above sea level) has been identified by an accelerating VT seismicity rate. Accelerations of seismicity have been reported either as a deterministic power law acceleration a few days prior to some andesitic explosions [e.g. *Voight*, 1988; *Kilburn and Voight*, 1998], or as an average power law when stacked over a large number (> 15) of time series 1-2 weeks before basaltic eruptions [*Chastin and Main*, 2003; *Collombet et al.*, 2003]. Therefore, the 1.2 year long exponential or power law pattern isolated by [*Lengliné et al.*, 2008] is unusual. They interpret VT seismicity as brittle failure in a disordered media. The global breakdown of the system is represented by a first order transition of the shallow part of the edifice and results in an eruption. It has been demonstrated that the cumulative damage, prior to the global failure, evolves with the stress as a power law [*Garcimartín et al.*, 1997; *Zapperi et al.*, 1997; *Johansen and Sornette*, 2000]. In this sense, the progressive damage of the reservoir walls due to the magma accumulation would eventually lead to a macro-failure of the reservoir. Such macro-failure is identified as the 1998 PdlF eruption by *Lengliné et al.* [2008], who assume that magma accumulates during the 1.2 years preceding the eruption. This long-term exponential acceleration is also observed at Kilauea and Mauna Loa during reservoir replenishment periods (lasting 5 and 9 years, respectively) [*Lengliné*

et al., 2008]. Average VT seismicity rates of $\sim$ 1, 0.5, 0.05 events/day are recorded at PdlF, Kilauea and Mauna Loa, respectively[1].

On Hawaiian volcanoes, the accelerating seismicity pattern is not affected by the occurrence of a number of 'intermediate' eruptions. It suggests that these eruptions do not affect the global reservoir pressure state. This implies that either the volume of lava withdrawn by each of these eruptions is negligible with respect to the volume of the reservoir, or that the flow rate of magma withdrawn from the reservoir over time is much lower than the flow rate feeding the reservoir from depth. The latter hypothesis agrees with the eruptive cycle proposed by *Peltier et al.* [2008] for the PdlF magma accumulations and transfers in the period 2004-2005. Using this model, there is a hierarchy between the distal eruptions that release the reservoir overpressure and the proximal eruptions that have negligible effect on the global reservoir pressure. Two scenarios are suggested by *Peltier et al.* [2008], the first includes an open system reservoir continuously supplied by deeper magmas, and the second a closed-system evolution of the magma reservoir only episodically supplied by deeper magma. In both cases, the early stages of the cycle, when the magma reservoir overpressure is still relatively low, involve smaller close-to-the-summit eruptions (âĂŸproximalâĂŹ). Due to the continuous refilling of magma in the reservoir for the former scenario, and to magma degassing in the latter, magma pressure continues to increase. This drives the system towards instability, which promotes larger distal eruptions. Eventually one of these distal eruptions is large enough to release most of the overpressure and to return the volcano to the beginning of a cycle. *Peltier et al.* [2008] showed, however, that 2004-2005 was the first period during which eruptive cycles can be observed. Between 1977 and 2004, 45 eruptions occurred, but the 1977 eruption is the only distal eruption.

We tested the seismicity patterns during the 2004-2005 period, where *Peltier et al.* [2008] identifies two cycles of continuous pre-eruptive inflation with a quiescent period between them (i.e. March to October 2005). A single magma reservoir is expected to have sustained all the eruptions occurring in this period. The volume of magma emplaced during these eruptions is too large to explain the observed deformation,

[1]We must note that the VT earthquakes used from PdlF and other volcanoes are shallow events located above the hypothesized storage area. This avoids reflecting any feeding process beneath the reservoir.

which supports the idea of refilling of the magma reservoir from depth. As shown in figure 5.2, accelerating seismicity rates observed during 2004-2005 support the model proposed by *Lengliné et al.* [2008] for seismicity accompanying magma accumulation. With seismicity alone, however, we do not observe any rest period. In fact, the seismicity pattern provides evidence of a continuous pressure increase during the whole 2004-2005 period. Whether this is driven by continuous magma accumulation in the shallow reservoir, or by continuous magma degassing, cannot be resolved by seismicity alone. This highlights the limitation of using only one observable dataset to understand volcano dynamics.

One must note that magma accumulation prior to 1998 eruption is unlikely based on chemistry and magma composition; *Bachélery* [1999] asserts that no significant refilling was involved on the PdlF shallow reservoir since 1977 eruption. The composition of lavas confirm the deep origin of the magma, which rose to the surface in a short period of time. The exponentially accelerating seismicity rate could be characteristic of a dyke which continuously rose from depth, passing through the shallow storage system and percolated toward the surface [*Battaglia et al.*, 2005b]. The exponential seismicity pattern is possibly associated with this deep dyke propagation, i.e. it does not fit the stationary seismicity that is observed during shallow dyke propagation [*Traversa and Grasso*, 2009-Chapter2].

5.3.2 At shorter time scales, the mean field characteristic (i.e. the 1-2 weeks power law acceleration before eruptions observed by *Collombet et al.* [2003]; *Chastin and Main* [2003] argues for weak stress changes before reservoir leakage. This average seismicity pattern weeks before an eruption is reminiscent of the stochastic inverse OmoriâĂŹs law pattern observed prior to earthquakes [see *Helmstetter et al.*, 2003a]. This eruption pattern may emerge from interactions among VT earthquakes. It argues for the possibility that the reservoir leakage before eruptions is induced by the cascade of localized earthquakes rather than the consequence of pressure variations. This process can be seen as a specific local divergence enhanced by the interaction of earthquakes driven by the global feeding of the reservoir (see #5.3.1). Accordingly, the apparent average local damage increase leading to reservoir leak may be spurious. It makes it difficult to identify and separate the earthquakes related to each phase, if any. Note also that a similar power law behavior can be obtained considering a constant

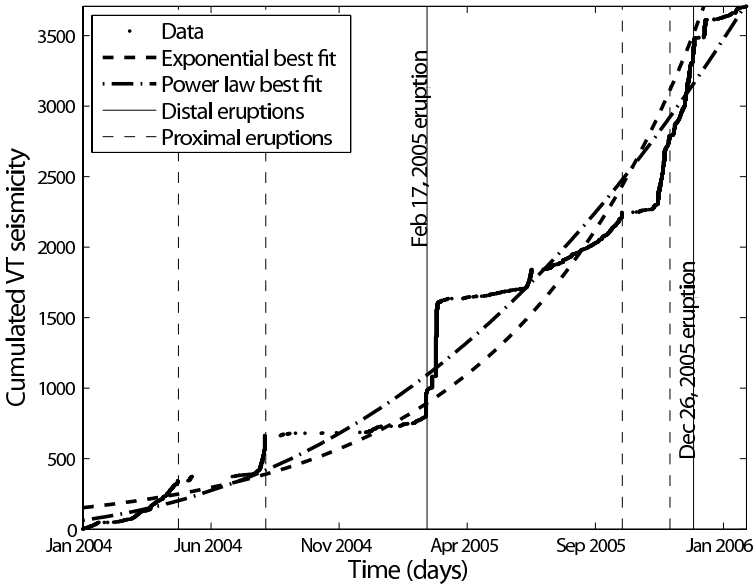

Figure 5.2: Evolution of the cumulative number of earthquakes recorded at PdlF in the period 2004-2005. Thin vertical dashed lines: eruptions occurring near the summit; thin vertical continuous lines: distal eruptions; thick dot-dashed line: best power law fit over the whole period; thick dashed line: best exponential fit over the whole period. Data courtesy of Observatoire Volcanologique du Piton de la Fournaise (OVPF).

stressing rate in equation 5.2.

We tested the validity of an average inter-eruptive accelerating seismicity rate several weeks before the 10 eruptions of the 2003-2005 period. During this period, summit, proximal and distal eruptions occurred [see classification by *Peltier et al.*, 2008]. Equation 5.4 still holds when stacking together the VT time series preceding all the 10 eruptions, with an α exponent of 0.6 ± 0.2. On the other hand, when considering earthquakes prior to the only 2 distal, oceanite-rich-magma eruptions (i.e. the February 2005 and the December 2005 eruptions), no accelerating pattern in seismicity is resolved at times scales of the tens of days before the eruption (figure 5.3). Accordingly, the average power law accelerating pattern preceding eruptions is rejected for distal eruptions. Non-distal eruptions correspond to the 'early-stage' of the reservoir cycle proposed by *Peltier et al.* [2008]. They are also the 'intermediate' eruptions, as labelled in the *Lengliné et al.* [2008] model, which do not correspond to the macro-failure of the reservoir storage area. The mean field law emerging when stacking time series, and in both models, argues for the pressure changes accompanying PdlF non-distal eruptions are not large. It implies either the erupted volumes are negligible with respect to the reservoir volume or the withdrawal rate of magma from the reservoir is much lower than the feeding rate.

5.3.3 The magma injection from the shallow reservoir to the surface is associated with a stationary VT seismicity rate of $\sim 100-200$ events/hour a few hours before the eruption [*Traversa and Grasso*, 2009-Chapter2]. Similarly identified for Mt Etna (2002) and Miyakejima (2000) dyke intrusions [*Traversa and Grasso*, 2009-Chapter2], this pattern appears to be a generic response of basaltic volcanoes to the shallow injection of low-viscosity magma. During this phase, few (if any) aftershocks have been resolved [*Traversa and Grasso*, 2009-Chapter2]. It suggests the correlated seismicity is missing either due to a high stressing rate preventing the development of cascades of events, or being 'hidden' within the huge seismicity rate contemporary with the injection.

The seismicity associated with intrusive events is related either to the brittle response of weak spots within the solid matrix to the dyke induced deformation, without necessarily reflecting the extension of the dyke [e.g. *Grasso and Bachelery*, 1995; *Rubin and Gillard*, 1998; *Pedersen et al.*, 2007; *Traversa and Grasso*, 2009-Chapter2], or

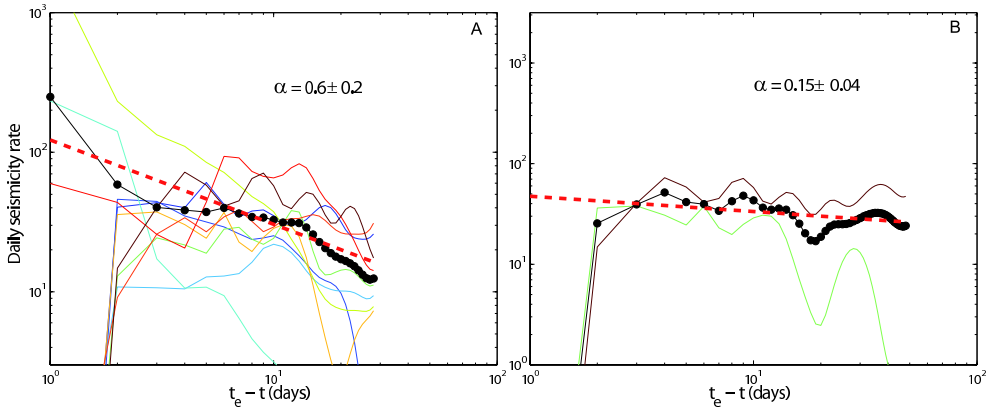

Figure 5.3: VT daily seismicity rate preceding PdlF eruptions in the period 2003-2005. A: all 2003-2005 eruptions; B: only distal, oceanite-rich magma eruptions. Thin solid lines: calculated seismicity rates; red dotted lines: average linear regressions. In accordance with the work of [*Collombet et al.*, 2003], we consider VT time series between subsequent eruptions. The maximum duration for which we compute pre-eruptive seismicity rates is the minimum inter-eruption time (i.e. $\sim$ 27 days), while we excluded the eruption day. By linear regression we approximately computed the α exponent of equation 5.3, equal to 0.8 ± 0.2 for the proximal eruption case. Data courtesy from OVPF.

to variations in the stressing rate induced by the intruding magma [e.g *Toda et al.*, 2002]. Accordingly, the best candidate for driving the seismicity induced by the dyke propagation is the volume change induced by the ongoing dyke intrusion within the shallow volcano structure. This argues for the recorded stationary seismicity rate to be a proxy for the magma flow rate injected into the dyke from the reservoir [*Traversa et al.*, 2010-Chapter3]. Since dyke intrusions are characterized by variations in propagation velocity and direction [e.g. *Peltier et al.*, 2005, among others], it implies there is no direct relationship between recorded seismicity and dyke propagation velocity. The idea of constant magma flow rate withdrawal from the reservoir to feed the dyke, implies low overpressures at the dyke inlet [*Traversa et al.*, 2010-Chapter3]. In addition, to keep the magma flux constant during the injection, the reservoir overpressure must have minimum variation [*Traversa et al.*, 2010-Chapter3]. This agrees with the hypothesis that proximal eruptions, which are characteristic of 'early stages' of the PdlF cycle [*Peltier et al.*, 2008], do not affect the overall process of continuous pressure growing in the magma reservoir. On the other hand, *Battaglia and Aki* [2003] compute a variable flow rate of magma rising during the deep seated dyke injection feeding the 1998 PdlF eruption. It suggests this 1998 extremely large dyke intrusion (figure 1) to be driven by a different mechanism than dykes originating at the roof of the shallow reservoir. We thus expect the 1998 dyke to have withdrawn a significant volume of magma from the deep reservoir and to be accompanied by a large pressure variation.

5.4 Concluding remarks

When comparing brittle damage during the three phases of the pre-eruption process we identify a 1-5 events per day seismicity rate value reported during either reservoir feeding phase (# 5.2.1), or the local reservoir leak (# 5.2.2). This is 1-2 orders of magnitude smaller than that recorded during dyke propagation (# 5.2.3. This emphasises the relative ductility of the reservoir walls compared to the shallow edifice brittleness. Since the largest seismicity rates correspond to the last phase before eruptions, it increases the difficulty to forecast an eruption days-weeks in advance. From a mechanical point of view, the highest seismicity rate occurs within the shallow edifice, which is assumed to be an open system. It questions whether dyke propagation is more brittle than the reservoir wall failure, and

thus about the role of ductility in the latter process.

Because most of the PdlF seismicity patterns appear common to basaltic volcanoes (e.g. Hawaiian volcanoes and Mt Etna) it can help to establish a generic model for basaltic volcano seismicity before eruptions. The components of such a model must include at least 3 phases, whose time scales span is 5 orders of magnitude (hours to years) and seismicity rate is 2 orders of magnitude. A deterministic acceleration of seismicity rate, as a power law, or exponential law, reproduces reservoir feeding over years. An average power law pattern precedes eruptions by 1-2 weeks during the reservoir replenishment phase. It corresponds to the brittle damage resulting in a reservoir leak. A sudden increase in the seismicity rate (by 2 magnitude orders) corresponds to the dyke injection phase a few hours before surface lava flow. Generic models that reproduce these statistical patterns will be considered as null hypothesis to test against any mechanical model for volcano reservoir dynamics before eruptions.

Acknowledgments

P.Traversa and J.R. Grasso are supported by Volume EC-FP6 and TRIGS projects.

Chapter 6

How is Volcano Seismicity Different from Tectonic Seismicity?

Paola Traversa and Jean-Robert Grasso

Laboratoire de Géophysique Interne et Tectonophysique,
CNRS - OSUG - Univeristé Joseph Fourier, BP 53 38041 Grenoble Cedex 9, France

Paper in press in: *Bull. Seismol. Soc. America* (2010).

Abstract

We analyze the temporal patterns of volcano seismicity using the statistics of waiting times between subsequent earthquakes. We compare waiting time distributions of seismicity at Mt. Etna and Mt. Vesuvius volcanoes during (i) inter-eruption phases and (ii) dyke propagations, with those of tectonic seismicity using the Southern California (SC) catalog. For inter-eruption phases, no matter their duration, statistics of interevent times are well approximated by the gamma distribution. This allows us to compute the proportion of background uncorrelated events [*Molchan*, 2005; *Hainzl et al.*, 2006], which is recovered in the range $20-40\%$ for Vesuvius, three Etna inter-eruptive periods, and the SC catalog. It argues for a rough 70% of the earthquake activity to be cascades of aftershocks for both, volcano inter-eruptive and tectonic seismicity. On the contrary, statistics of interevent times recorded during both, the 2001 and 2002 intrusive episodes at Etna volcano, reject

the gamma distribution to describe the observations. These seismic crises are characterized by an average seismicity rate about 2 order of magnitude larger than that of inter-eruptive periods. It suggests that the origin of the specificity of waiting time patterns during dyke injections is driven by the external forcing rate. Using ETAS model simulations we explore the effect of seismicity rate increases on inter-event time distributions. Departures from the gamma law progressively emerges from both (i) an increase of the background seismicity rate, and (ii) a screening effect. It prevents from quantifying the portion of uncorrelated seismicity within the considered catalog and to clearly quantify the forcing rate that characterizes the volcano dynamics during dyke intrusions.

Résumé

Nous analysons les motifs temporels de sismicité volcanique en utilisant les statistiques des temps d'attente entre événements suivantes. Nous comparons les distributions des temps d'attente à l'Etna et au Vésuve (Italie du Sud) pendant (i) les phases inter-éruptives et (ii) de propagation de dyke avec celle de la sismicité tectonique (en utilisant le catalogue de la Californie du Sud). Pour les phases inter-éruptives, quoiqu'elle soit leur durée, nous montrons que les statistiques des temps d'attente sont bien décrites par une distribution gamma, qui est généralement acceptée pour décrire la sismicité tectonique régulière. La même proportion d'événements de fond indépendants (dans la gamme 20-40$\%$) est retrouvée pour le Vésuve, les trois périodes inter-éruptives de l'Etna et le catalogue de la Californie du Sud. Cela implique qu'approximativement le 70% de l'activité sismique est caractérisée par des cascades de répliques dans les deux types de sismicité: inter-éruptive aux volcans, et tectonique. Au contraire, les statistiques des temps d'attente entre événements suivants enregistrés pendant les deux épisodes intrusifs du 2001 et 2002 à l'Etna, rejettent une distribution gamma pour décrire les observations. Ces crises sismiques sont caractérisées par un taux de sismicité moyen d'environ 2 ordres de grandeur majeur de celui des périodes inter-éruptives. Cela suggère que l'origine de la spécificité des temps d'attente pendant les injections de dyke est gouvernée par le taux de forçage externe qui déclenche la sismicité indépendante. A l'aide de simulations obtenues par un modèle ETAS nous explorons l'effet de l'augmentation du taux de sismicité sur la distribution des temps d'attente. Des départs d'une distribution gamma émergent progressivement de (i) augmentation du taux de sismicité de fond et (ii) un effet de filtrage. Cela empêche de quantifier la portion de sismicité indépendante dans le catalogue considéré et donc le taux de forçage qui caractérise la

dynamique d'un volcan pendant une intrusion de dyke.

6.1 Introduction

Volcanic processes induce significant changes in the stress state of a volcano. Seismicity recorded at volcanoes provides a way to access the mechanical response of crustal materials to these processes. In particular, Volcano-Tectonic (VT) earthquakes are shear brittle failures that can be used as an indicator of the volcano stress state [e.g. *Rubin and Gillard*, 1998; *Grasso and Bachelery*, 1995; *Traversa and Grasso*, 2009-Chapter2]. In this work we first study VT earthquakes during "repose", i.e. inter-eruptive, phases of volcanic activity. This allows us to analyze the mechanical behavior of the volcano rock materials during these quiet periods, and therefore to evaluate a reference state for volcano seismicity. We then compare occurrence patterns of observed seismicity during "repose" periods with those of seismicity immediately preceding an eruption, i.e. accompanying a dyke intrusion. All these data are also compared to ordinary tectonic seismicity patterns in order to derive implications about volcano seismicity peculiarities.

We use datasets from Vesuvius and Etna volcanoes (Southern Italy). Since 1944, the only activity observed on Mt. Vesuvius have been fumarolic activity in the crater area. Mt. Etna, in contrast, is characterized by continuous degassing, intermittent Strombolian activity at its summit craters [e.g. *Rittmann and Sato*, 1973; *Guest*, 1982; *Alparone et al.*, 2003], as well as by 4 effusive eruptions in the period 1999-2005. Episodic effusive activity on Mt. Etna is fed by dyke intrusions from a magma chamber [e.g. *Bonaccorso et al.*, 2002; *Patané et al.*, 2002; *Lanzafame et al.*, 2003; *Aloisi et al.*, 2003].

Using the 1972-2006 catalog, Mt. Vesuvius seismic activity is characterized by low to moderate seismicity (duration magnitude $M_D \leq 3.6$). Sporadic seismic swarms are related to the dynamics of an active hydrothermal system within the edifice [*Saccorotti et al.*, 2002]. At Mt. Etna (1999-2005), the rough stationary background seismic activity is occasionally modified by peaks of seismicity rate, i.e. the seismic crises preceding eruptions. This intense seismicity, which is the hallmark of dyke propagation at this volcano, is triggered by the stress perturbations induced by the combination of regional geodynamic processes with the local overpressure of a magma-filled dyke propagating towards the eruption site [e.g. *Patané et al.*, 2005; *Aloisi et al.*, 2006; *Traversa and Grasso*, 2009-Chapter2].

On Mt. Etna we consider as "repose" phases those periods during which, even if

degassing and/or strombolian activity is present within the craters, no dyke intrusion is ongoing. On Mt. Vesuvius the seismic data related to the current inter-eruptive phase cover about 30 years, while on Mt. Etna "repose" phase durations are in the 1.3-3.1 years range in the 1999-2005 period.

With the aim of evaluating the characteristics of volcano seismicity during repose periods, and to compare them with those of active periods and "ordinary" tectonic seismicity, we study statistics of waiting times between time-neighboring seismic events. This point of view can provide important insights in the physical mechanism driving earthquake occurrence [e.g. *Molchan*, 2005; *Hainzl et al.*, 2006; *Saichev and Sornette*, 2007].

In the past, various authors have explored statistics of tectonic seismicity interevent times by fitting empirical distributions to a gamma distribution [e.g. *Bak et al.*, 2002; *Corral*, 2003, 2004a,b; *Davidsen and Goltz*, 2004], with power law behavior at short and intermediate interevent times, and faster decrease in the number of events at larger interevent times. This pattern led them to propose a universal scaling law for the probability density function describing the observed waiting times, defined as the following gamma distribution [*Corral*, 2003]:

$$P(\tau) = C\tau^{\gamma-1}e^{-\tau/a}. \tag{6.1}$$

where $C = 0.5 \pm 0.1$, $\gamma = 0.67 \pm 0.05$, and $a = 1.58 \pm 0.15$. τ is the normalized interevent time obtained by multiplying the interevent time Δt by the average earthquake rate $\langle R \rangle$. Such distribution was claimed to be universal, i.e. independent of either, the choice of the area, the considered magnitude range, and the observation scale. However, *Molchan* [2005], on probabilistic basis, demonstrates that, if universality holds, the distribution of interevent times has to be exponential. This is realized in the case of the homogeneous Poisson model for seismicity. Such statement is thus in disagreement with the space-time seismic event clustering generally observed for tectonic sesmicity.

Yet, *Molchan* [2005] shows that, for large interevent time scales, the distribution decays exponentially, while the small-scale behavior of τ mimics the rate of clustered events, i.e. the Omori's law. Assuming that the seismicity is composed by Poisson background activity and triggered aftershocks obeying the Omori's law, he demonstrates that the parameter $1/a$ of equation (6.1) is the fraction of uncorrelated master events, i.e. the earthquakes directly driven by the external forcing acting on the system. Consequently, equation (6.1) is universal only if the fraction of uncorrelated events is constant and close to 60% (i.e.

$a = 1.58$) [*Hainzl et al.*, 2006].

Theoretical and statistical studies on interevent time distributions simulated by Epidemic Type Aftershock Sequences (ETAS) model [*Lindman et al.*, 2005; *Jonsdottir et al.*, 2006; *Hainzl et al.*, 2006; *Saichev and Sornette*, 2007; *Touati et al.*, 2009], have confirmed the physical interpretation given by *Molchan* [2005]. *Saichev and Sornette* [2007] generalize Molchan's argument to show that an approximate unified law compatible with the observations can be found, based on the established empirical seismicity laws, i.e. the Gutenberg-Richter and the Omori laws, together with the assumption that all earthquakes are statistically similar (i.e. no distinction is made about mainshocks, aftershocks or foreshocks).

All these works demonstrate that the analysis of interevent times provides important insights on the physical mechanisms of the earthquake process. Eventually, the fit of equation (6.1) to the interevent time distribution, yields a non-parametric estimate of the uncorrelated event rate for a given seismic region [*Molchan*, 2005; *Hainzl et al.*, 2006].

In the following, interevent time distributions of volcano seismicity recorded during inter-eruptive phases are compared with those of (i) active phases, (ii) tectonic seismicity and (iii) simulations by ETAS model. We choose the seismicity recorded between 1984 and 2002 in Southern California as a characteristic sample of tectonic seismicity. We show that, during inter-eruptive phases on Etna and Vesuvius volcanoes, earthquakes interact the same way among themselves, no matter the duration of the repose phase, nor the involved seismogenic volume. We also show that these local earthquake interactions on volcanoes are similar to those of tectonic seismicity and ETAS model with similar portion of background seismicity. It argues for the seismicity recorded at volcanoes when no volcano processes are reported to be active, (i) to behave the same way as tectonic seismicity, and/or (ii) to be simply driven by tectonics.

6.2 Data

6.2.1 Seismic catalogs

Catalog of seismic events recorded at Vesuvius in the 1972-2006 period ($-0.4 \leq M_D \leq 3.6$), consists of more than ten thousand local earthquakes recorded by the Vesuvius monitoring seismic network [see figure 1 in *Del Pezzo and Petrosino*, 2001]. Events we consider

are characterized by their occurrence time and magnitude, only 1363 events between 1998 and 2005 being located.

The permanent seismic network is composed of 10 low-dynamic range (60 dB) stations, equipped with 1 Hz Mark L4-C vertical component sensors. The OVO station, located at the ancient site of the Osservatorio Vesuviano [*Del Pezzo and Petrosino*, 2001], at 600 m asl on the volcano edifice, is equipped with a three-components Teledyne-Geotech S-13 sensor. Recorded signals are telemetered to the Data Analysis Center (Centro di Sorveglianza), where they are digitized at a sampling rate of 100 Hz [*Zollo et al.*, 2002]. The permanent seismic network configuration has maintained unchanged since 1972 [*Del Pezzo et al.*, 2003; *De Natale et al.*, 2004]. In addition, five digital, three component seismic stations equipped with 1 Hz Mark L4-3D geophones have operated almost continuously since 1987 on the volcano [*Del Pezzo and Petrosino*, 2001; *Zollo et al.*, 2002]. Events are characterized by a magnitude duration M_D, calibrated for the OVO station. M_D is calculated from measurements of seismogram coda duration according to the formula [Gruppo - Lavoro - Sismometria, 1981]

$$M_D = 2.75 \log(T) - 2.35, \tag{6.2}$$

where T is the duration measured between the P-wave first onset and the time where the signal to noise ratio is 1. Formula (6.2) has been calibrated on comparisons of 1980 Irpinia earthquake aftershock records at the OVO station and at a Wood-Anderson instrument in Rome [*Del Pezzo and Petrosino*, 2001]. In the following, only earthquakes with $M_D \geq M_c = 1.8$ (computed from the magnitude frequency distribution) will be considered. The 1972-2006 average earthquake rate is 0.13 eqs/day (see table 6.1 for a synthesis on data).

For the Etna case we use the 1999-2005 seismic catalog, which includes almost 5000 events in the magnitude range $0 \leq M_D \leq 4.4$. Earthquakes are recorded by the Mt.Etna permanent seismic network, which consists of 45 one-component analog stations, 6 three component stations, all equipped with short-period sensors (1 s), and 2 three-component broad-band stations. Signals are transmitted by radio or cable to Catania, where they are digitized at a sampling rate varying from 100 Hz in continuous mode to 200 Hz in triggering mode [*Bonaccorso et al.*, 2004]. Events are characterized by their occurrence time, a duration magnitude M_D and their location. Duration magnitude is estimated from the Serra La Nave (SLN) station seismograms according to the following equation:

Table 6.1: Seismic catalogs and corresponding parameters

Catalog* (mm/yy-mm/yy)	Duration (day)	M_{min}	M_{max}	b-value	M_c	$N_{M \geq M_c}$	$\langle R \rangle$ (eqs/day)	$\langle R^* \rangle$ (eqs/day/km^3)
VE (02/72-08/06)	12608	-0.4	3.6	$1.10 \pm 0.02 - 2.3 \pm 0.08$	1.8	1663	0.13	$1.0\text{x}10^{-6}$
ET (08/09-12/05)	2325	0	4.4	1.33 ± 0.04	2.4	992	0.43	$4.0\text{x}10^{-7}$
CA (01/84-12/02)	6936	2.3	6.6	1.15 ± 0.01	2.2	17108	2.47	$4.1\text{x}10^{-7}$
ET inter-erupt. (10/99-07/01)	623	0.7	3.6	1.54 ± 0.12	2.4	171	0.28	$2.6\text{x}10^{-7}$
ET inter-erupt. (07/01-10/02)	460	1	3.6	1.60 ± 0.15	2.4	112	0.24	$2.3\text{x}10^{-7}$
ET inter-erupt. (10/02-12/05)	1141	0.2	4.4	1.29 ± 0.08	2.4	292	0.26	$2.4\text{x}10^{-7}$
ET intrusion (07/01)	5.6	1.2	3.9	1.28 ± 0.08	2.4	290	52.11	$4.8\text{x}10^{-5}$
ET intrusion (10/02)	1.2	0	4.2	1.08 ± 0.11	2.4	91	74.21	$6.9\text{x}10^{-5}$

* VE is Vesuvius volcano, ET is Etna volcano, and CA is Southern California seismicity catalogs.
M_{min} is the detection magnitude,
M_{max} is the maximum magnitude,
b-value of the Gutenberg-Richter law (values and incertitudes calculated by maximum likelihood [*Aki*, 1965]),
M_c is the completeness magnitude,
$N_{M \geq M_c}$ is the number of events with $M \geq M_c$,
$\langle R \rangle$ is the average seismicity rate,
$\langle R^* \rangle$ is the average seismicity rate normalized to $M_c^* = 2.4$, $\Delta M^* = 1.8$ and $V_{seismogenic}$ of each volcano. $V_{seismogenic}$ is computed from seismic event locations as 45, 4200 and $3\text{x}10^4$ km^3 for Vesuvius, Etna and the considered portion of Southern California seismicity, respectively.

$$M_D = 2.2 \log(T) + 0.3 \log(L) - 1.5 \tag{6.3}$$

where T is signal duration and L is the earthquake hypocentral distance from the SLN station [e.g. *Barbano et al.*, 2000]. In the following we only use the complete catalog, i.e. all earthquakes with $M_D \geq M_c = 2.4$ (computed from the magnitude frequency distribution). The average seismicity rate for the whole catalog is 0.43 eqs/day (table 6.1).

As a reference for tectonic seismicity we use the Southern California seismic catalog, whose events are recorded by the Southern California Seismic Network (SCSN). It includes around 98000 earthquakes with magnitudes in the range $0 - 6.6$. The SCSN constitutes the southern part of the California Integrated Seismic Network (CISN) [e.g. *Powers and Jordan*, 2009]. The SCNS catalog, available at *http://www.data.scec.org*, is the standard catalog for Southern California, and contains events reported by all networks in the region. We selected events in the 1984-2002 time window, with latitude between 32° and 34° North, and longitude between 118° and 115° West. Events are characterized by their occurrence time and location and a local magnitude M_L. This latter is calculated using suitable attenuation curves on the base of synthetic Wood-Anderson amplitudes from the broad-band records [*Kanamori et al.*, 1993]. Completeness magnitude is evaluated from the magnitude frequency distribution at $M_c = 2.2$, and only events with $M_L \geq M_c$ are hereafter considered.

6.2.2 Inter-eruptive seismicity data: Mt. Vesuvius volcano

Somma-Vesuvius is the first volcano on Earth to be seismically monitored by a volcanologic observatory [*Zobin*, 2003, and *http://www.ov.ingv.it/inglese/storia/storia.htm*]. The eruptive activity of this volcano is composed of cycles starting with plinian or subplinian eruptions and, after sequences of mainly effusive to moderate explosive activity, terminating with an eruption which closes the conduit [*Santacroce*, 1987].

Since 1944 no eruption has occurred at Vesuvius volcano, which has however shown continuous fumarole and moderate ($M_D \leq 3.6$) seismic activity [e.g. *Zollo et al.*, 2002]. From then to present, Mt.Vesuvius seismicity has been characterized by hypocenter locations restricted to the volume beneath the crater area, at depths shallower than 6 km [see event locations cross sections in *Bianco et al.*, 1999; *Zollo et al.*, 2002; *Del Pezzo et al.*, 2003]. Figure 6.1 shows the 1972-2006 seismic activity recorded on Vesuvius volcano. A rough 45 km^3 seismogenic volume is estimated from earthquake locations.

Several authors have attempted to evaluate the reference state for the Vesuvius volcano during this repose period by characterizing the spatial and temporal evolution of the seismicity [e.g. *Zollo et al.*, 2002; *De Natale et al.*, 2004; *Del Pezzo et al.*, 2004]. Although the completeness magnitude of the catalog keeps constant over the years [*De Natale et al.*, 2004], the authors observe a decrease of the Gutenberg-Richter b-parameter over time, starting on 1982. b-values vary between ~ 2.2 and ~ 1 [*Zollo et al.*, 2002]. It suggests a progressive tendency to increase the maximum magnitude expected for seismic events, and consequently to increase the seismic energy release [*Zollo et al.*, 2002].

6.2.3 Inter-eruptive and eruptive seismicity data: Mt. Etna volcano

Mount Etna volcano (Sicily), located at the earth of the ancient Mediterranean civilization, is one of the best known volcanoes on Earth, with eruption recordings extending back to several centuries B.C. [e.g. *Tanguy*, 1981]. It is currently among the best monitored volcanoes worldwide, thanks to which, significant progresses in the knowledge of its dynamics have recently been made.

Eruptions at Etna are frequent. Recurrence times vary from few months to several decades. Between 1999 and 2005 a remarkable series of eruptions occurs, including two highly explosive and destructive flank eruptions in 2001 and 2002-2003, and a geodetically

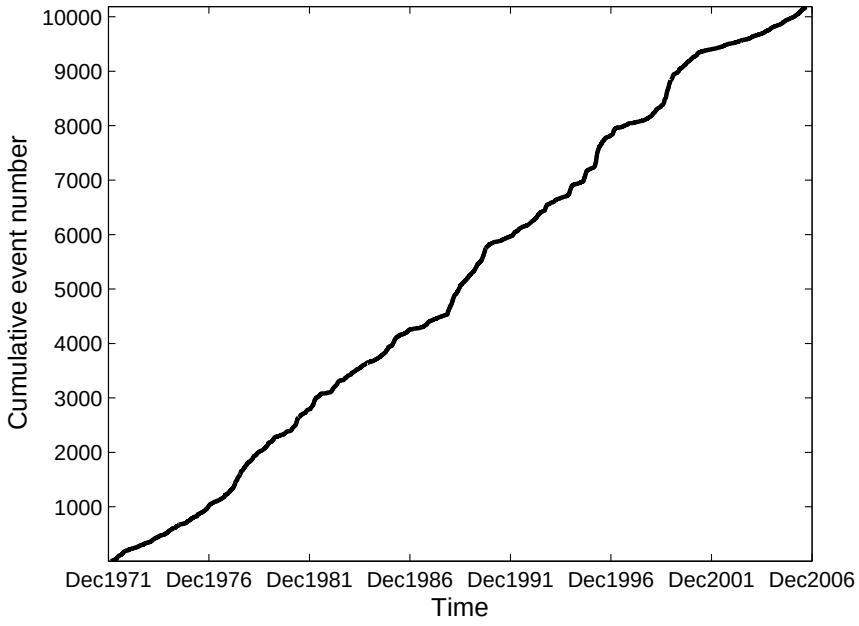

Figure 6.1: Cumulative seismicity ($M \geq M_c = 1.8$) recorded at Mt. Vesuvius during the period 1972-2006. Completeness of the catalog is constant over time.

passive and seismically silent flank eruption in 2004-2005 [e.g. *Bonaccorso et al.*, 2002; *Acocella and Neri*, 2003; *Patané et al.*, 2003; *Burton et al.*, 2005; *Allard et al.*, 2006; *Bonaccorso et al.*, 2006].

The July-August 2001 eruption is heralded by several days of intense ($\sim$ 52 events/day, table 6.1) seismicity [*Patané et al.*, 2002; *Bonaccorso et al.*, 2002]. On the other hand, only few hours of premonitory seismicity ($\sim$ 71 events/day) precede the opening of the 2002-2003 eruptive fractures [*Patané et al.*, 2005]. Still a different mechanism drives the 2004-2005 eruption, characterized by silent magmatic processes [e.g. *Burton et al.*, 2005]. Figure 6.2 illustrates the variety of the Etna host rock seismic response to the processes leading to the three eruptions.

The seismicity recorded at Mt. Etna volcano during the 1999-2005 period ($0 \leq M_D \leq 4.4$) is spread over the whole crustal seismogenic volume, up to about 35 km depth. As estimated from seismic event location on the the 1999-2005 period, the seismogenic volume is of order $4\text{x}10^3$ km^3.

As example of seismic crisis accompanying dyke magma rising towards the volcano

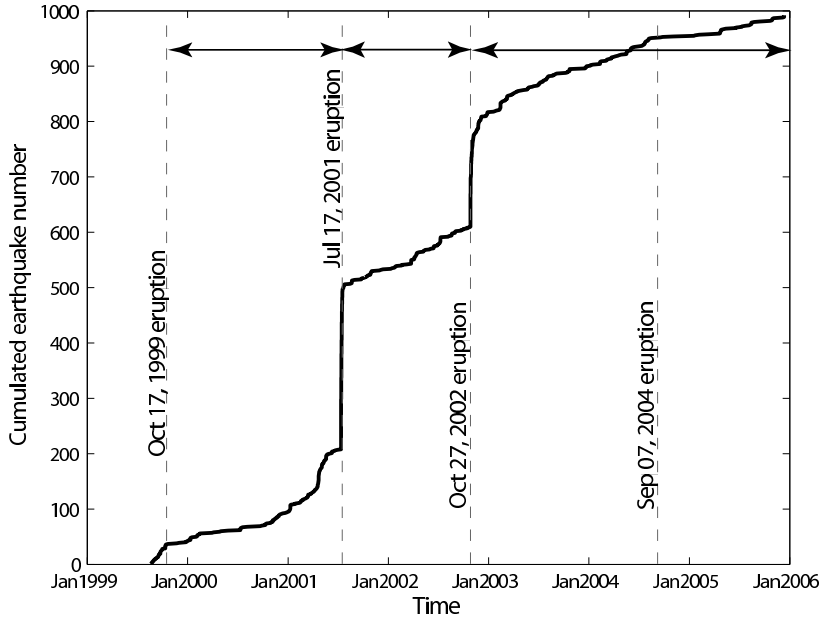

Figure 6.2: Cumulated number of seismic events ($M \geq M_c = 2.4$) recorded during the period 1999-2005 at Mount Etna volcano. Completeness magnitude M_c of the catalog keeps constant over the whole considered period. Horizontal lines and arrows delimit the inter-eruptive periods considered in the paper.

surface, we use the seismicity contemporary to the dyke intrusions that fed the 2001 and the 2002-2003 Etna eruptions. Following previous authors work, dyke-induced seismic crises are defined in the periods 2001/07/12 (21:46 LT) - 2001/07/18 (12:14 LT) [*Gambino et al.*, 2004; *Bonaccorso et al.*, 2002; *Patané et al.*, 2002], and 2002/10/26 (20:26 LT) - 2002/10/28 (07:30 LT) [*Aloisi et al.*, 2003; *Andronico et al.*, 2005]. Average seismicity rates during the two intrusions are 52.1 and 74.2 eqs/day (table 6.1), respectively.

We consider as inter-eruptive phases all periods away from these active magma injection phases, that is 1999/10/17 to 2001/07/12, 2001/07/18 to 2002/10/26, and 2002/10/28 to 2005/12/12 (the end of the catalog). Seismicity rates during these periods are, respectively: 0.23, 0.2 and 0.3 eqs/day. These imply seismic rate ratios of order 200 for dyke injection over inter-eruption phases.

6.3 Analysis of interevent time distributions

Interevent times are computed as the time separating two subsequent events, i.e. $\Delta t_i = t_i - t_{i-1}$. We represent them as probability density functions $f(x)$, such that, given any values a and b, with $a < b$, the probability of a variable X to be between a and b is equal to

$$P(a < X < b) = \int_a^b f(x)dx. \tag{6.4}$$

Figure 6.3 shows the probability density distribution of seismic interevent times during inter-eruption phases at Mt. Etna in the 1999-2005 period and Mt. Vesuvius in the 1972-2006 period. These are compared with waiting time density distributions of seismicity accompanying two dyke intrusions at Mt. Etna and of the Southern California seismicity, as an example of tectonic seismicity.

We perform a goodness of fit analysis to test whether empirical distributions follow a gamma law. For repose phases on both, Etna and Vesuvius volcanoes, the chi-squared test validates the null hypothesis that interevent time distributions follow the respective gamma law with 95% confidence level. The same holds for "ordinary" tectonic seismicity, as described by Southern California seismicity. On the other hand, the distributions of interevent times during the 2001 and 2002 dyke intrusions on Mt. Etna, significantly depart from inter-eruptive and tectonic time series (figure 6.3). Indeed, the chi-squared goodness of fit test allows us to reject the null hypothesis that these two distributions follow a gamma law with 99% confidence level.

When normalizing each of the density distributions by the respective earthquake occurrence rate, the waiting time distributions collapse on the same gamma distribution for all, inter-eruptive seismicity at Etna and Vesuvius volcanoes and tectonic seismicity, except for dyke intrusion seismicity (figure 6.4). One must note that we do not observe any change in pattern for the waiting time distributions as function of either, the inter-eruption time duration (i.e. 623, 460, 1141 and 12608 days for the three Etna inter-eruptive and Vesuvius sequences, respectively), or the seismic rate change (i.e. 0.28, 0.24, 0.26, 0.13, respectively). The distributions of interevent times induced by the 2001 and 2002 dyke intrusions at Mt. Etna, on the other hand, deviate from the generic pattern at both ends of the distribution, i.e. below 10 and above 10 normalized time units (figure 6.4).

As discussed in the introduction section, we can therefore estimate the fraction of

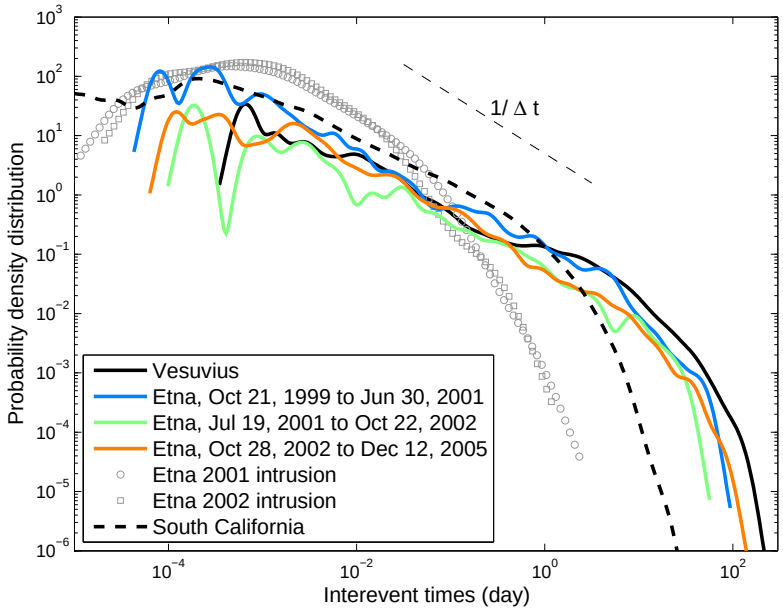

Figure 6.3: Interevent times probability density distributions. Solid black line: Vesuvius catalog (1972-2006). Solid color lines: Etna inter-eruptive periods: 1999/10/21-2001/06/30, blue; 2001/07/19-2002/10/22, green; 2002/10/28-2005/12/12, orange. Dashed black line: Southern California catalog (1984-2002). Gray dots and squares: Etna 2001 and Etna 2002 dyke intrusion seismicity, respectively. Thin black dotted line: power law with unit exponent, i.e. Δt^{-1}, for reference.

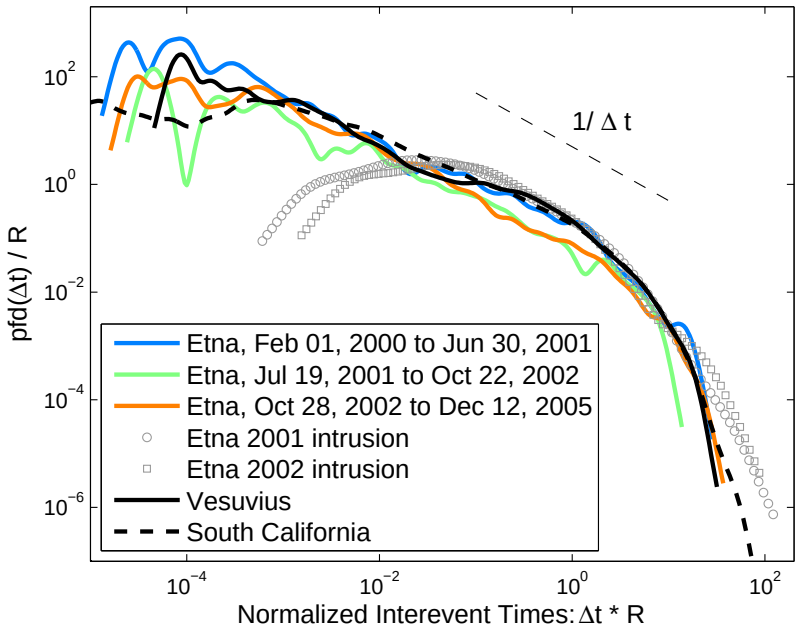

Figure 6.4: Interevent times probability density functions normalized by the seismic occurrence rate. Etna repose phases (three in the period 1999-2005), color plain lines; Vesuvius (1972-2006), black plain line; South California (1984-2002), black dashed line; 2001 Etna dyke intrusion, gray empty circles; 2002 Etna dyke intrusion, gray empty squares. Thin black dotted line: power law with unit exponent, i.e. Δt^{-1}, for reference.

background seismic activity by fitting a gamma law to each empirical distribution that do follow a gamma law (i.e. for each of the inter-eruptive and tectonic seismicity time series). We use the technique proposed by *Molchan* [2005] and further discussed by *Hainzl et al.* [2006]. The importance of calculating this quantity lies on the strict relationship between the background seismicity rate and the external forcing rate acting on the system. Such active external forcing, in fact, directly triggers the background seismicity. According to *Molchan* [2005] and *Hainzl et al.* [2006], the best gamma distribution to fit the empirical one is simply related to the mean and the variance of the observed data. The constant C in equation 6.1 is given by

$$C = (a^{\gamma}\,\Gamma(\gamma))^{-1}, \tag{6.5}$$

where $\Gamma(x)$ is the gamma function. The parameter a is given by

$$a = \frac{\sigma_{\tau}^{2}}{\overline{\tau}}, \tag{6.6}$$

where $\overline{\tau}$ and σ_{τ}^{2} are, respectively, the mean and the variance of the interevent times, and

$$\gamma = \frac{\overline{\tau}}{a}. \tag{6.7}$$

Background seismicity fractions are given by $1/a$ [*Molchan*, 2005; *Hainzl et al.*, 2006]. In figure 6.5 background seismicity fractions are reported for each of the inter-eruptive and tectonic seismicity time series. Values are corrected from the parabolic shift *Hainzl et al.* [2006] found to affect the estimation obtained with the above procedure.

In order to homogenize the seismic datasets from effects due to the different network configurations and characteristics, we normalize seismicity rates by both, common completeness magnitude M_c^*, and magnitude spread ΔM^*. Besides, in order to remove the influence of the seismogenic volume in the earthquake production, we normalize the seismicity rate by the seismogenic volume $V_{seismogenic}$. These allow us to compute a normalized seismicity rate R^* independent of the intrinsic characteristics of the site [e.g. *Traversa and Grasso*, 2009-Chapter2]. We then quantify a background event rate which is a direct proxy of the effective forcing rate that drives the observed seismicity. After normalization, average seismic daily rates $\langle R^* \rangle$ are of order 2.5x10^{-7} for the three Etna, and 10x10^{-7} for the Vesuvius inter-eruptive periods (table 6.1). In all four cases the fraction of background

uncorrelated seismicity is in the range $20-38\%$. This means that, taking into account the rough estimate of the seismogenic volume, the forcing rates acting on the different systems are of the same order.

The departures from a gamma law of the interevent times distributions during the 2001 and 2002 dyke intrusions, prevent us from quantifying the uncorrelated fraction of seismicity within these two catalogs by the described approach. Nonetheless, using the observed normalized seismic rate $\langle R^* \rangle$ (figure 6.5 and table 6.1), we expect an increase of about 200-fold in the forcing rate between repose and dyke-intrusion periods. These observations question for the influence of the large daily seismic rate and its control parameters on the waiting time distribution.

6.4 The ETAS model

6.4.1 Model overview

ETAS model is a self-excited stochastic point process in which every event produces its offspring events, i.e. each aftershock triggered by a previous event is able to trigger further aftershocks [e.g. *Ogata*, 1988; *Helmstetter and Sornette*, 2002a].

The ETAS model combines the Gutenberg-Richter (GR) distribution of event magnitudes with the Omori-Utsu (OU) law for the aftershock rate as function of time since a mainshock [*Utsu et al.*, 1995] and the productivity law, which defines the magnitude-dependent contribution of each event in the triggering of new earthquakes [e.g. *Helmstetter et al.*, 2005]. The GR and OU laws are ingredients such that the ETAS model can fully explain the empirically observed characteristics of earthquake recurrence time statistics [*Saichev and Sornette*, 2007].

The ETAS model is considered as a current null hypothesis for tectonic earthquake statistics and earthquake predictability [e.g. *Saichev and Sornette*, 2007].

According to the ETAS model, the seismic activity can be described, in time, as the superposition of two different processes: a homogeneous Poisson process generating the background, uncorrelated seismicity λ_0, and a non-homogeneous Poisson process corresponding to the Omori's law of aftershock decay following a given event [e.g. *Utsu et al.*, 1995; *Helmstetter and Sornette*, 2002a]. The seismicity rate R can therefore be expressed as follows

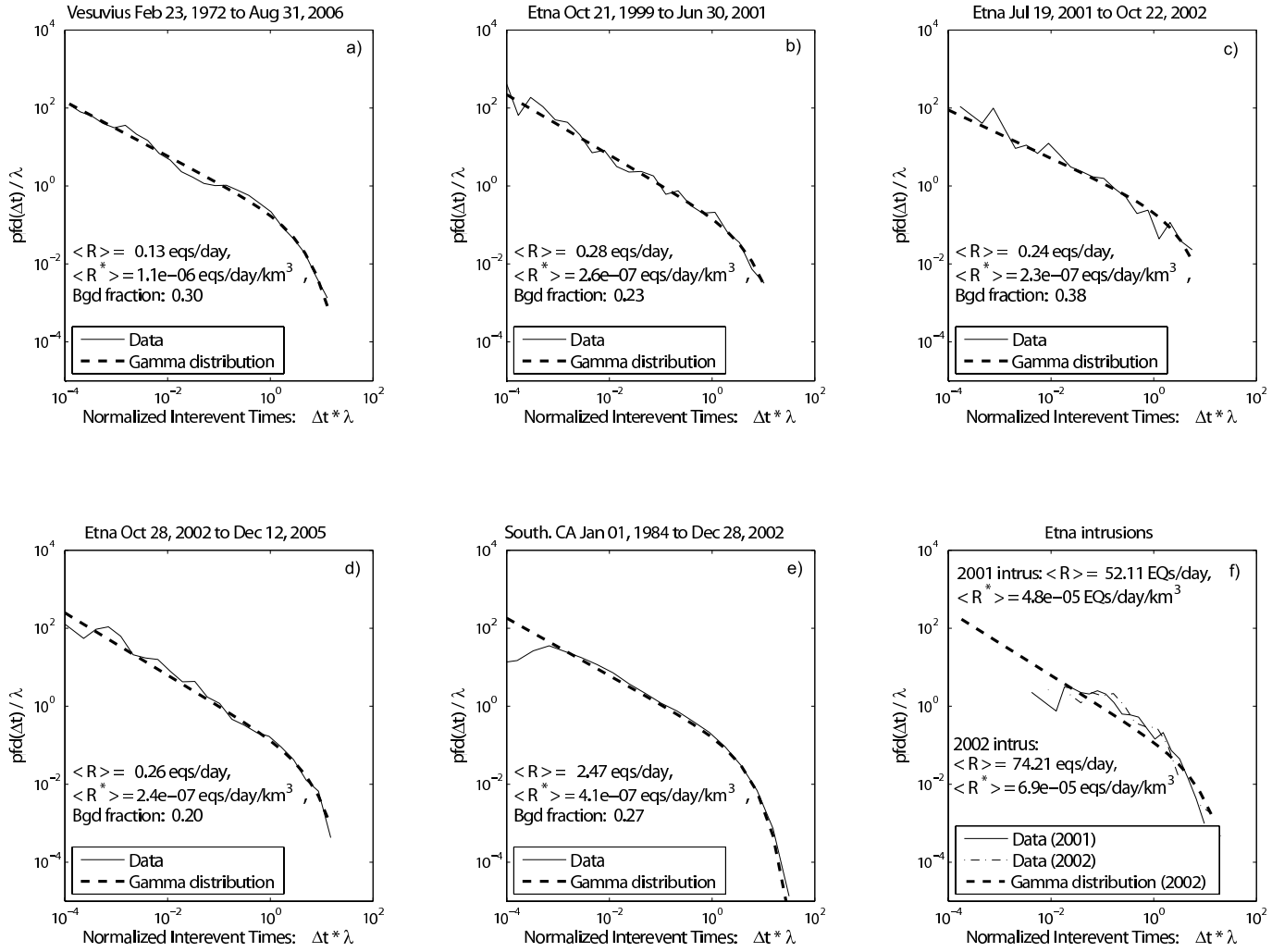

Figure 6.5: Interevent time distributions: Observed density distributions and gamma distribution fits (equation 6.1). Continuous or dash-dotted lines: normalized pdf of interevent times; thick dotted line: gamma distribution fit. On abscissa the interevent times are multiplied by the seismicity rate $\langle R \rangle$; on ordinates the density is divided by the seismicity rate $\langle R \rangle$ [*Corral and Christensen*, 2006; *Molchan*, 2005; *Hainzl et al.*, 2006]. For cases a) to e) the chi-squared goodness of fit test allows us to accept the null hypothesis that empirical data follow a gamma law with 95% confidence level. Estimation of the background event rate is thus computed as $1/a$ in equation 6.1. For case f) the null hypothesis is rejected with 99% confidence level. $\langle R \rangle$ is the observed average daily seismicity rate; $\langle R^* \rangle$ is the average daily seismicity rate normalized by $M_c^* = 2.4$, $\Delta M^* = 1.8$ and $V_{seismogenic}$ of each volcano (see table 6.1).

$$R = \lambda_0 + \sum_{t_i<t} \lambda_i(t), \tag{6.8}$$

where $\lambda_i(t)$ is the rate of aftershocks induced by an earthquake that occurred at time t_i with magnitude M_i, and is given by

$$\lambda_i(t) = \frac{K \cdot 10^{\alpha(M_i - M_0)}}{(t - t_i + c)^p}, \tag{6.9}$$

where K and c are empirical parameters; the exponential term $10^{\alpha(M_i-M_0)}$ describes the relationship between the magnitude of the mainshock and the number of aftershocks the mainshock is able to trigger, α being a productivity parameter; p is the exponent of the "local" Omori's law [e.g. *Helmstetter and Sornette*, 2002a].

The background rate λ_0 is assumed to be driven by the external forcing. For tectonic seismicity this forcing is due to the tectonic plate motion, while for volcano seismicity it is related to volcano processes such as mass movements and pressure and temperature variations [*Traversa and Grasso*, 2009-Chapter2]. Events in a homogeneous Poisson process occur at a constant underlying rate and are statistically independent from each other. The Poisson probability density function $P(\Delta t)$ for waiting times is given by:

$$P(\Delta t) = \lambda_0 e^{-\lambda_0 \Delta t}. \tag{6.10}$$

As mentioned above, the ETAS model assumes that earthquake magnitudes are statistically independent and drawn from the Gutenberg-Richter distribution [e.g. *Helmstetter and Sornette*, 2002a], which gives the probability that event magnitudes are larger than a given value. That is

$$P(M) = \beta 10^{-b(M-M_c)}, \tag{6.11}$$

where β is related to the Gutenberg-Richter b exponent as $\beta = b\ln(10)$.

6.4.2 Interevent time distributions from ETAS model

The ETAS model has been largely used to reproduce the dynamics of earthquake interaction in space and time, e.g. the Omori law aftershock decay following a mainshock [e.g. *Ogata*, 1988; *Guo and Ogata*, 1997; *Felzer et al.*, 2002], the aftershock diffusion from a

mainshock [e.g. *Helmstetter and Sornette*, 2002b; *Helmstetter et al.*, 2003b] and to identify periods of precursory quiescence [e.g. *Ogata*, 1992].

Number of studies have focused on the Omori's law waiting time probability density distributions [e.g. *Utsu*, 1970; *Utsu et al.*, 1995; *Lindman et al.*, 2005; *Jonsdottir et al.*, 2006], all showing that individual aftershock sequences are characterized by a power law distribution of intermediate waiting times. *Jonsdottir et al.* [2006] analytically and numerically demonstrate that, due to incomplete detection of aftershocks shortly following the mainshock, the probability density distribution of waiting times is roughly constant for very short times (i.e. for $\Delta t < c$), while a power law decay dominates for $\Delta t > c$. For the largest waiting times, a fall-off related to the finiteness of the considered time window is observed.

When considering interevent time distributions from seismic series characterized by a background homogeneous Poisson process and Omori'law sequences, an approximate power law decay (directly related to the Omori's law) still dominates for $\Delta t > c$. At Δt of the order of the inverse of the background rate λ_0, then, the distribution decays as an exponential function, related to the uncorrelated part of seismicity [e.g. *Molchan*, 2005; *Hainzl et al.*, 2006; *Saichev and Sornette*, 2007]. Using ETAS simulations *Touati et al.* [2009] demonstrate that the dependence of the power law exponent on the Omori's law p-value is not simple and also depends on the other ETAS parameters (i.e. λ_0, b, K, c and α, see table 6.2).

Touati et al. [2009] demonstrate that, by increasing the rate of independent events in a given seismic catalog, the rate at which aftershocks sequences are initiated grows. It induces overlapping of the aftershock sequences, which decreases the proportion of dependent interevent time series. The interevent time distribution tends therefore towards an exponential function as the rate of uncorrelated events grows [*Touati et al.*, 2009, and figure 6.6, top]. According to *Touati et al.* [2009], for "low to intermediate" values of background uncorrelated seismicity rates, the crossover between correlated and uncorrelated curves results in an apparent power law distribution (figure 6.6, top), whose exponent, however, does not have a simple relationship with any of the ETAS parameters [*Touati et al.*, 2009].

We push further the analysis on the impact of a strong seismicity rate on real observations. We consider the case in which the rate of independent events grows and the resolution in time of the recording system keeps constant, i.e. we simulate an increase in seismicity rate within a stable network, which is the case for volcano seismicity crises.

Table 6.2: ETAS model parameters used in the earthquake simulation

Parameter	Value
λ_0	1 eq/day
b	1
K	0.0094
c	0.001 days
p	1.1
α	0.8

With this purpose we simulate different ETAS seismic sequences with progressively larger background rate and we impose a time truncation that allows to reproduce the incomplete time detection of the seismic network. The shortest waiting time within the simulated time series are thus 10^{-4} days (figure 6.6, bottom) rather than 10^{-8} (figure 6.6, top). The other ETAS parameters remain unvariate (table 6.2). Due to the difficulty in inverting for ETAS parameters [Helmstetter A. and Werner M., personal communication, 2008], the parameters we use are regular values when simulating tectonic seismicity [see e.g. *Helmstetter and Sornette*, 2002a; *Helmstetter*, 2003; *Helmstetter et al.*, 2003a].

The truncation we introduce in the simulations induces small perturbations on the waiting time distributions concerning ETAS simulations with the smallest (1-10 eqs/day) background event rates, which remain close to a gamma distribution (figure 6.6, bottom). For the same truncation, the higher the background event rate, the more the interevent time distribution deviates from a gamma distribution (figure 6.6, bottom). All these demonstrate that such deviations are the cumulated effect of a high background event rate and of the incomplete detection of the seismic network for very small interevent times (e.g. $< 10^{-4}$ days).

6.5 Discussion

Volcano Tectonic (VT) earthquakes are brittle failures that aim at releasing stresses in response to volcano dynamics, the same way as tectonic earthquakes are the brittle response of the upper crust to the tectonic forcing.

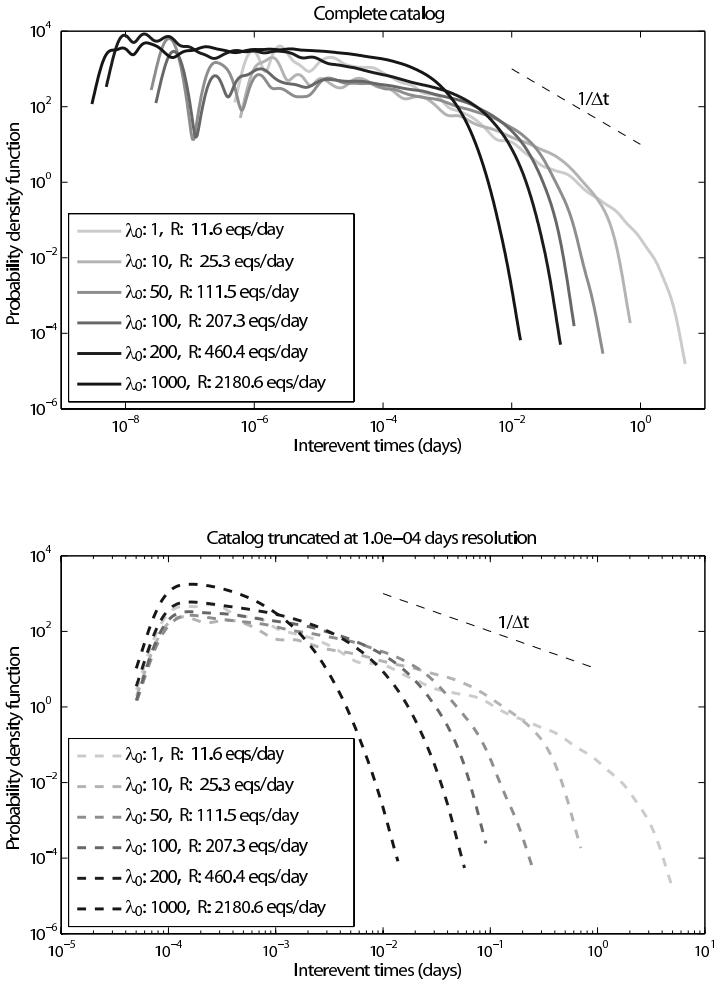

Figure 6.6: Interevent time distributions of ETAS simulations for different background seismicity rates (λ_0). Top: complete catalogs from the simulations; bottom: catalogs truncated with a minimum resolution in time of 10^{-4} days. Gray scale is related to the respective background event rate (λ_0 expressed in event/day in the legend). All catalogs have a duration of 100 days. R are seismicity rates. Thin black dotted line: power law with unit exponent, i.e. Δt^{-1}, for reference.

Because the size of a volcano and the space and time scales of volcano dynamics are respectively smaller and faster than the long lasting tectonic loading, we test how earthquakes interact in response to volcano dynamics.

When focusing on inter-eruption seismicity, we do not observe any difference between seismic time series during repose periods on andesitic and basaltic volcanoes, such as Mt. Vesuvius and Mt. Etna, respectively. The waiting time distributions of VT events during inter-eruptive phases at Etna and Vesuvius volcanoes show similar behavior, independently of the duration of the repose period since the last dyke intrusion, and of the volcano dynamics style. The waiting time distributions of seismic events on the two volcanoes are also similar to those of "classic" tectonic seismicity, as described by the Southern California seismicity. All of them are described by a gamma distribution, which has been shown to depend on the amount of uncorrelated background activity of the corresponding seismic catalog [e.g. *Molchan*, 2005; *Hainzl et al.*, 2006]. It allows us to quantify a $20 - 40\%$ of background seismicity during inter-eruptive periods on Vesuvius and Etna volcanoes. Being directly triggered by the external forcing acting on the system, the background seismicity rate is a direct proxy for the dynamics that drive the system.

During the 1999-2005 period, 4 eruptions take place on Mt. Etna volcano. Etna seismicity in this period is characterized by a rough background stationary activity, on which periodic peaks of seismicity rate accompanying dyke intrusions superimpose. Mt. Vesuvius seismicity in the period 1972-2006 (no eruption) remains stationary over time, but is characterized by a non-stationary seismic energy release, as measured by b-value fluctuations [e.g. *Zollo et al.*, 2002; *De Natale et al.*, 2004; *Del Pezzo et al.*, 2004]. In spite of the b-value variations (decrease, 1982-1997, and following increase, 1997-2006), we do not resolve any robust change in either, the seismicity rate, or the amount of background independent events.

When normalizing the seismicity rates to the same completeness magnitude, magnitude spread and seismogenic volume with the aim of removing site specificities, the background rates we estimate by fitting a gamma law to the empirical distributions, are 2.5, 4, 10 x 10^{-7} eqs d^{-1} km^{-3} (table 6.1), for Etna, California and Vesuvius seismicity, respectively. The corresponding amount of independent background events is of order 30% for all data. The brittle deformation rate, as estimated by the normalized seismicity, is thus within the same order of magnitude for the 3 cases study. The slight variations in the normalized seismicity rate (2.5 to 10), related to the stressing rate to which the system is

subject, do not result in significantly different rates of independent events. It argues for the amount of earthquake interactions to be stable for a given forcing rate, no matter the tectonic setting and the on-site country rock type (i.e. Etna basaltic volcano, Vesuvius andesitic volcano and Californian tectonic environment).

The seismic response of the crustal rock to a given perturbation of stressing rate appears thus to be a generic response when emphasizing the amount of earthquake interactions. This holds independently of either, the duration of the inter-eruptive period, and the daily seismicity rate for Etna and Vesuvius volcanoes.

These results question for a similar forcing acting on reposing volcanoes and tectonic environments, and argue for the volcano seismicity to be simply driven by tectonics and/or other low stressing rate perturbations when the magma chamber is steady (i.e. no magma refilling or excursion through dyke injections exist). As seen by the interevent time statistics, there is no evidence for memory of the volcano edifice to volcano history. The overall response of the volcano to stressing rate changes is the same, independently of local heterogeneities induced by past episodes of magma rising and cooling through dykes (i.e. weaker high fractured zones, or stronger ancient cooled dyke paths), explosions, and huge volumetric deformations. This response is also similar to that of California rocks submitted to tectonic loading.

The roughly constant amount of earthquake interactions we recovered within seismic time series when no large forcing rate is acting on the system, no matter its dynamics, breaks when analyzing seismicity triggered by a strong forcing rate such as during dyke intrusions. It argues for the seismicity recorded on a volcano to map the stressing rate to which the volcano is subject [e.g. *Toda et al.*, 2002]. During intrusions, the magma propagating towards the eruption site triggers seismicity rates more than 2 orders of magnitude larger than those recorded during inter-eruptive periods. The rough linearity observed in figure 6.6 between background event λ_0 and seismicity R rates suggests therefore that the 200-fold increase in seismicity rate R contemporary to the 2001 and 2002 dyke intrusions on Mt. Etna is driven by a similar increase in the forcing rate acting on the system during dyke intrusion periods.

Significant departures from the gamma distribution, which is accepted to reproduce "ordinary" tectonic seismicity [e.g. *Corral and Christensen*, 2006; *Molchan*, 2005; *Hainzl et al.*, 2006], are observed for seismic series contemporary to dyke intrusions at Mt. Etna volcano. On Mt. Etna the same seismic network records seismicity during both, inter-

eruptive and dyke crisis periods. Accordingly, there should be no instrumental bias that may disturb the waiting time distributions. It argues for the departure from the gamma law of waiting time distributions during dyke intrusions to be induced by the large external forcing rate that drives the dyke intrusions. Such departures of inter-event time distributions from the gamma one during dyke intrusions, prevent from estimating the uncorrelated event rate for these time series.

Figure 6.7 shows the global aftershock decay following mainshocks of any magnitude averaged together for each of the considered seismic catalogs. For the tectonic and inter-eruptive seismicity, a clear average aftershock decay following mainshocks emerges. On the other hand, when considering dyke-intrusion seismic sequences, we observe an apparent lack of aftershock activity [e.g. *Traversa and Grasso*, 2009-Chapter2]. It suggests that the high seismicity rate "masks" any possible decay pattern.

Forcing rates related to tectonic activity can be identified with the deformation rate induced by the slow tectonic plate motion, i.e. few centimeters per year. On volcanoes, magmatic intrusions induce volumetric deformations of few millions of cubic meters in few hours or few days [e.g. *Traversa et al.*, 2010-Chapter3; *Toda et al.*, 2002]. In the first case, stresses induced by the occurrence of seismic events, are redistributed into the solid matrix by the fully developed cascade of aftershocks following each master event. This latter being the characteristic pattern for the "classic" tectonic behavior at a regional scale. As shown in figure 6.7, the dramatic increase in background seismicity rate induced by the huge forcing rate generated by a dyke intrusion, "masks" the cascade of fracturing induced by stress redistribution, and tracked by aftershock occurrence. It suggests that there are threshold values for forcing rates, and consequently seismicity rates, above which either, we fail in identifying earthquake interactions, or earthquake interactions do vanish.

Using ETAS model simulations we explore the effect of seismicity rate changes on earthquake interactions. Departures from the gamma law progressively emerges from both (i) an increase of the background seismicity rate, and (ii) a screening effect (figure 6.6). The former drives an apparent increase of uncorrelated event rate [e.g. *Touati et al.*, 2009], which results in an exponential function for the inter-event time distribution. The latter is driven by the relative decrease of resolution in event counting when the seismicity rate increases, due to the constant detection resolution of the volcano-monitoring network during seismic crisis. The fact that the increase in seismicity rate is not accompanied by an increase in the time resolution of the recording system, results in a truncated inter-event time distribution

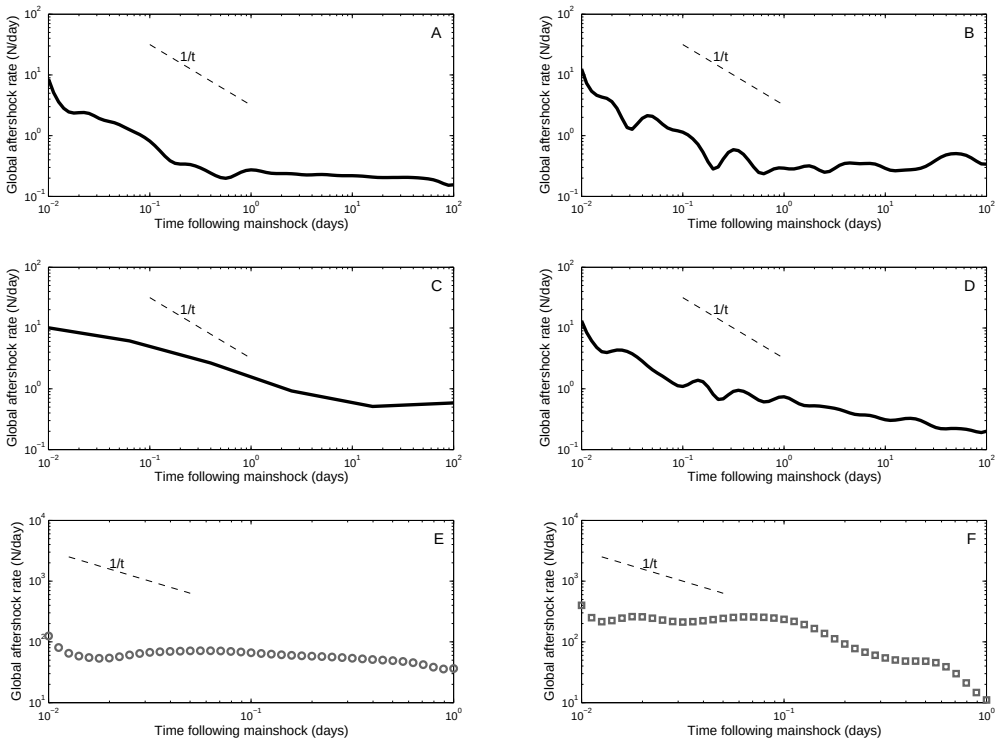

Figure 6.7: Average aftershock rates versus time since mainshock. A: Vesuvius (1972-2006), B: Etna inter-eruptive (1999-2001), C: Etna inter-eruptive (2001-2002), D: Etna inter-eruptive (2002-2005) E: Etna 2001 intrusion, F: Etna 2002 intrusion. $t = 0$ is mainshock occurrence, for $t > 0$ the averaged seismicity rates following mainshocks are shown. Mainshocks are events (i) of any magnitude not preceded by another event for a time equal to the median of interoccurrence times, and (ii) occurring within 10% and 90% of the intrusion duration window to avoid border affects [Helmstetter, personal comm., 2007]. Curves are averaged over (i) all mainshocks for a given magnitude class, and (ii) all magnitude classes. Thin black dotted line: power law with unit exponent, i.e. t^{-1}, for reference.

(figure 6.6, bottom).

ETAS simulations with a 200-fold increase of the background rate (as measured for average daily seismicity rates on Etna volcano, table 6.1) allow us to reproduce both, the relative shape and the departures from the gamma distribution we observe during intrusion periods as compared with inter-eruptive periods (figure 6.8). The ETAS simulations, thus, allow us to reproduce, with the seismicity rate and the time resolution as control parameters, the continuum of distributions from the gamma law during repose periods toward the hybrid-shape inter-event time distribution during dyke injections.

6.6 Concluding remarks

Tectonic earthquake sequences have been shown to be characterized by the superposition of a background rate of uncorrelated events plus a cascade of correlated events [e.g. *Ogata*, 1988; *Helmstetter and Sornette*, 2002a; *Corral and Christensen*, 2006; *Molchan*, 2005; *Hainzl et al.*, 2006]. When testing this model on volcano seismicity we find that inter-eruption volcano seismicity follows the same pattern as regular tectonic seismicity, as sampled using the southern California catalog. The gamma law distribution, which describes the inter-event time distribution, allows to quantify the amount of uncorrelated background events in the $20 - 40\%$ range.

During dyke intrusions, the seismicity rate, which increases by more than two orders of magnitude with respect to inter-eruptive periods, prevents us to extract and to quantify the two types of earthquakes and their possible interactions. The Omori law pattern is hidden behind the high background rate, and the inter-event time distribution departs from a gamma law.

Such apparent departure from regular earthquake interaction patterns, is driven by the increase of the earthquake rate, contemporary to a relative truncation effect due to the constant threshold for magnitude completeness and time resolution for event picking of the recording network during high seismicity rate crises. The first effect induces overlapping of different clusters of correlated earthquakes. These overlaps break the correlation within individual earthquake sequences, resulting in an exponential distribution of waiting times between subsequent earthquakes [*Touati et al.*, 2009].

Such a pattern is further modified by the truncation of time series due to a constant time resolution threshold of the seismic detection system. These two effects, reproduced

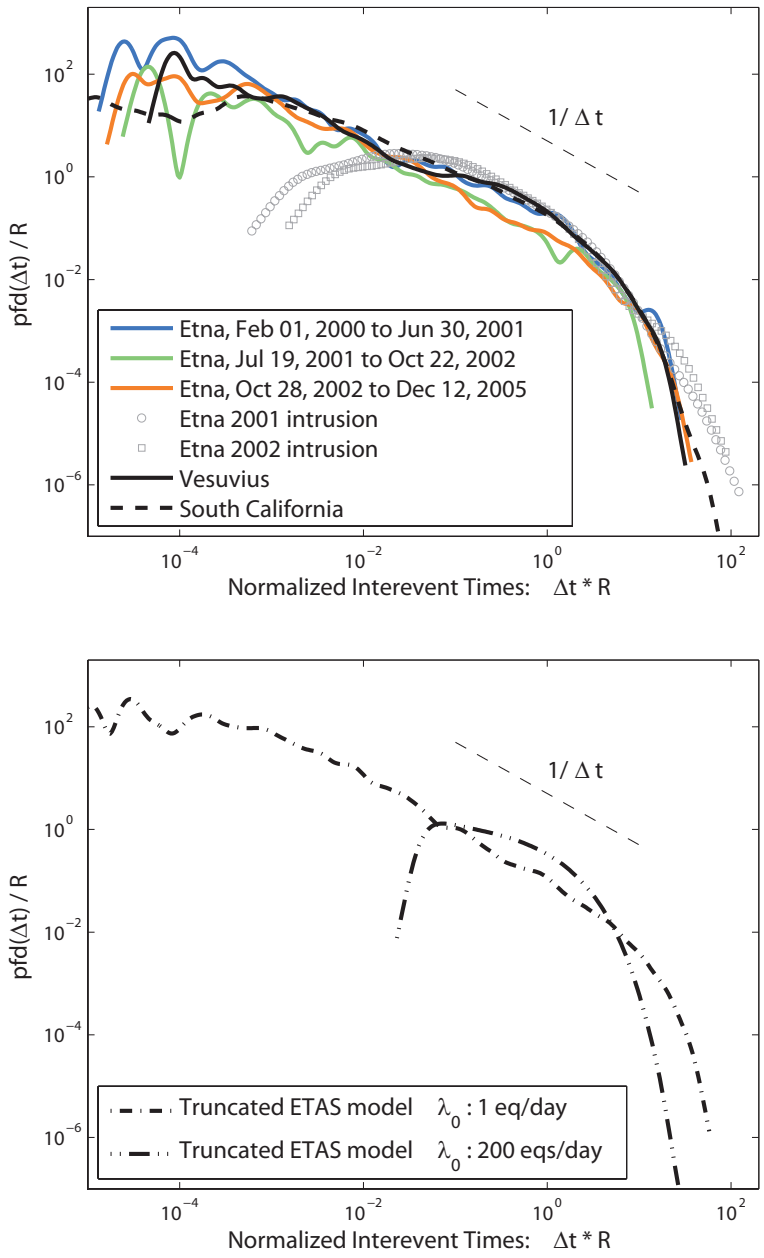

Figure 6.8: Interevent times probability density functions normalized by the seismic occurrence rate. Top: Same as figure 6.4. Bottom: ETAS simulation with parameters from table 6.2, dot-dashed black line; ETAS simulation with background seismicity rate 200 eq/day, dot-dot-dashed black line. The λ_0 ratio between the two ETAS simulations is 200. Both simulations are affected by a detection truncation at 10^{-4} days. Thin black dotted line: power law with unit exponent, i.e. Δt^{-1}, for reference.

through ETAS model with regular tectonic seismicity parameters, well reproduce both, the inter-eruption seismicity on Etna and Vesuvius volcanoes, and the seismic crises during dyke injections on Etna volcano.

The "classic" definition of VT earthquakes occurring in swarms with no foreshock-mainshock-aftershock pattern, typical of tectonic seismicity, therefore, simply emerges from a combination of these two effects, (i) a high seismicity rate induced by a strong forcing rate acting on the system, and (ii) the fact that the seismic recording system is not able any more to identify individual events becoming too close together in time when this forcing intervenes.

The interevent times patterns we observe appear to be independent of i) the size of the geophysical object the forcing is applied to, i.e. from a tectonic plate to a volcano edifice; ii) the length of the time series, i.e. from days to tens of years; iii) the local rock matrix properties, i.e. different volcano environments and tectonic plate.

6.7 Data and Resources

Seismic catalog of Vesuvius volcano in the period 1972-2006 is provided by INGV-OV (Istituto nazionale di Geofisica e Vulcanologia-Osservatorio Vesuviano), Naples, Italy. Catalog of Etna seismicity in the period 1999-2005 is provided by INGV Catania section, Italy. Sharing of these data has been possible thanks to the VOLUME European project. Seismic catalog for Southern California (by Southern California Earthquake Data Center) is available on line at: *http* : *//www.data.scec.org/catalog_search/date_mag_loc.php*. Plots in this paper are made using Matlab R2009a.

Acknowledgments

We would like to thank G. Daniel, A. Helmstetter and D. Amitrano for advises and interesting and stimulating discussions. We are grateful to G. Saccorotti for providing both, Vesuvius catalog and useful information on the Vesuvius seismic network, and to the INGV-Catania staff for providing the Etna catalog. We also like to thank the two reviewers, whose suggestions allowed for improving this paper. P.T. and J.R.G. are supported by Volume EC-FP6 and TRIGS projects, contracts n. 08471 and 043386, respectively.

Chapter 7

Short-Term Forecasting of Explosions at Ubinas Volcano

Résumé

L'objectif de ce chapitre est d'analyser et de quantifier l'évolution de la sismicité de type Long Période (LP) qui précède les explosions sur le volcan Ubinas (Pérou) pendant la période 2006-2008. Nous observons une augmentation du taux de LP quelques heures en avance sur l'occurrence d'une explosion, symptomatique d'un mécanisme de "charge" du volcan. Ce motif ressort clairement quand l'on moyenne différentes séries temporelles de LP précédant les explosions le plus énergétiques. Nous utilisons des techniques de "pattern recognition" pour caractériser les motifs intra-éruptives du taux de LP précurseur à une explosion. Cela nous permet d'évaluer la possibilité d'activer une alarme quelques heures en avance sur l'occurrence d'une explosion. L'algorithme de prédiction se base sur un balance de compromis entre trois paramètres : (i) le taux de seuil de LP à partir duquel une alarme est envoyée, (ii) la durée de l'alarme et (iii) la longueur de la fenêtre temporelle utilisée pour calculer le taux moyen de LP. L'emploi de diagrammes d'erreur nous permet d'évaluer la bonté de la prédiction obtenue par l'algorithme pour chaque combinaison des paramètres. Les résultats de la prédiction sont stables et l'algorithme de prédiction validé puisque meilleur d'un tirage aléatoire. Nous montrons des évidences en faveur d'un mécanisme de déclenchement commun pour LP et explosions, qui peuvent être identifiés dans la fracture fragile du magma suite à une contemporaine augmentation de la pression et de viscosité et cisaillement dans le conduit.

7.1 Introduction

An erupting volcano is a complex system, driven by non-linear dynamics [e.g. *Grasso and Bachelery*, 1995; *Sparks*, 2003; *Lahaie and Grasso*, 1998; *Melnik and Sparks*, 1999] and in which several processes are contemporaneously acting and interact [e.g. *Melnik and Sparks*, 1999; *Sparks*, 2003]. As a consequence, precisely modeling of volcano processes with the aim of forecasting future eruption episodes is extremely complex.

Two different approaches can be undertaken with eruption prediction goals. On one hand we may attempt the understanding of the long-term (i.e. $\gg$ inter-eruptive time) eruptive behavior of a volcano by catching periodicities, trends, or particular patterns characterizing the temporal distribution of eruptive episode occurrences. In this way we could evaluate the probability of occurrence of future eruptions using historical records. On the other hand we may try to improve the understanding of the short-term (i.e. $<$ inter-eruptive time) behavior of volcano processes leading to an eruption by studying the time behavior of some observables at a given volcano. This may allow to identify characteristic precursors to impending eruptions.

As regarding to the first approach, statistical analysis of eruption time sequences on active volcanoes in a given region, or worldwide, has allowed some authors to look for eruptive event time clustering, or for the presence of more regular recurrence times, i.e. for Poissonian distribution of eruption times [e.g. *Wickman*, 1966, 1976; *Mulargia et al.*, 1985; *Jones et al.*, 1999; *De la Cruz-Reyna*, 1991; *Ho*, 1991, 1996; *Bebbington and Lai*, 1996; *Pyle*, 1998; *Connor et al.*, 2003; *Gusev et al.*, 2003; *Marzocchi and Zaccarelli*, 2006; *Varley et al.*, 2006]. The drawback of such an approach, however, is the limited knowledge human beings dispose about the occurrence of past (pre-historical) eruptive events. This bounds the maximum duration of repose periods we are able to consider.

Within the second approach, a number of studies have focused on the geochemical and geophysical observables that generally precede and accompany eruptions on volcanoes, e.g. gas emission, seismicity, ground deformation, attempting to identify precursors to volcanic eruptions. *Voight* [1988] proposes an empirical rate-acceleration relation which is suggested to provide analytical bases for eruption prediction. The author introduces a fundamental law for material failure as self-accelerating processes to describe the temporal behavior of a suitable observable quantity Ω (i.e. seismic, geodetic or geochemical data) as eruption onset approaches. He validates his model by applying it to line length changes, tilt and

fault movement data before the March 1982 Mt. St. Helens eruption, and to seismic energy release data before the April 1960 Bezymyanny (Kamchatka) eruption. *Voight and Cornelius* [1991] carries on the application of this law in the form of the "inverse-rate" plot, combined with real-time monitoring of seismic activity as a tool for near-real time eruption prediction. According to this idea, time to failure can be estimated by extrapolation of the inverse rate $\dot{\Omega}^{-1}$ curve versus time to a predetermined intercept. *Voight and Cornelius* [1991] use as observable, Ω, continuous measurements of the real-time mean amplitude of seismicity on Mt. St. Helens and Redoubt volcanoes. The method results in few-days-earlier prediction dates for the May 1985, October 1986 eruptions at Mt. St. Helens, and December 1989 at Redoubt volcano (Alaska).

The interest of using the inverse rate lies on the fact that an infinite rate for the observed precursor quantity $\dot{\Omega}^{-1}$ is expected to imply an uncontrolled rate of change, which is associated with the collapse of the resistance to magma ascent, and therefore with the eruption onset [*Voight and Cornelius*, 1991]. The linear extrapolation of the time at which the inverse rate is zero would therefore predict the eruption time. A limit of this method lies however on the lack of any possibility to evaluate the quality of the prediction.

Subsequent applications of the inverse-rate method, combined with the assumption of similarity in behavior between large-scale and micro cracking, suggest it has potential as a tool for forecasting some types of eruptions, particularly explosive-type eruptions [e.g. *Cornelius and Voight*, 1994, 1995; *McGuire and Kilburn*, 1997; *Kilburn and Voight*, 1998; *De la Cruz-Reyna and Reyes-Dávila*, 2001; *Reyes-Dávila and De la Cruz-Reyna*, 2002; *De La Cruz-Reyna et al.*, 2008].

Among geochemical and geophysical precursors employed by the material-failure method, seismic event rate has been shown to be the most useful quantity when attempting to forecast volcanic eruptions [*Kilburn*, 2003]. As pointed by *McGuire and Kilburn* [1997], however, the static-failure mechanism is just one of the processes controlling how quickly a volcano approaches an eruption. A major problem is therefore how to decide whether a change in behavior of a given observable is actually precursor of an eruption [*McGuire and Kilburn*, 1997]. Bursts of anomalous seismicity recorded on the Soufriere Hill volcano in Monserrat in the 1930s and 1960s, for example, suggested an eruption might be imminent [*Wadge and Isaacs*, 1988]. The seismicity, however, gradually subsided without any eruptive activity. Similar behavior of seismic activity observed on July 1995, on the contrary, did herald an eruption [*McGuire and Kilburn*, 1997].

In addition to these deterministic models of volcanic eruption prediction, also statistic prediction methods based on a given observable have been proposed. *Minakami* [1960] uses the increase in the five-day frequency of earthquakes on Asama andesitic volcano to derive an increase in the probability for an eruption in the next 5 days. *Klein* [1984] tests the precursory significance of geodetic data, daily seismicity rate and tides before 29 eruption on Kilauea volcano (Hawaii) in the 1959-1979 period. His prediction scheme can give 1- or 30-day forecast on an eruption with a 90% confidence using the rate of small earthquakes. *Mulargia et al.* [1991, 1992], using pattern recognition techniques, identify clusters of seismic activity within 40 days before 9 out of 11 flank eruptions on Etna volcano in the period 1974-1989. None of the summit eruptions occurring in this period, however, is predicted. More recently, *Grasso and Zaliapin* [2004] explore the eruption predictability of Piton de la Fournaise volcano. The authors test the prediction quality using error diagrams [*Kagan and Knopoff*, 1987; *Molchan*, 1997]. They find that the best prediction performance is obtained by using five-day windows to compute the seismicity rate, and by issuing an alarm during 5 days. Nonetheless, this implies a 90% of issued alarm to be false alarms.

The object of this work is to analyze and quantify the evolution of LP earthquakes prior to explosions on Ubinas volcano (Perú) during the 2006-2008 period. Being thought to originate in the fluid and thus to reflect the state of the fluid (magma or gas) within the volcanic edifice [e.g. *Chouet*, 1996; *Neuberg*, 2000; *Chouet*, 2003], LP event production should depend on the pressurization state of the magmatic system. Accordingly, as suggested by *Chouet* [1996], we expect a direct link between the strength of the LP activity and the potential for explosions. Therefore, although models of material failure or tertiary creep lie on accelerations of brittle damage leading to system failure, LP earthquake rate is here used as the precursor of explosion occurrence within the current eruptive episode.

On Ubinas volcano we observe a few hours increase of the LP rate preceding explosions in the period 2006-2008. Such pattern clearly emerges when stacking over different LP time series prior to the most energetic explosions. We then use pattern recognition techniques [e.g. *Mulargia et al.*, 1991, 1992; *Grasso and Zaliapin*, 2004] to characterize the intra-eruptive precursory patterns of LP rate prior to Ubinas volcano explosions. By retrospective analysis on the 2006-2008 period, we explore thus the possibility, for the future, of issuing an alarm on explosions occurrence few hours in advance.

"Pattern recognition" is basically a search for structure in the data, assuming that the phenomenon under study occurs according to a number of complex, but well defined

and repetitive schemes [*Mulargia et al.*, 1991]. The advantage of this technique is that it extracts information from the considered variable (or combination of variables) and provides a phenomenological picture without need of any physical model [*Mulargia et al.*, 1991].

The forecasting algorithm is then based the trade-off of three parameters: the LP rate threshold above which the alarm is sent, the alarm duration, and the time window used to average LP occurrence. In order to validate our forecast algorithm, we then evaluate the effectiveness of its predictions using error diagrams, introduced by *Kagan and Knopoff* [1987] and *Molchan* [1997]. These diagrams allow us to provide the parameter combination that allows for intra-eruptive explosion forecasting on Ubinas volcano once sociology studies have defined the optimum trade-off between the portion of false versus missed alarms for explosions.

7.2 Ubinas volcano

The Ubinas strato-volcano (Arequipa, southern Perú) has a nearly symmetrical composite cone with a large summit crater, whose diameter ($\sim$ 1.75 km) allows to classify it as a caldera [*Bullard*, 1962]. *Thouret et al.* [2005], by coupling stratigraphic records with geophysical, mineralogical geochemical and isotopic data, reconstructs the volcano evolution history from middle Pleistocene to present. They identify two major periods. The first, from middle Pleistocene to about 376 ky ago, is characterized by andesite lava flow activity that built the lower part of the edifice [*Thouret et al.*, 2005]. This edifice collapsed, resulting in a debris-avalanche deposit. The second phase (376 ky to present) comprises several stages. The summit cone was built by a series of andesite and dacite lava flows. Subsequently a series of dome grew, and the summit caldera formed in association to a large-scale Plinian eruption. The last Plinian eruption occurred ca. in A.D. $1000 - 1160$. Since then and to the present day, Ubinas is in persistent, fumarolic and phreatic activity [*Bullard*, 1962; *Thouret et al.*, 2005].

Ubinas is known to be a very active volcano, with 24 episodes of high fumarolic activity since the A.D. 1550, with a frequency of 4 to 5 eruptions per century [*Rivera et al.*, 1998, and $http://www.igp.gob.pe/vulcanologia/Volcanes_Peru/Ubinas/HTML/Erupciones-Historicas-Ubinas.htm$]. The most recent eruption began in March 2006 and is still currently ongoing. The central vent eruption has been accompanied by explosive eruptions,

phreatic explosions and lava dome extrusion. From August 2005, a slight increase in fumarolic activity has been observed, which culminated in April 2006. On April 14^{th} 2006 the first notable explosion occurred [*Rivera et al.*, 2006], and phreatic activity continued till April 23. On April 27 activity becomes vulcanian, with eruption of andesitic materials.

Explosions on Ubinas volcanoes are a threat for the population living in the nearby zones, beside being a hazard for commercial flights due to the presence of ash in the atmosphere. The Buenos Aires Volcanic Ash Advisory Center (VAAC) reported for example ash plumes rising to more than 10 km during the period October 23-26, 2006 [*Smithsonian Institute*, 2009].

Thouret et al. [2005] find mineralogical and geochemical evidence for magma mixing, which, in combination with shallow aquifers of the over-pressurized hydrothermal system, is thought to trigger Ubinas eruptions. *Thouret et al.* [2005] observe a progressively increase of mixing, differentiation and contamination of magmas towards recent times eruptions. They imply that Ubinas is presently undergoing an increasing recharge rate regime.

7.3 Data

In this work we use the Ubinas seismic catalog in the period 2006/05/23-2008/12/04. Events are recorded by the IGP (Instituto Geofísico de Perú) seismic network (figure 7.1) which has been progressively installed since the beginning of the current eruption. No permanent seismic station operated in fact before this eruption [*Macedo et al.*, 2009]. During the first weeks analogue seismic recorders are operative at different locations on the west and north flanks. Then two digital portable stations (Guralp CMG40T-30 sec sensors with RefTek recorders) are installed at the end of April 2006. From May to June 2006, six additional portable stations (Guralp CMG40T-30 sec sensors with Agecodagis Titan recorders) are installed [*Macedo et al.*, 2009]. In May 2007 the first permanent telemetered station (equipped with a SS1 Kinemetrics-1Hz sensor) is installed on the northwest flank, while the other three permanent stations are installed in 2007 [*Macedo et al.*, 2009]. Data from the permanent stations are transmitted by radio to the Cayma Volcanological Observatory in Arequipa. During the considered period, the automatic signal classification procedure detects 35240 Long Period (LP) events, 445 hybrid events, 5461 tremor activity periods, 247 volcano Tectonic (VT) earthquakes, and 143 explosions (figure 7.3).

The variety of the recorded signals reflects different source processes, the extreme

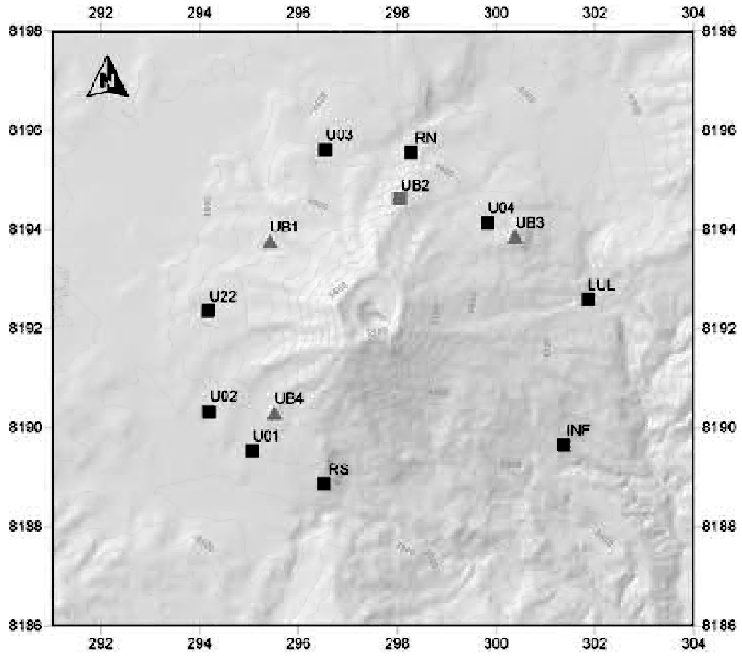

Figure 7.1: Ubinas volcano seismic network. Triangles: 1 Hz sensor stations; squares: broadband stations. Gray color indicates stations with radio telemetry; black color indicates portable stations.

structural heterogeneity and the strong topography effects that influence the signals [e.g. *Chouet*, 1996; *Bean et al.*, 2008]. VT earthquakes are the trace of shear brittle fractures occurring within the volcano rock matrix as a consequence of magma processes acting within the edifice. They are thus thought to act as gauges that map stress concentrations distributed over a large volume surrounding magma conduits and reservoir [e.g. *Grasso and Bachelery*, 1995; *Chouet*, 1996; *Rubin and Gillard*, 1998; *Traversa and Grasso*, 2009-Chapter2]. Their waveform and frequency content is very similar to that of tectonic earthquakes, with clear P and S phases.

LP earthquakes, even if consensus on their triggering mechanism has not been achieved yet, are thought to originate within the fluid as the result of fluid dynamic processes and fluid-rock interactions. They have emergent onset followed by a low frequency harmonic coda, which is interpreted by most authors as the signature of interface waves generated at a fluid-elastic boundary [e.g. *Aki et al.*, 1977; *Chouet*, 1986, 1988] and trapped in a resonating fluid-filled crack [e.g. *Chouet*, 1988; *Neuberg*, 2000; *Neuberg et al.*, 2000; *Kumagai et al.*, 2005; *Neuberg et al.*, 2006; *Saccorotti et al.*, 2007; *Lokmer et al.*, 2007, 2008]. They have unclear S phase and peaked frequency spectrum [e.g. *Chouet*, 1996].

Hybrid events are LPs with an additional high-frequency onset. Since these two types of event are very similar and are thought to share a common source process [e.g. *Neuberg*, 2000], in this work we group together LP and hybrid events as low-frequency (called hereafter simply LP) earthquakes.

Tremor at andesitic volcanoes is a continuous harmonic signal with waveform very similar to that of LP event, such that it is thought to be the result of the overlap of these events due to a high frequency excitation of the source. Tremor and LP activity would therefore be the manifestation of the same process of unsteady mass transport [e.g. *Chouet*, 1996; *Neuberg et al.*, 2000]. This does not seem to be the case at basaltic volcanoes, where tremor does not share spectral characteristics of LP events. Rather, an abrupt change of the spectral signature is observed [e.g. *Saccorotti et al.*, 2007, on Etna volcano]. At Piton de la Fournaise volcano for example, tremor activity with frequency content higher than 1.5 Hz is thought to originate at the eruption site and to represent the signature of the eruption itself [*Aki and Ferrazzini*, 2000; *Battaglia et al.*, 2005a; *Traversa et al.*, 2010-Chapter3]. Lower frequency tremor sources however, seem to have a deeper origin [*Battaglia et al.*, 2005a].

Explosion wavefield include a low-frequency onset followed by a high-frequency signal

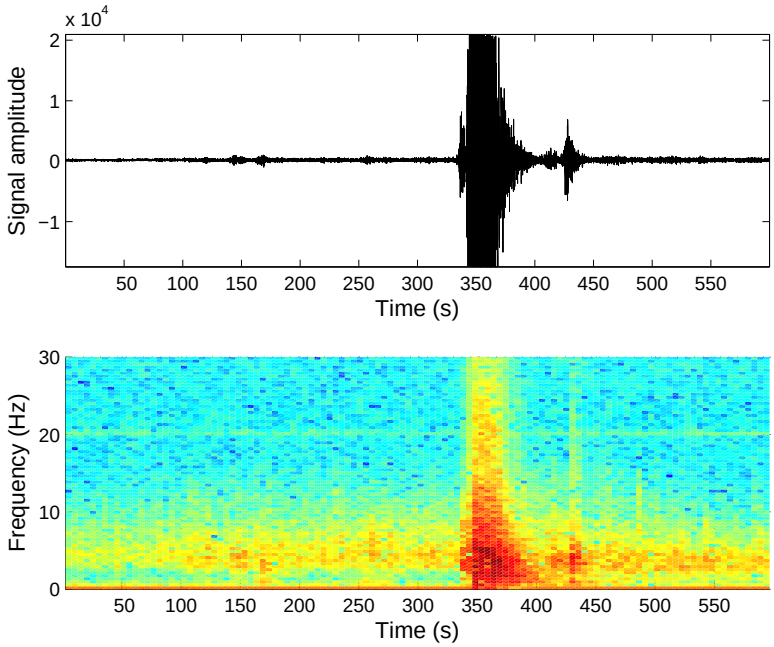

Figure 7.2: Ubinas volcano explosive event (May 24, 2006). Top: recorded time series; bottom: spectrogram of the recorded time series.

(figure 7.2). Explosions are explained as the result of bubble growth within a degassing rising melt, which causes magma fragmentation and the generation of a gas body in which pyroclasts are carried by the over-pressured gas toward the surface. At Ubinas volcano explosions are identified on the seismic recordings with the aid of phenomenological observations.

Computation of a magnitude duration M_D for the described events gives us a glimpse about the size of Ubinas seismic activity. M_D can be computed for example as follows:

$$M_D = 2.75 \log(\tau) - 2.35 \tag{7.1}$$

where τ is signal duration. This is the formula used for Mt. Vesuvius VT seismicity by the V Vesuvius Volcanological observatory [Gruppo-Lavoro-Sismometria, 1981]. Accordingly, VT events magnitude is in the range $0 - 2.9$. A magnitude for long period and hybrid events has not been defined. By using relation (7.1) we get a magnitude range of $-0.7 - 6$ for low-frequency events. No location is available for the considered seismicity, which is clearly dominated by low-frequency earthquakes (figure 7.3).

The seismic network encounter technical issues during the whole period of study, such

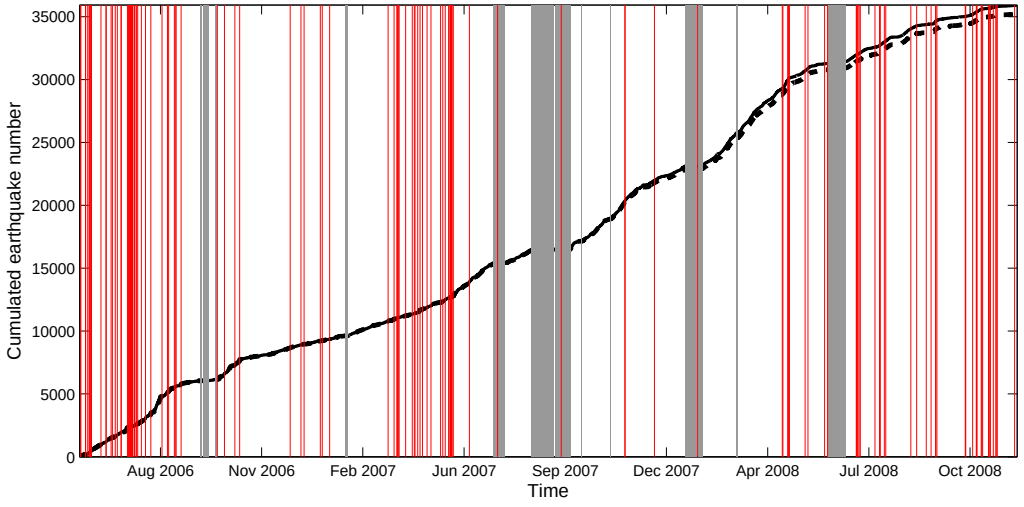

Figure 7.3: Ubinas volcano seismic activity in the period 2006/05/23 - 2008/12/04. Solid black line: cumulative number of earthquakes, including all types of event (Long Period, hybrid and VT events); dashed black line: cumulative number of LP events; gray boxes: seismic network interruption periods; thin red lines: explosion occurrences.

that 21 temporal gaps due to instrument functioning interruptions make discontinuous the seismic catalog (figure 7.3).

7.4 Long Period seismicity patterns before explosions

As mentioned above, in the October $23 - 26$, 2006 period, the highest rise of the ash plume was reported [*Smithsonian Institute*, 2009]. Figure 7.4 shows the LP activity recorded over the period October $21 - 29$, 2006. The explosion occurring on October 23, 2006 is preceded by an about 6-hours long non-linear increase of LP activity, while the October 26, 2006 explosion is characterized by a continuous acceleration of the LP rate during about 3 hours before explosion onset (figure 7.4).

When stacking together the LP activity time series preceding all explosions recorded on Ubinas volcano outside interruption periods of the seismic network, we observe an average increase in the LP activity rate 2-3 hours before explosion onset (figure 7.5). This average acceleration is recovered for all seismic recording periods (figure 7.5).

In order to draw the overall average pattern of LP activity prior to explosions, we

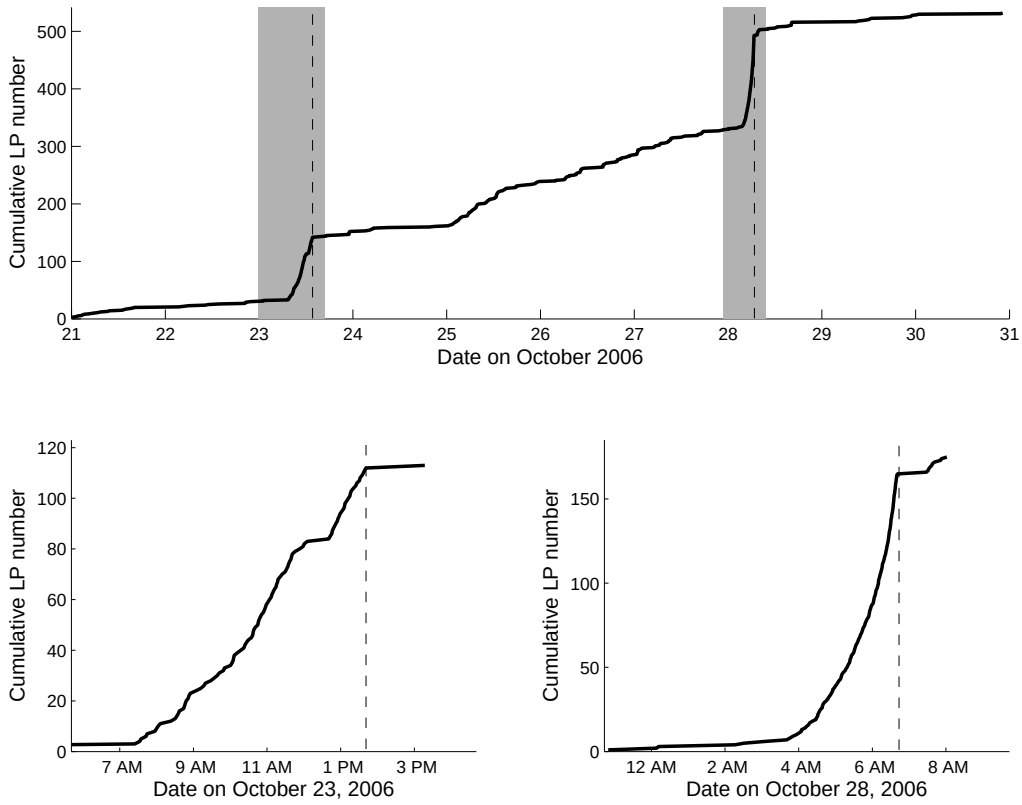

Figure 7.4: Top: Evolution of LP earthquakes at Ubinas volcano between October 21 and October 31 2006 (plain black line). Dashed lines indicate explosion occurrence times; gray boxes denote zoom time windows displayed in the bottom figures. Bottom: close-up view of the LP activity evolution prior to the two major explosions.

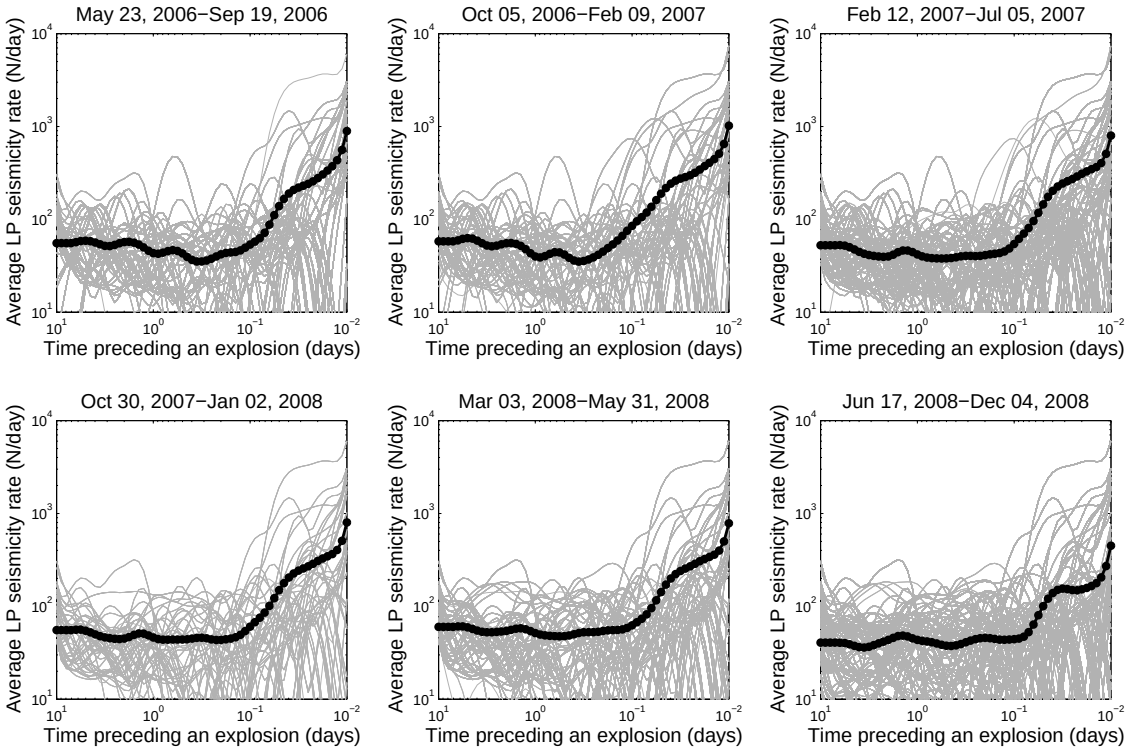

Figure 7.5: LP earthquake rate preceding explosions at Ubinas volcano during. LP rate is computed over 10 days before explosion occurrence for periods in which the seismic network was functioning for more than 10 consecutive days. Thin gray lines: LP rate before each explosion; thick black line with circles: LP event rate averaged over all explosions.

compute the temporal correlations between LP and explosion events. The average rate $R(t)$ of LP earthquakes before explosions can be written as follows:

$$R(t) = \frac{1}{TN_{expl}} \sum_{i=1}^{N_{expl}} \sum_{j=1}^{N} \Theta(t_i^{expl} - t_j^{LP} \in [t, t+T]), \tag{7.2}$$

where N_{expl} is the number of explosions in the catalog, N is the number of LP earthquakes in the catalog, T is the duration of the considered time interval, and Θ is a function such that $\Theta(P) = 1$ if P is true, and 0 otherwise. For each time interval T, we only use explosions that satisfy: $t_i^{expl} - T > t_j^{LP}$.

As shown in figure 7.6 (left), we observe an acceleration of the average LP event rate 0.1 days before an explosion onset. Being recovered during all seismic recording periods (figure 7.5), such average acceleration is not driven by a single episode pattern. LP earthquake rate preceding and following explosions is computed over a period whose duration is equal to the mean repose period between subsequent explosions, i.e. ~ 10 days. The LP rate accelerating pattern is stable when testing its dependence on the energy of the considered explosion. To do this, we divide the explosion dataset into two categories based on their explosive energy. The energy is a "duration" energy, i.e. it is calculated as the seismogram signal duration measured between the explosion onset and the time where the signal to noise ratio is 1. We define as "low energy" those explosions whose duration is less than 50 s, and "high energy" those whose duration is more than 50 s. LP rate can be computed for 140 explosions, 96 of which are classified as "low energy" and 44 as "high energy" explosions. Larger energy explosions are preceded by larger increases of LP rate, and steeper slopes of the accelerating LP rate towards explosion time (figure 7.6).

The decay of LP rate at very short times before an explosion (i.e. $< 10^{-3}$ days) may be related to inaccuracy of the explosion time, to possible incompleteness of the LP catalog very close to the explosion onset, or to the presence of tremor which prevents from distinguishing individual events.

In order to test whether LP acceleration preceding explosions does not simply arise from a statistical clustering of LP activity, we compute the average rate of LP events preceding and following another LP earthquake occurring later than 10 days after the beginning of the catalog, and earlier than 10 days before the end of the catalog (figure 7.6). As shown in figure 7.6, clustering of LP events is not negligible and, even if the LP rate is smaller for another LP event than for an explosion, LP time clustering is sufficiently

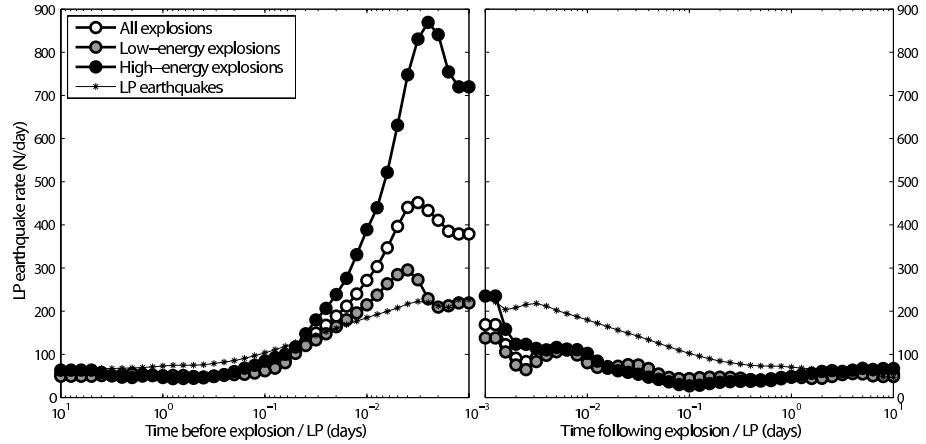

Figure 7.6: LP earthquake rate as function of time preceding and following explosions and other LP earthquakes: right and left plots, respectively. Gray scale is function of the explosion energy; white dots curve: LP rate averaged over all the explosions; black dots curve: LP rate for high-energy (i.e. duration > 50 s) explosions; gray dots curve: LP rate for low-energy (i.e. duration < 50 s) explosions; black asterisk curve: LP rate preceding and following another LP earthquake, left and right, respectively.

high to prevent one for arguing about an acceleration of LP activity before less energetic explosions. In the following we focus therefore on the 44 larger explosions in the catalog.

To note the similarity of pattern shown by the average LP rate preceding explosions and that preceding another LP event. This latter curve appears as a sort of continuum extending to still lower energy explosions. It argues for some analogy in the origin of the two processes.

It is also interesting to note that, at basaltic volcanoes, such an acceleration of seismic activity preceding eruptions has been observed 10 to 15 days before the eruption onset only when stacking several seismic time-series [*Collombet et al.*, 2003; *Chastin and Main*, 2003; *Traversa et al.*, 2009-Chapter5]. This power-law accelerating phase has been identified as the damage of the reservoir walls prior to the magma leak that initiates magma ascent towards the surface [*Collombet et al.*, 2003; *Grasso and Zaliapin*, 2004; *Traversa et al.*, 2009-Chapter5]. On the other hand, the seismicity immediately before (few hours) the eruption onset on basaltic volcanoes, is characterized by a stationary rate of shallow Volcano Tectonic (VT) events. Such a constant rate prevents any prediction of the time to eruption during the dyke propagation phase using seismicity rate alone [*Traversa and Grasso*, 2009-

Chapter2; *Traversa et al.*, 2009-Chapter5].

7.5 Predictability of explosions from LP earthquake rate on Ubinas volcano

The average acceleration of the LP earthquake rate preceding explosions on Ubinas volcano we showed in the previous section makes us think about the possibility of predicting the occurrence of an explosion few time in advance.

We follow a pattern recognition approach to predict extreme events in complex system [see *Keilis-Borok*, 2002, for a review]. A precursory process Σ to an explosion is defined in time as follows:

$$\Sigma(t, s) = \sum_i \frac{N_i}{s} \tag{7.3}$$

where the functional $\Sigma(t, s)$ is, in this case, the LP earthquake rate, and N_i is the number of observed LP earthquakes in the time window $[t-s, t]$, s being a numerical parameter. The premonitory seismicity pattern $\Sigma(t, s)$ is diagnosed by the condition $\Sigma(t, s) \geq C_\Sigma$, where the threshold C_Σ is chosen as a certain percentile of the functional $\Sigma(t, s)$ distribution.

We use this technique to predict whether an explosion will occur within the subsequent time interval $[t, t + \Delta]$. In the case $\Sigma(t, s) \geq C_\Sigma$, an alarm is declared for a time interval Δ. The alarm is relieved either, after an explosion occur, or the time Δ expires, any of the two comes first [*Grasso and Zaliapin*, 2004].

Analogously to *Grasso and Zaliapin* [2004], our prediction scheme depends on three parameters: the duration of the time window s, the threshold C_Σ, and the duration Δ of the alarm. The quality of this kind of prediction can be evaluated by using "error diagrams", introduced in seismology by *Kagan and Knopoff* [1987] and *Molchan* [1997]. Error diagrams show the trade-off between different outcomes of a prediction. In this retrospective analysis, we continuously compute the seismicity rate over windows of a given duration s, declare an alarm when the functional $\Sigma(t, s)$ exceeds the threshold C_Σ, and count the prediction outcomes (figure 7.7).

Over a number A of alarms issued, A_f happen to be false, N_e explosions occur, of which A_s are successfully predicted, and A_m are missed (figure 7.7). Altogether, the alarms issued cover a time D. Performance of the algorithm is characterized by three dimensionless parameters. The total relative duration of alarm $\tau = D/T$, where T is the

overall considered period; the rate of failures to predict $f_p = A_f/N_e$; and the rate of false alarms $f_a = A_s/A$. The values of τ, f_p and f_a are then reported on the error diagrams, which allow to quantify the goodness of a given prediction (figure 7.8) that depends on the three parameters s, C_Σ and Δ. Each point on the graph, thus, tells the reader successes and failures of a three-parameter prediction algorithm. The rise of the threshold C_Σ, for example, reduces the number of issued alarms, but may increase the number f_p of failures to predict. Rising the duration Δ of the alarm time window, on the other hand, will increase the relative duration τ of issued alarms, but reduce the number of failures to predict.

Following the results shown in figures 7.5 and 7.6, the parameters tested in this work are varied as follows: $0.005 < s < 0.1$ days, $50 < C_\Sigma < 400$ events per s days, $0.01 < \Delta < 1$ day. The results are stable no matter the chosen parameter values within these intervals. As illustrated in the error diagram (figure 7.8, left), the prediction algorithm is validated, i.e. its performance is better than the random guess during all the periods in which the Ubinas seismic network is working. Error diagram in figure 7.8 (right) allows to evaluate the counterpart of our prediction scheme, i.e. the amount of false alarms that the prediction algorithm would have issued for each parameter combination. To show it clearer, we isolate the error diagrams for the October 5, 2006 to February 9, 2007 period (figure 7.9). Here we are able for example to predict 63% of the largest explosions with 17% of the time of alarm activated (point A on figure 7.9, left). This correspond to a 58% of false alarm (figure 7.9, right). By increasing the duration of the time covered by an alarm (e.g. to 20%) we can predict a higher percentage of explosions (i.e. 75%), but the amount of false alarms rise drastically to 80%.

Grasso and Zaliapin [2004] predict 65% of Piton de la Fournaise eruptions with 20% of the time covered by alarms. They use 5 day window for computing the Volcano-Tectonic seismicity rate and declare alarms during 5 days. This leads however to a 90% of false alarms. Similarly, *Mulargia et al.* [1991, 1992], using regional seismicity in a 120 km radius around Etna volcano, predicts 50% of Etna eruptions (i.e. 80% of the 11 flank eruptions) in the 1974-1990 period. None of the summit eruptions can be however predicted. On Ubinas volcano, the 63% of the largest explosions predicted with 17% of the time covered by an alarm, face to a 58% of false alarm, argues for the LP seismicity rate to be a "better" precursor to explosions on andesitic volcanoes than the VT seismicity rate to effusive eruptions on basaltic volcanoes [*Mulargia et al.*, 1991, 1992; *Grasso and Zaliapin*, 2004].

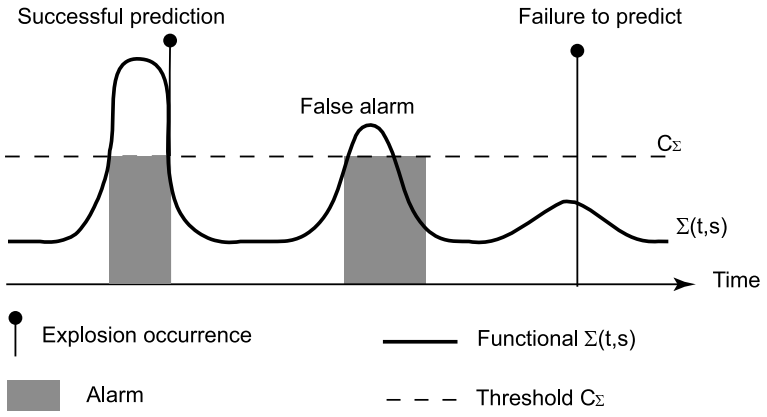

Figure 7.7: Prediction scheme and prediction outcomes, modified from *Keilis-Borok* [2002] and *Grasso and Zaliapin* [2004].

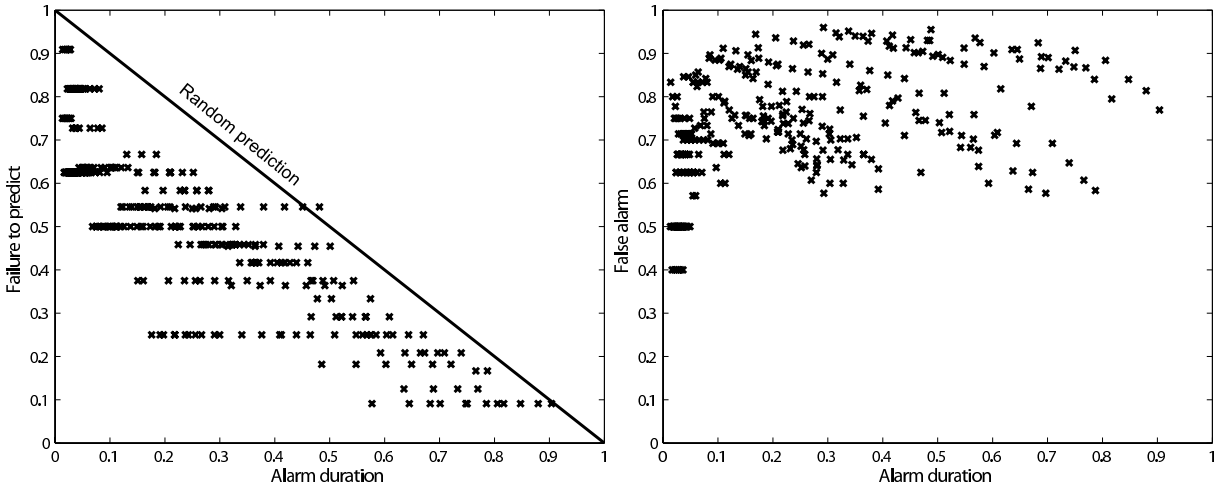

Figure 7.8: Error diagrams for prediction evaluation, exploration of the space parameters. The three parameters are varied as follows: $0.005 < s < 0.1$ days, $200 < C_\Sigma < 400$ events per s days, $0.01 < \Delta < 1$ day. Left: fraction of failures to predict as a function of alarm duration. The diagonal line corresponds to a random prediction. Deviations fro this line depict predictive power of the considered functional, i.e. the LP earthquake rate. Right: fraction of false alarms as a function of alarm duration.

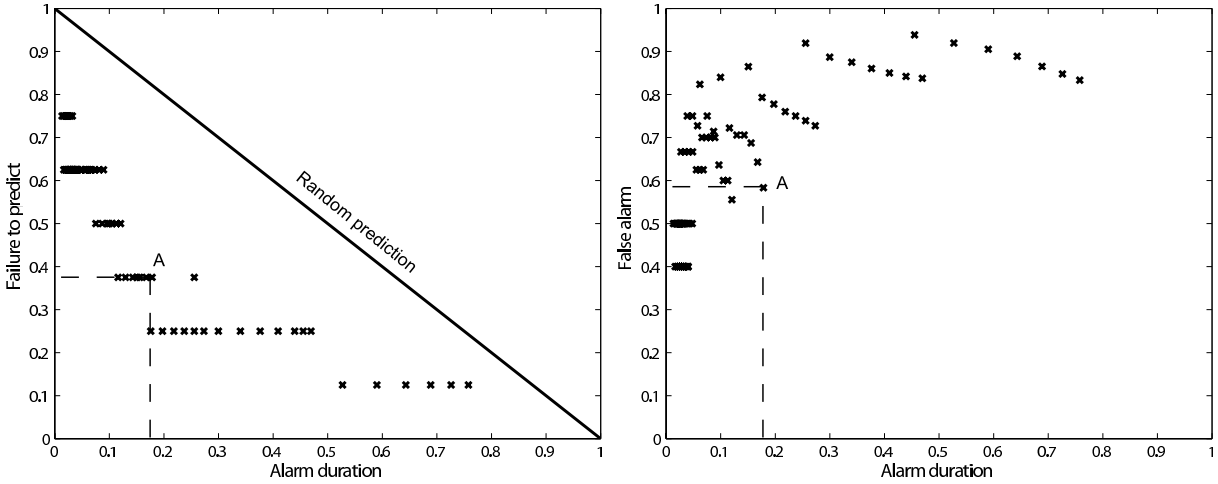

Figure 7.9: Error diagrams related to different combination of prediction parameters during the period October 5, 2006 - February 9, 2007. parameters are varied as follows: $0.005 < s < 0.1$ days, $200 < C_\Sigma < 400$ events per s days, $0.01 < \Delta < 1$ day. $s = 0.03$ days. Left: fraction of false alarms as a function of alarm duration. The diagonal line corresponds to a random prediction. Deviations fro this line depict predictive power of the considered functional, i.e. the LP earthquake rate. Right: fraction of false alarms as a function of alarm duration. Point A on the diagrams indicates a parameter combination allowing to predict 63% of Ubinas explosions with 17% of time covered by alarm and a 58% of issued alarms resulting false.

7.6 Discussion and conclusions

Observations of Long Period seismicity prior to explosions on Ubinas volcano show an accelerating pattern of the event rate toward explosion occurrence. This observation supports the hypothesis of LP events to be an indicator for a "charging mechanism" within a pressurized magmatic system. It highlights the significance of this type of seismic activity in the understandings of volcano dynamics. We test this observed pattern against a possible statistical tendency of LP events to cluster in time around another LP event. This allows us to validate the LP rate acceleration towards an explosion as significant only prior higher energy explosions (i.e. explosions characterized by a signal duration larger than 50 s). It questions for the possibility that the more the incoming explosion will be violent, the higher the LP seismicity rate will rise prior to explosion onset. This would imply a larger predictability for stronger than weaker explosions on Ubinas volcano. The continuum the LP rate behavior prior to an explosion and prior to another LP event form, however, questions about a possible common source mechanism for the two phenomena.

At silicic volcanoes LP events and tremor are found to share common spectral characteristics [*Chouet*, 1996; *Neuberg et al.*, 2000], and likely the same source process [e.g. *Neuberg et al.*, 2000; *Neuberg and Pointer*, 2000]. Accordingly, since it may mask the acceleration of LP events prior to an explosion at Ubinas volcano, the occurrence of tremor is noise when aiming at explosion forecasting.

On these basis we build a forecasting algorithm based on pattern recognition which uses LP event rate prior to explosion as the precursor. The prediction scheme relies on three parameters, the duration of the time window s used to compute the LP rate, the threshold value C_Σ whose exceeding causes an alarm to be activated, and the duration of the alarm window Δ. Reporting the results of the prediction algorithm on error diagrams allows us to estimate the goodness of the prediction for each combination of the three parameters. We show that the prediction results are stable and the forecasting algorithm validated, i.e. its performance is better than the random guess.

In order to improve on the prediction ability of the proposed algorithm, a statistic analysis on the temporal distribution patterns of explosion occurrence should be carried out. This will allow to identify a priori possible periodicities in the occurrence of explosions. During the 2006-2008 period, however, this is impossible due to the frequent interruptions of the seismic monitoring network.

LP seismicity is thought to be originated within the fluid, and therefore to be representative of the pressurization state of the volcano plumbing system, the state of the fluid, and the interactions between the fluid and the rock matrix [e.g. *Chouet*, 1996; *Neuberg et al.*, 1998; *Neuberg*, 2000; *Chouet*, 2003; *Sparks*, 2003; *OâĂŹBrien and Bean*, 2004; *Lokmer et al.*, 2007]. LP earthquakes are generally observed to occur in swarms, within which families of events with similar waveform have been recognized [e.g. *Chouet*, 1996; *Neuberg*, 2000; *Neuberg et al.*, 2006; *Lokmer et al.*, 2007; *Saccorotti et al.*, 2007]. This points to a repeatable, non-destructive source mechanism at a fixed location [e.g. *Chouet*, 1996; *Neuberg*, 2000; *Saccorotti et al.*, 2007].

Although the triggering mechanism of LP earthquakes is still debated, source models proposed for this type of events involve the resonance (i.e. harmonic oscillation) and the transport of fluid in a cavity within a magmatic or a hydrothermal system [e.g. *Chouet*, 1988, 1996; *Neuberg*, 2000; *Neuberg et al.*, 2000; *Cusano et al.*, 2008]. The low-frequency content of LP events has made many authors suggest they originate at the interface between the fluid and the surrounding rock [e.g. *Chouet*, 1988; *Neuberg*, 2000; *Neuberg et al.*, 2000; *Saccorotti et al.*, 2007]. Most of the seismic energy is trapped in the fluid-filled conduit, leading to resonance, and only a part propagates through the solid medium and is recorded by the seismic network [e.g. *Neuberg et al.*, 2006].

The triggering mechanisms that have been proposed in literature to kick-start the resonance include magma flow instabilities [*Julian*, 1994], magma-water interactions [*Zimanowski*, 1998], pressure drops (as ash venting or degassing events) [e.g. *Johnson and Lees*, 2000; *Neuberg*, 2000], and periodic release of gas-ash mixtures into open cracks [*Molina et al.*, 2004]. These latter mechanisms would imply a significant increase of gas emissions prior to explosions. A correlation between gas emissions and explosions is indeed observed on Ubinas volcano [*Macedo et al.*, 2009]. Combination of seismic and geochemical monitoring may thus allow to improve prediction on Ubinas explosion occurrence.

Recently, a quite revolutionary triggering mechanism has been proposed for the generation of LP seismicity. It involves the seismogenic fracture of magma [*Goto*, 1999; *Tuffen et al.*, 2003; *Neuberg et al.*, 2006; *Gonnermann and Manga*, 2003; *Tuffen et al.*, 2008]. Brittle failure of fluid silicic magmas has been suggested to occur when the product of magma viscosity and strain rate exceeds a certain threshold [*Goto*, 1999]. Gas exolution induces increases of magma viscosity and liquidus temperature. As a consequence, magma crystallization is promoted. The existence of crystals, in turn, heightens the strain rate of the melt,

and generates yield strength (which heightens the strain rate at a macro-scale) [*Goto*, 1999; *Melnik and Sparks*, 1999]. In this framework, brittle failure of high temperature magma can occur near the conduit walls, where flow takes place [*Goto*, 1999], i.e. stick-slip of magma at the conduit wall. Field evidence for brittle fracture of high temperature, high viscosity magma has been reported by *Tuffen et al.* [2003] at Torfajökull volcano (Iceland). The authors suggest observations of tuffisite veins are the trace of shallow, repeated cycles of fracture and healing of high viscosity magma. *Tuffen et al.* [2003] suggest these repeated fractures of the same magma body responding to stress accumulations are the rechargeable trigger mechanism for the observed low frequency seismicity. They demonstrate that such cycles result in a repeated stress built-up with minimum repeat times of the order of few seconds, which agrees with the occurrence frequency of LP events.

Such an evidence poses the basis for agreement between the models supporting LP to be generated within the fluid, and the work of *Harrington and Brodsky* [2007], who demonstrate, through source inversion, that observed low-frequency signals can be explained simply by brittle-failure combined with path effects and low rupture velocities. The idea of LP to be brittle fracture signals is also supported by the scale invariance we observe when considering LP event size, as computed by event duration (figure 7.10). This event size distribution is the known Gutenberg-Richter law characterizing brittle failures (e.g. tectonic, volcano tectonic, micro-cracking). It may also explain the fact that LP rate preceding another LP event shows the same pattern as LP rate preceding explosions (figure 7.6). The slope of the LP rate acceleration appears to be related to the energy of the impending explosion, with stronger acceleration prior to higher energy explosions. Accordingly, the slope of LP rate increase before another LP event looks as a continuum from higher to weaker energy explosions.

On these bases, and on seismic observations at Soufriere Hills (Montserrat), *Neuberg et al.* [2006] propose a conceptual model for LP seismicity triggered by brittle failure of rising magma in the glass transition, where the shear stress exceeds a critical value. The trigger position remains at the same depth, and the seismic energy is trapped into a resonator, forming the low-frequency coda of observed signals.

Gonnermann and Manga [2003] draw on this idea of shear fracture of the melt to demonstrate that this shear-induced fragmentation, by allowing for degassing via increased permeability at the conduit wall, may reduce the dynamic pressures in the conduit, and therefore reduce the likelihood for explosive behavior. This idea is supported by the corre-

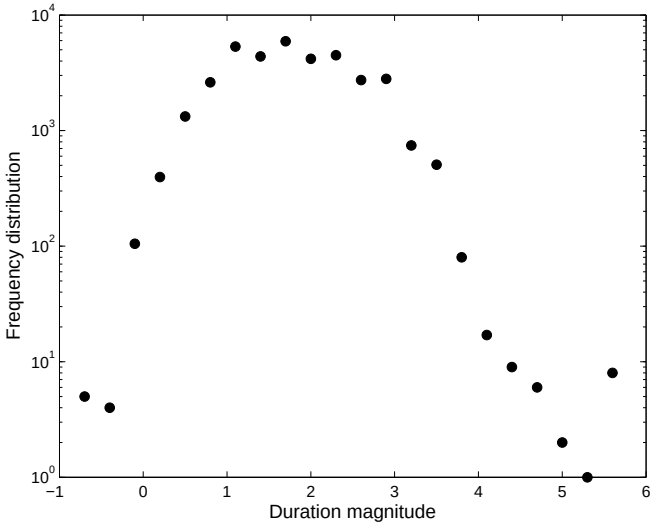

Figure 7.10: Duration magnitude M_D frequency distribution for low-frequency events recorded on Ubinas volcano in the period 2006-2008. M_D is computed as: $M_D = 2.75(T) - 2.35$, where T is the signal duration. This formula is used to compute VT earthquake magnitude at Vesuvius volcano [Gruppo - Lavoro - Sismometria].

lation observed on Ubinas volcano between gas emission bursts and LP event occurrence [*Macedo et al.*, 2009].

Tuffen et al. [2008], through acoustic emissions recorded during experimental deformation of silica-rich magmas under simulated volcanic conditions, bring new evidence for seismogenic fracture of high-temperature magma during ascent in the shallow conduit.

All these suggest a sort of common mechanism responsible for low-frequency earthquake and explosion generation, i.e. brittle damage of lava. In the first case, bubble growth induce pressure increase in the magma conduit, face to an increase of viscosity and strain rate in the rising magma. When the shear stress at the conduit walls exceeds a critical value, magma cyclingly fractures and heals, generating low-frequency events. As bubbles grow more and more, however, fragmentation leads to the explosive behavior. The degassing possibly resulting from shear-fracture of magma a the conduit walls, may delay the explosion occurrence by partly relaxing the overpressure.

In this framework, cycles of magma shear-fracturing may be indicative of pressurization processes within the conduit, which periodically relaxes through LP earthquake production. Eventually, rising growing bubbles may be too large and a fragmentation over

the whole conduit may occur, which causes the explosion.

General Conclusions

The study of volcano seismicity recorded on volcano surface during different phases of volcanic activity has enabled us to pursue a double objective. On one hand to shed light on the physics driving underlying active magma processes, as tracked by seismicity. On the other hand to explore and quantify the mechanisms that govern the generation of seismic events as the result of (i) the perturbation induced by the volcano forcing, and (ii) the earthquake interactions.

We have used temporal patterns of seismic occurrence to derive physical and mechanical implications about the active volcano process. We have investigated the role of earthquake triggers during different phases of volcanic activity from both, a deterministic (i.e. a stress triggering model) and a stochastic (i.e. a point process cascading model) points of view (Chapters 4 and 6). Results have been compared to the behavior we expect for the "classic" tectonic activity case. Accordingly, this work has explored the origins of the peculiarities shown by seismicity triggered by volcano processes when compared to ordinary tectonic seismicity.

We have used the brittle response (i.e. Volcano Tectonic (VT) seismicity) of the solid matrix during different phases of volcanic activity as a sensor that allows to capture the physics governing underlying magmatic processes (Chapters 2, 3, 4 and 5). In this framework, we are interested in identifying the fraction of recorded seismicity that is directly driven by a given active magma process over the fraction issued from earthquake interactions (Chapters 4 and 6). This latter is noise that prevents us from a direct mapping of the seismicity rate onto the volcano processes.

Brittle damage recorded at basaltic volcanoes allows to separate three phases describing the reservoir dynamics leading to an eruption (Chapters 2 and 5). An exponentially accelerating VT seismicity is interpreted as the long-term (years) replenishment of the storage area (the reservoir feeding phase). An average power law increase of the VT seismicity

rate 1-2 weeks before an eruption is identified as the damage of the reservoir walls prior to magma leak (reservoir leak phase). During the ultimate phase (hours) prior to eruption onset, the stationary rate of shallow VT events is associated with the dyke propagation phase. The seismicity rate during this last phase before an eruption sharply gets 2-3 orders of magnitude larger than during the previous two phases. It question for the first two phases to be associated to a higher ductility medium when compared to the more brittle shallow edifice.

The stationary rate observed during dyke intrusions at basaltic volcanoes prevents for making any prediction on eruption time using seismicity alone (Chapter 2). This is not any more the case when looking at the very last phase before an explosion on andesitic volcanoes, where an acceleration of Long Period (LP) earthquakes few hours before an explosion is recovered on Ubinas volcanoes in the period 2006-2008 (Chapter 7). It has allowed us to set up a forecasting algorithm able to send an alarm on explosion occurrence few hours in advance.

After having defined clear and recurrent seismicity patterns associated to isolated phases of magmatic activity at basaltic volcanoes (Chapter 4), we have focused on the very last phase before an eruption, i.e. the dyke intrusion. The stationarity we have observed for both, VT seismicity and seismic energy release rates argues for the intrusion to be a steady state brittle creep process (Chapter 2). It suggests that the seismic response of the shallow edifice to a magmatic intrusion is independent of the intrusion scale and deaf to both, geometric and mechanic heterogeneities of the dyke propagation. We have not resolved any cascading process within this strain driven system. It contrasts with clear earthquake interactions (i.e. the Omori's law following a mainshock) observed away from intrusions (Chapter 6). Such behavior has lighted on the seducing idea of a seismicity directly driven by the magma process accompanying the intrusive process.

Observations of rate stationarity, despite possible variations of the dyke tip velocity, are associated to (i) a frequent lack of clear and monotonic hypocenter migration following dyke propagation, (ii) backward event locations with respect to the dyke tip and (iii) event mechanisms that cannot be associated to tensile mode I fracture. Most of the seismicity contemporary to dyke propagation is in fact diffuse within the edifice and its triggering mechanism is typical of shear brittle fracture (Chapter 2 and 3). All these suggest that the seismicity accompanying dyke intrusion does not directly map the propagating dyke tip, but is instead the response of the volcano edifice to the volumetric deformation induced by

the magma intruding the solid matrix. In this framework, the stationary seismicity rate characteristic of dyke propagation at basaltic volcanoes, is a proxy for a constant flow rate of magma entering the dyke in the unit time (Chapters 2 and 3).

Using a two-phase dyke propagation numerical model we have explored both, under which geophysical conditions a rising dyke is fed at constant flow rate of magma, and the dyke propagation patterns (Chapter 3). We have demonstrated that dyke tip velocity depends on dyke size and dyke growth evolution. Then, while the propagation velocity varies of one order of magnitude between the vertical and lateral propagation phases (as commonly observed at basaltic volcanoes), the flux of magma can remain constant all along the propagation. It supports the idea of a direct scaling between the magma flux intruding the solid matrix and the observed VT seismicity rate, while it rejects a direct scaling between the seismicity rate and the dyke propagation velocity.

In agreement with fluid dynamics laws, the constant magma flux can be sustained by either, constant or slightly variable overpressure at the dyke inlet. This result demonstrates that the two apparently competing boundary conditions that have been proposed in literature for dyke propagation modeling (i.e. of a constant influx and of a constant overpressure at the dyke inlet) can co-exist and are not mutually excluding. We have demonstrated that only a magma reservoir with sufficiently small initial overpressure and sufficiently large volume is able to sustain a dyke injection fed at constant flux (Chapter 3).

The fact that the volume change induced by the intruding magma in the unit time scales with the observed seismicity rate supports that the stressing rate governs the seismicity associated with the intrusive process (Chapter 4). Assuming a simple Coulomb stress model for earthquakes and a rate and state dependent friction law, we have used observed seismicity during the 2000 Izu Island volcanic-induced seismic swarm to quantify the stress history to which the system is subject, i.e. the forcing represented by the intrusion. The stress perturbation induced by an intruding dyke can be described by a long-lasting and temporally evolving stressing rate change forced on the system. Accordingly, the intrusion can be assimilated to a sort of "60-day-long-lasting" silent earthquake, in contrast with the sudden stress step induced by the coseismic slip at the time of earthquake occurrence. The continuously active forcing induces a sort of damped behavior in the system, in which seismic occurrence is continuously supported by the stress perturbation. True relaxation of the system is therefore prevented until the forcing vanishes. At this very moment the

system, oblivious of the process that has perturbed it, relax in an Omori's law style, simply responding to the vanishing of the stress perturbation. In this sense, the only difference between a mainshock-aftershock style and a volcanic swarm systems, lies on the duration of the forcing imposed to the system (Chapter 4). The exploration of the 2000 Izu seismic swarm has also allowed to investigate the spatio-temporal characteristics of the seismicity induced by such a long lasting forcing, and to compare them with the patterns we would have expected for the seismicity induced by a large mainshock occurrence at tectonic environments (Chapter 4).

As mentioned above, when using temporal patterns of earthquake occurrence during dyke propagation at different basaltic volcanoes, we have recovered a constant seismicity rate within which no Omori's law like pattern could be resolved. We have been tempted to conclude that all the observed seismicity were generated by the intrusion, while the strong forcing rate acting during this phase did not allow for stresses to redistribute and for aftershocks cascades to develop following each shock (Chapter 2). Actually, this missing mainshock-aftershock pattern we have noticed during dyke intrusions, is not a sufficient condition to assert a lack of earthquake-interaction-induced events and a consequent complete control of the intrusion on the generated seismicity. Statistics of interevent times between subsequent events and the other available declustering techniques, however have demonstrated to be ineffective for seismic time series contemporary to dyke intrusions (Chapter 6). This has prevented us from quantifying the correlated fraction of seismicity (i.e. the part generated by earthquake interaction) versus the uncorrelated one (i.e. the part generate by the volcano forcing).

When using statistics of interevent times to explore the mechanisms governing earthquake interactions for different phases of volcanic activity we have realized, however, that the apparently lost interaction between earthquakes for the intrusion case, is due to an overlapping of aftershock sequences that masks the existence of clusters of correlated seismicity (Chapter 6). The high forcing rate acting during a dyke intrusion is responsible for a corresponding increase in the background seismicity rate. The time separating Poisson uncorrelated events becomes therefore comparable to the waiting time between subsequent events within Omori clustered sequences. These sequences of correlated events therefore overlap, and events of the considered time series result completely uncorrelated.

When using the rate and state formulation for the 2000 Izu Island dyke-induced swarm, we quantify a 30% of the recorded seismicity to be directly driven by the dyke

intrusion (Chapter 4). This result conflicts with the previous observation of seismicity becoming more and more uncorrelated as the the background seismicity rate increases (Chapter 6). It argues for correlated sequences of events generated by earthquake interaction mechanisms to be hidden behind the stationary seismicity rate induced by a strong forcing rate. In this sense the uncorrelated part of seismicity in a point process model for seismicity is not any more representative of the events directly driven by the external forcing when such a forcing is "too strong", i.e. it induces a background seismicity rate whose recurrence time is comparable with that of the cluster of events following a mainshock. In this framework, such sequences are not recoverable when considering the seismic time series as a point process composed of an uncorrelated and a correlated part of seismicity (Chapter 4). It explains the reason why available declustering techniques fail in quantifying these two quantities when a strong external forcing is acting on the system.

Future research directions should be oriented towards the definition of a way to trace the external forcing as tracked by background seismicity even when individual seismic sequences overlap. This would be essential for statistical studies of seismic time series when no information is available on the host rock properties or the regional stress field characteristics. Adaptation of existing declustering techniques for non-stationary seismic time series, moreover, will improve on the understandings of seismic swarms in general.

Conclusions Générales

L'étude de la sismicité volcanique enregistrée à la surface de plusieurs volcans pendant des phases diverses de l'activité volcanique nous a permis de poursuivre un double objectif. D'un coté d'utiliser la sismicité pour éclaircir et approfondir les connaissances sur la physique qui gouverne les processus magmatiques actifs. D'un autre coté d'explorer et de quantifier les mécanismes qui gouvernent la génération des événements sismiques qui est le résultat de (i) la perturbation induite par le forçage volcanique, et (ii) les interactions entre les séismes. Nous avons utilisé les motifs temporels d'occurrence sismique afin de dériver des implications physiques et mécaniques concernant le processus volcanique actif. Nous avons investigué le rôle joué par l'interaction entre les séismes dans le déclenchement de l'activité sismique pendant plusieurs phases de l'activité volcanique en utilisant deux points de vue : le déterministe (un modèle de déclenchement par changement de contrainte) et le stochastique (un modèle de déclenchement en cascade) - chapitres 4 et 6. Les résultats ont été comparés avec le comportement attendu pour le cas de l'activité tectonique "classique". Dans ce sens, ce travail a exploré les origines de la particularité qui caractérise la sismicité déclenchée par des processus volcaniques par rapport à la sismicité tectonique ordinaire. Nous avons utilisé la réponse fragile (c'est à dire la sismicité Volcano Tectonique - VT) de l'encaissant pendant plusieurs phases de l'activité volcanique comme un senseur qui nous permet de "capturer" la physique qui gouverne les processus magmatiques qui agissent en profondeur - Chapitres 2, 3, 4 et 5. Dans ce cadre, nous sommes intéressés à distinguer la fraction de sismicité enregistrée qui est gouvernée directement par un certain processus magmatique actif de celle qui est liée aux interactions entre les séismes - Chapitres 4 et 6. Ce dernier représente pour nous du bruit qui nous empêche d'établir une relation directe entre le taux de sismicité et le processus volcanique. L'endommagement enregistré aux volcans basaltiques nous permet de séparer trois phases qui décrivent la dynamique du réservoir qui mène à une éruption - Chapitres 2 et 5. Une accélération exponentielle de la sismicité VT est interprétée comme le remplissage de l'aire de stockage à longue échelle

(années): l'alimentation du réservoir. Une augmentation moyenne en loi de puissance du taux de sismicité VT 1-2 semaines avant l'éruption est associée avec l'endommagement des parois du réservoir avant la fuite de magma (fracturation du réservoir). Pendant la dernière phase (heures) avant le début de l'éruption, le taux stationnaire d'événements VT superficiels est associé avec la phase de propagation du dyke. Le taux de sismicité pendant cette dernière phase avant une éruption dépasse brusquement de 2-3 ordres de grandeur celui qui accompagne les deux phases précédentes. Cela pose des questions sur le fait que les premières deux phases soient associées à un milieu plus ductile par rapport à l'édifice superficiel. Le taux stationnaire observé pendant les intrusions aux volcans basaltiques empêche toute prédiction du moment de l'éruption à partir des seules données de sismicité - Chapitre 2. Cela n'est plus le cas quand l'on considère la toute dernière phase qui précède une explosion sur un volcan andésitique. Pour le volcan de l'Ubinas (Pérou), en effet, nous observons une accélération du taux d'événements Longue Période (LP) quelques heures avant l'explosion sur la période 2006-2008 - Chapitre 7. Cela nous a permis de concevoir un algorithme de prédiction capable d'envoyer une alerte quelques heures en avance par rapport à l'occurrence d'une explosion. Après avoir défini des motifs de sismicité claires et récurrents associés à des phases isolées d'activité magmatique sur des volcans basaltiques (Chapitre 4), nous avons concentré notre attention sur la toute dernière phase précédente une éruption, c'est à dire l'intrusion du dyke. Nous avons observé que la sismicité VT et l'énergie sismique relâchée suivent un régime stationnaire au cours du temps. Cela suggère que l'intrusion est un processus de fluage fragile de type "Steady State" (Chapitre 2). De plus, la réponse sismique de la partie superficielle de l'édifice volcanique est indépendante de l'échelle de l'intrusion et sourde envers les hétérogénéités géométriques et mécaniques liées à la propagation du dyke. Dans le cadre de ce processus gouverné par la déformation, nous n'avons pas résolu de processus en cascade. Cela contraste avec les interactions entre les séismes (c'est à dire la loi d'Omori qui suit l'occurrence d'un choc principal) clairement observées en dehors des phases intrusives (Chapitre 6). Ce comportement nous a inspiré la séduisante idée d'une sismicité gouvernée directement par le processus magmatique qui accompagne l'intrusion. Les observations du taux de sismicité stationnaire, en dépit de possibles variations de la vitesse de la pointe du dyke, sont associées à (i) un manque fréquent de migration des hypocentres claire et monotonique avec la propagation du dyke, (ii) des localisations d'événements en arrière par rapport à la pointe du dyke, et (iii) des mécanismes au foyer qui ne peuvent pas être associés à de la fracture en mode I (c'est à dire en traction). La plus grande partie de la sismicité contemporaine à la propagation du dyke est par contre diffuse à l'intérieur de l'édifice, et son

mécanisme focal est typique de la fracture en cisaillement (Chapitre 2 et 3). Tout cela suggère que la sismicité qui accompagne l'intrusion d'un dyke ne reflète pas directement la position de la pointe du dyke qui se propage, mais elle est plutôt la réponse de l'édifice volcanique à la déformation volumétrique induite par le magma qui s'introduit dans la matrice solide. Dans ce cadre, le taux de sismicité stationnaire qui caractérise la propagation des dykes sur les volcans basaltiques, implique en quelque sorte un débit de magma constant qui entre dans le dyke dans l'unité de temps (Chapitres 2 et 3). Grâce à un modèle numérique de propagation de dyke en deux phases, nous avons exploré sous quelles conditions géophysiques un dyke qui remonte vers la surface peut être alimenté à flux de magma constant, et quels sont les motifs caractéristique de la propagation du dyke (Chapitre 3). Nous avons démontré que la vitesse de la pointe du dyke dépend de la taille et de l'évolution de la croissance du dyke. Alors, au même temps que la vitesse de propagation varie d'un ordre de grandeur entre les phases de propagation verticale et latérale (comme il est fréquemment observé sur des volcans basaltiques), le flux de magma peut rester constant tout le long de la propagation. Cela suggère qu'il existe une proportionnalité directe entre le flux de magma qui s'introduit dans la matrice solide et le taux d'événements VT observé. D'un autre coté, cela rejette l'hypothèse d'une proportionnalité directe entre le taux de sismicité et la vitesse de propagation du dyke. En accord avec les lois de la dynamique des fluides, le débit constant de magma peut êre soutenu par une surpression constante ou faiblement variable à l'entrée du dyke. Ce résultat démontre que les deux conditions limite proposées en littérature pour modéliser la propagation des dykes (c'est à dire de flux constant de magma et de surpression constante à l'entrée du dyke), qui apparaissent en compétition l'une avec l'autre, peuvent co-exister et ne sont pas exclusives l'une par rapport à l'autre. Nous avons démontré que seulement un réservoir caractérisé par une surpression initiale suffisamment petite et un volume suffisamment large, est capable de soutenir l'injection d'un dyke alimenté à flux constant (Chapitre 3). Le fait que le changement de volume induit par le magma introduit dans l'édifice dans l'unité de temps est proportionnel au taux de sismicité observé, suggère que le taux de contrainte dirige la sismicité associée au processus intrusif (Chapitre 4). Si l'on assume un simple modèle de contrainte de Coulomb pour les séismes, et une loi de friction du type "Rate-and-State", nous pouvons utiliser la sismicité observée pendant l'essaim sismique d'origine volcanique enregistré en 2000 aux îles Izu (Japon) pour retracer quantitativement l'histoire de contrainte à laquelle le système est soumis, c'est à dire le forçage représenté par l'intrusion. La perturbation de contrainte induite par un dyke qui s'introduit dans l'édifice volcanique peut être décrite par un changement de taux de contrainte de longue durée qui évolue dans le temps

forcé sur le système. Dans cette optique, l'intrusion peut être assimilée à une sorte de séisme silencieux d'une durée de 60 jours. Cela en contraste avec le changement de contrainte brusque induit par le glissement co-sismique à l'instant où un séisme se produit. Ce forçage qui agit de manière continue induit une sorte de comportement amorti du système, où la production des séismes est continuellement alimentée par la perturbation de contrainte. La vraie relaxation du système est donc empêchée jusqu'au moment où le forçage externe s'évanoui. C'est à ce moment que le système, oublieux du processus qui vient de le perturber, se relaxe selon la loi d'Omori, c'est à dire qu'il répond simplement à l'évanouissement de la perturbation de contrainte. Dans ce sens, la seule différence entre un système caractérisé par un style choc principal - répliques et un essaim volcanique réside sur la durée du forçage imposé au système (Chapitre 4). Comme nous l'avons mentionné précédemment, les motifs temporels d'occurrence de séismes pendant la propagation de dyke sur différents volcans basaltiques sont indicateurs d'un taux de sismicité constant au sein duquel nous n'avons pas pu retrouver le style d'Omori classique. Nous avons été tentés de conclure que toute la sismicité observée était générée par l'intrusion, alors que le fort taux de forçage actif pendant cette phase ne permettrait pas aux contraintes de se redistribuer et à la cascade de répliques de se développer suite à l'occurrence d'un choc (Chapitre 2). En réalité, ce manque de motif choc principale-répliques que nous avons observé pendant l'intrusion de dyke ce n'est pas une condition suffisante pour conclure un manque d'événements induits par interaction entre séismes et donc un contrôle complet de l'intrusion sur la sismicité générée. Qui plus est, l'étude des statistiques des temps d'attente entre séismes qui se suivent et les autres techniques de declustering disponibles se sont démontrées inefficaces si appliquées aux séries temporelles de sismicité contemporaines aux intrusions de dykes (Chapitre 6). Ces techniques ont échoué afin de quantifier les fractions de sismicité corrélée (c'est à dire la part générée par l'interaction entre les séismes) et decorrélée (c'est à dire la partie induite par le forçage volcanique). Ensuite nous avons utilisé les statistiques des temps d'attente entre séismes consécutifs avec le but d'explorer les mécanismes qui gouvernent les interactions entre les séismes pendant différentes phases de l'activité volcanique. C'est à ce point que nous avons réalisé que la perte apparente d'interaction entre les séismes qui caractérise la phase intrusive, est due en réalité à une superposition des séquences de répliques qui masque les "clusters" de sismicité corrélée (Chapitre 6). Le taux de forçage très élevé qui caractérise l'intrusion d'un dyke est responsable de l'augmentation du taux de sismicité de fond. Le temps qui sépare les événements Poissoniens decorrélés devient alors comparable aux temps d'attente entre événements consécutifs au sein des séquences d 'événements corrélés d'Omori.

Ces d'événements corrélés, partie d'une séquence, donc, se superposent, et les événements des séries temporelles considérées apparaissent complètement decorrélés. En appliquant une formulation du type "Rate and State " lors de l'essaim sismique déclenché par la gigantesque intrusion de dyke qui s'est produite en 2000 aux îles Izu (Japon), nous avons quantifié un 30% de sismicité directement dirigée par le dyke en intrusion (Chapitre 4). Ce résultat est en opposition avec la précédente observation d'une sismicité de plus en plus decorrélée au fur et à mesure que le taux de sismicité de fond augmente (Chapitre 6). Cela suggère que les séquences d'événements corrélés générées par mécanismes d'interaction entre les séismes sont dissimulées derrière le taux de sismicité stationnaire induit par le fort taux de forçage. Dans ce cadre, la partie decorrélée d'un modèle de sismicité "point process", n'est plus représentatif des événements directement dirigés par le forçage externe quand celui-ci devient "trop fort", c'est à dire quand il génère un taux de sismicité de fond dont le temps de récurrence est comparable avec celui des séquences d'événements qui suivent un choc principal. Dans ce cadre, ces séquences ne peuvent plus être repérées lors qu'on considère les séries temporelles de sismicité comme un "point process" constitué par une partie corrélée et une partie decorrélée (Chapitre 4). Cela explique la raison pour laquelle les techniques de declustering existantes échouent à quantifier ces deux parties lorsqu'un fort taux de forçage externe agit sur le système. Des directions futures de recherche devraient être orientées vers la définition d'une manière de tracer le forçage externe à partir de la sismicité de fond même dans le cas où les séquences particulières se superposent. Cela résulte essentiel dans le cadre d'études statistiques sur de séries temporelles de sismicité lorsque l'information sur les propriétés de l'encaissant ou les caractéristiques du champ de contrainte régional ne sont pas disponibles. En outre, l'adaptation des techniques existantes de declustering pour des séries temporelles non-stationnaires, pourra améliorer la compréhension des essaims sismiques en général.

Appendix A

Line Creep in Paper Peeling

Jari Rosti[1], Juha Koivisto[1], Paola Traversa[2], Xavier Illa[1], Jean-Robert Grasso[2] and Mikko J. Alava[1]

[1] Department of Engineering Physics,
Helsinki University of Technology, 02015 HUT, Espoo, Finland

[2] Laboratoire de Géophysique Interne et Tectonophysique,
CNRS - OSUG - Univeristé Joseph Fourier, BP 53 38041 Grenoble Cedex 9, France

Paper published under the reference: *Int. J. Fract.*(2008), 151: 281-297.

Abstract

The dynamics of a "peeling front" or an elastic line is studied under creep (constant load) conditions.Our experiments show in most cases an exponential dependence of the creep velocity on the inverse force (mass) applied. In particular, the dynamical correlations of the avalanche activity are discussed here. We compare various avalanche statistics to those of a line with non-local elasticity, and study various measures of the experimental avalanche and temporal correlations such as the autocorrelation function of the released energy and aftershock activity. From all these we conclude, that internal avalanche dynamics seems to follow "line depinning"-like behavior, in rough agreement with the depinning model.

Meanwhile, the correlations reveal subtle complications not implied by depinning theory. Moreover, we also show how these results can be understood from a geophysical point of view.

A.1 Introduction

Creep is one of the fascinating topics in fracture for a physicist: the deformation and final fracture of a sample follow empirical laws with a rich phenomenology. It is expected that there are similarities and differences with "static" fracture encountered in brittle materials such that so-called "time-dependent rheology" is not relevant [*Alava et al.*, 2006]. However, the phenomenon of creep is visible in most any setting regardless of whatever a tensile test might indicate about the typical material response. A particular scenario where one can study creep is the advancement of a single crack under a constant driving force. One can study this in simple paper sheets, and for quite some time it has been noticed that this involves statistical phenomena, an intermittent response which could be characterized by "avalanches", in particular of Acoustic Emission (AE) events [*Sethna et al.*, 2001; *Kertész et al.*, 1993; *Salminen et al.*, 2002; *Santucci et al.*, 2004].

A particular experiment we analyze in this work is related to the dynamics of a crack line as it moves through a sample, largely constrained on a plane. This can be achieved in the case of paper in the so-called Peel-In-Nip (PIN) geometry (see below for a description). The tensile case has been already reported in *Salminen et al.* [2006] and an early account of the creep results published as Koivisto et al. (2007). The mathematical description of the line is a crack position $h(x,t)$, where x is along the average projection of the crack and h is the position coordinate of the line along the direction of line propagation. On the average, the crack moves with the creep velocity $v(\equiv vt)$.

The problem has here as in other such examples (the Oslo plexiglass experiment [*Schmittbuhl and Måløy*, 1997; *Måløy et al.*, 2006] three important ingredients: randomness in that the peeling line experiences a disordered environment coming from the fiber network structure, a driving force K_{eff} or a stress intensity factor, and the self-coupling of the interfacial profile h. In this particular problem, it takes place via a long-range elastic kernel [*Fisher*, 1998], expected to scale as $1/x$ or as k in Fourier space.

For a constant force K_{eff} the dynamics exhibits a depinning transition, of non-equilibrium statistical mechanics. This implies a phase diagram for $v(K_{eff})$. The crack

begins to move at a critical value K_c of K_{eff} such that for $K_{eff} > K_c$, $v > 0$. In the proximity of K_c the line geometry is a self-affine fractal with a roughness exponent ζ. The planar crack problem [*Ramanathan and Fisher*, 1997; *Schmittbuhl et al.*, 1995] has been studied theoretically via renormalization group calculations and numerical simulations, and via other experiments as noted above. The roughness exponent of theory $\zeta_{theory} \sim 0.39$ has traditionally been considered to be absent from experiments [*Rosso and Krauth*, 2002; *Schmittbuhl and Måløy*, 1997; *Måløy et al.*, 2006; *Rosso and Krauth*, 2001], but recent results of Santucci et al. imply that the regime might be visible upon coarse-graining. Imaging experiments prove in that case that as expected the line moves in avalanches, and the avalanche size s distribution seems to have the form $P(s) \sim s^{-1.6...-1.7}$ [*Schmittbuhl and Måløy*, 1997; *Måløy et al.*, 2006].

Here we look at the scenario of creep for the PIN geometry. This subject is such that ordinary "fracture creep" and the particular scenario related to depinning transitions coincide. The creep of elastic lines becomes important for $K_{eff} \leq K_c$ since thermally assisted movement due to fluctuations takes place with a non-zero temperature [*Nattermann*, 1987; *Ioffe*, 1987; *Nattermann et al.*, 1990; *Chauve et al.*, 2000; *Kolton et al.*, 2005]. In usual depinning, it is assumed that thermal fluctuations nucleate "avalanches" which derive their properties from zero-temperature depinning, and the avalanches then translate into a finite velocity $v_{creep} > 0$. There are two interesting differences in the fracture line creep to other such in depinning. First, the line elasticity is non-local, and second, in materials (such as paper here) where there is no healing, the line motion is irreversible, there are no fluctuations in metastable states as in the case of magnetic domain walls, for instance.

In this scenario, the creep velocity becomes a function of the applied stress intensity factor and the temperature, $v_{creep} = v_{creep}(K_{eff}, T)$. As creep takes place via nucleation events over energy barriers [*Nattermann*, 1987; *Ioffe*, 1987; *Nattermann et al.*, 1990], the description of those barriers is of fundamental importance. One can show by scaling arguments and more refined renormalization group treatments that the outcome has the form of the following creep formula:

$$v_{creep} \sim \exp(-C/K_{eff}^{\mu}). \tag{A.1}$$

This gives the relation to the driving force K_{eff} using the creep exponent, μ. The value of the exponent depends on the elastic interactions and the dimension of the moving object

(a line), and we expect

$$\mu = \theta/\nu = \frac{1-\alpha+2\zeta}{\alpha-\zeta}. \tag{A.2}$$

The exponents θ, ν, and ζ denote the energy fluctuation, correlation length, and equilibrium roughness exponents. All these exponents are functions of α, the k-space decay exponent of the elastic kernel. For long range elasticity, one would assume $\alpha = 1$.

The fundamental formula of Eq. (A.2) has been confirmed in the particular case of $1+1$-dimensional domain walls and other experiments [*Lemerle et al.*, 1998; *Braun et al.*, 2005; *Tybell et al.*, 2002]. We have ourselves reported on results, which show an inverse exponential dependence of $v_{creep}(m) \sim \exp(-1/m)$, where m is the applied mass in the experiment (see below), as is appropriate for non-local line elasticity with an equilibrium roughness exponent of $\zeta = 1/3$. In the current work we go further by two important steps. First, we consider creep simulations of an appropriate non-local line model and compare the avalanche statistics and $v(m)$ to those from the experiments (see Fig. A.1 for an example of the activity time series from an experiment and a simulation). Then, we ask the fundamental question: what can be stated of the correlations? This relates to the time series of released energy, to aftershock rates and we present extensive evidence. The experimental signatures show subtle correlations that are rather different from what one would expect from the (depinning) creep problem with non-existing avalanche to avalanche correlations.

The structure of the rest of the paper is as follows. In the next section, we discuss the experimental setup and the simulation model. Section A.3 shows results on $v(m)$ both from experiment and simulation. In Section A.4 we present data on avalanche statistics again comparing the two cases. Section A.5 offers an extensive analysis of correlations by using a number of techniques to look at the experiment. Finally, Section A.6 finishes with conclusions and a discussion.

A.2 Methods

A.2.1 Experiment

In Fig. A.2 we show the apparatus [*Salminen et al.*, 2006]. The failure line can be located along the ridge, in center of the Y-shaped construction formed by the unpeeled part of the sheet (below) and the two parts separated by the advancing line. Diagnostics

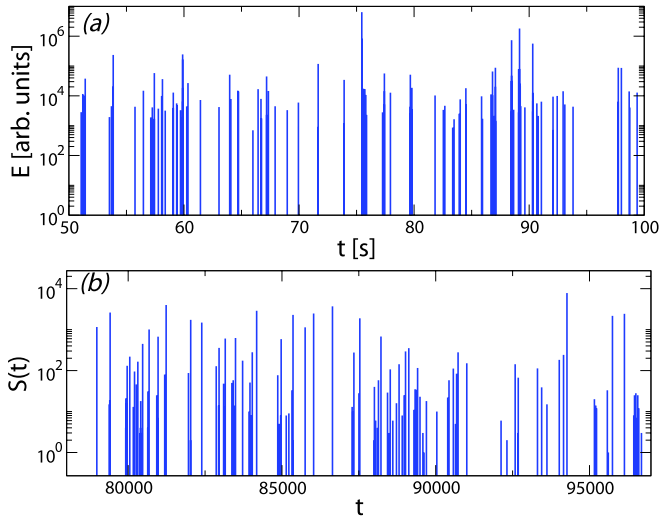

Figure A.1: Activity as a function of time inside a given time window (a) for the creep experiment with 410 g load, and (b) for simulations with $f = 1.87$ and $Tp = 0.002$. In both cases we neglect the duration of the avalanche and we only take into account the starting time and the size of each avalanche, obtaining a data series $\{t_i, E_i\}$ for the experiments and $\{t_i, S_i\}$ for simulations (definition of S_i is given in Section A.2.2).

consist of an Omron Z4D-F04 laser distance sensor for the displacement, and a standard plate-like piezoelectric sensor [*Salminen et al.*, 2006].

It is attached to the setup inside one of the rolls visible in Fig. A.2, and the signal is filtered and amplified using standard techniques. The data acquisition card gives us four channels at 312.5 kHz per channel. We finally threshold the AE data. The displacement data is as expected highly correlated with the corresponding AE, but the latter turns out to include much less noise and thus convenient to study. For paper, we use perfectly standard copy paper, with an areal mass or basis weight of 80 g/m^2. Industrial paper has two principal directions, called the "Cross" and "Machine" Directions (CD/MD). The deformation characteristics are much more ductile in CD than in MD, but the fracture stress is higher in MD [*Alava and Niskanen*, 2006]. We tested a number of samples for both directions, with strips of width 30 mm. The weight used for the creep ranges from 380g to 450g for CD case and from 450g to 533g for MD case. The mechanical (and creep) properties of paper depend on the temperature and humidity. In our setup both remain at constant levels during experiments, and the typical pair values for environment is 40 rH

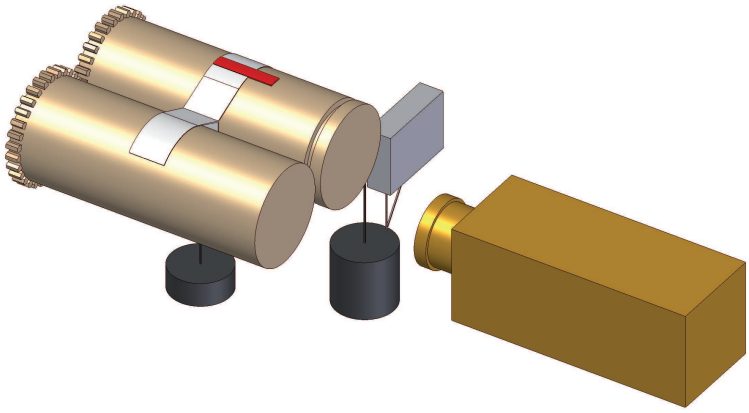

Figure A.2: Experimental setup for peeling experiment. The paper (white) is peeled between two cylinders (copper) separated by a few millimeters. The driving force is generated by a larger hanging weight (black). A smaller weight adjusts the peeling angle. The AE and distance data are collected by piezo transducer (red) and a laser sensor (gray).

and 26°C.

A.2.2 Simulations

We want to simulate the evolution of a discrete long-range elastic line of size L in a disordered media. The line is characterized by a vector of integer heights $\{h_1, ...h_L\}$ with periodic boundary conditions.

The long-range elastic force [*Tanguy et al.*, 1998] acting on a string element is given by

$$f_i^{elastic} = k_0 \left(\frac{\pi}{L}\right)^2 \sum_{\substack{j=1 \\ j\neq i}}^{L} \frac{h_j - h_i}{\sin\left(\frac{x_j - x_i}{L}\pi\right)}, \tag{A.3}$$

where all forces on all sites can be computed in a i$L \log L$ operations using a fast-Fourier-transform (FFT) algorithm [*Duemmer and Krauth*, 2007]. Simulations are done using $k_0 = 0.01$ and $L = 1024$. The random force due to the quenched disorder may be obtained from a standard normal distribution, i.e a Gaussian distribution with zero mean and a variance of one,

$$f_i^{random} = N(0, 1). \tag{A.4}$$

Then, the total force acting in a given element of the string is $f_i = f_i^{elastic} + f_i^{random} + f$, where f is the external applied force. At this point, we need to introduce a dynamics which mimic the experiment evolution. A basic characteristic of the experiment is that it is completely irreversible, so the dynamics has to include this important feature. We consider a discrete time evolution and the discrete dynamical rule [*Duemmer and Krauth*, 2007] is given by

$$h_i(t+1) - h_i(t) = v_i(t) = \theta[f_i] \;\; t = 1, 2, ... \tag{A.5}$$

where θ is the Heaviside step function. Then we apply the following procedure:

1. Start at $t = 0$ with a flat line located at $h = 0$ setting $h_i = 0 \; \forall \, i$.

2. Compute the local force (f_i) at each site and using the dynamical rule (Eq. A.5) compute the local velocity of each site. We can define the velocity of the string for this time, as
$$v(t) = \frac{1}{L} \sum_{i=1}^{L} v_i(i). \tag{A.6}$$

3. Advance the sites according their local velocities v_i.

4. Generate new random forces for those sites that have been advanced.

5. Go to steep (2) and advance the simulation time by one unit.

This evolution shows a depinning transition at $f_c \sim 1.88$ in which the velocity of the line $v(t \to \infty) > 0$ when $f > f_c and v(t \to \infty) = 0$ when $f < f_c$.

In order to simulate the creep evolution of the string we use an external force below the depinning threshold, and when the line gets stuck we let thermal fluctuations play a role. We scan all the sites and set $v_i(t) = 1$ with a probability $p = \exp \frac{f_i}{T_p}$ and $v_i(t) = 0$ with a probability $1 - p$, where T_p is proportional to temperature. This can trigger an avalanche which will have a finite duration T since the system is belowthe depinning threshold.We define the avalanche size as $S = \sum_T v(t)$. If we consider small enough temperatures compared to the typical internal forces, the avalanche needs some time to be triggered, which is defined as the waiting time τ . We define this waiting time as the time between the end of an avalanche and the starting time of the next one.

In summary, this long-range elastic line model in the creep regime has an avalanche-like behaviour. Each avalanche is characterized by three quantities: Waiting time τ ,

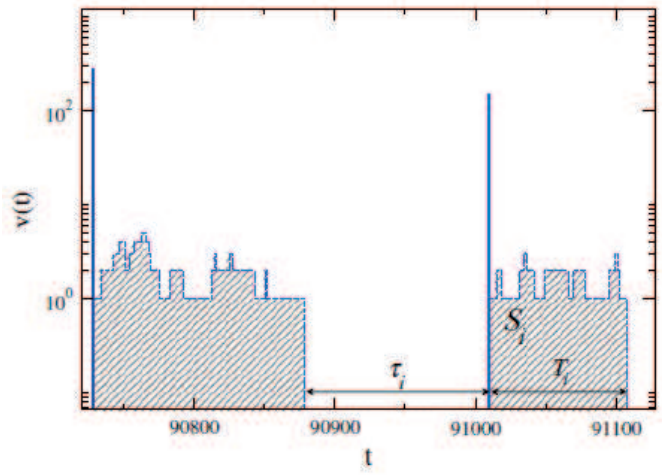

Figure A.3: Velocity of the long-range elastic string as a function of simulation time (dotted line). The vertical and solid lines represents the signal $S(t)$ plotted in Fig. A.1b. Avalanche properties are also shown: τ_i is the waiting time, T_i is the avalanche duration, and S_i is the avalanche size

duration T, and size S (see Fig. A.3). Moreover, we observe that for long times, when the steady state is reached, durations are small compared to waiting times, for that reason we can simplify the signal just taking into account the starting time of the avalanche and its size.

A.3 Creep velocity

The main data about both simulations and experiment on the creep velocity are shown in Fig. A.4. The prediction of Eq. A.1 is that the velocity is exponential in the effective driving force. In the case of the experiments at hand, we face the problem that we do not know $\langle K \rangle$ empirically. The average fracture toughness depends on the loading geometry, and on the material at hand. There are estimates for similar papers in the literature in the mode I case [e.g. *Yu and Karenlampi*, 1997] which indicate that the value of $\langle K \rangle$ (or "$\langle m \rangle$" to better compare with the actual control parameter) is lower by at least a factor of two compared with the actually used loads. One can try to work around the problem by guessing $m \sim K\langle K \rangle$ and checking how that affects the apparent functional relationship of v vs. the reduced mass. In the range of physically sensible values of $\langle K \rangle$

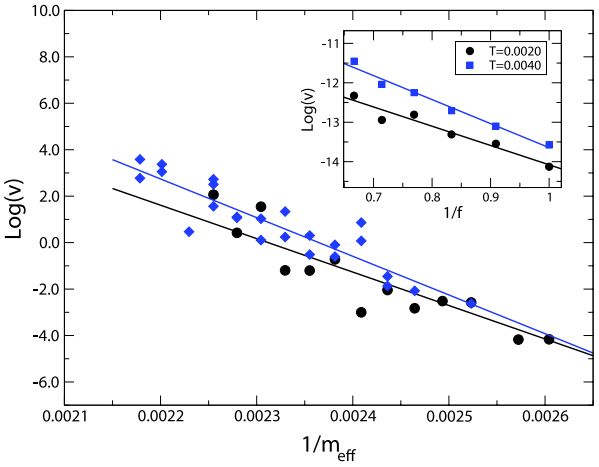

Figure A.4: The creep velocity vs. the inverse of the applied force or mass, $m_{eff} = m$. Inset: creep velocity vs f for the simulation model for two different temperatures.

this does not change the conclusions. Thus we take $m_{eff} = m$ here.

From the figure we may conclude that the effective creep exponent $\nu \sim 1$, though there is variability among the data sets. One of the data sets (black circles) shows some slight curvature. The main finding, interpreted via Eq. A.2 then indicates that the effective roughness exponent $\zeta \sim 1/3$, which is the expected equilibrium value for a long-range elastic problem with $\alpha = 1$ [*Koivisto et al.*, 2007]. The numerical simulation data agree qualitatively with the exponential decay except very close to the depinning transition. According to the creep formula [e.g. *Kolton et al.*, 2005], we should expect that the velocity of the long-range string was

$$v(f, T_p) \sim \exp\left[-\frac{C}{T_p}\left(\frac{1}{f}\right)^{\mu}\right]. \tag{A.7}$$

However, it appears that slope as a function of the temperature is not exactly the expected one. One reason is that the model is simplified: we only let thermal fluctuations act when the string gets stuck so avalanche nucleation during an avalanche is neglected. This may be of importance very close to f_c and for long avalanches.

The exponential average creep velocity can most directly be compared with the measured velocities from the distance sensor over short time-spans. Figure A.5 shows the probability distributions $P(v)$ for a very large number of different experiments, for the $v = \Delta h/\Delta t$ with $\Delta t = 0.5$ s. The general trend shows clear stick-slip characteristics in the sense that the local velocities vary with a power-law-like fashion. The typical slope of the

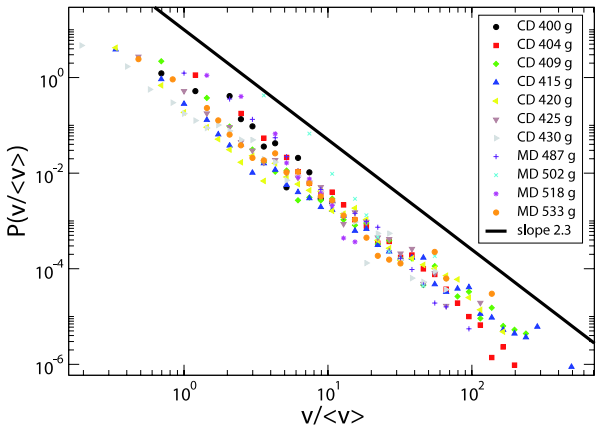

Figure A.5: Histogram of a normalized velocity obtained from discretized distance data. Velocity, v, is an average in a 0.5 s time window. $\langle v \rangle$ is an average over experiments with same weights.

data is about -2.3 though a more detailed look indicates that there is a tendency for the exponent to change with m and with Δt (increasing both decreases the slope). It is an interesting question of how this locally time-averaged velocity is related to the average creep velocity, and the avalanches that contribute to it, somewhat hindered by the relative large fluctuations in the distance sensor - for which reason we resort in the detailed avalanche dynamics studies to the AE. Typically, these avalanches observed in the experiment have very short durations that can be neglected.

A.4 Statistical distributions

Next we consider the statistics of the AE time series from the experiments as signatures of the intermittent avalanche activity in the system during creep. In our setup, we face the problem that direct imaging of the front dynamics is if not impossible then difficult to realize. Thus we take the AE data up to be scrutinized as detailed information. It can be studied from the viewpoint of the correlations of the creep or avalanche activity but the finer details there of are left to the next section. Here, we consider the typical averaged distributions of three quantities: (i) avalanche size as measured by the total AE energy E, (ii) the event interval τ , and (iii) their durations T . These are also confronted with

similar, direct data from the simulations using in case (i) the avalanche total size/area s. Simulation distributions are normalized in such a way to better match the experimental ones.

Figure A.6 shows three cases of the avalanche size distributions. We compare the creep data for one mass m to a similar dataset for a tensile experiment done at a constant average front velocity [*Salminen et al.*, 2006]. Moreover data is included from the creep model for the parameters shown in the caption. The normalization of the data for the experiments is such that the E_{min} has been scaled to unity. Recall that the events are restricted in size from below by a threshold applied to the original AE amplitude signal $A(t)$, from which the events are reconstructed. We can observe that the effective power-law exponents of the experimental data are ~ 1.6 for the creep and ~ 1.8 for the tensile cases, respectively. These are very close to each other, while the simulation data results imply ~ 1.4 not very far from the experimental values. We also can observe that there is no evident cutoff in any of them (the bending in the simulations case is a finite size effect). These data can be compared with the Oslo plexiglass experiment where for the avalanche size distribution the value of $\beta = 1.6 \pm 0.1$ has been found [*Schmittbuhl and Måløy*, 1997; *Måløy et al.*, 2006].

The waiting times are reported in Fig. A.7. For all the three cases $P(\tau)$ is broad. In the tensile case, it is known that there appears to be a "bump" in the distribution, or a typical timescale. This is absent from the creep one. It is interesting to note that here the simulation model agrees rather well with the creep case. For larger m it is possible that the waiting times start to look more like the tensile case. We also present the scaled distributions for all the experiments. Later, in the next section, we discuss the attempt to link this to a background plus correlated, triggered activity. Finally, in Fig. A.8 we show the avalanche durations from the simulations. In the case of the experiment this is more complicated due to the fact that the actual amplitude signal is convoluted via the pre-processing electronics and the response function of the piezos with which the AE is measured. Later we present some examples of the outcome, but here we just discuss the clear-cut case of the simulations also since they give an idea about what one might see in the experiment, ideally. The main points that one learns from the figure are that a true power-law-like $P(T)$ ensues only at the proximity of the f_c. For values higher or lower than that the shape of the distribution changes, in particular such that not only a cut-off appears but also the clear power-law character starts to disappear.

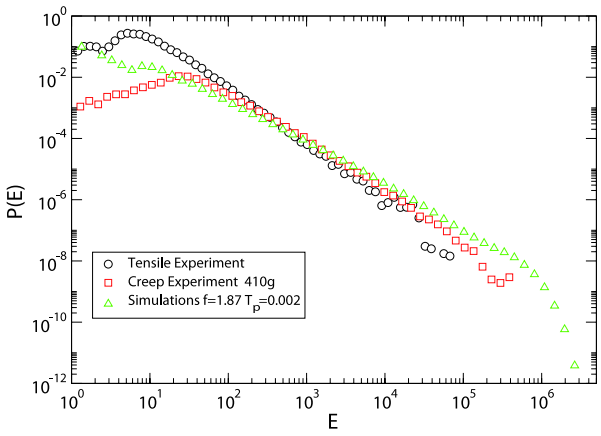

Figure A.6: Energy distributions for the tensile experiment (circle), for the creep experiment (square), and for the simulations (triangle up). For the simulations we are plotting the histogram of the avalanches sizes $\{S_i\}$. We can consider that the energy of an avalanche is proportional to its size, so $S_i \sim E_i$.

A.5 Measures of correlated dynamics

A.5.1 Correlations

Next we look at the detailed temporal structure of the AE signal, and compare it with the activity patterns from the creep simulations. The main question is whether the creep activity exhibits interesting features that would in particular differ from the theoretical expectations-based on elastic line depinning the inter-avalanche correlations should be expected to be negligible. In Fig. A.9 we show the autocorrelation function $R(u)$ of the event energy time series. The autocorrelation function is defined as:

$$R(u, \Delta t) = \frac{\frac{1}{N}\sum_{t=1}^{N} E_t E_{t+u} - \langle E \rangle^2}{\langle E \rangle^2 - \langle E \rangle}, \tag{A.8}$$

where E_t is the energy of the AE signal at time t and $\langle E \rangle$ is the average value of the energy. E_t is defined as a sum of squared amplitudes of the AE signal in the time interval $[t, t + \Delta t]$. The length of the interval is chosen to be 10^{-3}s in the tensile and 10^{-5}s in the creep peeling experiment in order to capture the correlations in both cases.

When compared to paper peeling experiments under a constant strain rate, the cor-

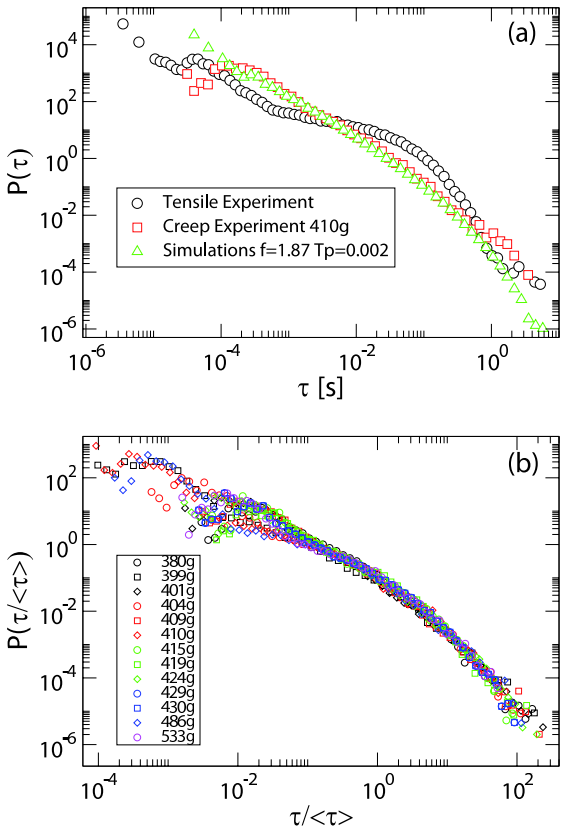

Figure A.7: (a) Waiting time distributions for the tensile experiment (circle), for creep experiment with 410 g (squares), and for the simulations with $f = 1.87$ and $T = 0.0020$ (triangles up). (b) Normalized waiting times for different creep experiments. τ is computed over each experiment from the corresponding data.

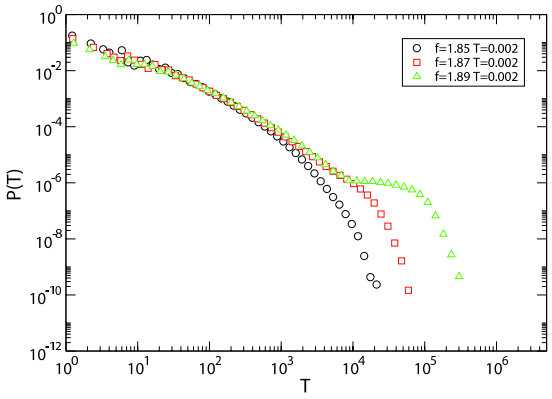

Figure A.8: Avalanche duration distributions for $T_p = 0.002$ and three different forces. For the case with $f = 1.89$ we are above the depinning threshold.

relation decays at a much faster rate than in tensile peeling experiments. In that case, the existence of a slow decay might be taken to be connected to the fact that there is a typical scale in the waiting time distribution which is not the case for creep, seemingly. The functional form of the shown case of a logarithmically decreasing autocorrelation function is $R(u) = -0.3 - 0.08 \ln(u\Delta t)$. The data are also compared to a randomized time series, and one can see that the correlations disappear. For the simulated data the autocorrelation function shows no difference to a randomized signal. All in all these results imply that there are contrary to theoretical models temporal correlations, albeit in creep on a very short timescale.

In Fig. A.10 we show an envelope event form for different events with different event energy. We see an exponential decay for the tail of the event, but the event envelope becomes more extended in time when the energy of the event is larger. Typical events extend up to 0.5 ms, which corresponds to decay of the correlation in the Fig. A.9. A correlation up to time-scales larger than the typical event length is only seen in the strain-controlled peeling.

Since the time series of AE is so intermittent it is better to concentrate on measures that consider directly the avalanches. In Fig. A.11 we depict the averaged energy as a function of a silent time before the event from paper peeling experiments in creep. The event energy is in many datasets slightly correlated to the waiting time before the event.

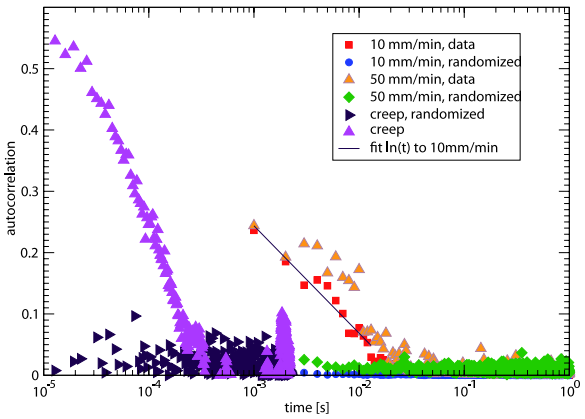

Figure A.9: The autocorrelation function of the averaged event energy in paper peeling under creep and tensile loading modes. Comparisons to the randomized data are also included. The numerical data and the corresponding randomized data are not distinguishable.

This correlation disappears if one considers the opposite case of the waiting time after the event. The suggested interpretation is that the elastic fracture line apparently as a physical system ages before a large event, while there is no real dependence of the waiting time on the energy dissipated in the previous event.

The difference in the autocorrelation between the creep and tensile peeling experiments might be attributed to the forcing the line to move in the latter, which induces a "fiber-scale" to results. This is also supported by observing the waiting time distribution, where the pdf deviates from a power-law. In paper peeling we study the clustering of events by computing the correlation integral $C(\Delta t)$, that is the probability that two events are separated smaller time than Δt.

The correlation integral is given by:

$$C(\Delta t) = \frac{2}{N(N-1)} \sum_{i<j} \Theta(T - t_j + t_i). \tag{A.9}$$

where N is number of events in the experiment and ti is the event occurrence time. Correlation integrals [*Weiss and Marsan*, 2003] are shown in the Fig. A.12 for the peel creep experiment. If the probability of the event occurrence is equal for every time interval, then one can assume that correlation integral increases as $C(\delta T) \sim \Delta T$. We see a power law

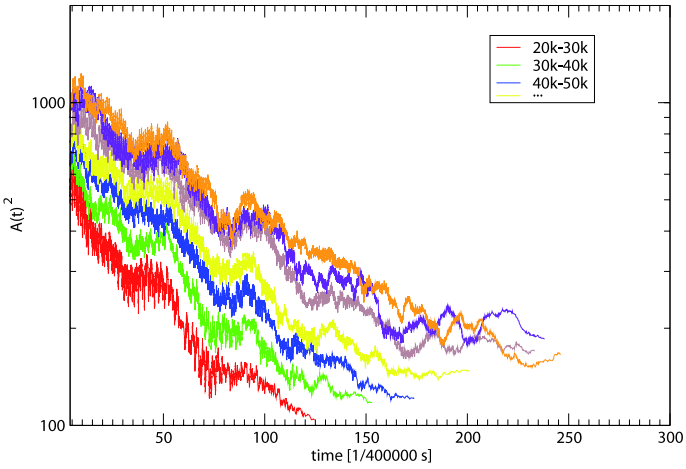

Figure A.10: Squared amplitude of an event averaged over all events in the creep peeling experiment. The average is taken over events with different sizes and the size is indicated as different colors in the figure.

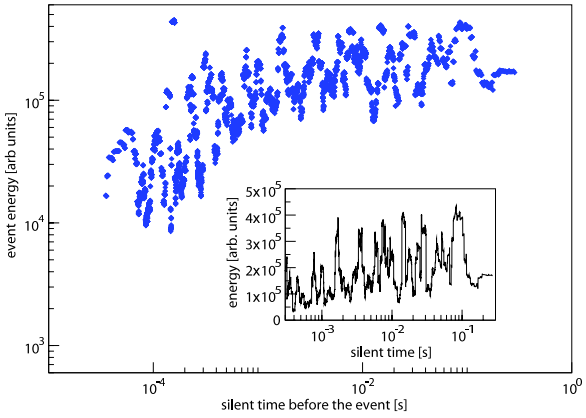

Figure A.11: Averaged energy as a function of silent time before the event with weight 410 g

$T^{0.9}$ in sufficiently large times, but when the distance of events approaches the experiment length we see small deflection in the curve. At temporal scales of the order of 10^{-2}s we see deviation from the power law behaviour, which indicates event clustering.

A.5.2 Seismicity: cascading occurrences as a model for the experimental data

In this part we will show how fracture in heterogeneous material, such as line creep in paper peeling, behaves, in time, similarly to the rupture at the Earth scale, e.g. the earthquakes driven by plate tectonic deformation.

From seismology it is known that seismicity can be described by two processes: the background seismicity and the triggered events. The first one is modelled as a homogeneous Poisson process, while the second one as a power law decay of seismic rate following the occurrence of any event, e.g. the OmoriâĂŹs law [*Kagan and Knopoff*, 1981; *Utsu et al.*, 1995; *Helmstetter and Sornette*, 2002a]:

$$R = \lambda_0 + \sum_{t<t_i} \lambda_i(t). \tag{A.10}$$

The first term in the right hand side of Eq. A.9 is the background seismicity, while the second term is the correlated part of the seismicity, that is, the superposition of time-dependent series of triggered seismicity following any event. The triggering process of the latter is reproduced by models of cascading effect for earthquake interactions, i.e. ETAS (Epidemic Type Aftershock Sequence) model [*Kagan and Knopoff*, 1981; *Utsu et al.*, 1995; *Helmstetter*, 2003]. This stochastic point process is based on the Gutenberg-Richter law for energy distribution and OmoriâĂŹs law for time distribution of seismicity rate. According to this model, the rate of aftershocks triggered by an earthquake occurring at time t_i with magnitude M_i is given by:

$$\lambda_i = \frac{K_0}{(c + t - t_i)^p} 10^{\alpha(M_i - M_c)}. \tag{A.11}$$

where K_0, α, c and p are constants and M_c is the completeness magnitude of the catalogue. The total earthquake rate of Eq.A.9 is therefore the sum of all preceding earthquakes (triggered directly by the background events or indirectly by previous triggered events) and the constant background rate λ_0. This model reproduces most of the statistical properties

of earthquakes, including aftershock and foreshocks distributions in time, space and energy [*Helmstetter and Sornette*, 2002a].

Figure A.13 illustrates the average acoustic event rate following any event for the peel creep experiments (load $m = 409$ g). It is reminiscent of OmoriâĂŹs law for tectonic seismicity, where we can observe the power law decay representing the cascade of aftershocks following an event. For times greater than 10^{-2} s, the event rate keeps constant, at the background rate level, which confirms Fig. A.12 results. The exponent of the power law decay of event rate is equal to 1.5 ± 0.1.

In this way AE triggered by line creep in paper peeling are characterized by power law distribution on energy (Fig. A.6) and power law relaxation of aftershock rate (Fig. A.13). ETAS style models reproduce these macroscopic patterns, including foreshocks as aftershocks of conditional mainshocks [*Helmstetter et al.*, 2003a]. *Corral* [2004a] shows that the inter-event time probability density for such kind of ETAS model for event occurrences follows a gamma distribution, according to:

$$P(\tau) = C\tau^{\gamma-1}\exp(-\tau/\beta). \tag{A.12}$$

where τ is the normalized inter-event time obtained by multiplying the inter-event time δt with the earthquake rate λ, that is $\tau = \delta t\lambda$.

Molchan [2005] showed that, in agreement with Eq. A.11, the distribution decays exponentially for large inter-event times and that the value $1/\beta$ is the fraction of mainshocks among all seismic events. According to *Hainzl et al.* [2006], $1/\beta$ is a regional quantity, allowing for non-parametric estimate of the background rate in a specific process. In order to simulate the AE properties of the creep fracture experiment ($m = 409$ g), we tuned an ETAS model to fit the estimated percentage of background activity of real data. One must notice that robust inversion of ETAS model parameters is not yet available. Figure A.14 shows the comparison between inter-event time distributions of a synthetic catalogue generated by ETAS model. Both, simulations and data inter-event time distributions fit a gamma distribution. Other possible data fittings are possible [*Saichev and Sornette*, 2007], but this lies outside our aim of comparison between data from paper peeling and ETAS simulations. The fit may underestimate here (see also Fig. A.7b) slightly the exponent of the power-law part of the waiting-time distribution. In any case, the relevant exponent here is definitely smaller than in the case of rock fracture [*Davidsen et al.*, 2007] ($p = 1.4$). To summarize, line creep in paper peeling at a scale of $\sim 10^{-1}$ m and $\sim 10^{2}$ s triggers brittle

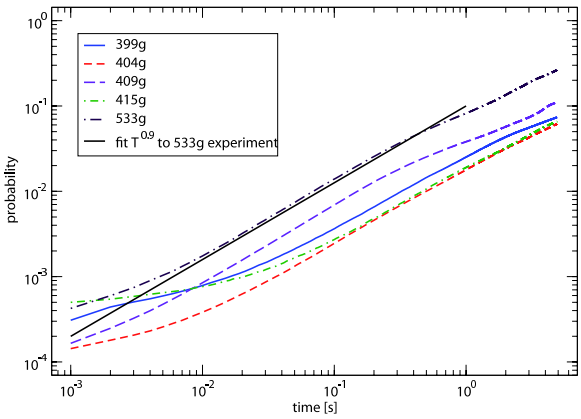

Figure A.12: Correlation integrals for the creep in peeling experiment.

creep damage that seems to share the same generic temporal properties than the ones observed for tectonic seismicity at scales of $\sim 10^6$ m, $\sim 10^2$ years. These properties can be reduced to a rough constant seismicity rate with bursts of correlated activity, contemporary to power law distribution of event sizes and (short-time) inter-event times. Estimates of OmoriâĂŹs law exponent suggest a faster relaxation for the paper peeling case than for Earth crust response to tectonic loading, p equal to 1.4 and 1 respectively [*Utsu et al.*, 1995]. The portion of uncorrelated events suggests a slightly lower triggered event rate in paper peeling than in the Earth crust deformation. Estimations of the background portion of AE did not show any sensitive dependence on the applied loading. Whether the difference between paper experiments and earthquakes come from experimental conditions or fracturing mode (i.e. tensile, creep or compression) remains an open question. For earthquakes no change in relative portions of background and triggered activity is resolved for compression, extensional or shear tectonic settings.

A.6 Conclusions

We have overviewed a simple creep experiment which uses paper and can be studied to investigate planar crack propagation in a disordered medium. The information that one can obtain and then compare to relevant theory extends from the average front velocity to details of the spatio-temporal dynamics.We have also for a comparison studied a classical

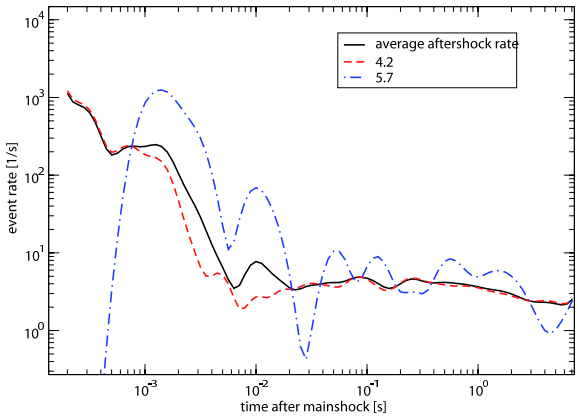

Figure A.13: Event rate following events in paper peel creep experiments with $m = 409$ g. Time $t = 0$ is the target event occurrence. Aftershock rates are averaged within each magnitude class of target event (blue line: 4.2-5.72; red line 5.72-7.2). We compute the magnitude class $M = \log_{10}\langle E_M \rangle$ where E_M is the energy of the target event. All magnitude classes are averaged together (thick black line). Correlation between events is characterized by a power law decay of the activity after the target event. The time for which events are correlated is a function of the target event magnitude, as well as the number of triggered events (see Eqs. A.9 and A.10). The observed duration of the aftershock sequence is bounded by the level of the background uncorrelated constant rate.

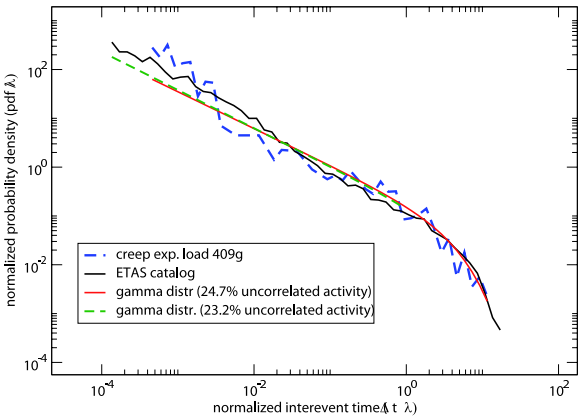

Figure A.14: Inter-event time probability distribution for experimental dataset (thin red curve) and synthetic catalogue generated by ETAS model (thin black curve). Dotted thick curves are gamma distribution fits to data and ETAS model (red dotted line for the real data and black dotted curve for ETAS). Estimations of background fraction of events according to *Hainzl et al.* [2006] technique are close together (23-25%) for both data and simulation. ETAS parameters are: $p = 1.4$, $K_0 = 0.09$, $\alpha = 0.9$ ($n = 0.9$), $b = 1$, $c = 0.001$ s.

non-local elastic line model under creep conditions. This shows similar features to the experiment: an exponential dependence of the creep velocity on the applied force or mass or stress-intensity factor.

The typical statistical distributions are power-law-like in particular for the event energy/size. It is perhaps useful to recall that the waiting time distribution is quite broad. There is currently no understanding as to why, in particular one should note that the current experimental setup allows to study this issue in a steady-state unlike in most other fracture related creep tests. In general as such distributions are regarded the line creep model agrees at least qualitatively with the experimental data. Our results are also in line with other similar planar crack data (though these are obtained usually in the constant-velocity ensemble, not in creep [*Schmittbuhl and Måløy*, 1997; *Måløy et al.*, 2006; *Bonamy et al.*, 2006]).

Looking in more detail at the correlations of the activity, differences transpire however. The experimental AE events show subtle correlations via the autocorrelation function, via the waiting times before events, and via the OmoriâĂŹs law. All these measure different aspects of the avalanche activity, and in all the cases the model differs in its behavior. Here, we lack completely theoretical understanding, in particular as regards such a quantitative measure as the Omori exponent. It is interesting to note that geophysics-oriented analysis methods produce results in agreement with observations from tectonic activity. Here again the steady-state character of the experiment at hand is of utility.

In the future such experiments and such comparisons can be used to study several different aspects of avalanche systems, creep fracture, and models for line depinning. A particularly pertinent question is for instance whether rate-dependent processes in the material at hand modify the kinetics of the creep in some suitable way that still maintains the creep vs. force relation intact. We shall ourselves attempt a more careful study of the creep model, and analyze how its correlation patterns could be matched with the experiment.

Acknowledgements

The authors would like to thank for the support of the Center of Excellence-program of the Academy of Finland, and the financial support of the European Commissions NEST Pathfinder programme TRIGS under contract NEST-2005-PATH-COM-043386. P. Traversa is supported by Volume EC-FP6 project. MJA is grateful for the hospitality of

the Kavli Institute of Theoretical Physics, China in Beijing, where the work at hand was to a large degree completed. Discussions with Lasse Laurson (Helsinki), StÃl'phane Santucci (Oslo), Daniel Bonamy (Saclay), and Stefano Zapperi (Modena) are also acknowledged.

Appendix B

Rate-and-State friction model

The concept at the base of this model is to treat a seismically active volume of the Earth as a population of sources that nucleate successive earthquakes to produce observed seismicity [*Deterich*, 1994]. The objective is thus to obtain a rate of earthquake activity resulting from some stressing history. The model describes the evolution of the friction coefficient μ as a function of the slip velocity $\dot{\delta}$ and of some state variables θ_i.

The rate- and state-dependent representation of fault constitutive parameters generalized for multiple state variables can be expressed as

$$\tau = \sigma \left[\mu_0 + A \ln \left(\frac{\dot{\delta}}{\dot{\delta}^*} \right) + B_1 \ln \left(\frac{\theta_1}{\theta_1^*} \right) + B_2 \ln \left(\frac{\theta_2}{\theta_2^*} \right) + ... \right], \tag{B.1}$$

where τ and σ are shear and normal stresses, respectively, $\dot{\delta}$ is slip speed, and θ_i are state variables. Parameters μ_0, A and B are empirical coefficients. The terms with asterisks are normalizing constants. Dimension of the state variables is that of time, so that θ can be assimilated to an aging variable, or an average life time for an asperity.

From experimental observations, state is inferred to depend on sliding and normal stress history. *Deterich* [1994] employs

$$d\theta_i = \left[\frac{1}{\dot{\delta}} - \frac{\theta_i}{D_{ci}} \right] d\delta - \left[\frac{\alpha_i \theta_i}{B_i \sigma} \right] d\sigma \tag{B.2}$$

for evolution of state θ by displacement δ and normal stress σ. D_{ci} is a characteristic displacement and α_i is a parameter governing normal stress dependence of θ_i. At steady state ($\sigma = \text{const}$, $d\theta/dt = 0$), $\theta_{ss} = D_c/\ \dot{\delta}$. When not at steady state, θ seeks θ_{ss} over the sliding distance D_c.

B.1 Earthquake nucleation

The nucleation process on faults with these properties is characterized by an interval of self-driven accelerating slip that precedes instability.

The nucleation source is represented as a single spring-slider system. Details of the model are given by *Dieterich* [1992], while appendix A in *Deterich* [1994] generalizes the results of *Dieterich* [1992] by incorporating multiple state representation of fault friction. In addition *Deterich* [1994] obtains results for the change of conditions on a source arising from a step in both, shear and normal stress. Equating the constitutive law B.1 for fault strength with fault stress gives

$$\frac{\tau(t) - k\delta}{\sigma} = \mu_0' + A \ln \dot{\delta} + \sum_{i=1}^{n} B \ln \theta_i, \tag{B.3}$$

where $\tau(t)$ is the remotely applied stress acting on the fault in absence of slip and $-k\delta$ is the decrease in stress due to fault slip (k is the effective fault patch stiffness). The constant terms μ_0, $A \ln \dot{\delta}^*$, and $B_i \ln \theta_i^*$ have been grouped into μ_0^*. *Deterich* [1994] assumes constant normal stress. When the nucleation process is underway and slip is accelerating, the slip speed soon greatly exceeds the steady state speed for all θ_i. In this case equation B.2 can be well approximated by

$$\left(\frac{\partial \theta_i}{\partial \delta}\right)_{\sigma=const} = -\frac{\theta_i}{D_{ci}}, \theta_i = \theta_{0i}\ e^{-\delta/D_{ci}}. \tag{B.4}$$

state is therefore only dependent on displacement, where θ_{0i} is state $\delta = 0$. Substituting equation B.4 into B.3 we get

$$\frac{\tau(t) - k\delta}{\sigma} = \mu_0' + A \ln \dot{\delta} + \sum_{i=1}^{n} B_i \ln \theta_{0i} - \delta \sum_{i=1}^{n} \frac{B_i}{D_{ci}}. \tag{B.5}$$

Under constant stressing rate, $\tau(t) = \tau_0 + \dot{\tau}\ t$, equation B.5 can be rearranged by solving for $\dot{\delta} = d\delta/dt$, giving

$$\dot{\delta}_0 \int_0^t \exp\left[\frac{\dot{\tau}\ t}{A\sigma}\right] dt = \int_0^\delta \exp\left[\frac{H\delta}{A}\right] d\delta, \tag{B.6}$$

where $\dot{\delta}_0$ and H contain terms for the initial conditions and model constants, respectively (see appendix A in *Deterich* [1994])

$$\dot{\delta}_0 = \left[(\theta_{01})^{-B_1/A} (\theta_{02})^{-B_2/A} ...\right] \exp\left[\frac{\tau_0/\sigma - \mu_0'}{A}\right], \tag{B.7}$$

$$H = -\frac{k}{\sigma} + \sum_{i=1}^{n} \frac{B_i}{D_{ci}}. \tag{B.8}$$

Slip speed is therefore determined by the independent variables τ, σ and θ. An accelerating slip patch evolution of θ is thus determined by slip, since the initial slip speed $\dot{\delta}_0$ fully describes the initial conditions τ_0 and θ_{0i}.

Solving equation B.6 gives the slip and slip speed history, and consequently the time of instability [see *Deterich*, 1994]). Time of instability is, therefore

$$t = \frac{A\sigma}{\dot{\tau}} \ln\left(\frac{\dot{\tau}}{H\sigma\ \dot{\delta}_0} + 1\right), \quad \dot{\tau} \neq 0, \tag{B.9}$$

$$t = \frac{A}{H}\left(\frac{1}{\dot{\delta}_0}\right), \quad \dot{\tau} = 0. \tag{B.10}$$

B.2 Effect of Stressing History on Earthquake Rate

Considering steady state reference rate of seismicity $r = dn/dt$, the time of an earthquake at source n is

$$t = \frac{n}{r}. \tag{B.11}$$

The distribution of initial slip speeds over the steady state population of patches is obtained by equating the results for time of instability (equation B.10) with equation B.11. If we use a single state variable γ that evolves with time and stressing history, we obtain:

$$\dot{\delta}\,(n) = \frac{1}{H\sigma\gamma\left[\exp\left(\frac{\dot{\tau}_r n}{A\sigma r}\right) - 1\right]}, \quad \dot{\tau}_r \neq 0. \tag{B.12}$$

where $H = B/D_c - k/\sigma$ and $\dot{\tau}_r$ is the reference constant stressing rate. For the initial steady state distribution, corresponding to the constant steady state seismicity rate r on a given source of the distribution, and a constant reference stressing rate $\dot{\tau}_r$, the state variable γ is equal to:

$$\gamma = \frac{1}{\dot{\tau}_r}, \tag{B.13}$$

Since slip speed increases as the nucleation process develops, the distribution of slip speeds evolves with time. The solutions found in equations B.10 and B.10 can be applied repeatedly by redefining the initial conditions at each time step through the prior stressing history and the prior distribution. The distribution of slip speed retains the form of equation B.12,

independently of the subsequent stressing history, while γ evolves with it according to

$$d\gamma = \frac{1}{A\sigma}\left[dt - \gamma d\tau + \gamma\left(\frac{\tau}{\sigma} - \alpha\right)d\sigma\right], \tag{B.14}$$

For positive shear stressing rates and $\dot{\sigma}= 0$, γ in equation B.14 seeks the steady state value, $\gamma_{ss} = 1/\dot{\tau}$, with the characteristic relaxation time

$$t_a = \frac{A\sigma}{\dot{\tau}}. \tag{B.15}$$

The distribution of earthquake times is obtained by substituting the distribution of initial conditions into the solutions for time to instability (equations B.10 and B.10). Seismicity rate R is instead obtained by differentiating the distribution of times, giving the general result

$$R = \frac{r}{\gamma\ \dot{\tau}_r}. \tag{B.16}$$

In the following we give some useful solutions of equation B.14 for simple stress perturbations cases. We always assume that seismicity is initially at steady state, i.e. $\gamma_0 = 1/\dot{\tau}_r$. In these cases the effect of the stressing history on the earthquake rate can be simply obtained substituting solutions of equation B.14 into equation B.16. For simulations of complex stressing histories, a straightforward procedure consists in breaking the stressing history into time step of constant shear stressing rate and stress steps, solving for γ (equation B.14) step by step, and substituting the result into equation B.16 in each step. Alternatively, numerical solutions of B.14 may be obtained.

Stress variations are intended here to be Coulomb stress variations. Because normal stress variations can be largely balanced by undrained changes in pore pressure, we assume a constant normal stress $d\sigma = 0$ [see *Deterich*, 1994; *Segall et al.*, 2006]. For sake of simplicity we therefore interpret the Coulomb stress variations as variations in the shear stress τ. The distribution of initial slip speeds is given in equation B.12, and evolves with time as a number of sources nucleate earthquakes after a given time has elapsed [see *Deterich*, 1994, for details].

Constant stress $\dot{\tau}= 0$, $\dot{\sigma}= 0$

$$\gamma = \gamma_0 + \frac{t - t_0}{A\sigma}. \tag{B.17}$$

where γ_0 is the state variable corresponding to the reference state

Stress step : the general solution for the state variable through a step in shear and normal stress is given by

$$\gamma = \gamma_0 \left(\frac{\sigma}{\sigma_0}\right)^{-\alpha/A} \exp\left(\frac{\tau_0}{A\sigma_0} - \frac{\tau}{A\sigma}\right) \tag{B.18}$$

where γ_0 denotes the value of γ immediately before the stress step, so as τ_0 and γ_0. Subsequent evolution of γ is independent of prior processes that caused γ to change. The results from a positive step in shear stress would also arise from a negative step of normal stresses. The obtained γ is the state variable just following the stress step, which will become the γ_0 in equation If we consider it as a positive shear stress $\Delta\tau$, with normal stress σ held constant, the solution becomes:

$$\gamma = \gamma_0 \exp\left[\frac{\Delta\tau}{A\sigma}\right] \tag{B.19}$$

where $\Delta\tau$ is the stress step value. The earthquake rate is still computed by using equation B.16.

Linear shear stressing , with shear stress is given by:

$$\tau = \tau_0 + \dot{\tau}\, t, \tag{B.20}$$

and $\dot{\sigma} = 0$, the solution for the state variable is

$$\gamma = \left[\gamma_0 - \frac{1}{\dot{\tau}}\right] \exp\left[\frac{-t\,\dot{\tau}}{A\sigma}\right] + \frac{1}{\dot{\tau}} \tag{B.21}$$

Stressing rate change : the solution for the case of a change in the shear stressing rate from the reference value $\dot{\tau}_r$ to a value $\dot{\tau}$ is the following

$$\gamma = \left[\gamma_0 - \frac{1}{\dot{\tau}}\right] \exp\left[-\frac{(t - t_0)\,\dot{\tau}}{A\sigma}\right] + \frac{1}{\dot{\tau}}. \tag{B.22}$$

where t_0 is the time at which the change in staring rate occurs and γ_0 is the initial state variable, i.e. $\gamma_0 = 1/\,\dot{\tau}_r$. Panels A and B in figure B.1 show an example of this case. A particular case of stressing rate change is the decrease in stressing rate: in this case the seismicity rate responds to the perturbation with a power law relaxation over time (figure B.2). In this sense, any drop of external forcing rate (i.e. a decrease of stressing rate) induce a decrease of the seismicity rate which takes the form of an

Omori style seismic relaxation as following:

$$\begin{aligned} R &= \frac{r}{\left[\left(\frac{1}{\dot{\tau}_r}-\frac{1}{\dot{\tau}}\right)\exp\left(-\frac{t}{t_a}\right)+\frac{1}{\dot{\tau}}\right]\dot{\tau}_r}, \\ &= \frac{r\ \dot{\tau}\ /\ \dot{\tau}_r}{\frac{\dot{\tau}}{\dot{\tau}_r}-\exp(t/t_a)+1}, \\ \text{for small } t/t_a & \\ R &= \frac{r\ \dot{\tau}\ /\ \dot{\tau}_r\ \ t_a}{\frac{\dot{\tau}}{\dot{\tau}_r}t_a+t} \equiv \frac{a}{b+t}. \end{aligned} \tag{B.23}$$

For all described cases, the earthquake rate corresponding to the given stressing history is calculated using equation B.16. For example, the earthquake rate resulting from a case of a stress history composed by a constant tectonic loading $\dot{\tau}_r$ with a shear stress step occurring at time t_0 is obtained as follows: first equation B.18 is used to evolve γ through the stress step and to obtain γ immediately after it. This γ becomes the γ_0 in equation B.21, which gives the evolution of γ for the subsequent time interval, in which the stressing rate is assumed constant. By substituting the combination of the two into equation B.16 we obtain the seismicity rate as function of the time after a stress step, which is the well known Omori's law for aftershock decay following a mainshock.

$$R = \frac{r\ \dot{\tau}\ /\ \dot{\tau}_r}{\left[\frac{\dot{\tau}}{\dot{\tau}_r}\exp\left(\frac{-\Delta\tau}{A\sigma}\right)-1\right]\exp\left[\frac{-(t-t_0)}{t_a}\right]+1}. \tag{B.24}$$

where t_a is the characteristic relaxation time for the perturbation of the earthquake rate (see equation B.15). Panels C and D in figure B.1 show an example of this case.

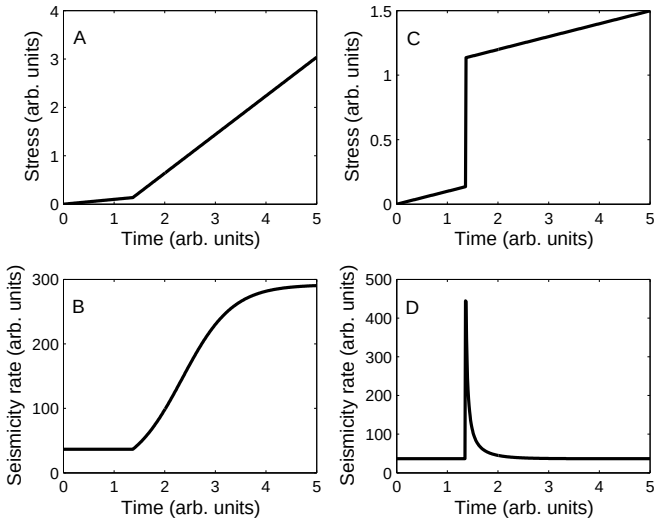

Figure B.1: Effect of stress perturbations on seismicity rate. Top: stress histories, C: stressing rate change; A: stress step; Bottom: seismicity rates.

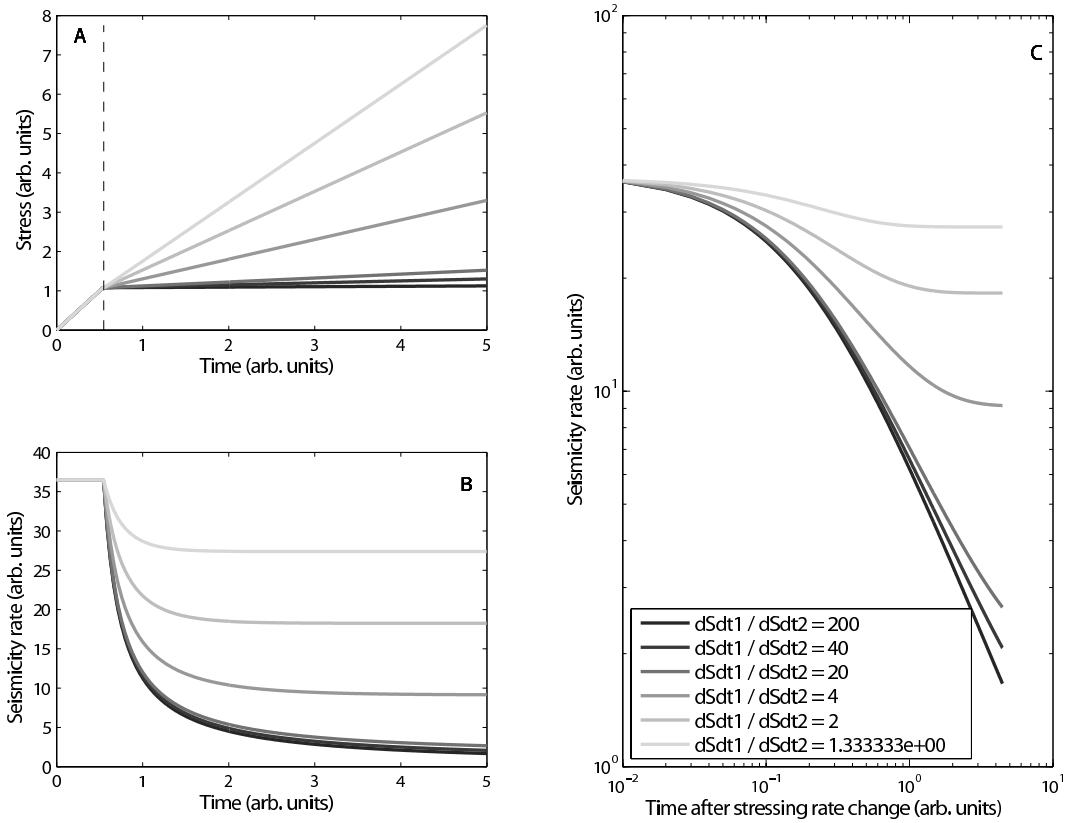

Figure B.2: Effect of a decrease in stressing rate on seismicity rate, for different ratios of stressing rate value after and before the change. A: stress histories, B: seismicity rates C: loglog plot of the seismicity rate since the time when change occurs.

Appendix C

Change Point Analysis

Mulargia and Tinti [1985] and *Mulargia et al.* [1987] propose a statistical procedure capable of detecting non-stationarities in a given distribution, under mild assumptions. They applied this technique to identify the incomplete part of the Italian seismic catalog [*Mulargia and Tinti*, 1985], and to recognize different regimes in the Etna volcano eruptive activity [*Mulargia et al.*, 1987].

Formerly, number of techniques had been proposed to infer changes in the process governing the distribution of a random variable. The major advances brought by the Mulargia and co-workers technique with respect to the existing ones, are the following:

1. it deals with an unknown number of regimes,
2. it allows the different regimes to follow different distributions,
3. it works with a small sample size ($\gtrsim 20$)

This new approach is based on the Kolmogorov-Smirnov two-sample non-parametric statistics $J3$, defined as follows:

$$J3 = \left(m\frac{n}{d}\right) \max_{-\infty<x<\infty} |G_n(x) - F_m(x)| \tag{C.1}$$

where m is the number of units in segment 1 (before the change-point, d the maximum common divisor of m and n), n the number of units in segment 2 (after the change-point), d the maximum common divisor of m and n, and $F(x)$ and $G(x)$ are empirical distribution functions of segment 1 and 2, respectively [e.g. *Hájek*, 1969]

$$F_m(x) = (1/m)\,\text{number of}\, X \le x \tag{C.2}$$

$$G_n(x) = (1/n)\,\text{number of}\, Y \le x \tag{C.3}$$

where the X and Y sets indicate, respectively, the set of samples before and after the change-point. $J3$ statistic is related to the significance level α at which samples 1 and 2 have a different distribution function, i.e.

$$H_0 : P(X < x) = P(Y < x), \quad -\infty < x < \infty. \tag{C.4}$$

The critical values $J3(\alpha, m, n)$ for m, n large (> 30), rewritten as

$$\begin{aligned} J'3 &= J3 \frac{d}{[(mn)(m+n)]^{1/2}} = \\ &= \left(\frac{mn}{m+n}\right)^{1/2} \max_{-\infty<x<\infty} |G_n(x) - F_m(x)| \end{aligned} \tag{C.5}$$

are well approximated by the distribution

$$P(J'3 < \lambda) = \sum_{j=-\infty}^{\infty} (-1)^j \mathrm{e}^{-2j^2\lambda^2}, \quad \lambda > 0, \tag{C.6}$$

which is tabulated in textbooks.

We assume that a single change point is present in a given set of N (unordered) data. We scan the data assuming a change-point corresponding to datum $i = 1$, then to datum 2, ... N and obtain the vector $J'3(i)$. The change-point i relative to the maximum $J'3$ component

$$i : \max\{J'3\} \tag{C.7}$$

yields therefore the most likely position for the change-point, and the corresponding $J'3$ gives a direct measure of the confidence level at which H_0 can be rejected, i.e. a measure of how significant is the inference attributing two different distributions to the segments before and after the change-point i.

Mulargia and Tinti [1985], by Monte-Carlo technique, simulate sets consisting of two regimes, i.e. a single change-point. They find the maximum $J'3(i)$ statistics to coincide with the change-point with an efficiency proportional to the contrast c between first and the second regime, defined as the the difference in the means divided by the mean standard deviation:

$$c = 2|\mu_2 - \mu_1|/(\sigma_1 + \sigma_2) \tag{C.8}$$

where μ_1, μ_2, σ_1, σ_2 are, respectively, the means and standard deviations of segments 1 and 2.

Mulargia and Tinti [1985] also emphasize that the maximum $J'3$ statistics corresponds to the change-point relative to the maximum contrast defined by the means and standard deviations of the segments preceding and following that particular change- point.

Applying the procedure to each of the two segments obtained by the first or principal change point, we can obtain a second (on segment 1) and a third (on segment 2) change-points. This procedure can thus be applied recursively on each segment progressively separated by a change-point. The change-point analysis terminates when the size of the segments become too small for practical significance.

Bibliography

Acocella V., and M. Neri (2003), What makes flank eruptions? The 2001 Etna eruption and its possible triggering mechanisms, *Bull. Volcanol.*, *65*(7), 517–529.

Akaike H. (1974), A new look at the statistical model identification, *Automatic Control, IEEE Transactions on*, *19*(6), 716–723.

Aki K. (1965), Maximum likelihood estimate of b in the formula log N= a-bM and its confidence limits, *Bull. Earthquake Res. Inst., Tokyo Univ*, *43*, 237–239.

Aki K., and V. Ferrazzini (2000), Seismic monitoring and modeling of an active volcano for prediction, *J. Geophys. Res.*, *105*(B7), 16,617–16,640.

Aki K., M. Fehler, and S. Das (1977), Source mechanism of volcanic tremor: fluid-driven crack models and their application to the 1963 Kilauea eruption, *J. Volcanol. Geotherm. Res.*, *2*, 259–287.

Alava M., and K. Niskanen (2006), The physics of paper, *Reports on Progress in Physics*, *69*(3), 669–724.

Alava M., P. Nukala, and S. Zapperi (2006), Statistical models of fracture, *Advances in Physics*, *55*(3), 349–476.

Albarède F. (1993), Residence time analysis of geochemical fluctuations in volcanic series, *Geochim. Cosmochim. Acta*, *57*(3), 615–621.

Allard P., B. Behncke, S. D'Amico, M. Neri, and S. Gambino (2006), Mount Etna 1993–2005: Anatomy of an evolving eruptive cycle, *Earth Science Reviews*, *78*(1-2), 85–114.

Aloisi M., A. Bonaccorso, S. Gambino, M. Mattia, and G. Puglisi (2003), Etna 2002 eruption imaged from continuous tilt and GPS data, *Geophys. Res. Lett.*, *30*(23), 2214.

Aloisi M., A. Bonaccorso, and S. Gambino (2006), Imaging composite dike propagation (Etna, 2002 case), *J. Geophys. Res.*, *111*(B06404), doi:10.1029/2005JB003908.

Alparone S., and E. Privitera (2001), Characteristics of the intermittent volcanic tremor at Mt. Etna, Italy, during the 15 September 1998–4 February 1999 eruptive episode, in *Proc. Cities on Volcanoes 2 Conference, Auckland, New Zealand, 12–14 February 2001.*

Alparone S., D. Andronico, L. Lodato, and T. Sgroi (2003), Relationship between tremor and volcanic activity during the Southeast Crater eruption on Mount Etna in early 2000, *J. Geophys. Res.*, *108*(B5), 2241.

Amitrano D., and A. Helmstetter (2006), Brittle creep, damage, and time to failure in rocks, *J. Geophys. Res.*, *111*(B11201), doi:10.1029/2005JB004252.

Andronico D., S. Branca, S. Calvari, M. Burton, T. Caltabiano, R. Corsaro, P. Del Carlo, G. Garfì, L. Lodato, L. Miraglia, et al. (2005), A multi-disciplinary study of the 2002–03 Etna eruption: insights into a complex plumbing system, *Bull. Volcanol.*, *67*(4), 314–330.

Aster R., S. Mah, P. Kyle, W. McIntosh, N. Dunbar, J. Johnson, M. Ruiz, and S. McNamara (2003), Very long period oscillations of Mount Erebus Volcano, *J. Geophys. Res.*, *108*(B11), 2522, doi:10.1029/2002JB002101.

Bachélery P. (1999), Le Fonctionnement des volcans boucliers, Habilitation à Diriger des Recherches thesis, Univ. de la Reunion, Saint Denis, France, 698 pages.

Bachélery P., P. Kowalski, P. Catherine, J. Delmond, P. Blum, and J. Croce (1998), *Precise Temporal and Mechanical Identification of Dyke Emplacement using Deformation Monitoring at Piton de la Fournaise.*, pp. 475 – 485, European Commission, EUR 18161 EN.

Bak P., K. Christensen, L. Danon, and T. Scanlon (2002), Unified scaling law for earthquakes, *Phys. Rev. Lett*, *88*(17), 178,501–178,501.

Barbano M., V. De Rubeis, P. Tosi, and S. Vinciguerra (2000), Clustering properties of Etna seismicity during 1981–1991, *Journal of Seismology*, *4*(2), 191–196.

Battaglia J., and K. Aki (2003), Location of seismic events and eruptive fissures on the Piton de la Fournaise volcano using seismic amplitudes, *J. Geophys. Res.*, *108*(B8), doi:10.1029/2002JB002193.

Battaglia J., K. Aki, and V. Ferrazzini (2005a), Location of tremor sources and estimation of lava output using tremor source amplitude on the Piton de la Fournaise volcano: 1. Location of tremor sources, *J. Volcanol. Geotherm. Res.*, *147*(3-4), 268–290.

Battaglia J., V. Ferrazzini, T. Staudacher, K. Aki, and J. Cheminee (2005b), Pre-eruptive migration of earthquakes at the Piton de la Fournaise volcano (Reunion Island), *Geophys. J. Int.*, *161*(2), 549–558.

Bean C., I. Lokmer, and G. O'Brien (2008), Influence of near-surface volcanic structure on long-period seismic signals and on moment tensor inversions: Simulated examples from Mount Etna, *J. Geophys. Res.*, *113*(B08308), doi:10.1029/2007JB005468.

Bebbington M., and C. Lai (1996), On nonhomogeneous models for volcanic eruptions, *Mathematical Geology*, *28*(5), 585–600.

Bianco F., M. Castellano, E. Del Pezzo, and J. Ibanez (1999), Attenuation of short-period seismic waves at Mt Vesuvius, Italy, *Geophys. J. Int.*, *138*(1), 67–76.

Bonaccorso A., M. Aloisi, and M. Mattia (2002), Dike emplacement forerunning the Etna July 2001 eruption modeled through continuous tilt and GPS data, *Geophys. Res. Lett.*, *29*(13), 1624.

Bonaccorso A., S. DâĂŹAmico, M. Mattia, and D. Patanè (2004), Intrusive mechanisms at Mt. Etna forerunning the July-August 2001 eruption from seismic and ground deformation data, *Pure Appl. Geophys.*, *161*(7), 1469–1487.

Bonaccorso A., A. Bonforte, F. Guglielmino, M. Palano, and G. Puglisi (2006), Composite ground deformation pattern forerunning the 2004–2005 Mount Etna eruption, *J. Geophys. Res.*, *111*(B12207), doi:10.1029/2005JB004206.

Bonamy D., L. Ponson, S. Prades, E. Bouchaud, and C. Guillot (2006), Scaling exponents for fracture surfaces in homogeneous glass and glassy ceramics, *Phys. Rev. Lett*, *97*(13), 135,504.

Bonnet E., O. Bour, N. Odling, P. Davy, I. Main, P. Cowie, and B. Berkowitz (2001), Scaling of fracture systems in geological media, *Reviews of Geophysics*, *39*(3), 347–383.

Bottari A., and G. Neri (1983), Some statistical properties of a sequence of historical Calabro-Peloritan earthquakes, *J. Geophys. Res.*, *88*(B2), 1209–1212.

Bottiglieri M., E. Lippiello, C. Godano, and L. de Arcangelis (2009), Identification and spatiotemporal organization of aftershocks, *J. Geophys. Res.*, *114*(B3), B03,303.

Bouchon M., and H. Karabulut (2008), The Aftershock Signature of Supershear Earthquakes, *Science*, *320*(5881), 1323.

Braun T., W. Kleemann, J. Dec, and P. Thomas (2005), Creep and relaxation dynamics of domain walls in periodically poled KTiOPO 4, *Phys. Rev. Lett*, *94*, 117,601.

Brodsky E., V. Karakostas, and H. Kanamori (2000), A new observation of dynamically triggered regional seismicity: earthquakes in Greece following the August, 1999 Izmit, Turkey earthquake, *Geophys. Res. Lett.*, *27*(17), 2741–2744.

Bullard F. (1962), Volcanoes of southern Peru, *Bull. Volcanol.*, *24*(1), 443–453.

Burton M., M. Neri, D. Andronico, S. Branca, T. Caltabiano, S. Calvari, R. Corsaro, P. Del Carlo, G. Lanzafame, L. Lodato, et al. (2005), Etna 2004–2005: an archetype for geodynamically-controlled effusive eruptions, *Geophys. Res. Lett.*, *32*(9), L09,303, doi:10.1029/2005GL022527.

Campbell K. (2003), Strong-motion attenuation relations, *International handbook of earthquake and engineering seismology*, pp. 1003–1012.

Carmichael I., J. Nicholls, F. Spera, B. Wood, and S. Nelson (1977), High-Temperature Properties of Silicate Liquids: Applications to the Equilibration and Ascent of Basic Magma, *Phil. Trans. R. Soc. Lond. A*, *286*(1336), 373–429.

Catalli F., M. Cocco, R. Console, and L. Chiaraluce (2008), Modeling seismicity rate changes during the 1997 Umbria-Marche sequence (central Italy) through a rate-and state-dependent model, *J. Geophys. Res.*, *113*(B11301), doi:10.1029/2007JB005356.

Cayol V., J. Dieterich, A. Okamura, and A. Miklius (2000), High magma storage rates before the 1983 eruption of Kilauea, Hawaii, *Science*, *288*(5475), 2343–2346.

Chastin S., and I. Main (2003), Statistical analysis of daily seismic event rate as a precursor to volcanic eruptions, *Geophys. Res. Lett.*, *30*(13), 1671.

Chauve P., T. Giamarchi, and P. Le Doussal (2000), Creep and depinning in disordered media, *Phys. Rev. Lett*, *62*(10), 6241–6267.

Chen Z., Z. Jin, and S. Johnson (2007), A perturbation solution for dyke propagation in an elastic medium with graded density, *Geophys. J. Int.*, *169*(1), 348–356.

Chouet B. (1986), Dynamics of a fluid-driven crack in three dimensions by the finite difference method, *J. Geophys. Res.*, *91*(B14), 13,967–13,992.

Chouet B. (1988), Resonance of a fluid-driven crack: radiation properties and implications for the source of long-period events and harmonic tremor, *J. Geophys. Res.*, *93*(B5), 4375–4400.

Chouet B. (1996), Long-period volcano seismicity: its source and use in eruption forecasting, *Nature*, *380*, 309–316.

Chouet B. (2003), Volcano seismology, *Pure Appl. Geophys.*, *160*(3), 739–788.

Collombet M., J. Grasso, and V. Ferrazzini (2003), Seismicity rate before eruptions on Piton de la Fournaise volcano: Implications for eruption dynamics, *Geophys. Res. Lett.*, *30*(21), 2099.

Connor C., R. Sparks, R. Mason, C. Bonadonna, and S. Young (2003), Exploring links between physical and probabilistic models of volcanic eruptions: The Soufriere Hills Volcano, Montserrat, *Geophys. Res. Lett.*, *30*(13), 1701.

Cornelius R., and B. Voight (1994), Seismological aspects of the 1989–1900 eruption at Rebout volcano, Alaska: The Materials Failure Forecast Method with RSAM and SSAM seismic data, *J. Volcanol. Geotherm. Res.*, *62*, 469–498.

Cornelius R., and B. Voight (1995), Graphical and PC-software analysis of volcano eruption precursors according to the Materials Failure Forecast Method (FFM), *J. Volcanol. Geotherm. Res.*, *64*(3-4), 295–320.

Cornet F. (1992), Fracture processes induced by forced fluid percolation, in *Volcanic Seismology, IAVCEI Proc. Volcanology*, vol. 3, pp. 407–431.

Corral Á. (2003), Local distributions are rate fluctuations in a unified scaling law for earthquakes, *Phys. Rev. E*, *68*(035102(R)).

Corral Á. (2004a), Universal local versus unified global scaling laws in the statistics of seismicity, *Physica A*, *340*(4), 590–597.

Corral Á. (2004b), Long-term clustering, scaling, and universality in the temporal occurrence of earthquakes, *Phys. Rev. Lett*, *92*(10), 108,501–108,501.

Corral Á., and K. Christensen (2006), Comment on âĂIJEarthquakes Descaled: On Waiting Time Distributions and Scaling LawsâĂİ, *Phys. Rev. Lett*, *96*, 109,801.

Creamer F., and C. Kisslinger (1993), The relation between temperature and the Omori decay parameter for aftershock sequences near Japan, *EOS*, *74*, 43.

Cusano P., S. Petrosino, and G. Saccorotti (2008), Hydrothermal origin for sustained long-period (LP) activity at Campi Flegrei volcanic complex, Italy, *J. Volcanol. Geotherm. Res.*, *177*(4), 1035–1044.

Das S., and C. Scholz (1981), Theory of time-dependent rupture in the Earth, *J. Geophys. Res.*, *86*(87), 6039–6051.

Davidsen J., and C. Goltz (2004), Are seismic waiting time distributions universal?, *Geophys. Res. Lett.*, *31*(21), L21,612, doi:10.1029/2004GL020892.

Davidsen J., S. Stanchits, and G. Dresen (2007), Scaling and universality in rock fracture, *Phys. Rev. Lett*, *98*, 125,502.

Davis S., and C. Frohlich (1991), Single-link cluster analysis of earthquake aftershocks: decay laws and regional variations, *J. Geophys. Res.*, *96*(B4), 6335–6350.

De la Cruz-Reyna S. (1991), Poisson-distributed patterns of explosive eruptive activity, *Bull. Volcanol.*, *54*, 57–67.

De la Cruz-Reyna S., and G. Reyes-Dávila (2001), A model to describe precursory material-failure phenomena: Application to short-term forecasting at Colima volcano, Mexico, *Bull. Volcanol.*, *63*, 297–308.

De La Cruz-Reyna S., I. Yokoyama, A. Martínez-Bringas, and E. Ramos (2008), Precursory seismicity of the 1994 eruption of Popocatépetl Volcano, Central Mexico, *Bull. Volcanol.*, *70*(6), 753–767.

De Natale G., and A. Zollo (1986), Statistical analysis and clustering features of the Phlegraean Fields earthquake sequence (May 1983-May 1984), *Bull. Seismol. Soc. America*, *76*(3), 801–814.

De Natale G., I. Kuznetzov, T. Kronrod, A. Peresan, A. Saraò, C. Troise, and G. Panza (2004), Three decades of seismic activity at Mt. Vesuvius: 1972–2000, *Pure Appl. Geophys.*, *161*(1), 123–144.

Del Pezzo E., and S. Petrosino (2001), A local-magnitude scale for Mt. Vesuvius from synthetic Wood-Anderson seismograms, *Journal of Seismology*, *5*(2), 207–215.

Del Pezzo E., F. Bianco, and G. Saccorotti (2003), Duration magnitude uncertainty due to seismic noise: inferences on the temporal pattern of GR b-value at Mt. Vesuvius, Italy, *Bull. Seismol. Soc. America*, *93*(4), 1847–1853.

Del Pezzo E., F. Bianco, and G. Saccorotti (2004), Seismic source dynamics at Vesuvius volcano, Italy, *J. Volcanol. Geotherm. Res.*, *133*(1-4), 23–39.

Delaney P., and D. McTigue (1994), Volume of magma accumulation or withdrawal estimated from surface uplift or subsidence, with application to the 1960 collapse of Kilauea volcano, *Bull. Volcanol.*, *56*(6), 417–424.

Deterich J. (1994), A constitutive law for rate of earthquake production and its application to earthquake clustering, *J. Geophys. Res.*, *99*(B 2), 2601–2618.

Dieterich J. (1992), Earthquake nucleation on faults with rate-and state-dependent strength, *Tectonophysics*, *211*(1-4), 115–134.

Dieterich J., and D. Smith (2006), Stress Relaxation on Geometrically Complex Faults, in *AGU, Fall Meeting 2006, abstract# S34A-06.*

Dieterich J., V. Cayol, and P. Okubo (2000), The use of earthquake rate changes as a stress meter at Kilauea volcano, *Nature*, *408*(6811), 457–460.

Dieterich J., V. Cayol, and P. Okubo (2003), Stress changes before and during the Puo-Kupaianaha eruption, US Geol, *Survey Professional Paper*, *1676*, 187.

Duemmer O., and W. Krauth (2007), Depinning exponents of the driven long-range elastic string, *J. Stat. Mech*, *P01019*, doi:10.1088/1742-5468/2007/01/P01019.

Einarsson P., and B. Brandsdottir (1980), Seismological evidence for lateral magma intrusion during the 1978 deflation of the Krafla volcano in NE Iceland, *J. Geophys.*, *47*, 160–165.

Emerman S., D. Turcotte, and S. D.A. (1986), Transport of magma and hydrothermal solutions by laminar and turbulent fluid fracture, *Phys. Earth Planet.*, *41*, 249–259.

Felzer K., and E. Brodsky (2006), Decay of aftershock density with distance indicates triggering by dynamic stress, *Nature*, *441*, 735–738.

Felzer K., T. Becker, and R. Abercrombie (2002), Triggering of the 1999 Mw 7.1 Hector Mine earthquake by aftershocks of the 1992 Mw 7.3 Landers earthquake, *J. Geophys. Res.*, *107*(B9), 2190, doi:10.1029/2001JB000911.

Feuillet N., C. Nostro, C. Chiarabba, and M. Cocco (2004), Coupling between earthquake swarms and volcanic unrest at the Alban Hills Volcano (central Italy) modeled through elastic stress transfer, *J. Geophys. Res.*, *109*(B02308), doi:10.1029/2003JB002419.

Fisher D. (1998), Collective transport in random media: from superconductors to earthquakes, *Physics Reports*, *301*(1), 113–150.

Freed A. (2005), Earthquake triggering by static, dynamic, and postseismic stress transfer, *Annu. Rev. Earth Planet.Sci.*, *33*, 335–367.

Froger J., Y. Fukushima, P. Briole, T. Staudacher, T. Souriot, and N. Villeneuve (2004), The deformation field of the August 2003 eruption at Piton de la Fournaise, Reunion Island, mapped by ASAR interferometry, *Geophys. Res. Lett.*, *31*(L14601), doi:10.1029/2004GL020479.

Frohlich C., and S. Davis (1990), Single-link cluster analysis as a method to evaluate spatial and temporal properties of earthquake catalogues, *Geophys. J. Int.*, *100*(1), 19–32.

Fujita E., Y. Ida, and J. Oikawa (1995), Eigen oscillation of a fluid sphere and source mechanism of harmonic volcanic tremor, *J. Volcanol. Geotherm. Res.*, *69*(3-4), 365–378.

Furuya M., S. Okubo, F. Kimata, R. Miyajima, I. Meilano, W. Sun, Y. Tanaka, and T. Miyazaki (2003a), Mass budget of the magma flow in the 2000 volcano-seismic activity at Izu-islands, Japan, *Earth Planets and Space*, *55*(7), 375–386.

Furuya M., S. Okubo, W. Sun, Y. Tanaka, J. Oikawa, H. Watanabe, and T. Maekawa (2003b), Spatiotemporal gravity changes at Miyakejima Volcano, Japan: Caldera collapse, explosive eruptions and magma movement, *J. Geophys. Res.*, *108*(B4), 2219, doi:10.1029/2002JB001989.

Gambino S., A. Mostaccio, D. Patanè, L. Scarfì, and A. Ursino (2004), High-precision locations of the microseismicity preceding the 2002–2003 Mt. Etna eruption, *Geophys. Res. Lett.*, *31*(L18604), doi:10.1029/2004GL020499.

Garcimartín A., A. Guarino, L. Bellon, and S. Ciliberto (1997), Statistical Properties of Fracture Precursors, *Phys. Rev. Lett*, *79*(17), 3202–3205.

Gomberg J., P. Reasenberg, P. Bodin, and R. Harris (2001), Earthquake triggering by seismic waves following the Landers and Hector Mine earthquakes, *Nature*, *411*(6836), 462–466.

Gomberg J., P. Bodin, and P. Reasenberg (2003), Observing earthquakes triggered in the near field by dynamic deformations, *Bull. Seismol. Soc. America*, *93*(1), 118–138.

Gonnermann H., and M. Manga (2003), Explosive volcanism may not be an inevitable consequence of magma fragmentation, *Nature*, *426*(6965), 432–435.

Goto A. (1999), A new model for volcanic earthquake at Unzen Volcano: melt rupture model, *Geophys. Res. Lett.*, *26*(16), 2541–2544.

Grasso J., and P. Bachelery (1995), Hierarchical organization as a diagnostic approach to volcano mechanics: Validation on Piton de la Fournaise, *J. Geophys. Res.*, *22*, 2897–2900.

Grasso J., and I. Zaliapin (2004), Predictability of volcano eruption: Lessons from a basaltic effusive volcano, *Geophys. Res. Lett.*, *31*(5), 5602–5602.

Gresta S., A. Montalto, and G. Patane (1991), Volcanic tremor at Mount Etna (January 1984–March 1985): its relationship to the eruptive activity and modelling of the summit feeding system, *Bull. Volcanol.*, *53*(4), 309–320.

Griffith A. (1921), The phenomena of rupture and flow in solids, *Phil. Trans. R. Soc. Lond. A*, pp. 163–198.

Griffith A. (1924), The Theory of Rupture: Proc, *First Intern. Cong. Applied Mechanics: Techniscke Backhandel Wattman, Delft*, pp. 55–63.

Guest J. (1982), Styles of eruption and flow morphology on Mt Etna, *Mem. Soc. Geol. Ital*, *23*, 49–73.

Guo Z., and Y. Ogata (1997), Statistical relations between the parameters of aftershocks in time, space, and magnitude, *J. Geophys. Res.*, *102*(B2), 2857–2873.

Gusev A., V. Ponomareva, O. Braitseva, I. Melekestsev, and L. Sulerzhitsky (2003), Great explosive eruptions on Kamchatka during the last 10,000 years: Self-similar irregularity of the output of volcanic products, *J. Geophys. Res.*, *108*(B2), 2126, doi:10.1029/2001JB000312.

Gutenberg B., and C. Richter (1949), Seismicity of the Earth and associated phenomena.

Hainzl S., and Y. Ogata (2005), Detecting fluid signals in seismicity data through statistical earthquake modeling, *J. Geophys. Res.*, *110*(B05S07), doi:10.1029/2004JB003247.

Hainzl S., F. Scherbaum, and C. Beauval (2006), Estimating Background Activity Based on Interevent-Time Distribution, *Bull. Seismol. Soc. America*, *96*(1), 313–320.

Hájek J. (1969), *A Course in Nonparametric Statistics*, Holden-Day.

Hardebeck J., J. Nazareth, and E. Hauksson (1998), The static stress change triggering model: Constraints from two southern California aftershock sequences, *J. Geophys. Res.*, *103*(B10), 24,427–24,437.

Harrington R., and E. Brodsky (2007), Volcanic hybrid earthquakes that are brittle-failure events, *Geophys. Res. Lett.*, *34*(L06308), doi:10.1029/2006GL028714.

Harris R. (1998), Introduction to special section: Stress triggers, stress shadows, and implications for seismic hazard, *J. Geophys. Res.*, *103*(B10), 24,347–24,358.

Hartzell S., P. Liu, and C. Mendoza (), The 1994 Northridge, California, earthquake: investigation of rupture velocity, risetime, and high-frequency radiation, *J. Geophys. Res.*, *101*(B9), 20,091–20,108.

Hawkes A., and L. Adamopoulos (1973), Cluster models for earthquakes–regional comparisons, *Bull. Int. Statist. Inst*, *45*(3), 454–461.

Helmstetter A. (2002), Ruptures et instabilités: Sisimcité et mouvements gravitaires, Ph.D. thesis, Université Joseph Fourier, Grenoble I.

Helmstetter A. (2003), Is Earthquake Triggering Driven by Small Earthquakes?, *Phys. Rev. Lett*, *91*(5), 58,501.

Helmstetter A., and B. Shaw (2006), Relation between stress heterogeneity and aftershock rate in the rate-and-state model, *J. Geophys. Res.*, *111*(B07304), doi:10.1029/2005JB004077.

Helmstetter A., and D. Sornette (2002a), Subcritical and supercritical regimes in epidemic models of earthquake aftershocks, *J. Geophys. Res.*, *107*(10), 1–21.

Helmstetter A., and D. Sornette (2002b), Diffusion of epicenters of earthquake aftershocks, Omori's law, and generalized continuous-time random walk models, *Phys. Rev. E*, *66*(6), 61,104.

Helmstetter A., and D. Sornette (2003), Importance of direct and indirect triggered seismicity in the ETAS model of seismicity, *Geophys. Res. Lett.*, *30*(11), 1576.

Helmstetter A., D. Sornette, and J. Grasso (2003a), Mainshocks are Aftershocks of Conditional Foreshocks: How do foreshock statistical properties emerge from aftershock laws, *J. Geophys. Res.*, *108*(B1), 2046, doi:10.1029/2002JB001991.

Helmstetter A., G. Ouillon, and D. Sornette (2003b), Are aftershocks of large Californian earthquakes diffusing, *J. Geophys. Res.*, *108*(B10), 2483, doi:10.1029/2003JB002503.

Helmstetter A., Y. Kagan, and D. Jackson (2005), Importance of small earthquakes for stress transfers and earthquake triggering, *J. Geophys. Res.*, *110*(B05S08), doi:10.1029/2004JB003286.

Hergarten S., and H. Neugebauer (2002), Foreshocks and aftershocks in the Olami-Feder-Christensen model, *Phys. Rev. Lett*, *88*(213), 238,501.

Hill D. (1977), A model for earthquake swarms, *J. Geophys. Res.*, *82*(B8), 1347–1352.

Hill D., F. Pollitz, and C. Newhall (2002), Earthquake-volcano interactions, *Physics Today*, *55*(11), 41–47.

Ho C. (1991), Nonhomogeneous Poisson model for volcanic eruptions, *Mathematical Geology*, *23*(2), 167–173.

Ho C. (1996), Volcanic time-trend analysis, *J. Volcanol. Geotherm. Res.*, *74*(3-4), 171–177.

Huc M., and I. Main (2003), Anomalous stress diffusion in earthquake triggering: Correlation length, time dependence, and directionality, *J. Geophys. Res.*, *108*(B7), 2324, doi:10.1029/2001JB001645.

Ida Y. (1999), Effects of the crustal stress on the growth of dikes: Conditions of intrusion and extrusion of magma, *J. Geophys. Res.*, *104*(B8), 17,897–17,909.

Ioffe L. (1987), Dynamics of interfaces and dislocations in disordered media, *J. Physics*, *C 20*, 6149–6158.

Irwan M., F. Kimata, N. Fujii, S. Nakao, H. Watanabe, S. Sakai, M. Ukawa, E. Fujita, and K. Kawai (2003), Rapid ground deformation of the Miyakejima volcano on 26-27 June 2000 detected by kinematic GPS analysis, *Earth Planet Space*, *55*(12), 13–16.

Irwin G. (1958), Fracture, in *Handbuch der Physik*, vol. VI, edited by B. Springer.

Ito T., and S. Yoshioka (2002), A dike intrusion model in and around Miyakejima, Niijima and Kozushima in 2000, *Tectonophysics*, *359*(1-2), 171–187.

Jacques E., J. Ruegg, J. Lepine, P. Tapponnier, G. King, and A. Omar (1999), Relocation of $M \geq 2$ events of the 1989 Dobi seismic sequence in Afar: evidence for earthquake migration, *Geophys. J. Int.*, *138*(2), 447–469.

Janssen M., J. Zuidema, and R. Wanhill (2003), *Fracture Mechanics*, Spon Press, Taylor and Francis group, London and New York.

Johansen A., and D. Sornette (2000), Critical ruptures, *The European Physical Journal B*, *18*(1), 163–181.

Johnson J., and J. Lees (2000), Plugs and chugsâĂŤseismic and acoustic observations of degassing explosions at Karymsky, Russia and Sangay, Ecuador, *J. Volcanol. Geotherm. Res.*, *101*(1-2), 67–82.

Johnson P., and X. Jia (2005), Nonlinear dynamics, granular media and dynamic earthquake triggering, *Nature*, *437*(7060), 871–874.

Jones G., D. Chester, and F. Shooshtarian (1999), Statistical analysis of the frequency of eruptions at Furnas Volcano, São Miguel, Azores, *J. Volcanol. Geotherm. Res.*, *92*(1-2), 31–38.

Jonsdottir K., M. Lindman, R. Roberts, B. Lund, and R. Bödvarsson (2006), Modelling fundamental waiting time distributions for earthquake sequences, *Tectonophysics*, *424*(3-4), 195–208.

Julian B. (1994), Volcanic tremor: nonlinear excitation by fluid flow, *J. Geophys. Res.*, *99*(B6), 11,859–11,877.

Kagan Y. (1991), Fractal dimension of brittle fracture, *Journal of Nonlinear Science*, *1*(1), 1–16.

Kagan Y. (2002), Aftershock zone scaling, *Bull. Seismol. Soc. America*, *92*(2), 641–655.

Kagan Y. (2004), Short-Term Properties of Earthquake Catalogs and Models of Earthquake Source, *Bull. Seismol. Soc. America*, *94*(4), 1207–1228.

Kagan Y., and L. Knopoff (1981), Stochastic synthesis of earthquake catalogs, *J. Geophys. Res.*, *86*(B4), 2853–2862.

Kagan Y., and L. Knopoff (1987), Statistical short-term earthquake prediction, *Science*, *236*(4808), 1563–1567.

Kanamori H. (1973), Mode of strain release associated with major earthquakes in Japan, *Ann. Rev. Earth Planet. Sci.*, *1*(1), 213–239.

Kanamori H., and D. Anderson (1975), Theoretical basis of some empirical relations in seismology, *Bull. Seismol. Soc. America*, *65*(5), 1073–1095.

Kanamori H., J. Mori, E. Hauksson, T. Heaton, L. Hutton, and L. Jones (1993), Determination of earthquake energy release and ML using TERRAscope, *Bull. Seismol. Soc. America*, *83*(2), 330–346.

Katsumata A. (1996), Comparison of magnitudes estimated by the Japan Meteorological Agency with moment magnitudes for intermediate and deep earthquakes, *Bull. Seismol. Soc. America*, *86*(3), 832–842.

Keilis-Borok V. (2002), Earthquake Prediction: State-of-the-Art and Emerging Possibilities, *Ann. Rev. Earth Planet. Sci.*, *30*(1), 1–33.

Kertész J., K. Viktor, and F. Weber (1993), Self-affine rupture lines in paper sheets, *Fractals*, *1*(1), 67–74.

Kilburn C. (2003), Multiscale fracturing as a key to forecasting volcanic eruptions, *J. Volcanol. Geotherm. Res.*, *125*(3-4), 271–289.

Kilburn C., and B. Voight (1998), Slow rock fracture as eruption precursor at Soufriere Hills volcano, Montserrat, *Geophys. Res. Lett.*, *25*, 3665–3668.

King G., and M. Cocco (2000), Fault interaction by elastic stress changes: new clues from earthquake sequences, *Advances in Geophysics*, *44*, 1–38.

King G., R. Stein, and J. Lin (1994), Static stress changes and the triggering of earthquakes, *Bull. Seismol. Soc. America*, *84*(3), 935–953.

Kisslinger C., and L. Jones (1991), Properties of aftershock sequences in southern California, *J. Geophys. Res.*, *96*(B7), 11,947–11,958.

Klein F. (1984), Eruption forecasting at Kilauea Volcano, Hawaii, *J. Geophys. Res.*, *89*, 3059–3073.

Klein F., R. Koyanagi, J. Nakata, and W. Tanigawa (1987), The seismicity of Kilauea's magma system, *Volcanism in Hawaii*, *2*, 1019–1185.

Klein F., T. Wright, and J. Nakata (2006), Aftershock decay, productivity, and stress rates in Hawaii: Indicators of temperature and stress from magma sources, *J. Geophys. Res.*, *111*(B07307), doi:10.1029/2005JB003949.

Koivisto J., J. Rosti, and M. Alava (2007), Creep of a fracture line in paper peeling, *Phys. Rev. Lett*, *99*(14), 145,504.

Kolton A., A. Rosso, and T. Giamarchi (2005), Creep motion of an elastic string in a random potential, *Phys. Rev. Lett*, *94*, 047,002.

Kumagai H., B. Chouet, and P. Dawson (2005), Source process of a long-period event at Kilauea volcano, Hawaii, *Geophys. J. Int.*, *161*(1), 243–254.

Lahaie F., and J. Grasso (1998), A fluid-rock interaction cellular automaton of volcano mechanics: Application to the Piton de la Fournaise, *J. Geophys. Res.*, *103*, 9637–9649.

Lahr J., B. Chouet, C. Stephens, J. Power, and R. Page (1994), Earthquake classification, location, and error analysis in a volcanic environment: implications for the magmatic system of the 1989-1990 eruptions at Redoubt Volcano, Alaska, *J. Volcanol. Geotherm. Res.*, *62*(1), 137–152.

Lanzafame G., M. Neri, V. Acocella, A. Billi, R. Funiciello, and G. Giordano (2003), Structural features of the July-August 2001 Mount Etna eruption: evidence for a complex magma supply system.

Lee M., and D. Sornette (2000), Novel mechanism for discrete scale invariance in sandpile models, *The European Physical Journal B*, *15*(1), 193–197.

Lemarchand N., and J. Grasso (2007), Interactions between earthquakes and volcano activity, *Geophys. Res. Lett.*, *34*(L24303), doi:10.1029/2007GL031438.

Lemerle S., J. Ferre, C. Chappert, V. Mathet, T. Giamarchi, and P. Le Doussal (1998), Wall creep in an Ising ultrathin magnetic film, *Phys. Rev. Lett*, *80*(4), 849–852.

Lénat J., and P. Bachèlery (1990), Structure et fonctionnement de la zone centrale du Piton de la Fournaise, in *Le Volcanisme de La Réunion*, edited by J. Lénat, pp. 257–296, Centre de Recherches Volcanologiques, Clermont-Ferrand, France.

Lengliné O., D. Marsan, J.-L. Got, V. Pinel, V. Ferrazzini, and P. Okubo (2008), Seismicity and deformation induced by magma accumulation at three basaltic volcanoes, *J. Geophys. Res.*, *113*(B12305), doi:10.1029/2008JB005937.

Lindman M., K. Jonsdottir, R. Roberts, B. Lund, and R. Bödvarsson (2005), On waiting time distributions and scaling laws, *Phys. Rev. Lett*, *94*, 108,501.

Lister J. (1990a), Buoyancy-driven fluid fracture: the effects of material toughness and of highly viscous fluids, *J. Fluid Mech.*, *210*, 263–280.

Lister J. (1990b), Buoyancy-driven fluid fracture: similarity solutions for the horizontal and vertical propagation of fluid-filled cracks, *J. Fluid Mech.*, *217*, 213–239.

Lister J., and R. Kerr (1991), Fluid-mechanical models of crack propagation and their application to magma transport in dykes, *J. Geophys. Res.*, *96*(B6), 10,049–10,077.

Lokmer I., C. Bean, G. Saccorotti, and D. Patanè (2007), Moment-tensor inversion of LP events recorded on Etna in 2004 using constraints obtained from wave simulation tests, *Geophys. Res. Lett.*, *34*(L22316), doi:10.1029/2007GL031902.

Lokmer I., G. Saccorotti, B. Di Lieto, and C. Bean (2008), Temporal evolution of long-period seismicity at Etna Volcano, Italy, and its relationships with the 2004–2005 eruption, *Earth and Planet. Sci. Lett.*, *266*(1-2), 205–220.

Lombardi A., W. Marzocchi, and J. Selva (2006), Exploring the evolution of a volcanic seismic swarm: The case of the 2000 Izu Islands swarm, *Geophys. Res. Lett.*, *33*(L07310), doi:10.1029/2005GL025157.

Maaløe S. (1998), Shape of ascending feeder dikes, and ascent modes of magma, *J. Volcanol. Geotherm. Res.*, *81*(3-4), 207–214.

Macedo O., J. Métaxian, E. Taipe, D. Ramos, and A. Inza (2009), Seismicity associated with the 2006-2008 eruption, Ubinas volcano, in *The VOLUME Project - VOLcanoes, Understanding Mass MovEments*, edited by C. Bean, B. A.K., I. Lokmer, F. Martini, and G. O'Brien, pp. 262–270, VOLUME Project EU PF6 (N. 018471) Consortium, Dublin.

Måløy K., S. Santucci, J. Schmittbuhl, and R. Toussaint (2006), Local waiting time fluctuations along a randomly pinned crack front, *Phys. Rev. Lett*, *96*, 045,501.

Marsan D. (2006), Can coseismic stress variability suppress seismicity shadows? Insights from a rate-and-state friction model, *J. Geophys. Res.*, *111*(B06305), doi:10.1029/2005JB004060.

Marsan D., and O. Lengliné (2008), Extending Earthquakes' Reach Through Cascading, *Science*, *319*(5866), 1076.

Marsan D., C. Bean, S. Steacy, and J. McCloskey (2000), Observation of diffusion processes in earthquake populations and implications for the predictability of seismicity systems, *J. Geophys. Res.*, *105*, 28–081.

Marzocchi W., and L. Zaccarelli (2006), A quantitative model for the time-size distribution of eruptions, *J. Geophys. Res.*, *111*(B04204), doi:10.1029/2005JB003709.

Matsuúra R., and I. Karakama (2005), A Point-process Analysis of the Matsushiro Earthquake Swarm Sequence: The Effect of Water on Earthquake Occurrence, *Pure Appl. Geophys.*, *162*(6), 1319–1345.

McGuire W., and C. Kilburn (1997), Forecasting volcanic events: some contemporary issues, *Geologische Rundschau*, *86*(2), 439–445.

McKenzie D. (1984), The Generation and Compaction of Partially Molten Rock, *J. Petrology*, *25*(3), 713–765.

McNutt S. (2002), Volcano seismology and monitoring for eruptions, *International handbook of earthquake and engineering seismology*, pp. 383–406.

Melnik O., and R. Sparks (1999), Nonlinear dynamics of lava dome extrusion, *Nature*, *402*(6757), 37–41.

Menand T., and S. Tait (2002), The propagation of a buoyant liquid-filled fissure from a source under constant pressure: an experimental approach, *J. Geophys. Res.*, *107*(B11), 2306, doi:10.1029/2001JB000589.

Meriaux C., and C. Jaupart (1998), Dike propagation through an elastic plate, *J. Geophys. Res.*, *103*, 18,295–18,314.

Mériaux C., J. Lister, V. Lyakhovsky, and A. Agnon (1999), Dyke propagation with distributed damage of the host rock, *Earth and Planet. Sci. Lett.*, *165*(2), 177–185.

Miller A., R. Stewart, R. White, R. Luckett, B. Baptie, W. Aspinall, J. Latchman, L. Lynch, and B. Voight (1998), Seismicity associated with dome growth and collapse at the Soufriere Hills Volcano, Montserrat, *Geophys. Res. Lett.*, *25*(19), 3657–3660.

Minakami T. (1960), Fundamental research for predicting volcanic eruptions (Part 1). Earthquakes and crustal deformations originating from volcanic activities, *Bull. Earthq. Res. Inst. Tokyo Univ.*, *38*, 497–544.

Minakami T. (1974), Seismology of volcanoes in Japan, *Physical Volcanology*, pp. 1–28.

Mogi K. (1962), On the time distribution of aftershocks accompanying the recent major earthquakes in and near Japan, *Bull. Earthquake Res. Inst. Univ. Tokyo*, *40*, 175–185.

Mogi K. (1963), Some Discussions on Aftershocks, Foreshocks and Earthquake Swarms: the Fracture of a Semi-infinite Body Caused by an Inner Stress Origin and Its Relation to the Earthquake Phenomena, *Bull. Earthquake Res. Inst. Univ. Tokyo*, *38*, 615–658.

Mogi K. (1967), Earthquakes and fractures, *Tectonophysics*, *5*(1), 35–55.

Mogi K. (1968), Source locations of elastic shocks in the fracturing process in rocks (1), *Bull. Earthquake Res. Inst. Univ. Tokyo*, *46*, 1103–1125.

Molchan G. (1997), Earthquake prediction as a decision-making problem, *Pure Appl. Geophys.*, *149*(1), 233–247.

Molchan G. (2005), Interevent time distribution in seismicity: a theoretical approach, *Pure Appl. Geophys.*, *162*(6), 1135–1150.

Molina I., H. Kumagai, and H. Yepes (2004), Resonances of a volcanic conduit triggered by repetitive injections of an ash-laden gas, *Geophys. Res. Lett.*, *31*(L03603), doi:10.1029/2003GL018934.

Mulargia F., and S. Tinti (1985), Seismic sample areas defined from incomplete catalogues: an application to the Italian territory, *Phys. Earth Planet. Int*, *40*, 273–300.

Mulargia F., S. Tinti, and E. Boschi (1985), A statistical analysis of flank eruptions on Etna volcano: Jour, *Volcanol. Geotherm. Res*, *23*(3), 263–272.

Mulargia F., P. Gasperini, and S. Tinti (1987), Identifying different regimes in eruptive activity: an application to Etna Volcano, *J. Volcanol. Geotherm. Res.*, *34*(1-2), 89–106.

Mulargia F., P. Gasperini, and W. Marzocchi (1991), Pattern recognition applied to volcanic activity: identification of the precursory patterns to Etna recent flank eruptions and periods of rest, *J. Volcanol. Geotherm. Res.*, *45*, 187–196.

Mulargia F., W. Marzocchi, and P. Gasperini (1992), Statistical identification of physical patterns to Etna recent flank eruptions and periods of rest, *J. Volcanol. Geotherm. Res.*, *53*, 289–296.

Muskhelishvili N. (1963), *Some Basic Problems of the Mathematical Theory of Elasticity: Fundametal Equations, Plane Theory of Elasticity, Torsion and Bending*, Noordhoff.

Nattermann T. (1987), Interface roughening in systems with quenched random impurities, *Europhys. Lett*, *4*(1241), 343.

Nattermann T., Y. Shapir, and I. Vilfan (1990), Interface pinning and dynamics in random systems, *Physical Review B*, *42*(13), 8577–8586.

Nercessian A., A. Hirn, J. Lépine, and M. Sapin (1996), Internal structure of Piton de la Fournaise volcano from seismic wave propagation and earthquake distribution, *J. Volcanol. Geotherm. Res.*, *70*(3-4), 123–143.

Neuberg J. (2000), Characteristics and causes of shallow seismicity in andesite volcanoes, *Phil. Trans. R. Soc. Lond. A*, *358*(1770), 1533–1546.

Neuberg J., and T. Pointer (2000), Effects of volcano topography on seismic broad-band waveforms, *Geophys. J. Int.*, *143*(1), 239–248.

Neuberg J., R. Luckett, M. Ripepe, and T. Braun (1994), Highlights from a seismic broadband array on Stromboli volcano, *Geophys. Res. Lett.*, *21*(9), 749–752.

Neuberg J., B. Baptie, R. Luckett, and R. Stewart (1998), Results from the broadband seismic network on Montserrat, *Geophys. Res. Lett.*, *25*(19), 3661–3664.

Neuberg J., R. Luckett, B. Baptie, and K. Olsen (2000), Models of tremor and low-frequency earthquake swarms on Montserrat, *J. Volcanol. Geotherm. Res.*, *101*(1-2), 83–104.

Neuberg J., H. Tuffen, L. Collier, D. Green, T. Powell, and D. Dingwell (2006), The trigger mechanism of low-frequency earthquakes on Montserrat, *J. Volcanol. Geotherm. Res.*, *153*(1-2), 37–50.

Nishimura T., S. Ozawa, M. Murakami, T. Sagiya, T. Tada, M. Kaidzu, and M. Ukawa (2001), Crustal deformation caused by magma migration in the northern Izu Islands, Japan, *Geophys. Res. Lett.*, *28*(19), 3745–3748.

Noir J., E. Jacques, S. Bekri, P. Adler, P. Tapponnier, and G. King (1997), Fluid flow triggered migration of events in the 1989 Dobi earthquake sequence of Central Afar, *Geophys. Res. Lett.*, *24*(18), 2335–2338.

Ogata Y. (1988), Statistical models for earthquake occurrences and residual analysis for point processes, *Journal of the American Statistical Association*, *83*(401), 9–27.

Ogata Y. (1992), Detection of precursory relative quiescence before great earthquakes through a statistical model, *J. Geophys. Res.*, *97*(B13), 19,845–19,871.

Ogata Y. (1999), Seismicity Analysis through Point-process Modeling: A Review, *Pure Appl. Geophys.*, *155*(2), 471–507.

Ojala I., I. Main, and B. Ngwenya (2004), Strain rate and temperature dependence of Omori law scaling constants of AE data: Implications for earthquake foreshock-aftershock sequences, *Geophys. Res. Lett.*, *31*(L24617), doi:10.1029/2004GL020781.

Omori F. (1894), On the aftershocks of earthquakes, *J. Coll. Sci. Imp. Univ. Tokyo*, *7*, 111–120.

Omori F. (1911), The Usu-san Eruption and the Earthquake and Elevation Phenomena II: Comparison of the Bench Mark Heights in the Base District before and after the Eruption, *Bull. Imper. Earthq. Invest. Com.*, *5*, 1–38.

Omori F. (1912), Eruptions and Earthquakes of Asama-yama, *Bull. Imper. Earthq. Invest. Com.*, *6*, 1912–19.

Omori F. (1914), The Sakura-jima eruptions and earthquakes, *Bull. Imper. Earthq. Invest. Com.*, *8*, 1–6.

Omori F. (1922), The Sakura-jima Eruptions and Earthquakes VI [Notes on the Destructive Earthquake of Jan. 12, 1914, and Miscellaneous Remarks on the Eruptions of Sakura= jima]), *Bull. Imper. Earthq. Invest. Com.*, *8*, 467–524.

Ozawa S., S. Miyazaki, T. Nishimura, M. Murakami, M. Kaidzu, T. Imakiire, and X. Ji (2004), Creep, dike intrusion, and magma chamber deflation model for the 2000 Miyake eruption and the Izu islands earthquakes, *J. Geophys. Res.*, *109*(B02410), doi:10.1029/2003JB002601.

OâĂŹBrien G., and C. Bean (2004), A discrete numerical method for modeling volcanic earthquake source mechanisms, *J. Geophys. Res.*, *109*(B09301), doi:10.1029/2004JB003023.

Parsons T. (2002), Global Omori law decay of triggered earthquakes: Large aftershocks outside the classical aftershock zone, *J. Geophys. Res.*, *107*(B9), 2199, doi:10.1029/2001JB000646.

Pasteris J. (1984), Kimberlites: Complex Mantle Melts, *Annu. Rev. Earth Planet. Sci.*, *12*(1), 133–153.

Patané D., C. Chiarabba, O. Cocina, P. De Gori, M. Moretti, and E. Boschi (2002), Tomographic images and 3D earthquake locations of the seismic swarm preceding the 2001 Mt. Etna eruption: evidence for a dyke intrusion, *Geophys. Res. Lett.*, *29*(10), 1497.

Patané D., P. De Gori, C. Chiarabba, and A. Bonaccorso (2003), Magma ascent and the pressurization of Mount Etna's volcanic system, *Science*, *299*(5615), 2061–2063.

Patané D., M. Mattia, and M. Aloisi (2005), Shallow intrusive processes during 2002-2004 and current volcanic activity on Mt. Etna, *Geophys. Res. Lett.*, *32*(L06302), doi:10.1029/2004GL021773.

Pedersen R., F. Sigmundsson, and P. Einarsson (2007), Controlling factors on earthquake swarms associated with magmatic intrusions; Constraints from Iceland, *J. Volcanol. Geotherm. Res.*, *162*(1-2), 73–80.

Peltier A., V. Ferrazzini, T. Staudacher, and P. Bachèlery (2005), Imaging the dynamics of dyke propagation prior to the 2000–2003 flank eruptions at Piton de La Fournaise, Reunion Island, *Geophys. Res. Lett.*, *32*, doi:10.1029/2005GL023720.

Peltier A., T. Staudacher, and P. Bachèlery (2007), Constraints on magma transfers and structures involved in the 2003 activity at Piton de La Fournaise from displacement data, *J. Geophys. Res.*, *112*(B03207), doi:10.1029/2006JB0004379.

Peltier A., V. Famin, P. Bachčlery, V. Cayol, Y. Fukushima, and T. Staudacher (2008), Cyclic magma storages and transfers at Piton de La Fournaise volcano (La Réunion hotspot) inferred from deformation and geochemical data, *Earth and Planet. Sci. Lett.*, *270*, 180–188.

Peltier A., P. Bachèlery, and T. Staudacher (2009), Magma transport and storage at Piton de La Fournaise (La Réunion) between 1972 and 2007: A review of geophysical and geochemical data, *J. Volcanol. Geotherm. Res.*, *184*, 93–108.

Pinel V., and C. Jaupart (2000), The effect of edifice load on magma ascent beneath a volcano, *Phil. Trans. R. Soc. Lond. A*, *358*(1770), 1515–1532.

Pinel V., and C. Jaupart (2004), Magma storage and horizontal dyke injection beneath a volcanic edifice, *Earth and Planet. Sci. Lett.*, *221*(1-4), 245–262.

Pitcher W. (1979), The nature, ascent and emplacement of granitic magmas, *J. Geol. Soc.*, *136*(6), 627–662.

Pollard D. (1973), Derivation and evaluation of a mechanical model for sheet intrusions, *Tectonophysics*, *19*(3), 233–269.

Pollard D. (1988), Elementary fracture mechanics applied to the structural interpretation of dykes, in *Mafic Dyke Swarms*, pp. 5–24, Halls H.C. and Fahrig W.H. Geol Soc. Canada.

Powers P., and T. Jordan (2009), Distribution of Seismicity Across Strike-Slip Faults in California, *J. Geophys. Res.*, in press.

Prôno E., J. Battaglia, V. Monteiller, J. Got, and V. Ferrazzini (2009), P-wave velocity structure of Piton de la Fournaise volcano deduced from seismic data recorded between 1996 and 1999, *J. Volcanol. Geotherm. Res.*, *184*(1-2), 49–62.

Pyle D. (1998), Forecasting sizes and repose times of future extreme volcanic events, *Geology*, *26*(4), 367.

Ramanathan S., and D. Fisher (1997), Dynamics and instabilities of planar tensile cracks in heterogeneous media, *Phys. Rev. Lett*, *79*(5), 877–880.

Reasenberg P. (1985), Second-order moment of central California seismicity, 1969-1982, *J. Geophys. Res.*, *90*, 5479–5495.

Reid H. (1911), *The elastic-rebound theory of earthquakes*, University of California Press.

Reyes-Dávila G., and S. De la Cruz-Reyna (2002), Experience in the short-term eruption forecasting at Volcan de Colima, Mexico, and public response to forecasts, *J. Volcanol. Geotherm. Res.*, *117*(1-2), 121–127.

Rice J. (1968), Mathematical analysis in the mechanics of fracture, in *Fracture: An Advanced Treatise*, vol. 2, pp. 191–311, San Diego Academics.

Ripepe M., S. Ciliberto, and M. Della Schiava (2001), Time constraints for modeling source dynamics of volcanic explosions at Stromboli, *J. Geophys. Res.*, *106*(B5), 8713–8727.

Rittmann A., and M. Sato (1973), Structure and Evolution of Mount Etna [and Discussion], *Phil. Trans. R. Soc. London. A.*, pp. 5–16.

Rivalta E., and T. Dahm (2006), Acceleration of buoyancy-driven fractures and magmatic dikes beneath the free surface, *Geophys. J. Int.*, *166*(3), 1424–1439.

Rivalta E., M. Böttinger, and T. Dahm (2005), Buoyancy-driven fracture ascent: Experiments in layered gelatine, *J. Volcanol. Geotherm. Res.*, *144*(1-4), 273–285.

Rivera M., J. Thouret, and A. Gourgaud (1998), Ubinas, el volcán más activo del sur del Perú desde 1550: geología y evaluación de las amenazas volcánicas, *Boletín de la Sociedad geológica del Perú, Lima*, *88*, 53–71.

Rivera M., J. Mariño, L. Cacya, V. Cruz, and J. Thouret (2006), Evolution of the 2006 explosive activity of Ubinas volcano, Peru, *Ubinas Report*.

Roper S., and J. Lister (2005), Buoyancy-driven crack propagation from an over-pressured source., *J. Fluid Mech.*, *536*, 79–98.

Rosso A., and W. Krauth (2001), Origin of the roughness exponent in elastic strings at the depinning threshold, *Phys. Rev. Lett*, *87*(18), 187,002–187,002.

Rosso A., and W. Krauth (2002), Roughness at the depinning threshold for a long-range elastic string, *Phys. Rev. E*, *65*(025101), 1–4.

Rubin A. (1993a), Tensile fracture of rock at high confining pressure: implications for dyke propagation, *J. Geophys. Res.*, *98*(B 9), 15,919–15,935.

Rubin A. (1993b), Dikes vs. diapirs in viscoelastic rock, *Earth and Planet. Sci. Lett.*, *119*(4), 641–659.

Rubin A. (1995), Propagation of Magma-Filled Cracks, *Annu. Rev. Earth Planet. Sci.*, *23*(1), 287–336.

Rubin A., and D. Gillard (1998), Dike-induced earthquakes: Theoretical considerations, *J. Geophys. Res.*, *103*(B5), 10,017–10,030.

Rubin A., and D. Pollard (1987), Origins of blade-like dikes in volcanic rift zones, *Volcanism in Hawaii*, *2*, 1449–1470.

Rubin A., D. Gillard, and J. Got (1998), A reinterpretation of seismicity associated with the January 1983 dike intrusion at Kilauea Volcano, Hawaii, *J. Geophys. Res.*, *103*(B5), 10,003–10,015.

Ryan M. (1987), Neutral buoyancy and the mechanical evolution of magmatic systems, *Magmatic processes: physicochemical principles: a volume in honor of Hatten S. Yoder, Jr*, p. 259.

Saccorotti G., G. Ventura, and G. Vilardo (2002), Seismic swarms related to diffusive processes: The case of Somma-Vesuvius volcano, Italy, *Geophysics*, *67*, 199.

Saccorotti G., I. Lokmer, C. Bean, G. Di Grazia, and D. Patanè (2007), Analysis of sustained long-period activity at Etna Volcano, Italy, *J. Volcanol. Geotherm. Res.*, *160*(3-4), 340–354.

Sagiya T., S. Miyazaki, and T. Tada (2000), Continuous GPS Array and Present-day Crustal Deformation of Japan, *Pure Appl. Geophys.*, *157*(11-12), 2303–2322.

Sagy A., E. Brodsky, and G. Axen (2007), Evolution of fault-surface roughness with slip, *Geology*, *35*(3), 283.

Saichev A., and D. Sornette (2007), Theory of earthquake recurrence times, *J. Geophys. Res.*, *112*(B4), 4313.

Salminen L., A. Tolvanen, and M. Alava (2002), Acoustic emission from paper fracture, *Phys. Rev. Lett*, *89*(18), 185,503–185,503.

Salminen L., J. Pulakka, J. Rosti, M. Alava, and K. Niskanen (2006), Crackling noise in paper peeling, *Europhysics Letters*, *73*(1), 55–61.

Santacroce R. (1987), Somma-Vesuvius, *Quaderni della Ricerca Scientifica, CNR Roma*, *114*, 1–251.

Santucci S., L. Vanel, and S. Ciliberto (2004), Subcritical statistics in rupture of fibrous materials: experiments and model, *Phys. Rev. Lett*, *93*, 95,505–95,505.

Sapin M., A. Hirn, J. Lépine, and A. Nercessian (1996), Stress, failure and fluid flow deduced from earthquakes accompanying eruptions at Piton de la Fournaise volcano, *J. Volcanol. Geotherm. Res.*, *70*(3-4), 145–167.

Schmittbuhl J., and K. Måløy (1997), Direct observation of a self-affine crack propagation, *Phys. Rev. Lett*, *78*, 3888.

Schmittbuhl J., S. Roux, J. Vilotte, and K. Maloy (1995), Interfacial crack pinning: Effect of nonlocal interactions, *Phys. Rev. Lett*, *74*(10), 1787–1790.

Scholz C. (1968), Microfractures, aftershocks, and seismicity, *Bull. Seismol. Soc. America*, *58*(3), 1117–1130.

Scholz C. (2002), *The mechanics of earthquakes and faulting*, Cambridge University Press.

Segall P., E. Desmarais, D. Shelly, A. Miklius, and P. Cervelli (2006), Earthquakes triggered by silent slip events on Kilauea volcano, Hawaii, *Nature*, *442*(7098), 71.

Sethna J., K. Dahmen, and C. Myers (2001), Crackling noise, *Nature*, *410*(6825), 242–250.

Shaw H. (1980), The fracture mechanisms of magma transport from the mantle to the surface, *Phys. Magmat. Proc.*, pp. 201–264.

Shlien S., and M. Nafi Toksoz (1970), A clustering model for earthquake occurrences, *Bull. Seismol. Soc. America*, *60*(6), 1765–1787.

Sigmarsson O., M. Condomines, and P. Bachèlery (2005), Magma residence time beneath the Piton de la Fournaise Volcano, Reunion Island, from U-series disequilibria, *Earth and Planet. Sci. Lett.*, *234*(1-2), 223–234.

Sigurdsson H., B. Houghton, S. McNutt, H. Rymer, J. Stix, and A. McBirney (2000), *Encyclopedia of volcanoes*, Academic Press, Elsevier.

Smith K., D. von Seggern, G. Blewitt, L. Preston, J. Anderson, B. Wernicke, and J. Davis (2004), Evidence for Deep Magma Injection Beneath Lake Tahoe, Nevada-California, *Science*, *305*(5688), 1277–1280.

Smithsonian Institute (2009), Global Volcanism Project, web adress: http://www.volcano.si.edu/world/.

Sparks R. (2003), Forecasting volcanic eruptions, *Earth and Planet. Sci. Lett.*, *210*(1-2), 1–15.

Spence D., and P. Sharp (1985), Self-similar solutions for elastohydrodynamic cavity flow, *Proc. R. Soc. London A.*, pp. 289–313.

Spence D., and D. Turcotte (1985), Magma-driven propagation of cracks, *J. Geophys. Res.*, *90*(B1), 575–580.

Spence D., and D. Turcotte (1990), Buoyancy-driven magma fracture: a mechanism for ascent through the lithosphere and the emplacement of diamonds, *J. Geophys. Res.*, *95*, 5133–5139.

Spence D., P. Sharp, and D. Turcotte (1987), Buoyancy-driven crack propagation: a mechanism for magma migration, *J. Fluid Mech.*, *174*, 135–153.

Spera F. (1980), Aspects of magma transport, *Phys. Magmat. Proc.*, pp. 265–323.

Steacy S., J. Gomberg, and M. Cocco (2005), Introduction to special section: Stress transfer, earthquake triggering, and time-dependent seismic hazard, *J. Geophys. Res.*, *110*(B05S01), doi:10.1029/2005JB003692.

Stein R. (1999), The role of stress transfer in earthquake occurrence, *Nature*, *402*(6762), 605–609.

Stein R., and M. Lisowski (1983), The 1979 Homestead Valley earthquake sequence, California: control of aftershocks and postseismic deformation, *J. Geophys. Res.*, *88*, 6477–6490.

Stein R., G. King, and J. Lin (1994), Stress triggering of the 1994 M= 6.7 Northridge, California, earthquake by its predecessors, *Science*, *265*(5177), 1432–1435.

Taisne B., and C. Jaupart (2009), Dyke Propagation Through Layered Rocks, *J. Geophys. Res.*, doi:10.1029/2008JB006228, in press.

Tajima F., and H. Kanamori (1985a), Global survey of aftershock area expansion patterns, *Phys. Earth Planet. Inter*, *40*(2), 77–134.

Tajima F., and H. Kanamori (1985b), Aftershock area expansion and mechanical heterogeneity of fault zone within subduction zones, *Geophys. Res. Lett.*, *12*, 345–348.

Takada A. (1990), Experimental study on propagation of liquid-filled crack in gelatin: shape and velocity in hydrostatic stress condition, *J. geophys. Res*, *95*, 8471–8481.

Tanguy A., M. Gounelle, and S. Roux (1998), From individual to collective pinning: Effect of long-range elastic interactions, *Phys. Rev. E*, *58*(2), 1577–1590.

Tanguy J. (1981), Les éruptions historiques de lâĂŹEtna: chronologie et localisation, *Bull. Volcanol.*, *44*(3), 585–640.

Thouret J., M. Rivera, G. Wörner, M. Gerbe, A. Finizola, M. Fornari, and K. Gonzales (2005), Ubinas: the evolution of the historically most active volcano in southern Peru, *Bull. Volcanol.*, *67*(6), 557–589.

Tilling R., and J. Dvorak (1993), Anatomy of a basaltic volcano, *Nature*, *363*, 125–133.

Tinard P. (2007), Caractérisation et modélisation des déplacements du sol associés a l'activité volcanique du Piton de la Fournaise, ile de la Réunion, a partir de donées interférométriques. Aout 2003 - Avril 2007, Ph.D. thesis, Université Blaise Pascal - Clermont-Ferrand II.

Toda S., R. Stein, and T. Sagiya (2002), Evidence from the AD 2000 Izu islands earthquake swarm that stressing rate governs seismicity, *Nature*, *419*(6902), 58–61.

Toda S., R. Stein, K. Richards-Dinger, and S. Bozkurt (2005), Forecasting the evolution of seismicity in southern California: Animations built on earthquake stress transfer, *J. Geophys. Res.*, *110*(B05S16), doi:10.1029/2004JB003415.

Touati S., M. Naylor, and I. Main (2009), Origin and Nonuniversality of the Earthquake Interevent Time Distribution, *Phys. Rev. Lett*, *102*, 168,501.

Toutain J., P. Bachelery, P. Blum, J. Cheminee, H. Delorme, L. Fontaine, P. Kowalski, and P. Taochy (1992), Real time monitoring of vertical ground deformations during eruptions at Piton de la Fournaise, *Geophys. Res. Lett.*, *19*(6), 553–556.

Traversa P., and J. Grasso (2009-Chapter2), Brittle Creep Damage as the Seismic Signature of Dyke Propagations within Basaltic Volcanoes, *Bull. Seismol. Soc. America*, *99*(3), 2035–2043.

Traversa P., and J. Grasso (2010-Chapter6), How Volcano Seismicity is Different from Tectonic Seismicity, *Bull. Seismol. Soc. America*, in press.

Traversa P., J. Grasso, O. Lengliné, and V. Ferrazzini (2009-Chapter5), Seismic Signature of Magma Reservoir Dynamics at Basaltic Volcanoes, lesson from the Piton de la Fournaise Volcano, in *The VOLUME Project - VOLcanoes, Understanding Mass MovEments*, edited by C. Bean, B. A.K., I. Lokmer, F. Martini, and G. O'Brien, pp. 271–287, VOLUME Project EU PF6 (N. 018471) Consortium, Dublin.

Traversa P., V. Pinel, and J. Grasso (2010-Chapter3), A Constant Influx Model for Dyke Propagation. Implications for Magma Reservoir Dynamics, *J. Geophys. Res.*, *115*(B01201), doi:10.1029/2009JB006559.

Tsuboi C. (1954), Determination of the Gutenberg-Richter's magnitude of earthquakes occurring in and near Japan, *J. Seism. Soc. Japan*, *7*, 185–193.

Tuffen H., D. Dingwell, and H. Pinkerton (2003), Repeated fracture and healing of silicic magma generate flow banding and earthquakes?, *Geology*, *31*(12), 1089–1092.

Tuffen H., R. Smith, and P. Sammonds (2008), Evidence for seismogenic fracture of silicic magma, *Nature*, *453*(7194), 511–514.

Tybell T., P. Paruch, T. Giamarchi, and J. Triscone (2002), Domain Wall Creep in Epitaxial Ferroelectric Pb(Zr0.2Ti0.8)O3 Thin Films, *Phys. Rev. Lett*, *89*(9), 97,601–97,601.

Ueda H., E. Fujita, M. Ukawa, E. Yamamoto, M. Irwan, and F. Kimata (2005), Magma intrusion and discharge process at the initial stage of the 2000 activity of Miyakejima, Central Japan, inferred from tilt and GPS data, *Geophys. J. Int.*, *161*(3), 891–906.

Uhira K., T. Baba, H. Mori, H. Katayama, and N. Hamada (2005), Earthquake swarms preceding the 2000 eruption of Miyakejima volcano, Japan, *Bull. Volcanol.*, *67*(3), 219–230.

Utsu T. (1961), A statistical study on the occurrence of aftershocks, *Geophys. Mag*, *30*(4), 521–605.

Utsu T. (1970), Aftershocks and earthquake statistics (II)–Further investigation of aftershocks and other earthquake sequences based on a new classification of earthquake sequences, *J. Faculty Sci., Hokkaido Univ*, *3*, 197–266.

Utsu T. (1972a), Aftershocks and earthquake statistics (IV), *J. Fac. Sci. Hokkaido Univ. Ser. VII Geophys*, *4*, 1–42.

Utsu T. (1972b), Large earthquakes near Hokkaido and the expectancy of the occurrence of a large earthquake off Nemuro, *Report of the Coordinating Committee for Earthquake Prediction*, *7*, 7–13.

Utsu T. (2002), Statistical features of seismicity, *International Handbook of Earthquake & Engineering Seismology*, pp. 719–32.

Utsu T., Y. Ogata, and R. Matsu'ura (1995), The centenary of the Omori formula for a decay law of aftershock activity, *Journal of Physics of the Earth*, *43*(1), 1–33.

Varley N., J. Johnson, M. Ruiz, G. Reyes, K. Martin, F. de Ciencias, and M. Colima (2006), Applying statistical analysis to understanding the dynamics of volcanic explosions, in *Statistics in Volcanology*, edited by H. Mader, S. Coles, C. Connor, and L. Connor, pp. 57–76, Special Publications of the International Association of Volcanology and Chemistry of the Earth's Interior, London.

Vere-Jones D. (1970), Stochastic models for earthquake occurrence, *J. Royal Statist. Soc. B*, *32*(1), 1–62.

Vere-Jones D., and R. Davies (1966), A statistical survey of earthquakes in the main seismic area of New Zealand. Part II: Time series analysis, *NZJ Geol. Geophys*, *9*, 251–284.

Vidale J., and P. Shearer (2006), A survey of 71 earthquake bursts across southern California: Exploring the role of pore fluid pressure fluctuations and aseismic slip as drivers, *J. Geophys. Res.*, *111*(B05312), doi:10.1029/2005JB004034.

Villeneuve N., D. Neuville, P. Boivin, P. Bachèlery, and P. Richet (2008), Magma crystallization and viscosity: A study of molten basalts from the Piton de la Fournaise volcano (La Réunion island), *Chemical Geology*, *256*(3-4), 241–250.

Voight B. (1988), A method for prediction of volcanic eruptions, *Nature*, *332*(6160), 125–130.

Voight B., and R. Cornelius (1991), Prospects for eruption prediction in near real-time, *Nature*, *350*, 695–698.

Wadge G., and M. Isaacs (1988), Mapping the volcanic hazards from Soufriere Hills Volcano, Montserrat, West Indies using an image processor, *J. Geol. Soc. London*, *145*(4), 541–551.

Weertman J. (1971a), Theory of water-filled crevasses in glaciers applied to vertical magma transport beneath oceanic ridges, *J. Geophys. Res.*, *76*(5), 1171–1183.

Weertman J. (1971b), Velocity at which liquid-filled cracks move in the Earth's crust or in glaciers, *J. Geophys. Res.*, *76*, 8544–8553.

Weiss J., and D. Marsan (2003), Three-dimensional mapping of dislocation avalanches: clustering and space/time coupling, *Science*, *299*(5603), 89–92.

Wells D., and K. Coppersmith (1994), New empirical relationships among magnitude, rupture length, rupture width, rupture area, and surface displacement, *Bull. Seismol. Soc. America*, *84*(4), 974–1002.

Wickman F. (1966), Repose period patterns of volcanoes, *Ark. Mineral. Geol*, *4*, 291–367.

Wickman F. (1976), Markov models of repose-period patterns of volcanoes, *Random Processes in Geology*, pp. 135–161.

Wright T., C. Ebinger, J. Biggs, A. Ayele, G. Yirgu, D. Keir, and A. Stork (2006), Magma-maintained rift segmentation at continental rupture in the 2005 Afar dyking episode, *Nature*, *442*, 291–294.

Wyss M., K. Shimazaki, and S. Wiemer (1997), Mapping active magma chambers by b values beneath the off-Ito volcano, Japan, *J. Geophys. Res.*, *102*(B9), 20,413–20,422.

Yamaoka K., M. Kawamura, F. Kimata, N. Fujii, and T. Kudo (2005), Dike intrusion associated with the 2000 eruption of Miyakejima Volcano, Japan, *Bull. Volcanol.*, *67*(3), 231–242.

Yu Y., and P. Karenlampi (1997), On crack stability in paper toughness testing, *Journal of Materials Science*, *32*(24), 6513–6517.

Zapperi S., P. Ray, H. Stanley, and A. Vespignani (1997), First-Order Transition in the Breakdown of Disordered Media, *Phys. Rev. Lett*, *78*(8), 1408–1411.

Zhuang J., Y. Ogata, and D. Vere-Jones (2002), Stochastic Declustering of Space-Time Earthquake Occurrences, *Journal of the American Statistical Association*, *97*(458), 369–380.

Zimanowski B. (1998), Phreatomagmatic explosions, *From magma to tephra*, pp. 25–54.

Zobin V. (2003), *Introduction to volcanic seismology*, Elsevier Science.

Zollo A., W. Marzocchi, P. Capuano, A. Lomax, and G. Iannaccone (2002), Space and time behavior of seismic activity at Mt. Vesuvius volcano, southern Italy, *Bull. Seismol. Soc. America*, *92*(2), 625–640.